7. SITE 797[1]

Shipboard Scientific Party[2]

HOLE 797A

Date occupied: 31 July 1989

Date departed: 31 July 1989

Time on hole: 8 hr

Position: 38.616°N, 134.536°E

Bottom felt (rig floor; m, drill-pipe measurement): 2873.6

Distance between rig floor and sea level (m): 11.4

Water depth (drill-pipe measurement from sea level, m): 2862.2

Total depth (rig floor, m): 2886.33

Penetration (m): 3.4–12.73

Number of cores (including cores with no recovery): 1

Total length of cored section (m): 9.5

Total core recovered (m): 9.73

Core recovery (%): 102

Oldest sediment cored:
Depth (mbsf): 12.90
Nature: clay/silty clay
Age: Quaternary
Measured velocity (km/s): 1.57

Comments: Overshot mud line

HOLE 797B

Date occupied: 31 July 1989

Date departed: 4 August 1989

Time on hole: 3 days, 21 hr, 30 min

Position: 38.616°N, 134.536°E

Bottom felt (rig floor; m, drill-pipe measurement): 2873.6

Distance between rig floor and sea level (m): 11.4

Water depth (drill-pipe measurement from sea level, m): 2862.2

Total depth (rig floor, m): 3369.3

Penetration (m): 495.7

Number of cores (including cores with no recovery): 53

Total length of cored section (m): 495.7

Total core recovered (m): 370.69

Core recovery (%): 74

Oldest sediment cored:
Depth (mbsf): 495.7
Nature: claystone
Age: middle Miocene
Measured velocity (km/s): 1.7

HOLE 797C

Date occupied: 4 August 1989

Date departed: 18 August 1989

Time on hole: 14 days

Position: 38.616°N, 134.536°E

Bottom felt (rig floor; m, drill-pipe measurement): 2876.0

Distance between rig floor and sea level (m): 11.4

Water depth (drill-pipe measurement from sea level, m): 2864.6

Total depth (rig floor, m): 3776.1

Penetration (m): 900.1

Number of cores (including cores with no recovery): 45

Total length of cored section (m): 416.1

Total core recovered (m): 164.18

Core recovery (%): 39

Oldest sediment cored:
Depth (mbsf): 553.4
Nature: claystone
Age: early Miocene or older
Measured velocity (km/s): 2.05

Hard rock:
Depth (mbsf): 900.1
Nature: basalt
Measured velocity (km/s): 4.9

Principal results: The objectives at Site 797, located in the southern Yamato Basin, were (1) to determine the age and nature of acoustic basement, (2) to measure the direction and magnitude of the present stress field, and (3) to characterize the sedimentation, subsidence, and oceanographic evolution of the area. The results at Site 797 are summarized below and in Figure 1. The principal results at Site 797 are as follows:

1. Acoustic basement and an overlying seismic interval at this site comprise basalts and dolerites and interlayered volcaniclastic sandstones, siltstones, and silty claystones. The age of the sediments which overlie the shallowest basalt layer is estimated to be about 19 Ma. Based on paleodepth estimates using microfossils within these sediments and the sedimentologic interpretation of the underlying volcaniclastic sediments, this part of the Yamato Basin probably subsided rapidly during the early Miocene. The uppermost basalts most likely represent submarine lava flows, whereas the bulk of the underlying igneous units are sills and dikes. The upper nine units are high-Al basalt in composition, consistent with generation during the early stages of arc rifting. However, the units below these are mildly alkaline basalts and enriched tholeiites, which are unrelated to the overlying basalts and were probably derived from a different mantle source.

2. The *in-situ* stress field could not be determined, because poor hole conditions precluded packer/hydrofracture tests. A borehole televiewer log over one basalt interval showed fractures but no borehole breakouts for stress directions.

3. The lithologic and paleontological data indicate at least four principal stages in the evolution of this part of the Yamato Basin: (a) an early Miocene period of submarine basaltic volcanism and concomitant deposition of gravity-flow and current-reworked volcani-

clastic sandstones and siltstones on a shelf or slope, probably outboard of a delta; (b) a late early to early middle Miocene phase of diminishing submarine volcanic activity, warm surface waters, and deposition of calcareous and slightly phosphatic hemipelagic claystones at lower middle bathyal depths (1500–2000 m) in a poorly oxygenated basin; (c) a late Miocene to late Pliocene cooling period beginning with an interval of anomalously slow sedimentation (5 m/m.y.) or a hiatus and characterized by dominant but variable diatomaceous sedimentation at lower middle bathyal depths (1500–2000 m); and (d) a latest Pliocene to Holocene stage during which diatomaceous sedimentation diminished volcanic-ash production and terrigenous input increased, subsidence continued, and climate oscillated to produce a sequence of interlayered light- and dark-colored silty clays having variable organic-carbon contents. In contrast with the more northern sites drilled during Leg 127, the sediments at Site 797 contain more carbonate suggesting that the site was at or near the carbonate compensation depth (CCD) throughout much of its sedimentary history. Dissolution of silica is pronounced at this site, and the opal-A/opal-CT and opal-CT/quartz diagenetic transitions are well defined.

Location and Approach

Site 797 is located in the southwestern Yamato Basin at the base of the slope leading to the Yamato Rise and the Kita-Oki Bank and slightly northwest of approved location J-1e. The site was confirmed by two *JOIDES Resolution* seismic lines, one bearing northwest, the other southwest. Both lines are parallel to preexisting seismic lines. The beacon was launched on the second crossing of the northwest-southeast *JOIDES Resolution* line in order to avoid any local closures and to select the most promising seismic character for acoustic basement.

Lithology

The sedimentary section cored in Holes 797A, 797B, and 797C consists of lower Miocene to Quaternary mostly fine-grained hemipelagic diatomaceous and terrigenous sediments with minor tuff. The division of units is as follows:

Unit I: 10–119.9 mbsf; Quaternary–late Pliocene

Silty clay and clay. The upper 82 m of this unit is color banded, light and dark silty clay and clay with minor diatom ooze and scattered thin ash layers. Dark layers are moderately well laminated, decrease in abundance with depth, and have common pyrite, diatoms, and organic matter. Light layers are bioturbated or faintly laminated. Subtle size grading occurs in the silty clays. The lower 38 m is similar but with increasing diatom content and bioturbation.

Unit II: 119.9–224.0 mbsf; late Pliocene–early Pliocene

Diatom clay and clayey diatom ooze. A high diatom content characterizes this unit, which consists of diatom clay and ooze. All lithologies are extensively bioturbated. Minor dolomitic zones and nodules and some ash occur.

Unit III: 224.0–301.5 mbsf; early Pliocene–late Miocene

Diatom clay and silty claystone. This unit is mostly bioturbated to indistinctly mottled diatom clay and silty claystone with scattered thin layers of bioclastic sand, minor ash, and carbonate layers and nodules. Faint to distinct light and dark color banding is common. Sands contain foraminifers, sponge spicules, quartz, and feldspar. The opal-A/opal-CT boundary occurs at 299 mbsf. Sponge spicules increase and diatoms decrease downsection.

Unit IV: 301.5–426.6 mbsf; late–middle Miocene

Claystone, silty claystone, and siliceous claystone. Claystone and siliceous claystone characterize this unit. The upper 48.5 m consists of indistinctly color-banded layers. Dark layers are faintly laminated to slightly bioturbated; light layers are moderately to extensively bioturbated and characterized by compacted, horizontal burrows. Secondary-carbonate layers are common. Chert occurs rarely. The lower 76.6 m consists of interbedded claystone, siliceous claystone, porcellanite, and chert, which are moderately to extensively bioturbated. Chert is common. One thin,

carbonate-cemented, lithic sandstone layer occurs in this interval. The sandstone is normally graded and contains faint laminations.

Unit V: 426.6–627.3 mbsf; middle–early Miocene

Siliceous claystone, phosphatic and calcareous claystone, and tuff. This unit consists mostly of faintly laminated claystone with numerous horizontal, compacted burrows. The claystone is slightly siliceous near the top of the unit but becomes hard and carbonate-cemented at the base. Small, vertically anastomosing, clay-filled fractures are common in the claystone. Stringers and small nodules of secondary carbonate, pyrite, and thin glauconitic layers are also present. Altered tuff layers, up to 10 cm thick, and rare layers of tuffaceous sandstone, occur throughout the unit. The lower 73 m of this unit contains interbedded basalts. The sediments of this part of the unit are claystones similar to those above, and conglomerate composed entirely of porcellanite pebbles in a siliceous claystone matrix.

Unit VI: 646.9–900.1 mbsf; early Miocene

Sandstone, siltstone, and silty claystone. Interbedded volcaniclastic and carbonaceous siltstone, sandstone, and minor silty claystone characterize the sediments of this unit. These rocks occur in intervals 1–10 m thick, which are interbedded with basalts. Planar and cross-laminations, normal size grading, scoured surfaces, load structures, fluid-escape features, and extensive grain alteration to clay are common throughout the sandstones. The siltstones are planar laminated and commonly contain flattened, bedding-parallel lenses of darker siltstone which may represent either burrows or rip-up clasts or both. Rare primary dips to 30° and associated small-scale slump structures are present.

Age and Sedimentation Rates

Sedimentation rates are well constrained by diatom zones and, to a lesser degree, by paleomagnetic data in Units I through III (0–301 mbsf). Below this level, all diatoms have been dissolved except those protected in calcareous concretions. Units IV, V, and VI are dated using these sporadic samples together with sparse control from foraminifers, radiolarians, and calcareous nannofossils. The oldest paleontological controls are the top and bottom of the middle Miocene calcareous nannofossil *Sphenolithus heteromorphus* Zone, which occur at 438 and 494 mbsf. The age of the sediment which overlies the shallowest basalt unit at 553.5 mbsf is about 19 Ma, based on extrapolation of the sedimentation rate calculated using the three deepest nannofossil datums. Using all of the age data, sedimentation rates are 20–25 m/m.y. for the early and early middle Miocene, 5 m/m.y. for of the late Miocene, 43–56 m/m.y. for the latest Miocene and Pliocene, and 46 m/m.y. for the Quaternary. Because of the lack of microfossil control, the sedimentation rate for the lower Miocene volcaniclastic sandstones, siltstones, and silty claystones which are interbedded with the basalts in the lower part of the section is unknown.

Paleomagnetism

The intensity of magnetization of the sediments at Site 797 is generally quite weak, with a mean value of about 1 mA/m. Sediments cored using the APC yielded a recognizable polarity from the Brunhes Chron to the Mammoth Subchron. Below 170 mbsf, the polarity record is not resolvable, owing to core disturbance caused by XCB coring.

Sediments interbedded with the basaltic sills sometimes showed reversals associated with baking upon intrusion. The magnetic susceptibility of the basalts showed a close correlation with chemistry, with the upper group of high-Al basalts having lower susceptibilities (generally below 2000×10^{-6} cgs units) than the lower group of altraline and tholeiitic basalts (to 8000×10^{-6} units.).

Geochemistry

The sediments from Site 797 are characterized by an increase in diagenetic silica below about 300 mbsf and by moderate but variable amounts of organic carbon (TOC range, 0.2%–8.5%, avg. 1.0%) and carbonate. Diatoms and dissolved silica contents of interstitial waters decrease markedly below about 300 mbsf. This diagenetic boundary restricts fluid communication and divides the sedimentary section into upper and lower diffusive regimes. Carbonate values are generally less than 5% below about 300 mbsf, but intervals having

5%–20% $CaCO_3$ against a very low background level occur above this depth. The organic-carbon content fluctuates between high and low values coincident with dark and light interlayering in the Quaternary and uppermost Pliocene sediments. Organic-carbon values are also high in the uppermost Miocene diatomaceous sediments (290–330 mbsf). Organic matter is derived from both terrestrial and algal sources. Sulfate is present throughout the section and reflects variations in the sedimentation rates and organic matter. Sulfate shows two peaks, one near the seafloor and a smaller peak at 350 mbsf. Small amounts of methane (3–200 ppm) occurred, with only traces of ethane and propane, but no safety problems related to gas were encountered.

Igneous Rocks

High-Al basalt, mildly alkaline basalt, and enriched tholeiitic basalt interlayered with sediments represent acoustic basement and an overlying seismic interval cored in Hole 797C. These igneous rocks describe two broad and overlapping groups containing 21 separate units which are defined on the basis of contact relations, intervening sedimentary rocks, composition, and texture.

Group 1: Units 1, 2, and 4 (553.5–609.4 mbsf)

These rocks consist of aphyric and sparsely plagioclase olivine phyric basalts interbedded with conglomerate and tuffaceous claystone of sedimentary Unit V. Their brecciated and highly fractured nature, relatively fine grain size, and lack of chilled margins indicate that they most likely represent submarine lava flows. Unit 1 consists of a loose breccia with intercalated clasts of conglomerate and is perhaps a talus deposit. Units 1 and 2 are petrographically and compositionally similar, although highly altered, and may have erupted during the same effusive episode.

Group 2: Units 3 and 5–21 (580.2–900.1 mbsf)

The igneous rocks of this group consist of typically highly altered aphyric and sparsely plagioclase phyric basalt and dolerite interlayered with laminated sandstones, siltstones, and claystones of sedimentary Unit VI and tuffaceous claystones of sedimentary Unit V. Some of the basalts are only slightly to moderately altered. Their massive nature, relatively coarse grain size, and chilled borders, the latter often associated with baked or alteration margins affecting both the basalts and sediments, indicate that they represent intrusive sills and dikes.

The upper nine igneous units of Hole 797C are high-alumina basalts with low amounts of the large-ion lithophile elements Rb, Ba, and K, and low amounts of Nb and Ce. Some are quite primitive, with several samples having MgO, Cr, and Ni values exceeding 10%, 150 ppm, and 350 ppm, respectively. They are rich in Al_2O_3, show no decrease in Al_2O_3 with lowering MgO, and lack an iron-enrichment trend. These two features imply that the samples have relatively high water contents, which caused suppression of plagioclase. The extremely low Nb contents are consistent with an arc-related origin, but the low incompatible-element contents (with the possible exception of Sr) indicate that the lavas interacted very little with continental crust. In contrast, the lowermost sills and dikes are alkali basalts and enriched tholeiites containing large amounts of the high field-strength elements Zr, Y, Ti, and Nb; high amounts of the alkalis; and high Rb, Ba, and Ce. These upper and lower suites of igneous rocks are genetically unrelated, with the lower suite of rocks lacking typical arc signatures. The geologic setting of this site and the igneous compositions suggest that these intrusive and extrusive rocks were emplaced and erupted during the rifting apart of a volcanic arc. The relative timing of emplacement of the different compositional suites is unknown.

Seismic Stratigraphy

Six distinct seismic intervals occur at this site. From top to bottom, these are (1) an upper weakly stratified interval, (2) a transparent interval, (3) a faintly stratified interval, (4) a well-stratified interval, (5) a lowermost irregularly stratified interval, and (6) an unstratified, acoustically opaque zone. Interval 1 correlates with Unit I. Interval 2 corresponds to Units II and III. Interval 3 correlates with

Subunit IVA. The opal-A/opal-CT diagenetic boundary is in the uppermost part of Interval 3. Interval 4 correlates with Subunit IVB and the upper part of Unit V. Interval 5 correlates with the interbedded part of the basalt and sedimentary rocks of Unit V. The last interval represents acoustic basement and correlates with the lowermost part of Unit V and Unit VI. It is composed of interbedded sedimentary rocks and basalt sills and flows and is representative of much of the acoustic basement of the Yamato Basin. Seismic reflection alone cannot address the thickness of this interbedded sequence.

Heat Flow

Successful temperature measurements were made using the Uyeda probe at six points down to 185.5 mbsf in Hole 797B. The measured gradient is 121°C/km. The calculated heat-flow value using this gradient and measured thermal conductivities is 101 mW/m². This value is identical to a nearby seafloor measurement and similar to the average heat flow for the entire Yamato Basin (97 ± 12 mW/m²).

Logging and Physical Properties

Successful logging runs were completed in the upper part of Hole 797C between 80 and 516 mbsf. The combination sonic/lithodensity/temperature/induction string and the formation microscanner (FMS) log were run in the open hole over this interval. Below 516 mbsf, logging was restricted by unstable hole conditions caused by rapidly swelling clays in highly altered tuffs and volcaniclastic strata. The geochemical log was run behind pipe from 0 to 633 mbsf, and partial runs were made with the FMS (485–610 mbsf) and the borehole televiewer (549–603 mbsf) using the side-entry sub. The rotatable, single-element packer was in the drill string during the logging runs, but poor hole conditions precluded its use. The logging data above 516 mbsf provide a useful characterization of the sediments, particularly over the chert and porcellanite interval (350–430 mbsf), where recovery was poor. The geochemical and FMS logs provided compositional and structural data in the uppermost interbedded basalts and sediments.

Physical properties correlate well with lithologic variation observed at Site 795 and show striking similarity to profiles observed at Site 794. Within the sedimentary section, the most conspicuous changes in physical properties occur at the opal-A/opal-CT boundary. Within the underlying interbedded sediments and basalts, physical properties clearly delineate the igneous and sedimentary lithologies and show qualitative correlation to degrees of alteration in the basalt.

BACKGROUND AND OBJECTIVES

Background

Location and Bathymetry

Site 797 lies in the south-central Japan Sea, about 300 km from the western coast of Honshu (Fig. 2). It is situated in the southwestern Yamato Basin in 2869 m of water at the base of the slope which connects the Yamato Rise and the Kita-Oki Bank. Immediately north of the site lies the Yamato Bank, a shallow (250 mbsl), 280-km-long, northeast-southwest-trending, flat-topped ridge. This bank is one of three principal highs making up the Yamato Rise. It is paired with a similar high to the northwest, the Kita-Yamato Bank, and is separated from it by the deep and narrow Kita-Yamato Trough (Fig. 2). West of Site 797 is a broad bathymetric sill that connects the Yamato Bank with the shallow (400 mbsl), flat-topped Kita-Oki Bank to the south. This bank also trends northeast-southwest but is much broader and shows less relief than the Yamato Bank. A large and fairly wide canyon breaches the northeastern flank of this high; its northeast projection passes just southeast of the site.

To the east and southeast of Site 797 lies the flat floor of the Yamato Basin. This abyssal plain is punctuated in places by seamounts that constitute the southwesternmost elements of the Yamato seamount chain. The closest seamount lies approximately 65 km east of the site.
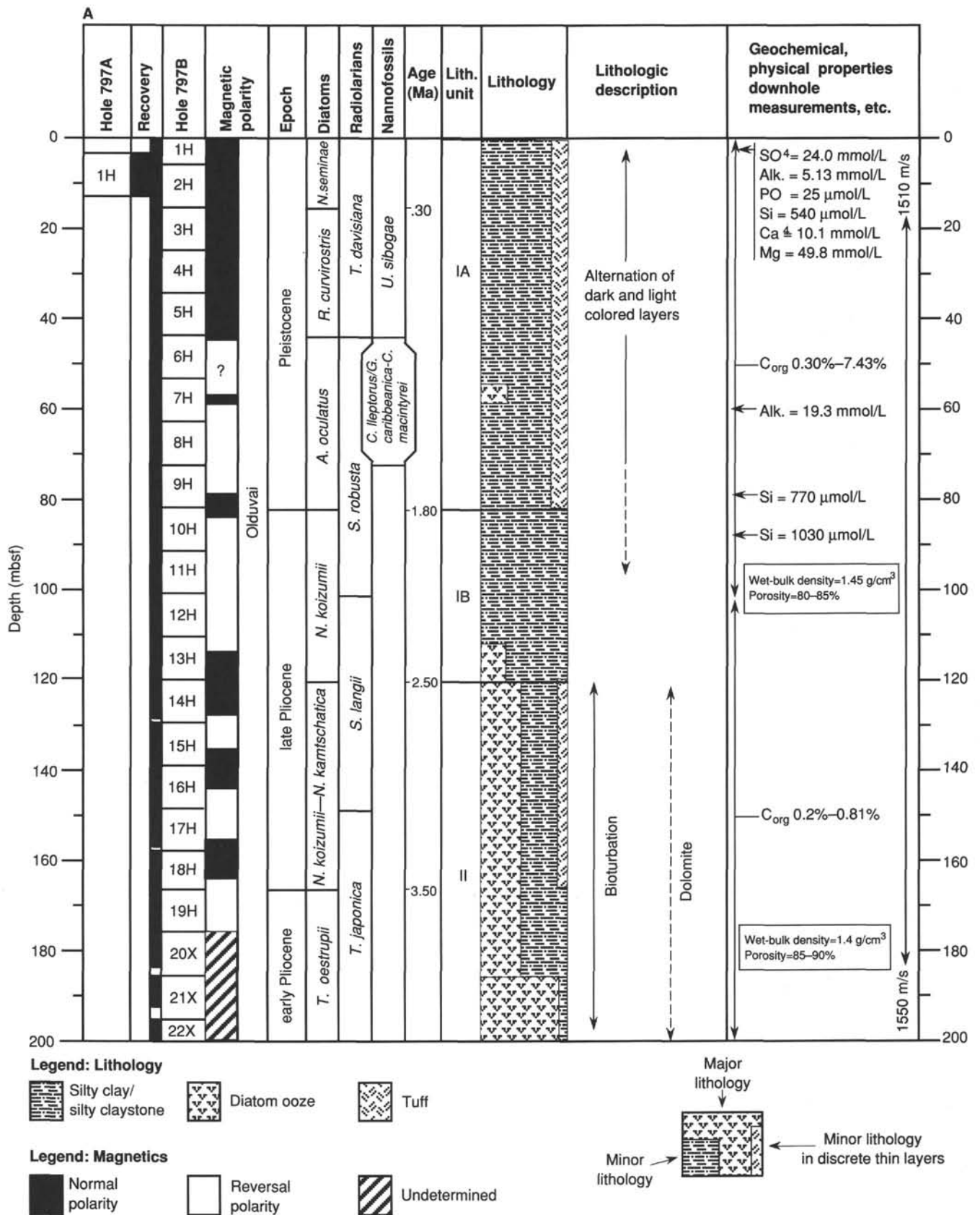
Figure 1. Stratigraphic summary column for Site 797.
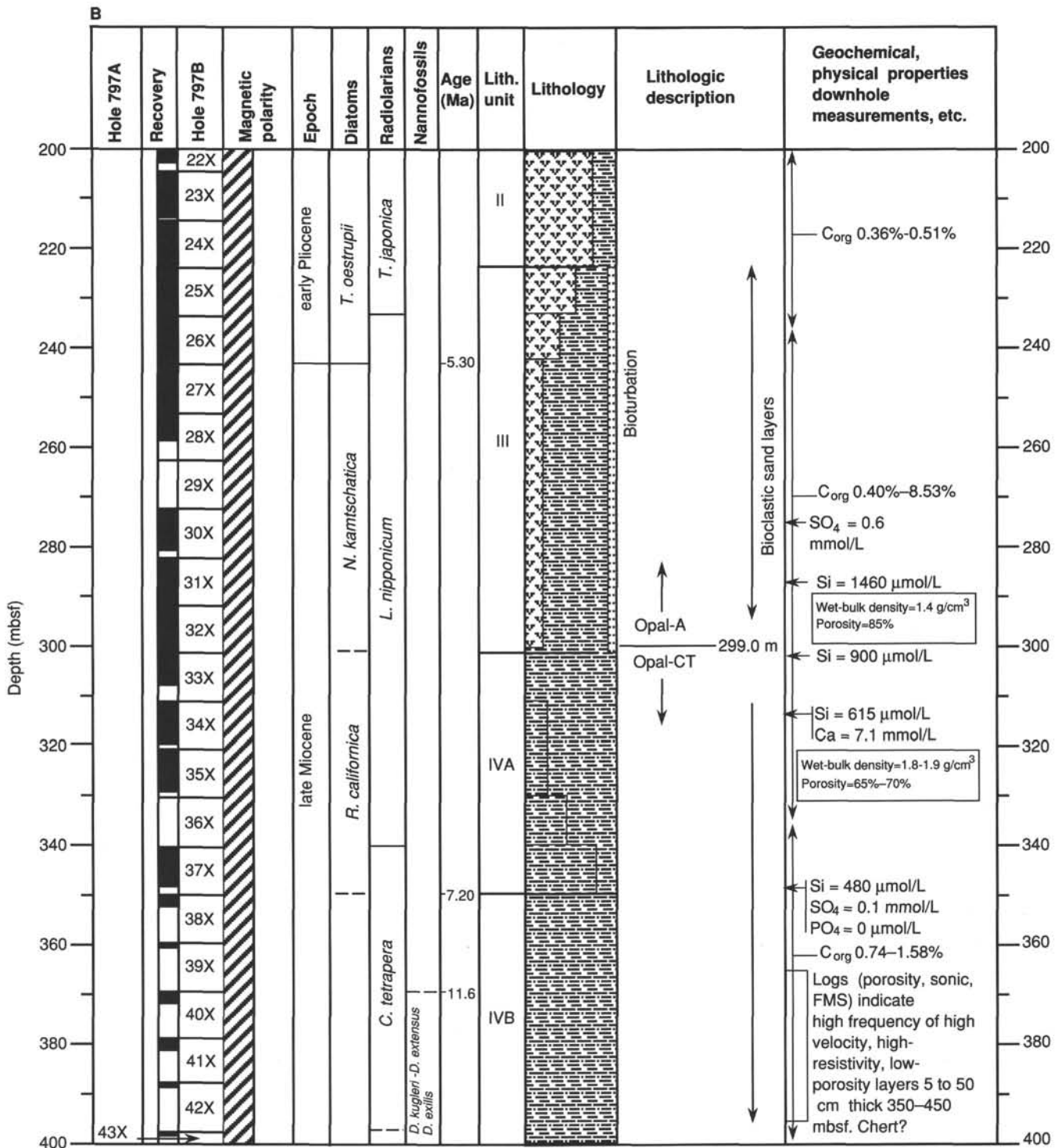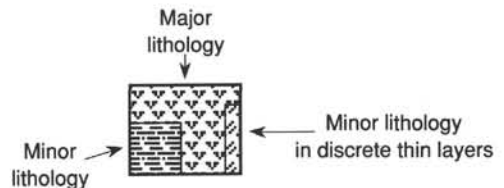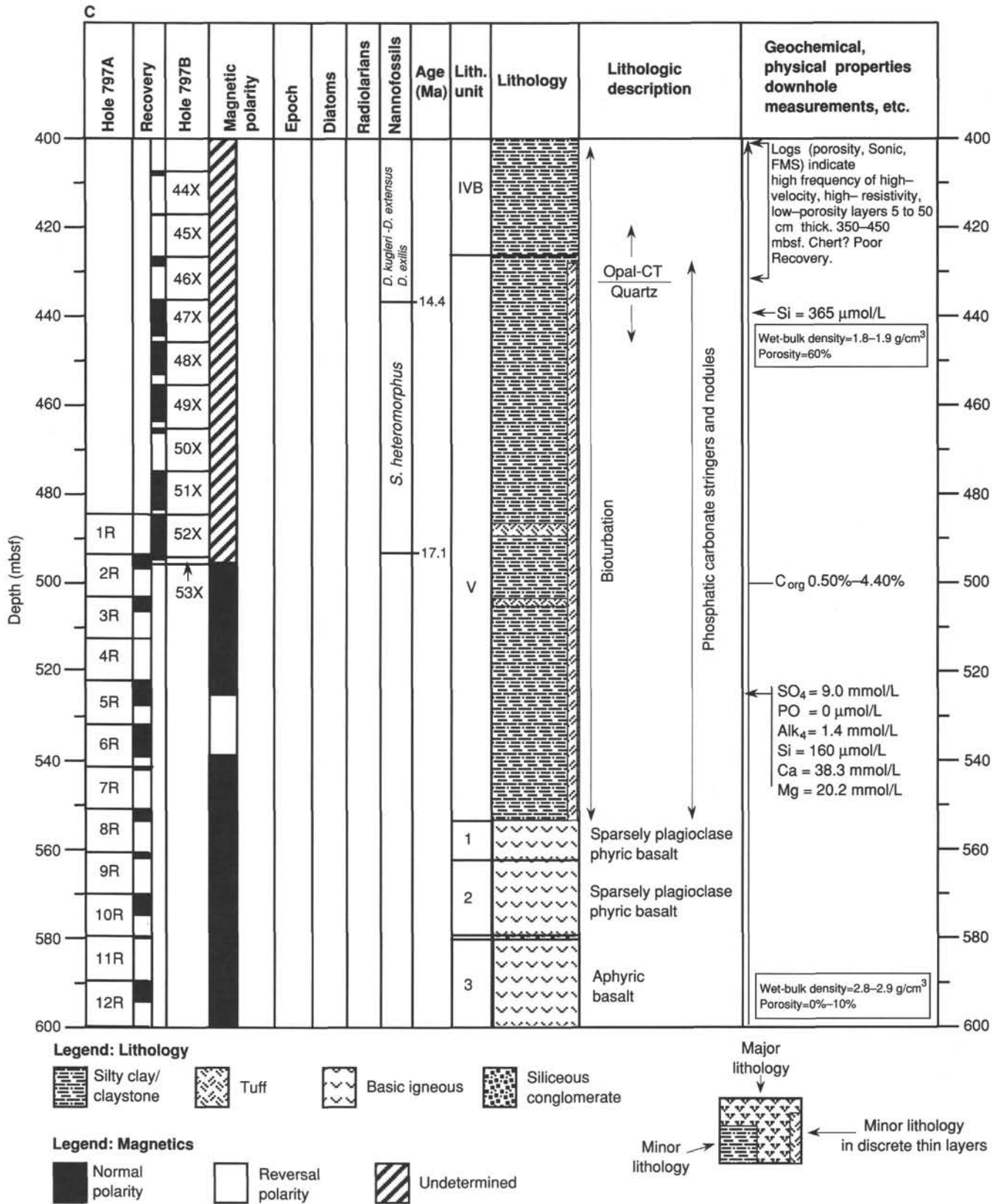
Figure 1 (continued).
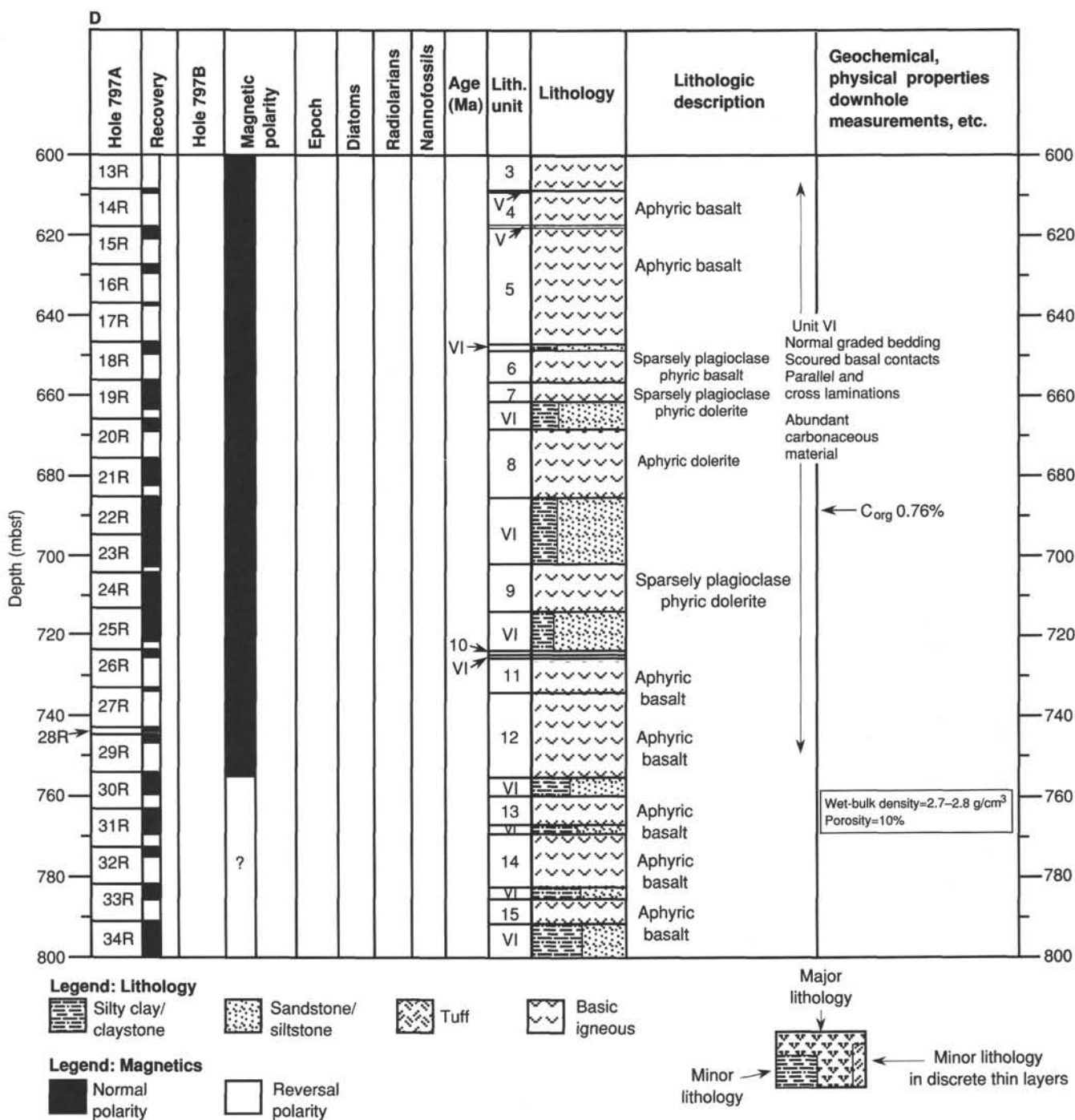
Figure 1 (continued).

Figure 1 (continued).

Crustal Structure

The crustal structure in the vicinity of Site 797 is constrained by two separate sources of seismic refraction data. The nearest data come from a detailed seismic refraction survey of the central Yamato Basin, which was acquired using an ocean-bottom seismometer (OBS) array (Hirata et al., 1987; Figs. 3 and 4). The second profile lies slightly northeast of the first and is constructed from sonobuoy and two-ship refraction surveying (Ludwig et al., 1975; Figs. 3 and 4). This profile crosses the Yamato Rise and permits comparison of the crustal structure of the Yamato Basin with the Yamato Rise.

Both sets of seismic refraction data show similar crustal structure beneath the Yamato Basin. In the Site 797 area, the mantle has a velocity of 7.6–8.3 km/s, and the crust/mantle boundary lies 15–17 km below sea level (Fig. 3). This crustal thickness is similar to that observed at Site 795 (13.5–17 km) on the northern margin of the Japan Basin and is slightly less than that of the central Yamato Basin (18–19 km; Ludwig et al., 1975; Hirata et al., 1989). It is also considerably thicker than typical oceanic crust (5–10 km) but is not as thick as typical continental crust (30–35 km).

Above the Moho in the Site 797 area, several intervals or layers can be recognized, based on velocity. Using ocean-crust ter-
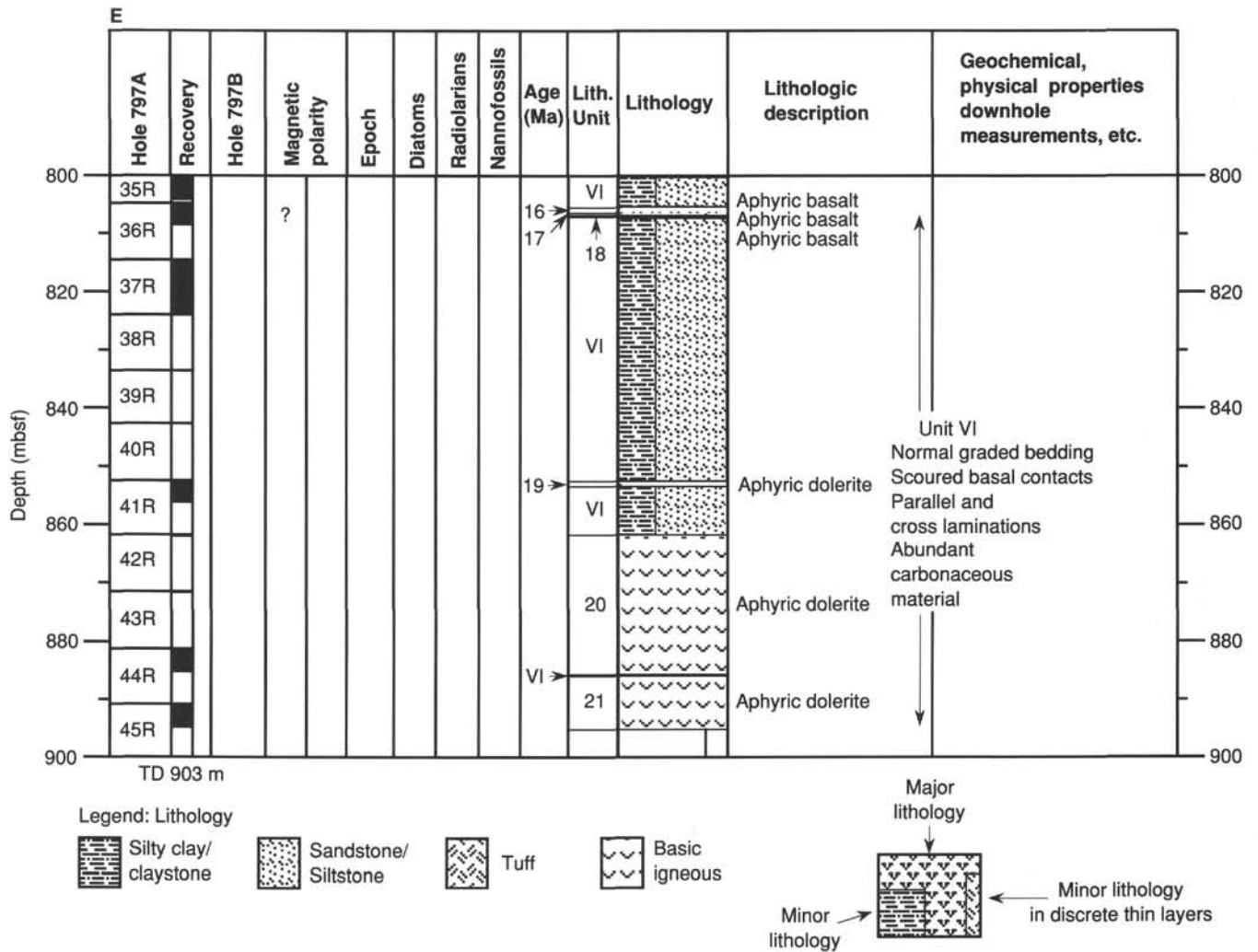
Figure 1 (continued).

minology, "Layer 3" extends from the Moho to about 6.5–8 km below sea level and has a velocity in the range of 6.7–7.4 km/s. "Layer 2" is 3–4 km thick and shows rather variable vertical and lateral velocities that range from 3.8 to 5.5 km/s. Beneath Site 797, the velocities are about 4.4–4.6 km/s, typical of basalts. The overlying sedimentary "Layer 1" is 0.5–1.5 km thick, with velocities of 1.7–2.4 km/s. Northwest of the site, "Layers 2 and 3" both apparently thicken beneath the Yamato Bank (Fig. 4). The total crustal thickness below this bank is not well constrained but is on the order of 20 km (Ludwig et al., 1975). This estimate is much greater than typical oceanic crust but is still short of representative continental values.

Heat Flow

The measured heat-flow values in the area surrounding Site 797 range from 67 to 111 mW/m² (Fig. 3). Heat flow is consistently about 10 mW/m² higher in this part of the Yamato Basin than it is over the Kita-Oki Bank and the Yamato Rise. The average value in this part of the basin is 87 mW/m² vs. 76 mW/m² for the bank areas; both are less than the average heat-flow value for the Yamato Basin (97 ± 12 mW/m²; Tamaki, 1986). The heat-flow value measured nearest to Site 797 is 102 mW/m². Using this value and a correlation between age and heat flow (Davis and Lister, 1977; Parsons and Sclater, 1977), a first approximation of the basement age at Site 797 is 20–22.5 Ma. This estimate increases to 30–33.5 Ma if the average heat-flow value

for the Yamato Basin in this area, 87 mW/m², is used. This wide disparity and the underlying assumption that the basement represents crust formed at an oceanic-type spreading ridge make these estimates rather tenuous.

Magnetics and Gravity

Magnetic anomalies near Site 797 show an east-west transition from low-amplitude, high-frequency anomalies, which typify much of the Yamato Basin, to mixed high-amplitude, longer wavelength, and low-amplitude, high-frequency anomalies more representative of the bank areas (Fig. 5; Isezaki, 1986). Profiles closest to the site show a mixed signal but with a bias toward anomalies having peak-to-peak amplitudes of 200–400 nT and wavelengths of about 50 km. The mixed character and transitional nature of these anomalies coincide with the rather abrupt physiographic transition from a flat basin to the rugged adjacent banks, suggesting that a change from a largely volcanic basement terrane to a more mixed volcanic, plutonic, and metasedimentary(?) basement terrane may occur there.

Free-air gravity anomalies in the vicinity of the site range from −20 to 80 mgal (Fig. 6). The highest anomalies correspond to the crestal areas of the Yamato, Kita-Yamato, and Kita-Oki Banks; the lowest gravity values coincide with the southern Yamato Basin and the Kita-Yamato Trough. These anomalies primarily reflect depth to basement, with low values coinciding with thicker sediment cover and deeper basement. Site
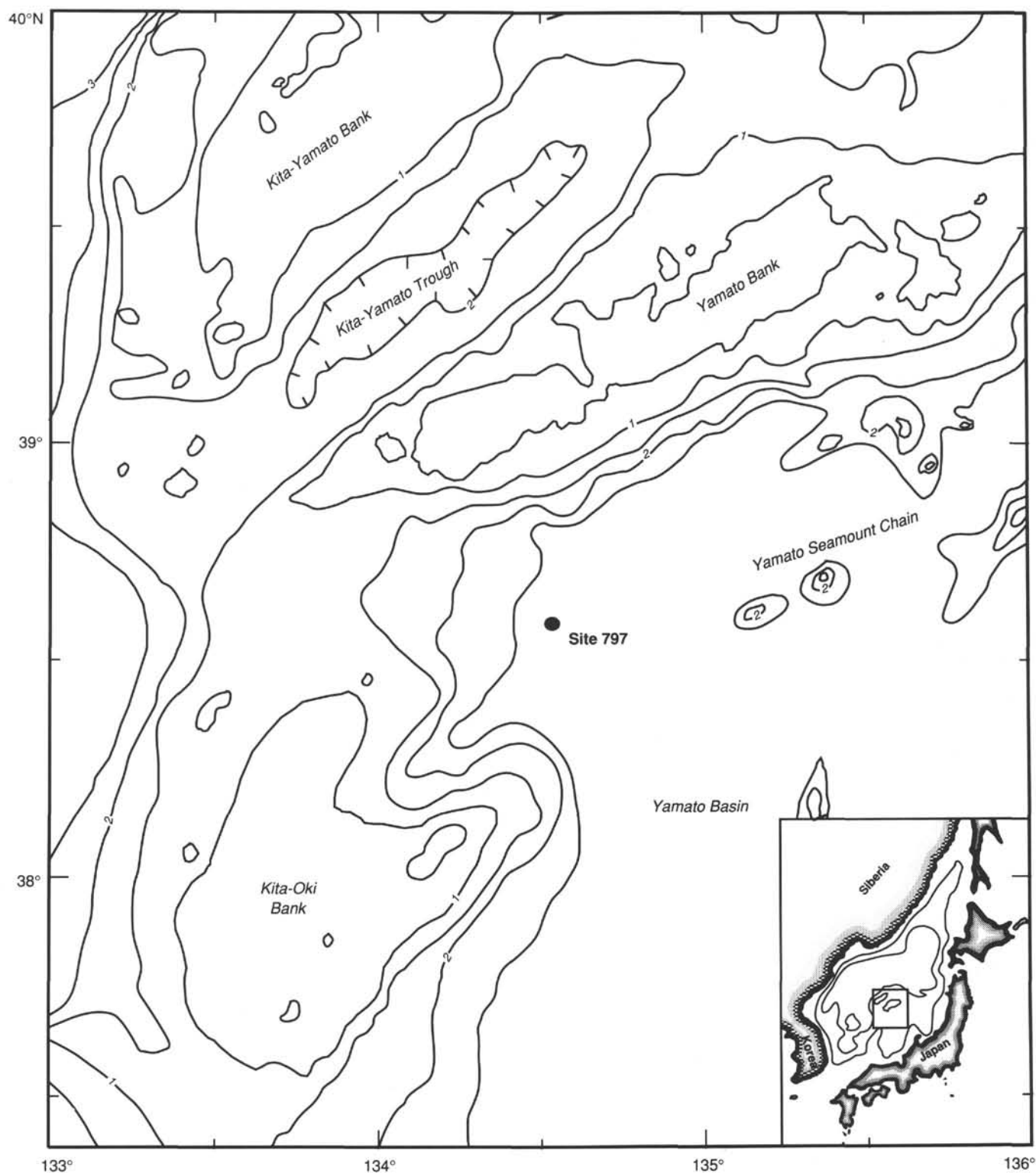
Figure 2. Location map of area surrounding Site 797, showing site location. Bathymetric contours in kilometers.

797 lies on the edge of the gravity low which occurs in the southern Yamato Basin, suggesting that the underlying basement at the site is more akin to that of the Yamato Basin than to that of the adjacent banks. This low is divided from the northeast by higher gravity values which coincide with the Yamato seamount chain. The bearing of this high changes to a more southerly direction at about the latitude of Site 797, suggesting

that the seamount chain may trend beneath the sediments in that direction rather than toward the site.

Basement Rocks

Figure 3 summarizes the distributions, ages, and types of basement rocks which have been recovered by dredging operations in the vicinity of Site 797. Only those dated samples whose
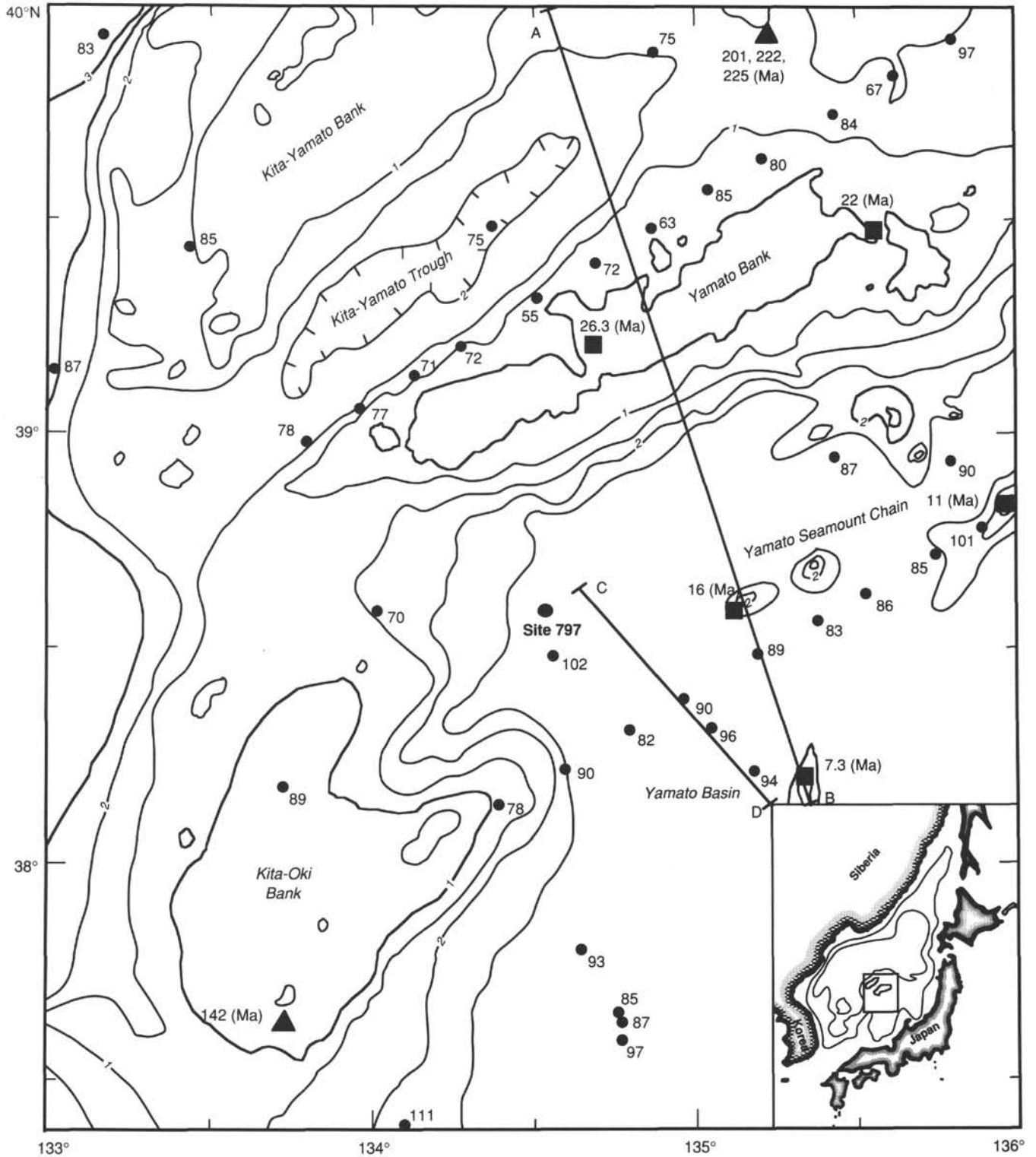
Figure 3. Location map of heat-flow values, basement dredge samples, and seismic refraction profiles near Site 797. Heat-flow values are represented by dots; units are in mW/m², and data are from Yoshii and Yamano (1983). Basement samples are represented by solid squares (volcanic rocks) and solid triangles (granitic rocks); see text for descriptions and references. A–B and C–D mark positions of crustal sections shown as Figure 4. Bathymetric contours in kilometers.
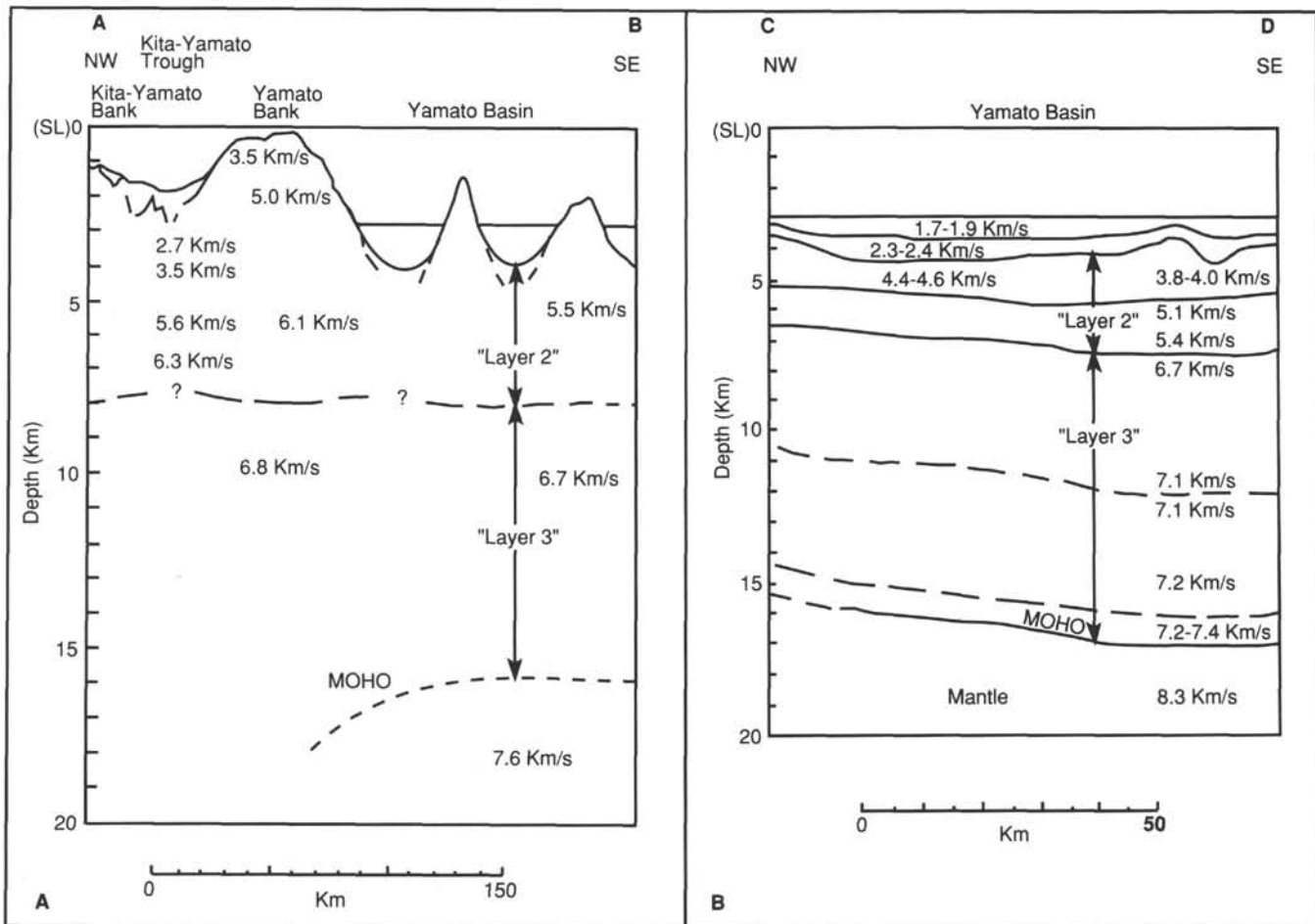
Figure 4. Crustal sections based on seismic refraction data for the central Yamato Basin and Yamato Rise near Site 797. **A.** Profile A–B, taken from Ludwig et al. (1975). **B.** Profile C–D, taken from Hirata et al. (1989). Note differences in scales. See Figure 3 for locations of sections.

dredging localities are well identified have been plotted. The rocks consist of Mesozoic granitic rocks and upper Oligocene–upper Miocene volcanic rocks. Summaries of published ages of dredged materials from the Yamato Rise can be found in Kaneoka (1986), Tamaki (1988), Kaneoka et al. (1988, in press), and Kaneoka and Yuasa (1988). These results should be used cautiously, as the rocks are typically somewhat altered.

The oldest rocks recovered are granodiorites from a locality on the Yamato Rise north of the Yamato Bank. K-Ar and Rb-Sr ages of these rocks range from 201 to 225 Ma (Kaneoka, 1986). Mesozoic granitic rocks have also been recovered from the Kita-Oki Bank. These rocks are somewhat younger than the Yamato Rise granitic rocks and have been dated by the K-Ar method at 142 Ma (Kaneoka, 1986).

The volcanic rocks also vary in age and composition. These samples have been dated using the K-Ar and $^{40}Ar/^{39}Ar$ methods (Kaneoka, 1986; Kaneoka et al., 1988; Kaneoka and Yuasa, 1988; Kaneoka et al., in press). In most cases, the generally more accurate $^{40}Ar/^{39}Ar$ ages are older than those determined by K-Ar dating. An andesite recovered from the central Yamato Bank yielded a $^{40}Ar/^{39}Ar$ age of 26.3 Ma (Kaneoka and Yuasa, 1988). Basalt and andesite from this locality had been dated previously at 20 Ma using the K-Ar method (Kaneoka, 1986). Farther to the northeast on the Yamato Bank, basalt and andesite also were recovered and dated at 22 Ma by K-Ar (Kaneoka, 1986). All younger volcanic rocks come from the Yamato seamount

chain. The oldest sample from this group is a 16-Ma ($^{40}Ar/^{39}Ar$) trachyandesite recovered from a seamount about 65 km east of Site 797 (Fig. 3; Kaneoka et al., in press). To the northeast, similar rocks, dated at 7–13 Ma (K-Ar) and 11.1 Ma ($^{40}A/^{39}Ar$), were recovered from a larger, composite seamount. The youngest volcanic rocks in the area are 7.3-Ma (K-Ar) andesitic rocks collected from a seamount in this chain which lies about 100 km southeast of Site 797 (Fig. 3; Kaneoka et al., 1988).

To summarize, andesitic volcanic rocks constitute the nearest sampled basement to Site 797. These include rocks of two age groups: (1) upper Oligocene–lower Miocene rocks from the Yamato Bank, and (2) middle to upper Miocene rocks from the Yamato seamount chain. In addition, Mesozoic granitic rocks have been recovered from the Kita-Oki Bank south of the site and from the northern Yamato Rise north of the site.

Onshore geologic trends are less applicable to Site 797 than to previous sites because of the great distance from shore. However, as with the previous sites, the ages and compositions provide some perspective on offshore basement types. On southwestern Honshu, Upper Cretaceous and Paleogene intrusive rocks crop out extensively and are the principal basement rock type present (Geological Survey of Japan, 1982). These rocks trend northeast-southwest, and there is no indication that they extend toward Site 797. Miocene volcanic rocks are also common on southwestern Honshu. These rocks mostly occur along the coastal region and on offshore islands in the Japan Sea.
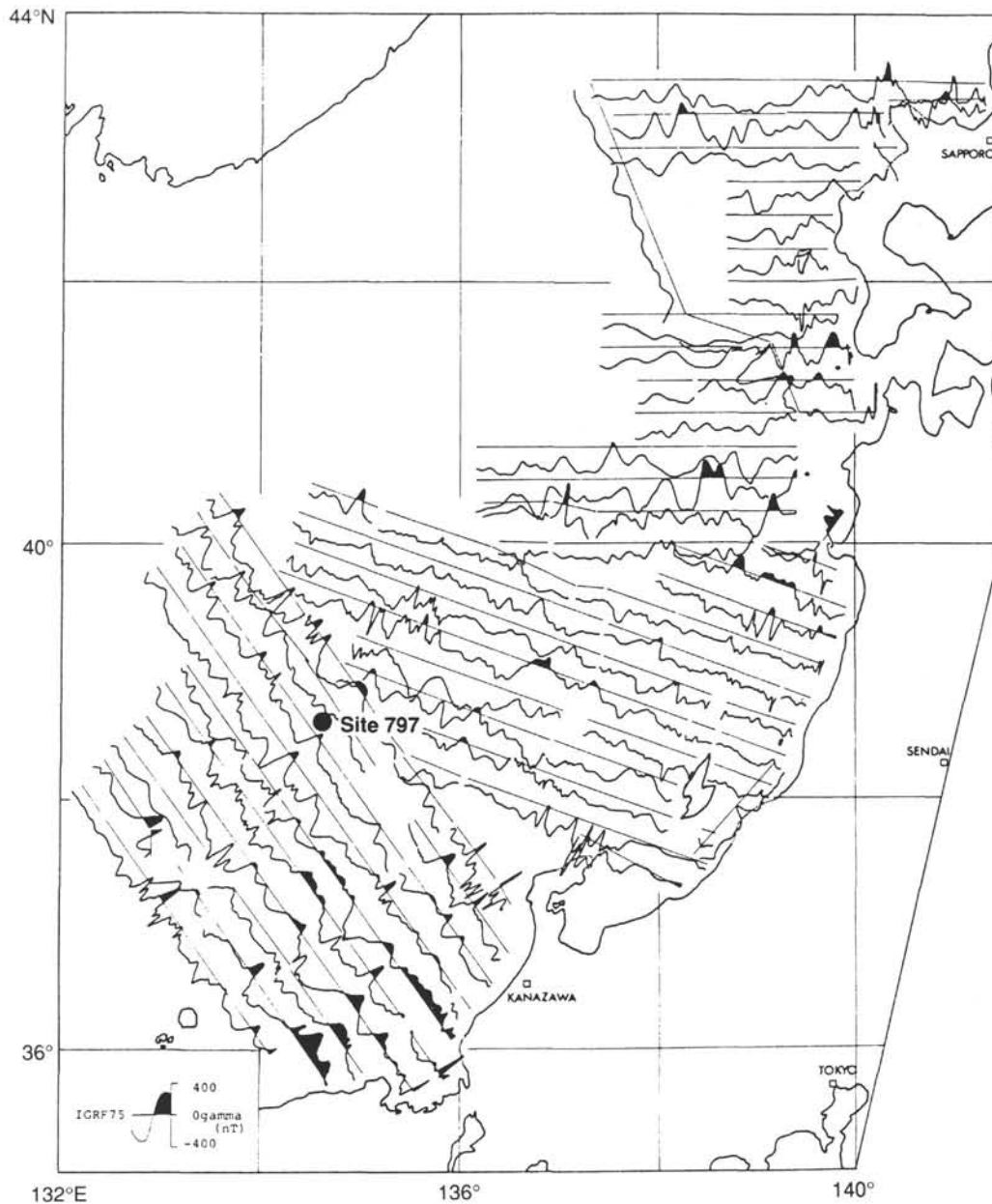
Figure 5. Magnetic anomalies around Site 797. Data are from Honza (1979).

They typically comprise basalts, andesites, and dacites. As with the granitic rocks, the general outcrop trend of these rocks is northeast-southwest with little evidence to show how far these extend toward Site 797. Nevertheless, these onshore data provide additional perspective on basement-rock types occurring in the Japan Sea area.

Tectonic Setting

Much of the information regarding the tectonic setting of Site 797 comes from structural trends observed within the adjacent Yamato Rise and Kita-Oki Bank. These areas are typified by sparse northeast-southwest-trending folds and faults in basement (Figs. 7 and 8). The most conspicuous features are steep normal faults which occur within and on the flanks of the Kita-Yamato Trough. Vertical displacements on these faults have mostly affected acoustic basement and are on the order of 1–2 km. Sediments which have filled the troughs opened by these faults show

little evidence of subsequent deformation. Drilling results at DSDP Site 302 on the northern flank of the Yamato Rise (Karig, Ingle, et al., 1975) and ages of basement dredge samples show that the extensional faulting that affected the Yamato Rise occurred prior to the late Miocene. Folding of basement strata probably preceded this period, but the inadequate data available cannot constrain its timing.

Site 797 lies in a marginal part of the Yamato Basin that has not been affected by significant faulting or folding. In addition, there is no modern, shallow seismicity near the site. Together, these results suggest that the immediate area surrounding Site 797 has been tectonically quiescent probably since the middle Miocene.

Sedimentation

The sedimentary section which overlies acoustic basement in the vicinity of Site 797 is approximately 500–600 m thick (Fig. 8).
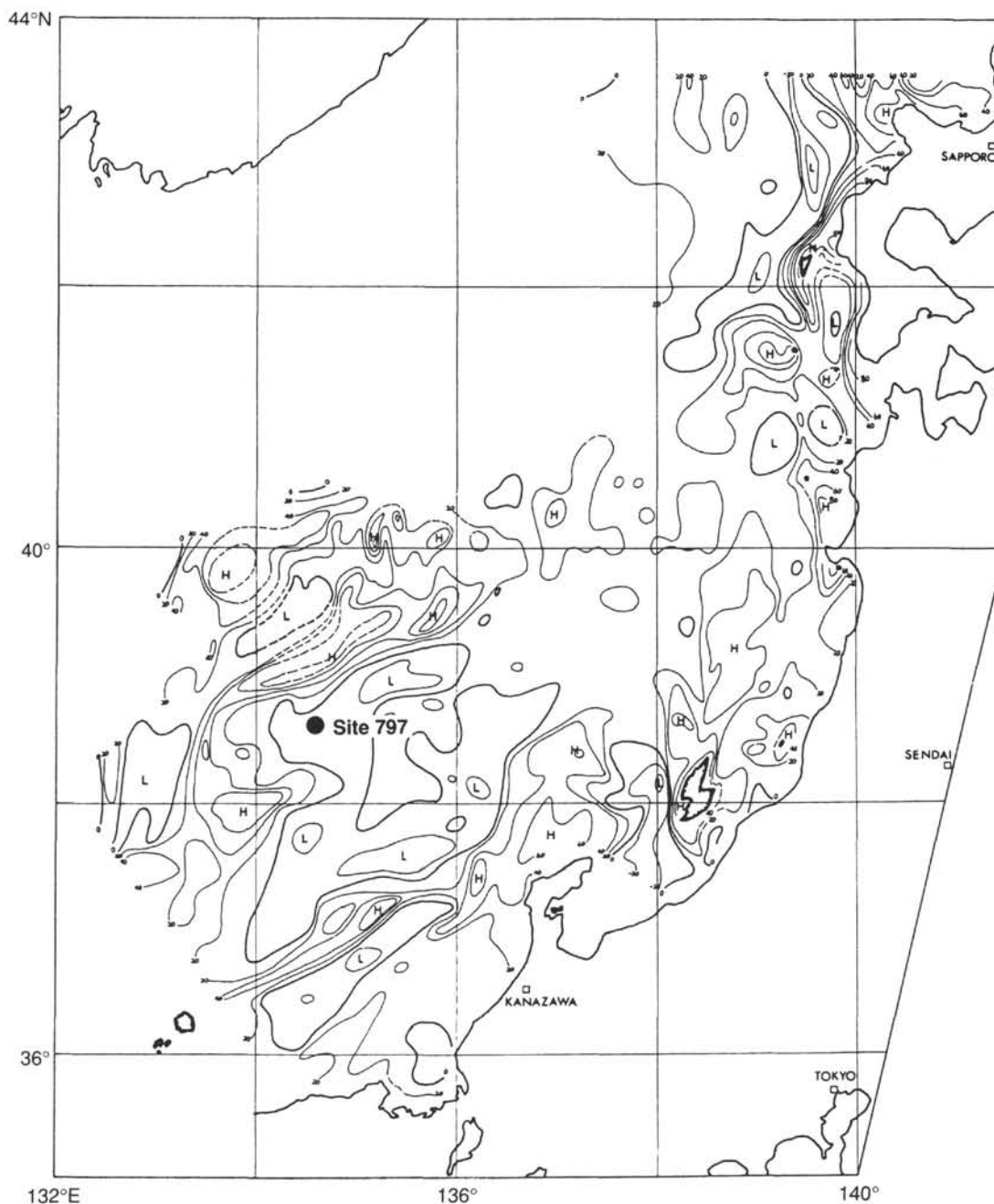
Figure 6. Free-air gravity anomaly map in the vicinity of Site 797. Contour interval is 20 mgal. Data are from Honza (1979).

It is characterized by flat-lying to gently dipping, conformable sediments. Based on the seismic data and our experience at the previous sites, we expected to find a middle(?) Miocene to Quaternary hemipelagic section similar to that at Site 794.

At least four seismic intervals are present above acoustic basement in the site area. From top to bottom these are (1) an upper weakly to moderately stratified interval, (2) a transparent interval, (3) a well-stratified interval, and (4) a moderately well-stratified interval. To the east a correlative section occurs which thickens considerably toward the center of the Yamato Basin and corresponds to Quaternary and upper Pliocene distal turbidites (Fig. 8; Tokuyama et al., 1987). These intervals form a

mostly conformable package draped over acoustic basement. We expected these intervals to represent mostly hemipelagic sediments. Prior to drilling, the uppermost interval 1 was estimated to be about 150 m thick at the site location and thought to represent alternating dark and light Quaternary silts and clays. The thickness of the second interval was estimated at about 150 m and was thought to comprise mostly diatomaceous ooze. The third interval was expected to be composed of about 175 m of siliceous claystone, with its upper boundary formed by the opal-A/opal-CT diagenetic transition. The lowest interval was estimated to be about 100 m thick and was predicted to consist of claystones with minor tuffaceous and volcaniclastic interbeds.
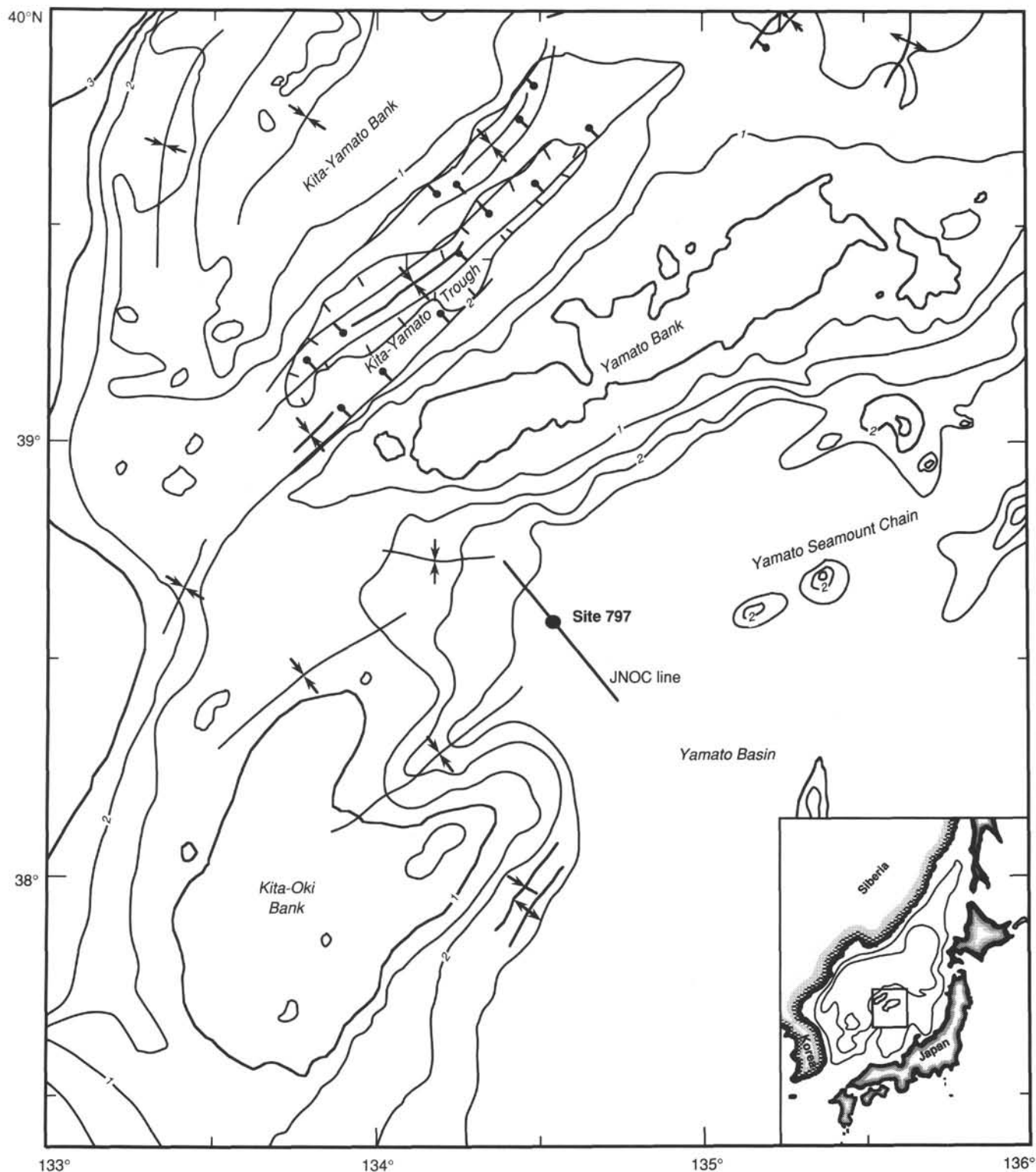
Figure 7. Tectonic map of area surrounding Site 797, showing recognized faults and fold axes and the location of JNOC seismic line illustrated in Figure 8. Data are from Tamaki et al. (1981). Bathymetric contours in kilometers.

Objectives

Style and Dynamics of Back-Arc Rifting

The principal objective at Site 797 was to determine the nature and age of the acoustic basement at a basinal location in the Japan Sea. Together with the results from additional sites

drilled during Legs 127 and 128, these data would add constraints and permit assessment of the style and dynamics of rifting of the Japan Sea. More specifically, Site 797 constitutes the first basinal site in this part of the deep Yamato Basin. The only other information on the age and composition of basement in this area has come from the dredging results. While these results
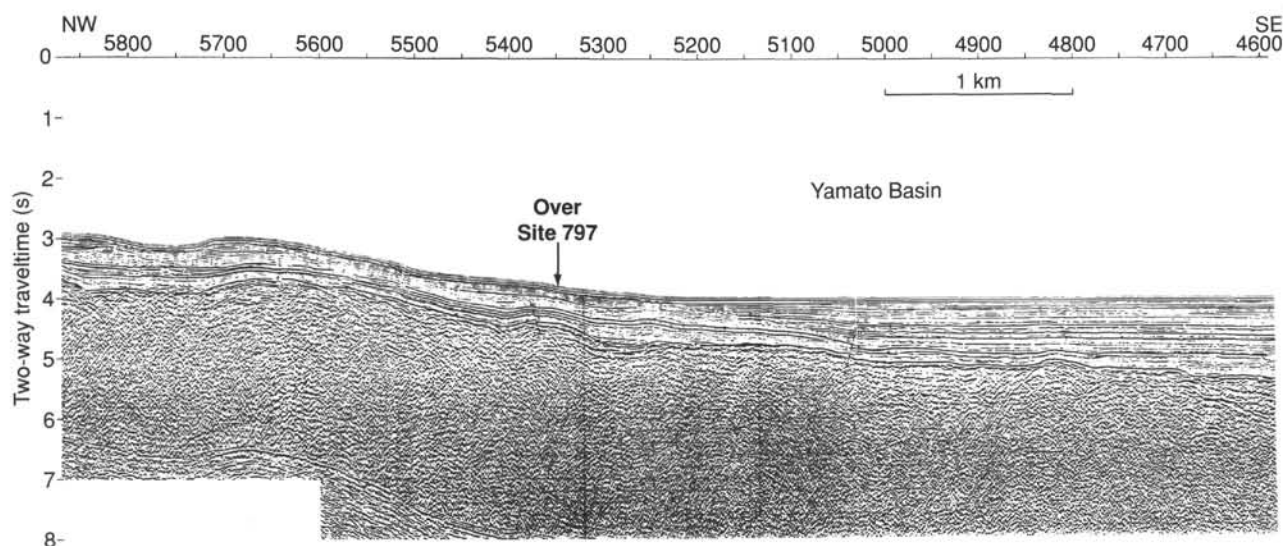
Figure 8. Northwest-southeast multichannel seismic reflection profile crossing Site 797. Data are from the Japan National Oil Corporation. Note that parts of reflectors are traced over. The line location is shown in Figure 7.

established the existence of nearby volcanic terranes and foundered continental blocks composing the Yamato Rise, they shed little light on the nature and age of the basement underlying the Yamato Basin. Site 794 penetrated dolerite sills beneath hemipelagic sediments in the northernmost part of this basin, and DSDP Site 299, just southwest of this position, was stopped well short of basement by concerns about ethane levels in the Pliocene sediments. By drilling Site 797 we hoped to establish the nature and age of the basement in the southern Yamato Basin in order to constrain the timing and style of its formation.

In-situ *Stress Field*

A second goal of the drilling at Site 797 was the determination and assessment of the present stress field of the central Japan Sea. Previous attempts at obtaining measurements of the magnitude and direction of stress in coherent basement rocks during this leg were thwarted by hole problems. Site 797 was our last opportunity to obtain useful data that would be germane to understanding the regional stress field in this marginal-sea area.

Oceanographic and Sedimentary History

The third objective of the drilling at Site 797 was to characterize the history of sedimentation and water-mass fluctuations at a southern basinal position in the Japan Sea. Like Sites 794 and 795, this site was situated so as to obtain mostly hemipelagic sediments rather than terrigenous gravity-flow deposits. Hemipelagic sediments are more likely to contain the microfossils and lithofacies needed for temporal reconstructions of climate, water mass, and subsidence. Except for the differing geographic position, our specific goals were identical to those at the previous sites, namely: (1) to establish the history of anoxia, circulation, and sea level in relation to climate and subsidence; (2) to identify fluctuations in the CCD; and (3) to document time- and temperature-controlled post-depositional processes, particularly those involving organic matter, biogenic silica, and carbonate. This site lies between two bank-top localities on either side of the Yamato Basin which are the principal drilling targets for Leg 128. Together, these three sites should provide

key reference sections for the deep and shallow parts of the southern Japan Sea. The integration of these results with other offshore and onshore regional data will form the basis for an understanding of the sedimentation and oceanographic history of the Japan Sea and of the western Pacific margin.

OPERATIONS

Preamble

After finishing our post-site survey at Site 796 on 29 July 1989, we steamed southwest to our final location off the southeastern flank of the Yamato Rise in the western Yamato Basin. Our average speed for this transit was about 10 kt, and we acquired seismic and magnetometer data of moderate quality en route. By about 0800 hr on 31 July (2300 hr on 30 July UTC), we were in a position about 12 nmi southeast of the site to begin our seismic survey.

Site Approach

The seismic-survey plan for Site 797 was identical to all previous surveys acquired on this leg. Our first crossing was to be along a proprietary multichannel line beginning about 12 nmi southeast of the location and continuing 2 nmi beyond it to the northwest. Following this, we planned to swing to the south to obtain a northeast-southwest crossing along a preexisting Geological Survey of Japan single-channel line. Pending confirmation of the location and the absence of local closure, we would return along the northeast-southwest line and launch the beacon.

We approached the primary site location from the west along a proprietary multichannel seismic line at a speed of about 6 kt (Figs. 9 and 10). Our first crossing line began about 12 nmi southeast of the location and extended 2 nmi beyond it as planned. We then turned to the south and made the transit to the beginning of our second crossing about 2 nmi southwest of the site. We reduced our speed to 4.5 kt and shot this line to the northeast about 2 nmi past the site. Our reviews of this line, and our experience at Site 794, showed that the uppermost part of
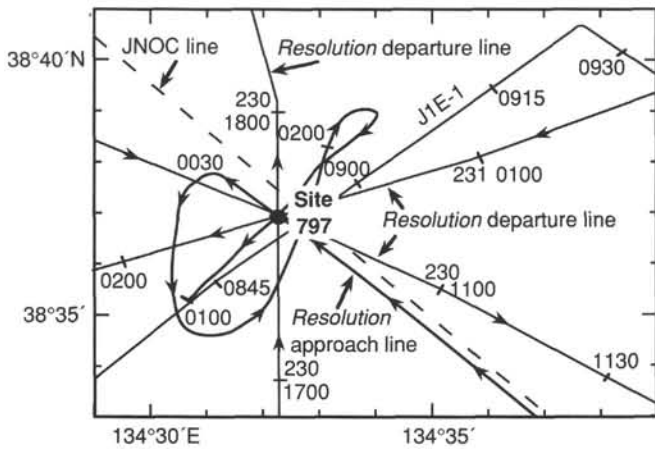
Figure 9. Chart showing locations of *JOIDES Resolution* single-channel approach line, Geological Survey of Japan single-channel Line J1e-1, and a proprietary multichannel line for Site 797.

acoustic basement consisted of flat, strong reflectors suggestive of an igneous sill complex. Since our first line demonstrated that this seismic character did not extend far to the north-northwest, we shot a third line that was parallel to, but just north of, our second line (Fig. 11). The seismic character of acoustic basement along this line was more opaque and thought to be more representative of true basement in the area. We dropped the beacon near the intersection of this line with our first line, then continued profiling to the southwest for about 1 nmi before slowing to retrieve the gear and position the ship.

Drilling and Logging Summary

Our drilling plan for Site 797 called for two adjacent holes, the second a reentry hole, to achieve our scientific objectives. Hole 797A was to be an APC/XCB hole drilled as deeply as possible into indurated sediments. We planned to take one core to establish the mudline, then conduct a jet-in test for reentry purposes before continuing with coring. *In-situ* temperature measurements, using the Uyeda probe, were scheduled routinely after every third core until the sediments became too indurated to yield reliable information. Hole 797B was to be a reentry RCB hole with coring beginning at the total depth reached in Hole 797A and carrying into basement at least 50 m. At this stage, logs would be run over the complete sedimentary and basement sections and packer/hydrofracture experiments performed in the basement interval. An optional vertical seismic profile was also planned after finishing the logging and packer work. Following this, we planned to make a round trip to retrieve the packer, then reenter the hole and continue coring basement. We would either continue coring basement until time expired or leave a final window for logging this lower interval, depending on hole conditions, recovery, and rock type. Our decision to set a reentry cone and a 16-in. casing string to 80 mbsf would afford us the greatest flexibility for continued operations in the hole that would carry us to the end of the leg. In addition, if left in good condition, the hole could serve as a site for future drilling or downhole measurements.

Hole 797A

Hole 797A was a single-core event. This core, shot from a depth of 2877 m below the driller's datum, had 100% recovery, indicating that we had pushed the bottom-hole assembly (BHA)
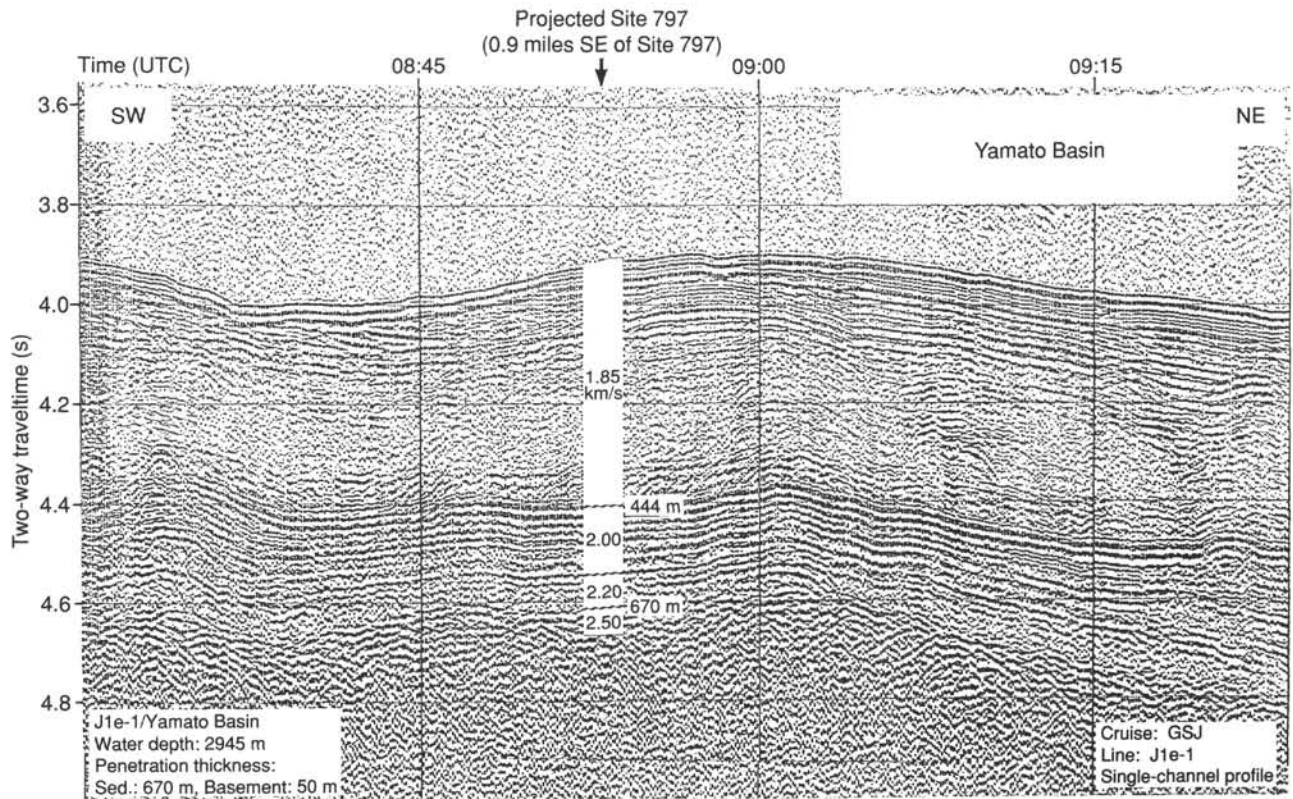
Figure 10. Geological Survey of Japan single-channel seismic reflection Line J1e-1 southeast of Site 797. See Figure 9 for location.

into the sediments past the mud line. To remedy this, we raised the pipe to 2870 m above the driller's datum and spudded Hole 797B.

Hole 797B

The first core in Hole 797B established the mud line at 2873.6 m below the driller's datum. A successful jet-in test was completed to 100 mbsf following Core 127-797B-1H, indicating ideal subsurface conditions for setting a reentry cone. After this test, APC coring commenced and carried to 175.9 mbsf before it became necessary to change to the XCB. Nineteen APC cores were taken with excellent recovery and minimal drilling disturbance (Table 1). We also completed six excellent temperature measurements within the sediments of this interval. No hole problems were encountered, nor was any gas detected.

We switched to XCB coring after Core 127-797B-19H (175.9 mbsf) and took 34 cores to 495.7 mbsf. Recovery was variable but generally good down to about 360 mbsf, where brittle siliceous lithologies were encountered and recovery dropped (Table 1). We experienced minor hole problems at about 331 mbsf (Core 127-797B-35X), but a short wiper trip and several flushes effectively neutralized these difficulties. Recovery improved again below 436 mbsf after passing through the siliceous interval. At about 495 mbsf (Core 127-797B-53X) we encountered hard, carbonate-cemented zones which reduced the coring rate considerably. At this point, we opted to terminate Hole 797B and make a trip for the RCB and reentry cone in order to drill Hole 797C.

The newly developed sonic core monitor (SCM) was tried for the first time on an ODP cruise and was used from Core 127-797B-34X through the rest of the XCB coring in Hole 797B (Core 127-797B-53X at 495.7 mbsf). This device seats at the top of the core barrel and is designed to track the variable rate at which sediment and rock enter the core barrel during coring. The purpose of this device is to permit real-time monitoring of coring progress; these data would be used to increase coring efficiency by signaling plugging problems when they happen. Despite several minor problems, six of eight attempts with the SCM prototype were successful. Plots of core recovery and penetration vs. drilling time clearly delineated the periods of good recovery and no recovery. These successful results will greatly aid in the further development of this device.

Hole 797C

We moved 30 m southeast of Hole 797B and launched the reentry cone and 16-in. casing for Hole 797C at 0245 on 5 August (1745 on 4 August UTC). After lowering the assembly to the seafloor, the casing was jetted 80 m below the seafloor and the pipe was unlatched. We drilled out from under the shoe only to find that the 8 ½-in. drill collar in the BHA would not pass through the 8 ½-in. inner diameter of the latch sleeve. We had no alternative but to trip the pipe, retrieve the latch sleeve and remove the paddle running tool from the BHA, then run back into the hole to continue with Hole 797C. We reentered the hole at 0330 on 6 August (1830 on 5 August UTC) and washed to 484 mbsf to begin rotary coring.

At this point our plans were to core until a change of bit was required, then pull the string, install the single-element packer, and run back into the hole for logging and packer work. Following that, we would continue RCB coring to the end of the leg. Accordingly, we washed to 484 mbsf and then took 34 cores to 800 mbsf before stopping at 1030 hr on 9 August (0130 UTC) for a round trip to make up the logging and packer BHA. Recovery was variable but averaged a respectable 43% over this interval (Table 1). Basalt was encountered at 554 mbsf, and interlayered basalts and sediments continued below this to 800 mbsf. Minor hole problems occurred within this interval, but these were countered with short pipe trips. After reaching 800 mbsf,

we made a wiper trip to the casing shoe to prepare the hole for logging. Some drag was noted on the trip up, and hard resistance was encountered on the return trip at 650 mbsf. After reaming and flushing the hole with mud, the pipe was retrieved.

The logging and packer BHA was made up and the hole was reentered without incident. We set the pipe at 80 mbsf and ran the formation microscanner (FMS) log. This log encountered a blockage at 516 mbsf, about the level where we recovered the first thin layers of tuff. We acquired this log and then followed with a successful run of the "quad-combo," a string of logging tools which includes sonic, density, conductivity, and neutron porosity devices along with gamma-ray, caliper, and temperature instruments. We elected to run the geochemical tool after moving the pipe through the bridge on our next set of runs.

At this point we lowered the pipe to 643 mbsf, where hard resistance was encountered, then reamed to total depth before pulling back to 543 mbsf. The FMS log was deployed but it could not be worked past 566 mbsf. We logged this open-hole interval, then washed without rotation to 638 mbsf and set the pipe at 623 mbsf and ran the geochemical log through 10 m of open hole and then behind pipe to the seafloor. Given the hole difficulties, we washed without rotation to 639 mbsf, then pulled back to 494 mbsf and rigged up the side-entry sub (SES) along with the FMS tool. The FMS/SES combination permitted us to acquire the log from 605 mbsf to about 485 mbsf and overlap our shallower run. This run was followed by a borehole televiewer (BHTV) run between 603 and 549 mbsf, also using the SES. The caliper data from the FMS indicated that the clay-rich formations swelled into the borehole almost immediately after transit of the pipe past them. The FMS and BHTV data also delineated a possible interval for packer work at about 588 mbsf. Accordingly, we retrieved the BHTV tool and removed the SES from the drill string, then lowered the packer toward the target interval. Unfortunately, we encountered a tight hole and were forced to ream against excessive torque, drag, and circulating pressure. At this point, we decided to abandon the packer attempt because of the rapidly deteriorating hole conditions and the slim prospect of getting meaningful permeability data. We retrieved the drill pipe and found that the outer rubber covering of the packer was completely stripped off.

We exchanged the packer BHA for an RCB bit and BHA and reentered Hole 797C for a third time. After reaming the hole, we took three cores with good recovery before making a precautionary wiper trip. The ensuing two cores had no recovery. Suspecting a plugged bit, we pumped a core breaker down to the bit and retrieved it. Increasing circulating pressure dictated that we make another wiper trip before attempting the next core. When this core also came up empty, we decided to make a round trip to inspect the flapper valve or clear the obstruction.

The pipe was retrieved, and the bit was found to be plugged with several hard fragments of basalt core. After clearing the bit, we reentered the hole a fourth time. Locating the hole was more difficult this time because the cone was covered with sediments and obscured from view. We reamed the hole to total depth and began RCB coring once again.

Difficult hole conditions continued, and we made a precautionary wiper trip after three cores. Recovery improved in the next two cores, but during the cutting of the third core the weight on bit suddenly dropped 50,000 lb. The weight loss could only mean a loss of the BHA and several stands of pipe. We retrieved the pipe and found that it had failed nine stands above the BHA. With only 24 hr of operational time remaining in the leg and no BHA available for further RCB drilling, we were forced to abandon the site. With the little time remaining, we had planned to obtain several extended seismic crossings of the site, which would permit us to tie to existing single- and multichannel seismic data.
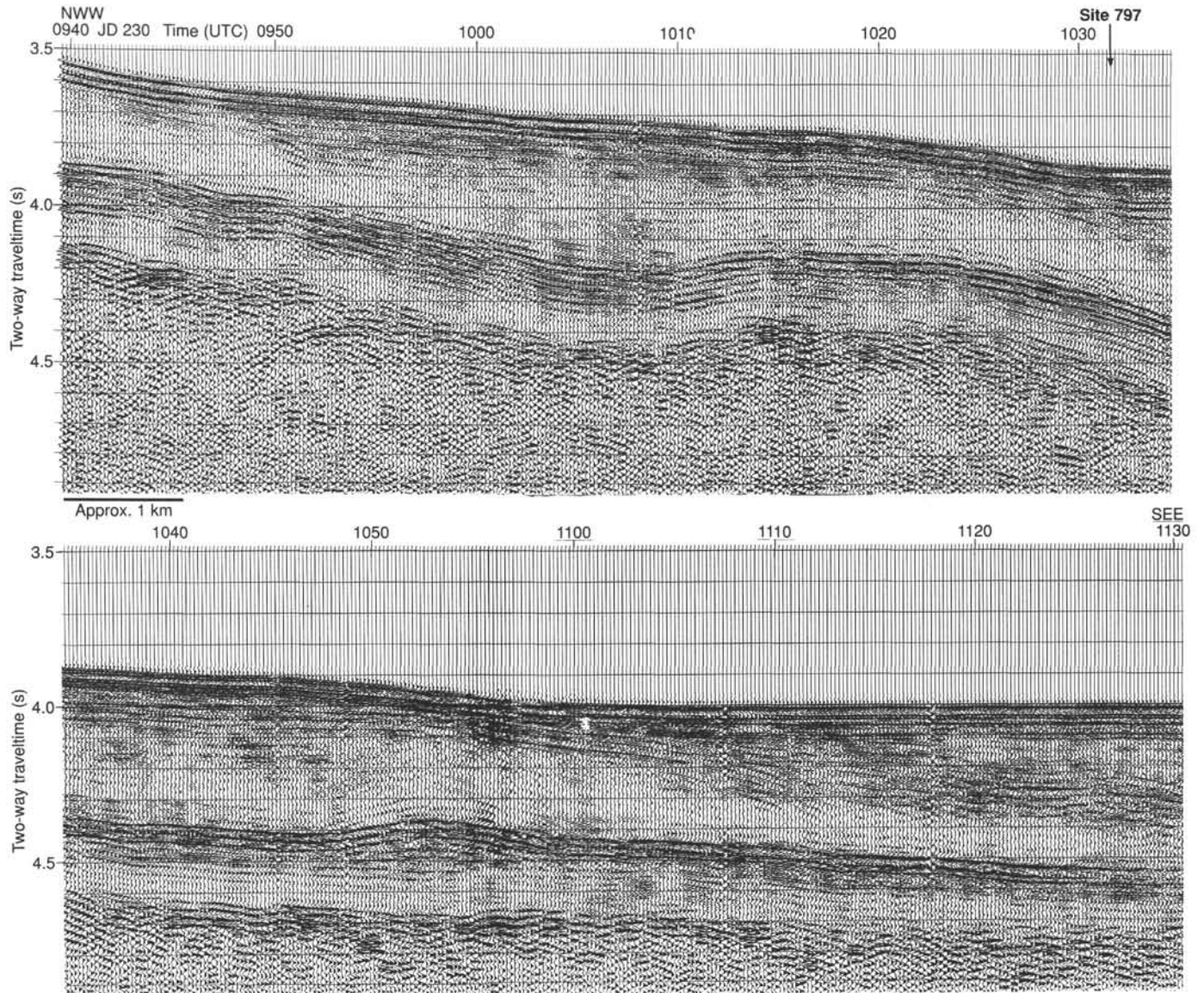
Figure 11. *JOIDES Resolution* single-channel departure approach line for Site 797. See Figure 9 for location.

Site Departure

We departed Site 797 at 1700 hr (0200 hr UTC) on 18 August 1989 and steamed 3 nmi west-northwest to begin the first line. The profiling speed for this survey was 6 kt, and transits between lines were made at 10 kt. The first profile was a northwest-southeast crossing beginning about 5 nmi from the site and continuing approximately 11 nmi past it. After completing this line we turned to the south and steamed to a position about 15 nmi south of the site. The second line was a 30-nmi north-south profile through the site location. Another transit was made following this to a position about 20 nmi northeast of the site. We completed this profile through the Site 797 location on the afternoon of 20 August 1989 and then made the 1.5-day transit to Pusan, South Korea, for the end of the leg.

LITHOSTRATIGRAPHY

Lithologic Units

The Neogene stratigraphic succession encountered at Site 797 is over 800 m thick. The upper 554 m of the sequence is com-

posed entirely of lower(?) Miocene to Holocene sediments. Below this depth to the bottom of the hole at 900 m sedimentary strata occur interlayered with altered basalts. The sedimentary section is divided into six major lithologic units (Fig. 12). The units have been determined on the basis of texture, mineralogy, biogenic content, and sedimentary structures of the sediments. Figure 13 shows the variations in the relative abundance of several key sediment components as a function of depth.

Unit I (0–119.9 mbsf)

Cores 127-797A-1H and 127-797B-1H through 127-797B-13H.

Unit I consists of 119.9 m of upper Pliocene to Holocene clay and silty clay with a minor admixture of vitric ash and diatoms. The unit is divided into two subunits on the basis of variations in the dominant lithofacies as recognized by bedding characteristics, sedimentary structures, and color. Subunit IA is characterized by dark, indistinctly laminated clay and silty clay, with alternating interbeds of well-bioturbated, nonlaminated, light clay and silty clay. Subunit IB is distinguished from Subunit IA by the dominance of light, well-bioturbated silty clay that con-
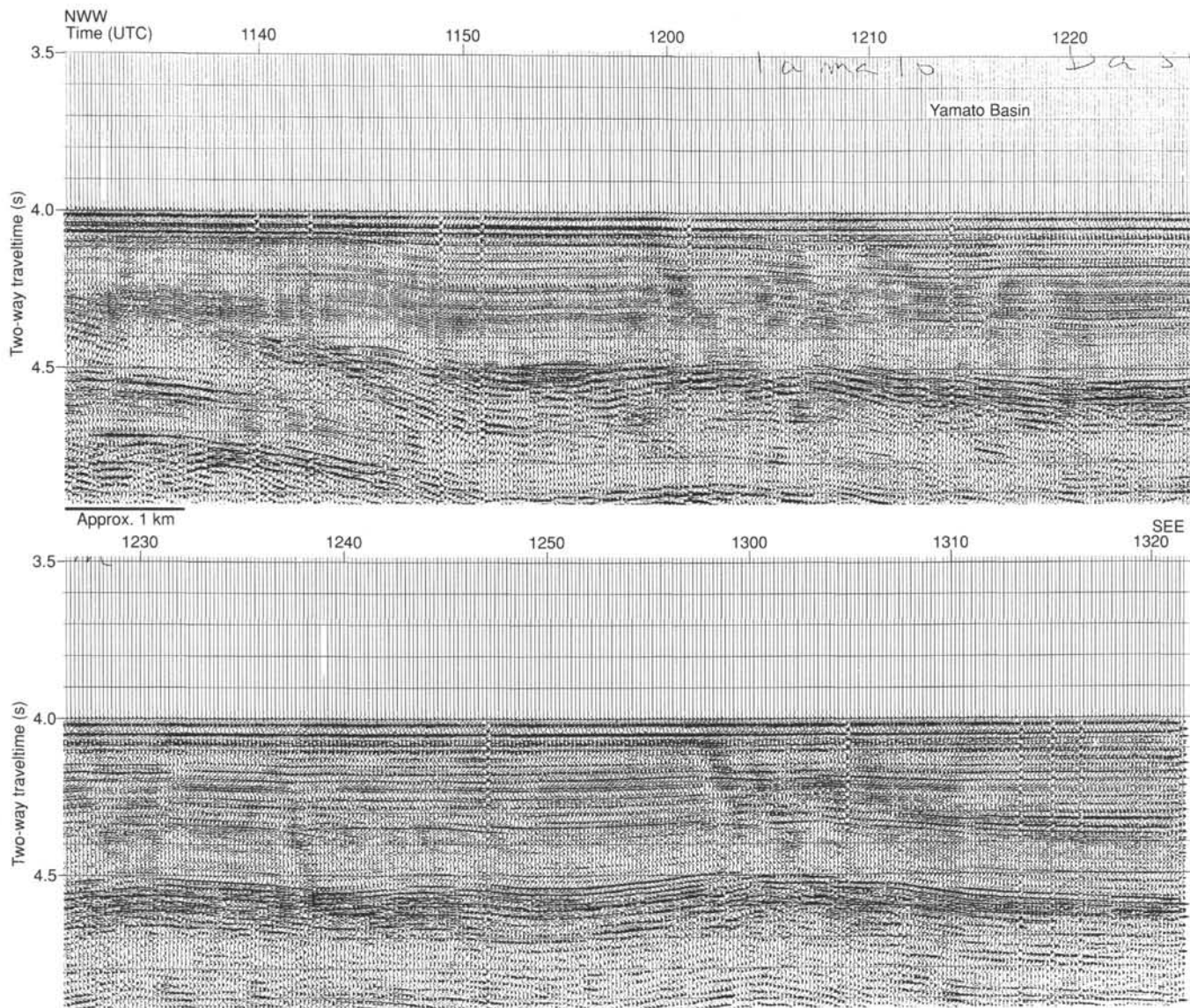
Figure 11 (continued).

tains disseminated vitric ash and diatoms but few dark layers. Several grayish yellow dolomicritic layers, up to 5 cm thick, occur within this unit.

Subunit IA (0–81.9 mbsf)

Cores 127-797A-1H and 127-797B-1H through 127-797B-9H.

Subunit IA consists of 81.9 m of lower Pleistocene to Holocene clay and silty clay. The unit is distinguished by a large number (more than 100) of thin interbeds of dark, faintly to moderately well-laminated clay and silty clay that alternate with light-colored, well-bioturbated clay and silty clay. Some of the latter contain faint ("wispy") laminations at or near their base. Most hue contacts between alternating layers are sharp, although some layers are gradational with the overlying sediment. Many of the dark-colored layers contain pyrite, diatom tests, and organic matter in varying amounts, though only one interval in Core 127-797B-7H could be termed a diatom ooze, s.s. The number of dark-colored layers decreases toward the base of Subunit IA (Cores 127-797B-8H and 127-797B-9H); this decrease corresponds with an increase in disseminated vitric ash and dia-

tom tests within the light-colored silty clay. More than 80 discrete vitric-ash layers, 0.5–5 cm thick, occur throughout the subunit. They decrease in number below 70 mbsf.

Subunit IB (81.9–119.9 mbsf)

Cores 127-797B-10H through 127-797B-13H.

Subunit IB consists of 38 m of upper Pliocene to lower Pleistocene light gray, moderately to highly bioturbated, diatom-bearing ashy clay and silty clay with few dark-colored layers. Nannofossils occur toward the base of Subunit IB (127-797B-13H, 104.4–119.9 mbsf). Diatoms increase in abundance downsection.

Unit II (119.9–224 mbsf)

Cores 127-797B-14H through 127-797B-24X.

Unit II is distinguished from Unit I by a significant increase in the diatom content in Cores 127-797B-13H and 127-797B-14H (Fig. 12) and by the absence of color bands below about 120 mbsf (Core 127-797B-13H). The sediment consists of 104.1 m of upper to lower Pliocene diatom clay, clayey diatom ooze, and

341

Table 1. Coring summary, Site 797.

Core no.	Date (1989)	Time (UTC)	Depth (mbsf)	Cored (m)	Recovered (m)	Recovery (%)	Age
127-797A-							
1H	Jul 31	0145	3.4–12.9	9.5	9.73	102.0	Quaternary
Coring totals				9.5	9.73	102.0	
127-797B-							
1H	31	0245	0.0–5.9	5.9	5.85	99.1	Quaternary
2H	31	0600	5.9–15.4	9.5	9.85	103.0	Quaternary
3H	31	0700	15.4–24.9	9.5	9.80	103.0	
4H	31	0930	24.9–34.4	9.5	9.73	102.0	Quaternary
5H	31	1015	34.4–43.9	9.5	9.85	103.0	Quaternary
6H	31	1115	43.9–53.4	9.5	9.89	104.0	Quaternary
7H	31	1300	53.4–62.9	9.5	9.98	105.0	Quaternary
8H	31	1340	62.9–72.4	9.5	9.84	103.0	Quaternary
9H	31	1425	72.4–81.9	9.5	9.93	104.0	Quaternary
10H	31	1630	81.9–91.4	9.5	9.81	103.0	late Pliocene
11H	31	1710	91.4–100.9	9.5	10.02	105.5	late Pliocene
12H	31	1800	100.9–110.4	9.5	9.98	105.0	late Pliocene
13H	31	2000	110.4–119.9	9.5	9.90	104.0	late Pliocene
14H	31	2050	119.9–129.4	9.5	8.73	91.9	late Pliocene
15H	31	2140	129.4–138.9	9.5	9.93	104.0	late Pliocene
16H	31	2330	138.9–148.4	9.5	9.69	102.0	late Pliocene
17H	Aug 1	0030	148.4–157.9	9.5	8.51	89.6	late Pliocene
18H	1	0130	157.9–166.4	8.5	8.53	100.0	late Pliocene
19H	1	0230	166.4–175.9	9.5	9.87	104.0	early Pliocene
20X	1	0730	175.9–185.5	9.6	7.93	82.6	early Pliocene
21X	1	0930	185.5–195.2	9.7	6.92	71.3	early Pliocene
22X	1	1015	195.2–204.8	9.6	7.95	82.8	early Pliocene
23X	1	1100	204.8–214.3	9.5	9.28	97.7	early Pliocene
24X	1	1145	214.3–224.0	9.7	9.73	100.0	early Pliocene
25X	1	1220	224.0–233.7	9.7	9.69	99.9	early Pliocene
26X	1	1435	233.7–243.4	9.7	9.49	97.8	early Pliocene
27X	1	1525	243.4–253.1	9.7	9.72	100.0	late Miocene
28X	1	1610	253.1–262.8	9.7	5.48	56.5	late Miocene
29X	1	1650	262.8–272.5	9.7	0.02	0.2	late Miocene
30X	1	1740	272.5–282.2	9.7	8.21	84.6	late Miocene
31X	1	1840	282.2–291.9	9.7	9.64	99.4	late Miocene
32X	1	1950	291.9–301.5	9.6	9.48	98.7	late Miocene
33X	1	2130	301.5–311.2	9.7	6.41	66.1	Unknown
34X	1	2325	311.2–320.9	9.7	8.46	87.2	
35X	2	0245	320.9–330.6	9.7	8.42	86.8	
36X	2	0500	330.6–340.3	9.7	0.05	0.5	
37X	2	0645	340.3–350.0	9.7	7.74	79.8	late Miocene
38X	2	0900	350.0–359.7	9.7	2.19	22.6	
39X	2	1100	359.7–369.3	9.6	0.87	9.1	
40X	2	1250	369.3–379.0	9.7	2.29	23.6	
41X	2	1500	379.0–387.9	8.9	2.18	24.5	
42X	2	1700	387.9–397.6	9.7	0.83	8.6	
43X	2	1930	397.6–407.3	9.7	0.74	7.6	
44X	2	2150	407.3–417.0	9.7	0.96	9.9	
45X	3	0000	417.0–426.6	9.6	0.24	2.5	
46X	3	0245	426.6–436.2	9.6	2.15	22.4	
47X	3	0515	436.2–445.9	9.7	8.22	84.7	
48X	3	0700	445.9–455.5	9.6	7.35	76.5	
49X	3	0830	455.5–465.2	9.7	8.28	85.3	
50X	3	1030	465.2–474.9	9.7	0.93	9.6	
51X	3	1150	474.9–484.5	9.6	8.82	91.9	
52X	3	1400	484.5–494.2	9.7	9.77	101.0	
53X	3	1615	494.2–495.7	1.5	0.56	37.3	
Coring totals				495.7	370.69	74.8	
127-797C-							
1R	6	0200	484.0–493.5	9.5	0.18	1.9	
2R	6	0315	493.5–503.0	9.5	3.14	33.0	
3R	6	0445	503.0–512.5	9.5	3.38	35.6	
4R	6	0600	512.5–522.0	9.5	0.02	0.2	
5R	6	0730	522.0–531.6	9.6	5.68	59.1	
6R	6	0830	531.6–541.3	9.7	7.41	76.4	
7R	6	1000	541.3–550.9	9.6	0.63	6.6	
8R	6	1205	550.9–560.6	9.7	2.81	28.9	
9R	6	1430	560.6–570.0	9.4	1.42	15.1	
10R	6	1715	570.0–579.5	9.5	4.85	51.0	
11R	6	1935	579.5–589.3	9.8	0.65	6.6	
12R	6	2240	589.3–598.8	9.5	5.04	53.0	
13R	7	0200	598.8–608.3	9.5	2.25	23.7	
14R	7	0345	608.3–617.8	9.5	1.14	12.0	

Table 1 (continued).

Core no.	Date (1989)	Time (UTC)	Depth (mbsf)	Cored (m)	Recovered (m)	Recovery (%)	Age
127-797C- (Cont.)							
15R	7	0600	617.8–627.3	9.5	3.15	33.1	
16R	7	0915	627.3–636.9	9.6	2.88	30.0	
17R	7	1140	636.9–646.5	9.6	0.83	8.6	
18R	7	1500	646.5–656.1	9.6	3.05	31.8	
19R	7	1745	656.1–665.9	9.8	7.41	75.6	
20R	7	2030	665.9–675.6	9.7	3.13	32.2	
21R	8	0200	675.6–685.1	9.5	6.80	71.6	
22R	8	0315	685.1–694.6	9.5	9.63	101.0	
23R	8	0445	694.6–704.1	9.5	8.06	84.8	
24R	8	0800	704.1–713.6	9.5	8.32	87.6	
25R	8	0930	713.6–723.2	9.6	8.54	88.9	
26R	8	1240	723.2–732.9	9.7	2.02	20.8	
27R	8	1605	732.9–742.6	9.7	1.60	16.5	
28R	8	1845	742.6–744.6	2.0	1.24	62.0	
29R	8	2300	744.6–754.0	9.4	2.04	21.7	
30R	9	0245	754.0–763.0	9.0	5.65	62.8	
31R	9	0615	763.0–772.4	9.4	6.34	67.4	
32R	9	0915	772.4–781.6	9.2	2.55	27.7	
33R	9	1300	781.6–791.0	9.4	4.09	43.5	
34R	9	1630	791.0–800.3	9.3	9.48	102.0	
35R	14	1855	800.3–804.8	4.5	3.92	87.1	
36R	14	2150	804.8–814.4	9.6	3.48	36.2	
37R	14	2340	814.4–824.0	9.6	9.15	95.3	
38R	15	0630	824.0–833.7	9.7	0.00	0.0	
39R	15	1000	833.7–842.7	9.0	0.00	0.0	
40R	15	1725	842.7–852.4	9.7	0.00	0.0	
41R	16	1920	852.4–861.9	9.5	3.81	40.1	
42R	16	2155	861.9–871.6	9.7	0.20	2.1	
43R	17	0215	871.6–881.3	9.7	0.19	2.0	
44R	17	1015	881.3–890.9	9.6	4.02	41.9	
45R	17	1410	890.9–900.1	9.2	4.00	43.5	
Coring Totals				416.1	164.18	39.5	

diatom ooze with subordinate calcareous clayey diatom ooze and silty-clay diatom ooze. All lithofacies are heavily bioturbated and mottled. Diatom clay is dominant in the upper section of the unit (Cores 127-797B-14H through 127-797B-17H), but the sediment is more diatomaceous in the middle and lower parts of the unit below 175.9 m (Cores 127-797B-20X through 127-797B-24X; Fig. 12). Minor dolomicritic layers and dolomite nodules, generally yellowish in color, occur in some intervals of Cores 127-797B-14H through -17H and Cores 127-797B-20X through -22X. Rare ash layers, up to several centimeters thick, occur in the upper part of the unit (Cores 127-797B-14H through -18H; 119.9–166.4 mbsf).

Unit III (224–301.5 mbsf)

Cores 127-797B-25X through 127-797B-32X.

Unit III is distinguished from Unit II on the basis of a significant decrease in diatom content and the first appearance of bioclastic sand layers. The unit is also characterized by a slight increase in the content of the silt-sized grains in the sediment, the reappearance of color bands, and the dominance of sponge spicules over diatoms especially in the lower part of the unit. The strata consist of 77.5 m of lowermost Pliocene to uppermost Miocene diatom clay, silty claystone, and spicular silty claystone with subordinate diatom ooze and diatom-bearing claystone. The sediments are moderately to heavily bioturbated and indistinctly mottled. Fine-grained bioclastic sand layers less than 2 cm thick are present in Cores 127-797B-25X, -27X, -30X, and -32X (Fig. 14). Rare ash and carbonate layers and nodules occur in a few sections. The first opal-CT chert layer appears near the bottom of the unit in Core 127-797B-32X at 299 mbsf. The strata contain faint to distinct dark and light color bands (especially in Cores 127-797B-27X, -30X, and -32X). Dark-colored layers, gen-

erally 5 to 20 cm thick, are slightly coarser grained than lighter colored layers, which are 20 to 100 cm thick. Bioclastic sand layers are also present at the base of many of the dark layers. The bioclastic sand contains abundant foraminifers and sponge-spicule fragments with trace amounts of quartz and feldspar.

Unit IV (301.5–426.6 mbsf)

Cores 127-797B-33X through 127-797B-45X.

The unit consists of 125.1 m of upper to middle Miocene claystone and siliceous claystone with subordinate silty claystone, chert, and porcellanite. Carbonate layers and nodules are common in the upper half of the unit. Ash layers are absent in this unit. The unit is distinguished from Unit III by the absence of bioclastic sand layers and by the absence of diatoms below 301.5 m. The disappearance of diatoms is a result of the transition from opal-A to opal-CT, which occurs at the base of Unit III.

Subunit IVA (301.5–350 mbsf)

Cores 127-797B-33X through 127-797B-37X.

Subunit IVA is characterized by a gradual downward dominance of claystone over silty claystone. The strata consist of 48.5 m of upper Miocene claystone and silty claystone with rare intercalations of chert. The upper to middle sections contain faint dark and light color bands; the bands gradually disappear in the lower part of the subunit. The dark-colored layers are indistinctly laminated to slightly bioturbated, whereas the light-colored layers are moderately to heavily bioturbated and slightly mottled. Sediments in the lower part of the subunit are heavily bioturbated and homogeneous throughout. Carbonate layers are common.
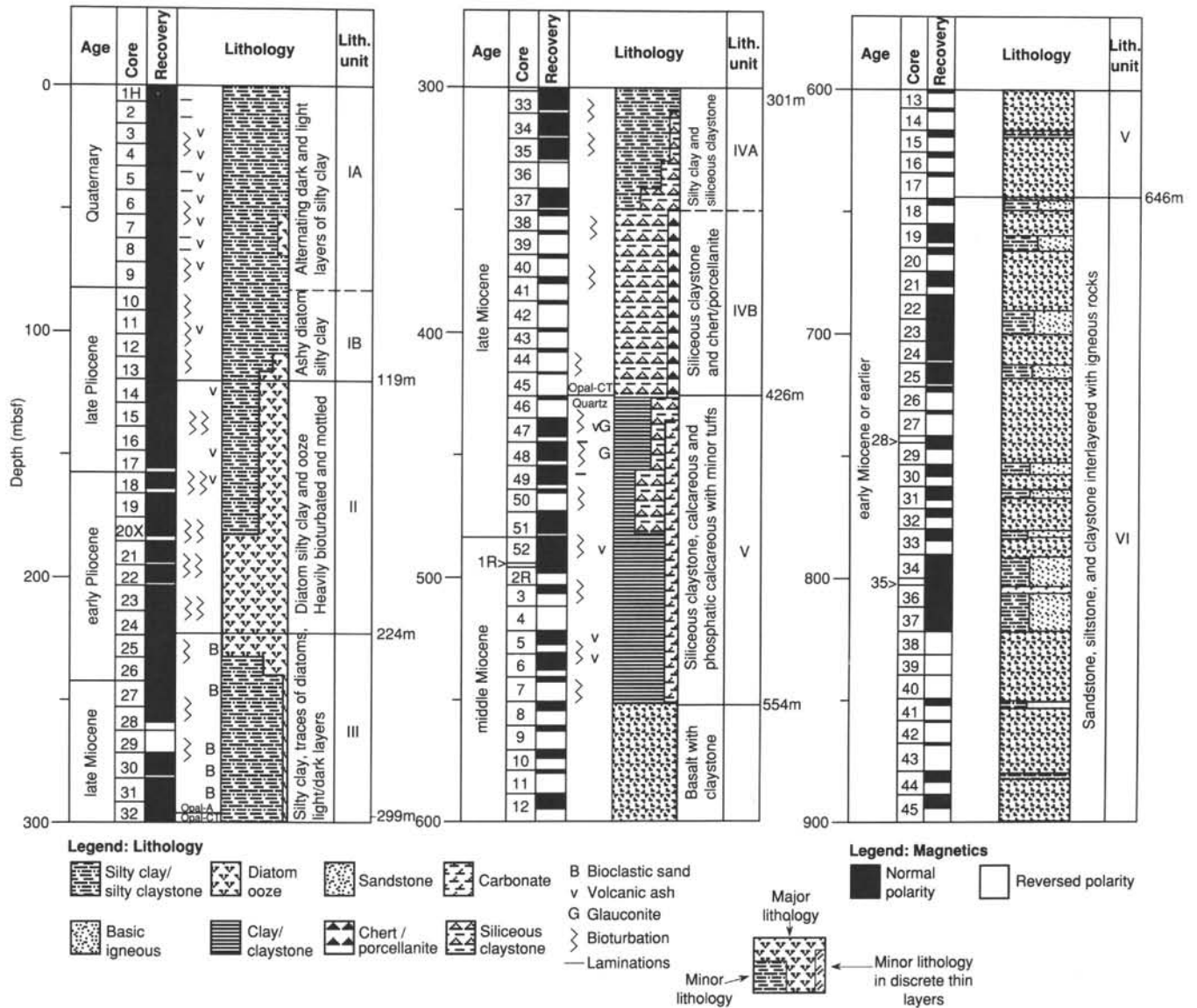
Figure 12. Lithostratigraphic summary of Site 797. Core 127-797A-1H is not shown but is included in the description of Unit I.

Subunit IVB (350–426.6 mbsf)

Cores 127-797B-38X through 127-797B-45X.

Subunit IVB consists of 76.6 m of upper Miocene moderately to well-bioturbated siliceous claystone, claystone, and chert. The siliceous claystone and claystone are lighter in color and are characterized by compacted horizontally flattened burrows. Siliceous claystones within this subunit are hard porcellanites and show a distinct matte luster. Chert occurs in 10- to 30-cm-thick layers and is dark in color. A sandstone layer 5 cm thick occurs at the top of Core 127-797B-43X at 397 mbsf. The sandstone is medium to fine grained, normally graded with faint planar lamination, and cemented with carbonate; it contains abundant lithic fragments.

Unit V (426.6–627.3 mbsf)

Cores 127-797B-46X through 127-797C-15R.

Unit V is distinguished from Unit IV by the absence of chert layers, better preserved parallel lamination, and the occurrence of phosphatic carbonate stringers and nodules. The shallowest appearance of basaltic breccia occurs at 554 mbsf. The strata above the basaltic breccia consist of 126.9 m of middle Miocene and upper lower Miocene(?) claystone and siliceous claystone which are faintly laminated to moderately bioturbated; most burrows are compacted and horizontal. Many of the claystones contain thin (less than 0.5 cm) stringers and small (less than 1 cm diameter) nodules of phosphatic carbonate (Fig. 15). Small pyrite nodules are common throughout. The claystone of this unit contains small amounts of clinoptilolite or mordenite. Numerous small-scale vertical, anastomosing mud-filled fractures (possible fluid-escape structures) are found within the claystone. Traces of glauconite are found in Cores 127-797B-47X and -48X. Large foraminifers were recognized in Core 127-797B-49X. Altered fine vitric(?) tuff layers up to 10 cm thick are common throughout the unit. Three layers of tuffaceous(?) sandstone up to 11 cm thick were also found in Core 127-797B-51X (474.9–484.9 mbsf). Dark-colored, dense, hard carbonate-cemented claystone layers are common to 554 mbsf.

Cores 127-797C-9R, 127-797C-11R, and 127-797C-15R contain conglomerate intervals up to 7 cm thick and claystone beds
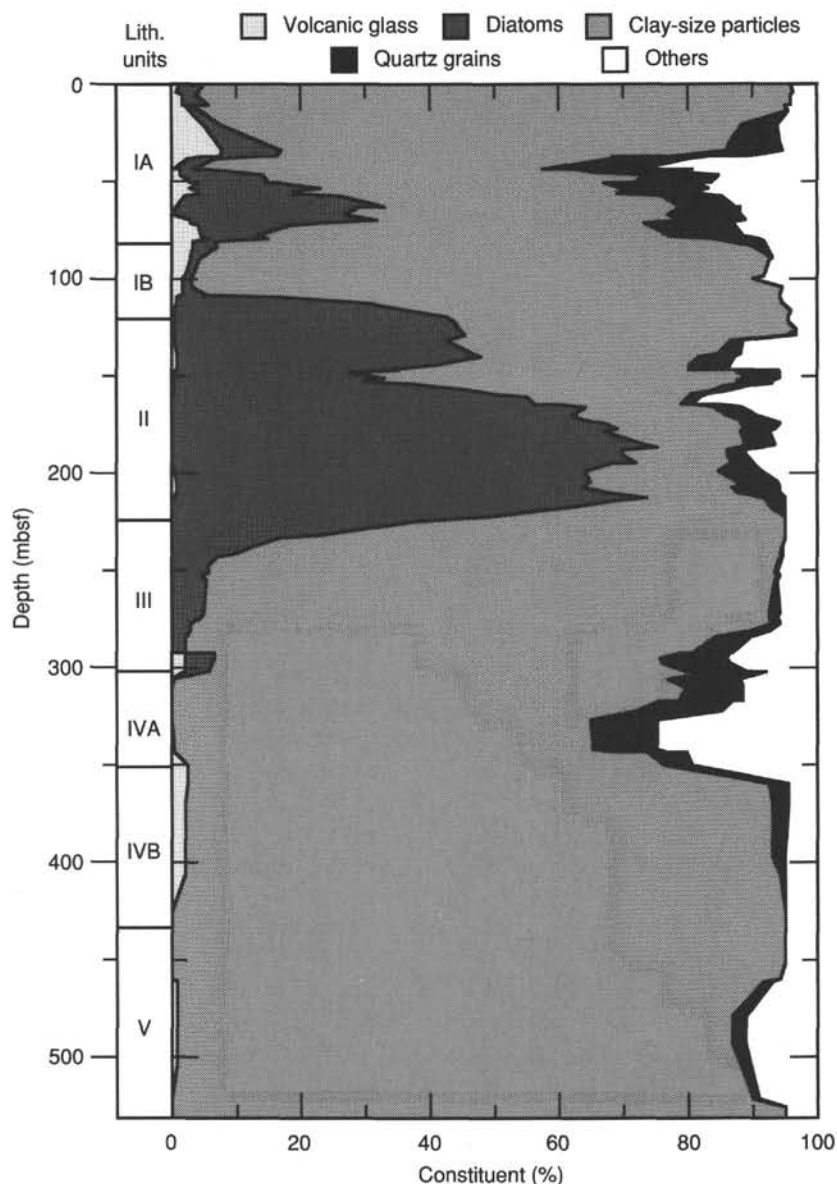
Figure 13. Stack plot of semiquantitative mineralogic data from smear-slide analysis vs. depth for Site 797. Lithologic units are shown.

between 5 and 65 cm thick. The conglomerate and claystone occur between igneous-rock layers. The conglomerate is composed entirely of porcellanite pebbles within a siliceous mud matrix. The porcellanite pebbles contain highly recrystallized radiolarian skeletons and diatom tests. The claystone is slightly tuffaceous and contains traces of pumice, although the overall composition is similar to that of the claystone in Unit V. For this reason we tentatively include this interval within Unit V.

Igneous rocks are present from the base of Unit V at 627.3 m to the top of Unit VI at 646.9 m (see "Basement Rocks" section, this chapter). No exact contacts were recovered at the sediment/basement interface.

Unit VI (646.9–900.1 mbsf)

Cores 127-797C-18R through 127-797C-34R.

Unit VI consists of 153.4 m of lower Miocene(?) alternating carbonaceous siltstone, sandstone, and minor silty claystone in-

tercalated with generally aphanitic basalt ("Basement Rocks," this chapter). The unit contains scattered pyroclastic strata, which consist of rare thin-bedded and strongly altered bentonitic tuff. Minor microfaults and calcite-filled veins are also present. The sediment within the unit is composed of siltstone, sandstone, carbonaceous siltstone, and minor silty claystone, with abundant planar lamination, small-scale cross-lamination, and minor climbing ripple-drift cross-lamination. A 1.5-m section of the unit is illustrated in Figure 16. Lamination and a strong horizontal-planar fabric in very fine- to medium-grained sandstone and siltstone beds are defined by the presence of abundant platy, horizontally orientated carbonaceous wood fragments. The sandstones are composed primarily of subangular to subrounded grains of feldspar, volcanic lithic fragments, quartz, carbonaceous material, and minor glass shards. Alteration is extensive, with silicification and alteration of lithic and vitric fragments to clay and zeolite. The sedimentary section is dominated by sandstone and siltstone beds, commonly 1 to 15 cm thick but rang-
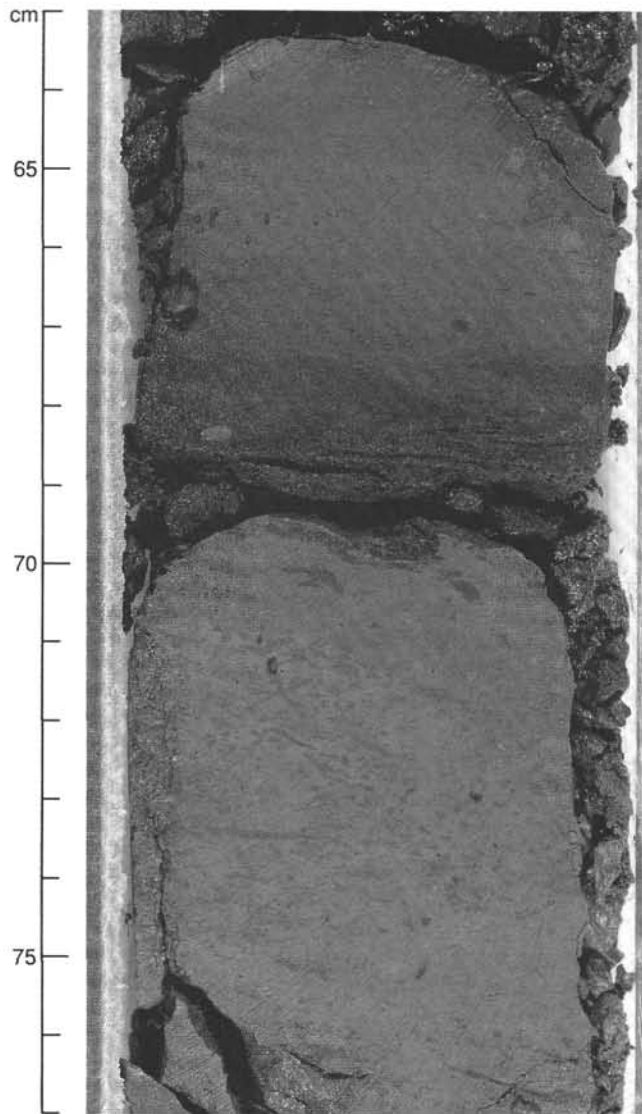
Figure 14. Core 127-797B-32X (Unit III), showing bioclastic sand at the base of a dark silty-claystone layer. Note also bioturbation in the light-colored layer.

Figure 15. Core 127-797B-51X (Unit V), showing small carbonate and phosphatic nodules and stringers (light colored) within dark-colored claystone.

ing to 30 to 50 cm thick. Most sandstone beds have sharp scoured basal contacts and display overall normal size grading (Figs 17 through 20). Some layers lack distinct grading but contain alternating layers, each characterized by grains of nearly uniform size. The scoured basal contacts of sandstone and siltstone beds are commonly disrupted by load and probable water-escape structures, including flame structures. Siltstone beds, with common basal scoured contacts, planar lamination, and abundant carbonaceous material, are generally graded upward to silty claystone. These siltstones commonly contain abundant, small, generally dark-colored, flattened, oval to irregularly shaped lenses of siltstone (Fig. 21). These features are present mainly in the siltstone and may be rip-up clasts, burrows, or both. Recognizable trace fossils include *Zoophycos*-like horizontal burrows concentrically laminated, possible *Asterosoma*, and rare flattened vertical burrows of probable *Skolithos* affinity.

The unit is generally coarser grained between depths of approximately 695 and 723 mbsf (Cores 127-797C-22R, -23R, and -25R). Finer grained silty claystone is more abundant from approximately 754 to 800 mbsf (Cores 127-797C-30R, -31R, -33R, and -34R). Darker colored siltstone is present in the lower sec-

tion of the unit below approximately 850 mbsf (Core 127-797C-41R). Rare primary dips, ranging up to 20°, are associated with small-scale slump deformation structures (Core 127-797C-30R).

There are 16 transitions between basaltic rocks and sediments in Unit VI, among which only one exact contact was recovered in Core 127-797C-19R. Within that core the silty claystone and siltstone below the basaltic layer are baked, being much harder and showing obvious color alteration. Slight alteration in color is observed in sediments below basaltic layers in Cores 127-797C-22R, -33R, and -34R and above basaltic layers in Cores 127-797C-18R, -20R, -23R, -26R, -30R, and -31R, which suggests thermal alteration at the contact.

Sediment Grain Size

Grain-size analysis was carried out on sediment to a depth of 289 mbsf. In general, two samples (from Sections 2 and 5) were analyzed from each core. Below 289 mbsf, samples could not be disaggregated owing to silica cementation. Sediments analyzed have a mean grain size that ranges from 7.8 to 19.2 μm and are composed predominantly of material in the clay- and silt-size fraction. As at previous sites, the presence of diatom tests (mean grain size of 8–15 μm) and vitric ash tends to skew the mean grain size toward the silt-size range. Semi-quantitative smear-slide analysis indicates that the sediments from 289 through 627 mbsf are of a similar grain size to those determined quantitatively. Sedimentary material interlayered with igneous rocks in Unit VI consists of fine to medium sand and coarse silt to clay.

Frequency of Ash-Layer Occurrence

A plot showing the frequency of ash-layer occurrences in sediments at Site 797 is shown in Figure 22. The plot shows a maximum in ash-layer frequency in Quaternary and Pliocene sediments, a minimum in upper Miocene and uppermost middle Miocene sediments, and another maximum in upper middle Miocene sediments. A similar pattern of occurrence was noted at Site 794 (see "Lithostratigraphy" section, Site 794 chapter).
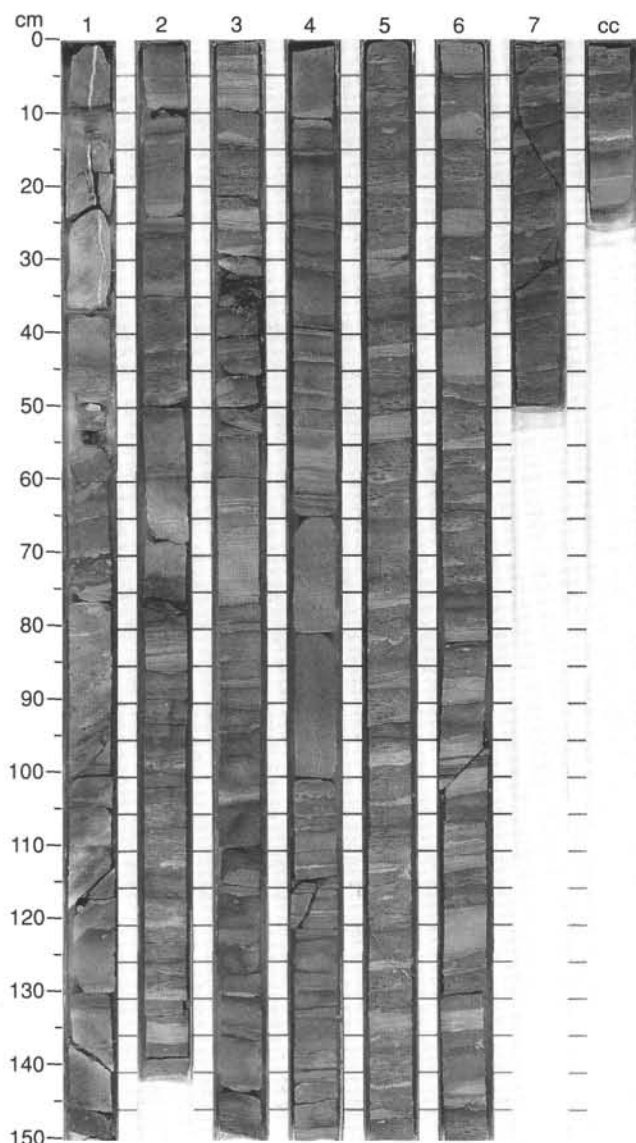
Figure 16. Core 127-797C-22R, illustrating interlayered sandstone (light colored), siltstone, and silty claystone typical of Unit VI. Numerous oval to irregular lenses are present in Sections 2, 5, and 6. The top 37 cm of Section 1 is basaltic rock.

Figure 17. Core 127-797C-22R (Unit VI), showing a normal-size-graded sandstone to siltstone unit. The upper section of the sequence contains micro-cross-laminated carbonaceous siltstones (67-70 cm, light color), soft-sediment deformation features (71–73 cm), and thin organic-rich laminae (72–75 cm).

Silica Diagenesis

The opal-A to opal-CT transition occurs in Site 797 sediments between 294.3 and 299.1 mbsf. The transition at this site is difficult to detect by XRD analysis of samples because the original content of biogenic silica is generally low in Unit III and Subunit IVA (224–350 mbsf). A weak opal-CT peak first occurs in XRD plots of samples from the diatom-bearing silty claystone from 298.8 mbsf, and the first opal-CT chert layer occurs at 299.1 mbsf. Distinct opal-CT occurs only within discrete cherty layers in Subunit IVA, as the claystone of Subunit IVA does not generally contain detectable amounts of opal-CT. The depth interval for the opal-A/opal-CT transition corresponds with the depth at which siliceous microfossils disappear (ca. 305 mbsf), interstitial-water silica concentration decreases dramatically (288.1–314.2 mbsf), and physical properties change significantly (299–312 mbsf; see "Inorganic Geochemistry" and "Physical Properties" sections, this chapter). The temperature for the opal-A/opal-CT at this Site is 36°C, based upon the estimated

temperature profile ("Physical Properties" section). This value is in good agreement with those stated for the previous Sites (36°–43°C).

The opal-CT/quartz transition at Site 797 occurs between 428 and 438 mbsf. The transition occurs within siliceous claystone of Unit V. No significant change in physical properties and interstitial-water chemistry was observed corresponding to the transition (see "Inorganic Geochemistry" and "Physical Properties" sections, this chapter). The temperature estimated for the opal-CT/quartz transition is 52°C.

Depositional History

The sediments recovered at this site are the first complete section recovered from this part of the Yamato Basin and provide a first insight into the depositional environment prior to the middle Miocene. The complete sedimentary sequence suggests that deposition evolved from a slope to a basin environment.

The strata of Unit VI are middle Miocene or older and are composed of interbedded fine-grained sandstone, siltstone, and silty claystone. Scoured basal contacts, planar lamination, small-scale cross-lamination, rip-up clasts, and normal size grading are dominant characteristics of the sandstones and siltstones. Many of the features, especially nearly ubiquitous grading and the presence of Bouma sequences, indicate common deposition by sediment gravity flows.

The presence of abundant scour structures, rip-up clasts, soft-sediment deformation, water-escape structures, and climbing ripple cross-lamination especially in the upper parts of the unit, where suspension-deposited sediment is rare, suggests overall rapid sediment deposition. Bioturbated claystones are more
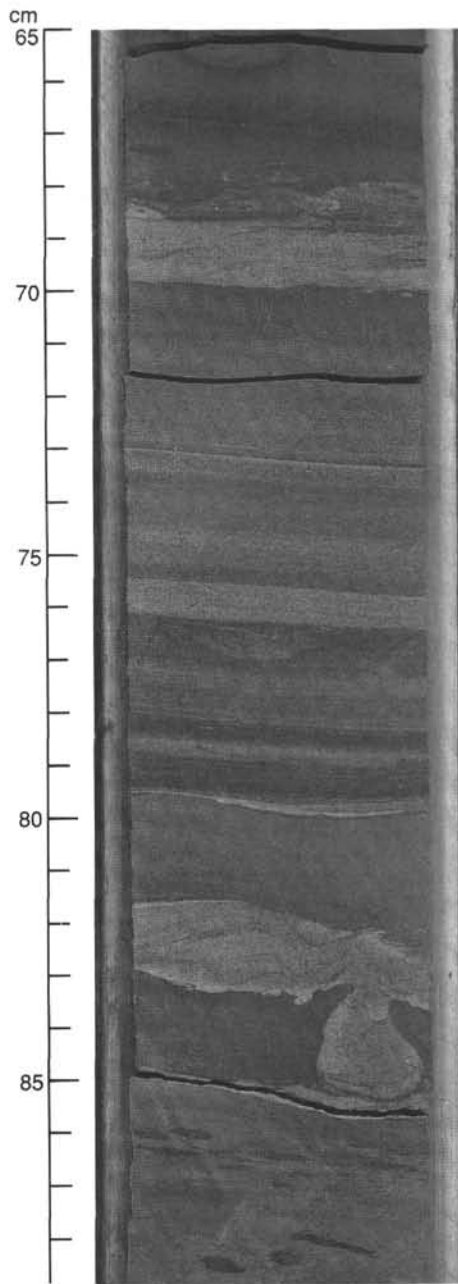
Figure 18. Core 127-797C-25R (Unit VI), showing laminated sandstone (82–83 cm), with soft-sediment deformation at base, overlying planar-laminated sandstone-siltstone interval (70–79 cm), and sandstone layer with micro-cross-laminations and soft-sediment deformation features at the upper contact with siltstone (68–70 cm). Minor lens-like structures (dark colored) with halo (light colored) features occur between 86 and 89 cm. These examples are burrows.

Figure 19. Core 127-797C-34R (Unit VI), showing parallel-laminated, normal-size-graded sandstone with micro-cross-laminations (27–30 cm) and carbonaceous material (27–34 cm). Note basal scour and persistent dip of approximately 10°.
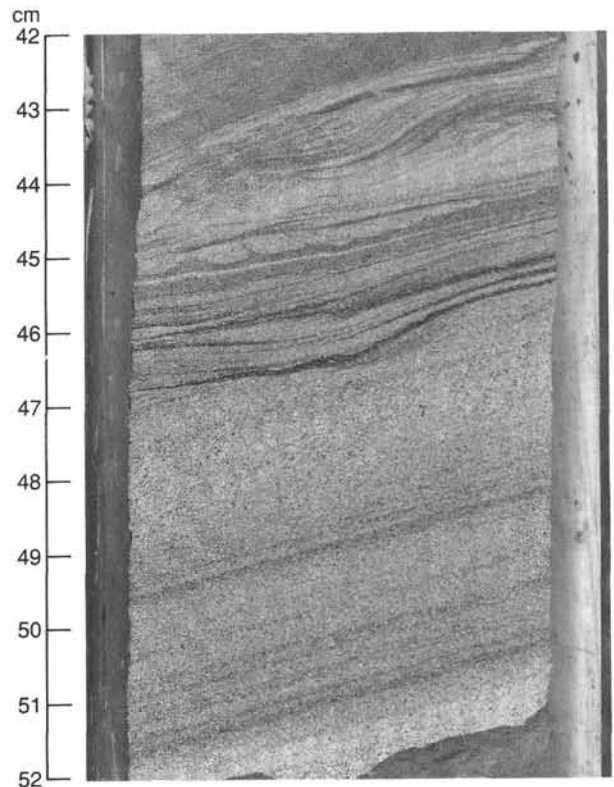
Figure 20. Core 127-797C-34R (Unit VI), showing planar-laminated sandstone (47–52 cm) below normal-size-graded sandstone (43–47 cm), with carbonaceous laminae (45–47 cm) and micro-cross-lamination (43–45 cm). Dip is approximately 10°.

common at the base of Unit VI and suggest episodic and more protracted suspension sedimentation. The abundance of carbonaceous detritus and higher plant material disseminated throughout the sequence suggests a marine setting proximal to terrestrial sediment input. The depositional environment could range from shallow marine to upper bathyal water depths. The lower, generally finer grained part of this section contains syndepositional deformation features suggestive of a submarine slope.

Deposition of Unit VI probably took place on a progradational(?) shelf-slope setting along the narrow margin of a ma-

Figure 21. Core 127-797C-22R (Unit VI), showing two sandstone intervals (light colored) interbedded within siltstone (dark colored). The sandstones are micro-cross-laminated with soft-sediment deformation or fluid-escape features at their upper contacts. The claystone (16–23 cm) contains lenses of dark siltstone within lighter siltstone that probably are burrows.

rine basin. Abundant plant debris and indications of rapid sediment accumulation, especially in the upper parts of the section, suggest a depositional site basinward (below wave base) but relatively proximal to a deltaic depositional system of significant size (Fig. 23). Such a depositional system has been described from the Paleogene fore-arc region of central Oregon (Dott and Bird, 1979) and resembles the description of upper Miocene volcaniclastic strata deposited "on a slope setting in a series of small basins" exposed on western Hokkaido Island and described by Klein et al. (1979, p. 372).

The claystone sequence (Unit V) above the brecciated igneous rocks from 554 to 426.6 mbsf is of latest early Miocene age. The claystone is characterized by faint lamination and horizontally flattened burrows and several intercalations of phosphatic carbonate stringers and nodules. Together, these features suggest poorly oxygenated bottom-water conditions. Similar lithologies occur at Sites 794 and 795, suggesting that comparable conditions probably prevailed throughout the Yamato Basin. The benthic foraminiferal assemblage in this claystone (see "Biostratigraphy" section, this chapter) indicates a lower bathyal depth. This depth is somewhat greater than the upper to mid-bathyal depth inferred for the sandstones and siltstones of Unit VI. If these interpretations are correct, then this part of the Yamato Basin subsided at a rate of approximately 250 m/m.y. during the late Miocene.

Subunit IVB was deposited between late middle to late Miocene time and is characterized by the common intercalation of chert. The section consists of light-colored, heavily bioturbated siliceous claystone, interbedded with dark-colored, slightly bioturbated chert and porcellanite. This siliceous interval may represent enhanced productivity of diatoms within the photic zone or a reduction in the input of terrigenous material during this time interval.

In contrast to Subunit IVB, the overlying sedimentary section is slightly coarser grained in the uppermost Miocene (Subunit IVA and Unit III). The interval is characterized by light- and dark-colored bands, abundant sponge spicules, reworked fossils, and common bioclastic sand intercalations, especially within Unit III. These sediments, especially the bioclastic sand, are unique to this site and probably represent reworked material originating from the Yamato Rise. Wave or current access to the Yamato Rise may have been gained by the fall in global sea level during latest Miocene time. Sedimentation rates are high during this period (43 to 56 m/m.y.; see "Sediment Accumulation Rates," this chapter) and support this interpretation.

The Pliocene (Unit II) sedimentary sequence is slightly finer grained and more diatom-rich than the underlying unit. The sediments are heavily bioturbated, suggesting well-oxygenated bottom-water conditions. The presence of diatom ooze in this sequence is probably indicative of periods of enhanced productivity as a result of increased nutrient supply. The presence of upwelling-specific diatoms (see "Biostratigraphy") within the upper section of the sequence at Site 797 (0–140 mbsf) reinforces the interpretation of increased vertical circulation (upwelling) and the introduction of nutrients to the photic zone. Detrital fluvial input could also account for an increase in nutrient supply to the photic zone, but we see no evidence for this in the sediments.

Sediments of latest Pliocene, Pleistocene, and Holocene age are characterized by dark and light color banding and several intervals enriched in diatoms, nannoplanktons, and foraminifers. Many sedimentary and paleoceanographic processes have been proposed to account for the deposition of alternating light- and dark-colored sediments. The following paleoceanographic controls are proposed to account for the deposition of such layers within the Pleistocene-Holocene sediments (Subunit IA) in the Japan Sea.

The first control which could account for the deposition of light- and dark-colored layers corresponds to periods when the oxygen level at the seafloor fluctuated between oxic, suboxic, and anoxic. The oxygen levels are directly related to the amount of surface-, intermediate-, and deep-water circulation and mixing taking place. The degree of circulation and mixing could have been controlled by sea-level changes in an area of shallow bathymetric sills and could ultimately have been governed by tectonic activity and climatic fluctuation. During periods of reduced or depleted oxygen, dark-colored, organic-rich layers were preserved, whereas during oxygenated conditions, light-colored, well-bioturbated layers accumulated.

A second possible control of light and dark interlayering relates to gravity flows. Some of the dark-colored layers contain distinct size grading, which supports turbidite deposition, rapid burial, and enhanced organic-matter preservation. The light-colored layers represent periods when hemipelagic and pelagic sedimentation occurred. These intervals are characterized by faint parallel laminations with limited size grading at the base, together with well-bioturbated upper intervals.

Variations in the supply of nutrients to the photic zone may also have contributed to the light-dark cyclicity. In particular, conditions favorable for dark-layer deposition and preservation may have resulted from variable upwelling of nutrient-rich bottom or intermediate waters, from fluctuating detrital input rich
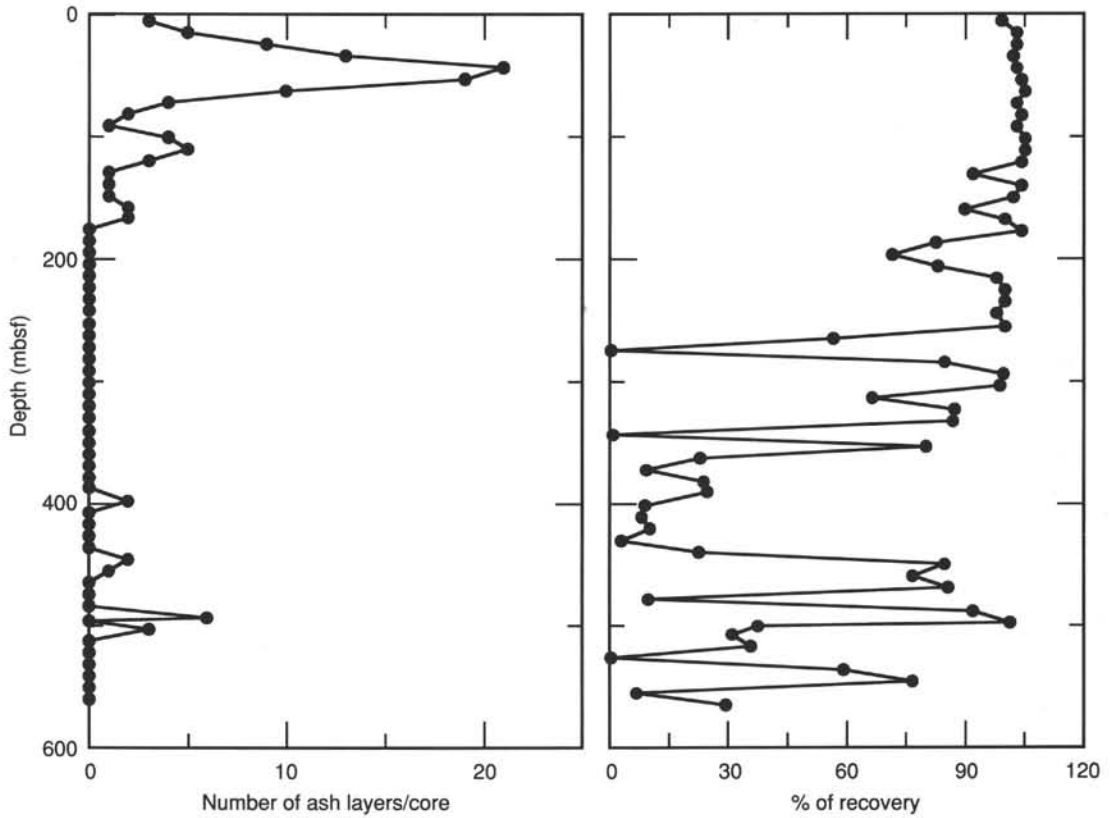
Figure 22. Plot showing frequency of ash layers per core at Site 797, with a comparison plot of core recovery vs. depth.
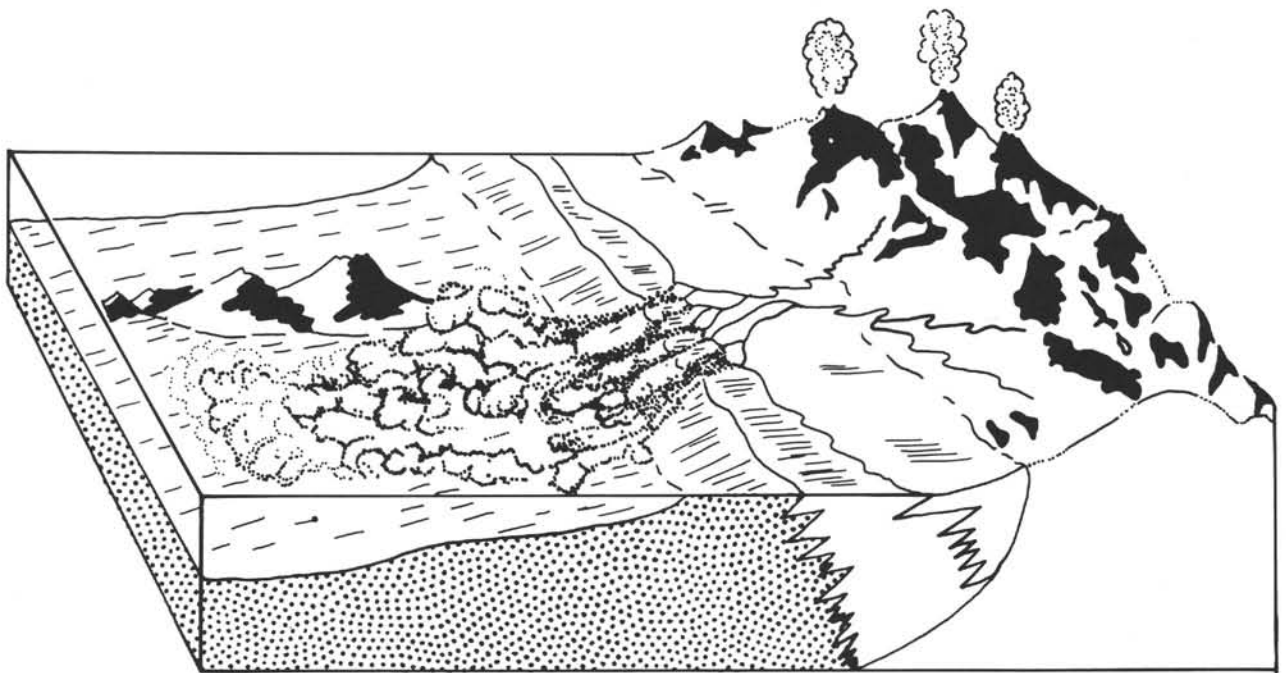
Figure 23. Block diagram showing a possible depositional environment of Unit VI. The diagram shows channels seaward of a delta cutting across a narrow continental slope and feeding a submarine fan. The stippled area represents a probable depositional area for the sequence recovered at Site 797. (Modified from Dott and Bird, 1979.)

in nutrients, or by episodic overflow across sills by surface waters rich in nutrients.

BIOSTRATIGRAPHY

Introduction

Trends in microfossil abundance and preservation at Site 797 reflect both post-depositional processes and environmental conditions at the time of deposition. As at other sites of Leg 127, the opal-A/opal-CT transition has a profound effect on the distribution of siliceous microfossils. Diatoms and radiolarians are, in general, common to abundant and moderately to well preserved above the transition and poorly preserved or absent below the transition. Above the transition, variations in abundance and preservation reflect environment. Diatom silty clays and oozes reflect upwelling from 5.3 to 2.6 Ma at this site and are correlative with high-productivity events known in marginal basins throughout the North Pacific rim. Preservation and abundance of both carbonate and siliceous microfossils are highly variable in the Quaternary, reflecting alternation of environmental modes and preservation during glacial cycles.

Carbonate microfossils are best preserved and most abundant in Quaternary and middle Miocene sequences of Site 797. In contrast to other sites cored during Leg 127, calcareous benthic foraminifers occur, throughout Site 797 except in lower Miocene units, where rare calcareous nannofossils occur, and an upper Miocene unit, where sporadic intervals bearing calcareous nannofossils occur in a cherty, porcellaneous siliceous claystone. Site 797 apparently lay near or above the CCD in the Yamato Basin throughout most of the Neogene and Quaternary.

An interval of slow sedimentation between 350 and 374 mbsf in the upper Miocene caps a claystone that contains porcellanite and chert (lithologic Unit IVB) and is barren of foraminifers (Table 2). The interval of slow sedimentation forms a boundary zone between moderate sedimentation rates of 25 m/m.y. in middle Miocene sequences and fast sedimentation rates of 50 m/m.y. in younger units. It is unclear at this moment if the different sedimentation rates above and below the boundary zone reflect environmental change or compaction and post-depositional processes.

Diatom zones best divide the sequence above the opal-A/opal-CT transition and one diatom datum level was reported from a diatom assemblage preserved in a carbonate nodule below the transition. Calcareous-nannofossil datum levels best divide the middle Miocene sequence and are consistent with occurrences of planktonic foraminifers. The age of sediment above the basal basaltic units is 20 m.y. based on extrapolation of the sedimentation-rate curve from three calcareous-nannofossil datum levels. The age of sediment intercalcated among basaltic breccias, flows, and sills in basal Unit VI of Hole 797C is no older than early Miocene based on the occurrence of one species of calcareous nannofossil.

Diatoms

Lithologic Subunit IA consists of banded silty clays with rare to abundant diatoms of Quaternary age and includes Samples 127-797B-1H-CC through 127-797B-9H-CC (Fig. 24). Samples 127-797B-1H-CC and 127-797B-2H-CC contain *Neodenticula seminae* but do not have *Rhizosolenia curvirostris* and are assigned to the *Neodenticula seminae* Zone (Fig. 24). Samples 127-797B-3H-CC through 127-797B-5H-CC are assigned to the *Rhizosolenia curvirostris* Zone based on the presence of *R. curvirostris*. The lower Quaternary *Actinocyclus oculatus* Zone occurs in Samples 127-797B-6H-CC through 127-797B-9H-CC, based on the presence of *A. oculatus*. The base of the *Actinocyclus oculatus* Zone in Sample 127-797B-9H-CC corresponds to

the Pliocene/Pleistocene boundary and the boundary between lithologic Subunits IA and IB.

Lithologic Subunit IB includes ashy diatom silty clay with few to abundant diatoms that show poor to good preservation (Table 2). The presence of common *Neodenticula koizumii* in Samples 127-797B-10H-CC through 127-797B-13H-CC suggests that this unit is part of the upper Pliocene *Neodenticula koizumii* Zone (Fig. 24).

Unit II consists mainly of diatom silty clay and ooze, encompasses Samples 127-797B-14H-CC through 127-797B-24X-CC, and is Pliocene in age. Samples 127-797B-14H-CC through 127-797B-18H-CC contain mostly common diatoms with good preservation (Table 2). The diatom assemblages in these samples include both *Neodenticula koizumii* and *Neodenticula kamtschatica*, characteristic of the upper Pliocene *Neodenticula koizumii–Neodenticula kamtschatica* Zone (Fig. 24). In Samples 127-797B-19H-CC through 127-797B-24X-CC, diatoms are more abundant than in Samples 127-797B-14H-CC through 127-797B-18H-CC (Table 2). Samples 127-797B-19H-CC through 127-797B-24X-CC have both *Neodenticula kamtschatica* and *T. oestrupii* and are assigned to the lower Pliocene *Thalassiosira oestrupii* Zone (Fig. 24).

Samples 127-797B-25X-CC through 127-797B-32X-CC consist of silty clays (lithologic Unit III) with few to abundant diatoms showing only moderate preservation (Table 2). Samples 127-797B-25X-CC and 127-797B-26X-CC both have *Neodenticula koizumii* and *Thalassiosira oestrupii* and are also part of the lower Pliocene *Thalassiosira oestrupii* Zone. The Pliocene/Miocene boundary is between Samples 127-797B-26X-CC and 127-797B-27X-CC. The upper Miocene *Neodenticula kamtschatica* Zone occurs in Samples 127-797B-27X-CC through 127-797B-32X-CC, based on the presence of *N. kamtschatica* and *Rouxia californica*. The opal-A/opal-CT transition is near the base of lithologic Unit III in Core 127-797B-32X, and below this depth diatoms are preserved only in carbonate concretions. Reworked older Miocene diatoms are found throughout Hole 797B and are particularly common in Samples 127-797B-26X-CC, 127-797B-28X-CC, 127-797B-30X-CC, and 127-797B-31X-CC (Fig. 24) of the uppermost Miocene and lowermost Pliocene.

Lithologic Subunit IVA is mainly silty clay and siliceous claystone and includes Cores 127-797B-33X through 127-797B-37X. It is within the opal-CT zone and is therefore barren of diatoms. Diatoms are preserved in a carbonate concretion found at approximately 350 mbsf (Sample 127-797B-37X-1, 84–85 cm). It contains *Rouxia californica* and *Actinocyclus ingens* and is assigned to the upper Miocene *Rouxia californica* Zone (Fig. 24).

No age-diagnostic diatoms were preserved in carbonate concretions below 350 mbsf. Ages below this depth are provided by several calcareous-nannofossil datum levels, which suggest an unusually slow rate of sedimentation between the last diatom datum level and the first nannofossil datum level (see section on "Sedimentation Accumulation Rates," this chapter).

Calcareous Nannofossils

Nannofossils at Site 797 are more common and better preserved than at other sites of Leg 127. Where nannofossils are present, relative abundance varies from abundant to rare, and preservation varies from good to poor (Tables 2 and 3). In contrast to previous sites, the nannofossil assemblages at Site 797 are more diverse and include a larger number of warm-water species. Nannofossils occur only in Pleistocene and in middle Miocene sediments.

Only one core was recovered from Hole 797A, and it is barren of nannofossils. From Hole 797B, 11 of 53 core-catcher samples contain nannofossils. In Pleistocene sediments, nannofossils occur sporadically, are common to few in abundance, and

Table 2. Abundance and preservation of microfossils in Holes 797A and 797B.

Core	Diatoms		Nannofossils		Planktonic foraminifers		Benthic foraminifers		Radiolarians	
	Abundance	Preservation	Abundance	Preservation	Abundance	Preservation	Abundance	Preservation	Abundance	Preservation
127-797A-										
1H-CC	abundant	good	barren		few	moderate	barren		abundant	moderate to good
127-797B-										
1H-CC	common	good	barren		abundant	poor	few	moderate	common	moderate
2H-CC	rare	poor	barren		few	moderate	barren		rare	moderate
3H-CC	abundant	good	common	moderate	abundant	moderate	few	moderate	rare	good
4H-CC	rare	poor	abundant	good to moderate	abundant	moderate	few	moderate	rare	moderate
5H-CC	few	moderate	abundant	good	abundant	moderate	common	moderate	common	good
6H-CC	few	moderate	barren		common	poor	few	poor	abundant	good
7H-CC	few	moderate	barren		rare	moderate	barren		abundant	good
8H-CC	abundant	good	few	good	few	moderate	barren		common	good
9H-CC	common	good	few	good	rare	poor	barren		common	moderate
10H-CC	few	poor	barren		common	moderate	rare	poor	few	moderate
11H-CC	common	good	barren		common	moderate	common	moderate	common	moderate
12H-CC	abundant	good	barren		barren		rare	moderate	common	good
13H-CC	abundant	good	barren		barren		few	moderate	common	moderate to good
14H-CC	abundant	good	common	poor	barren		few	moderate	abundant	good
15H-CC	common	good	barren		rare	poor	common	moderate	abundant	good
16H-CC	common	moderate	barren		barren		rare	moderate	common	moderate
17H-CC	common	good	barren		rare	moderate	few	moderate	common	moderate
18H-CC	common	good	barren		rare	moderate	few	moderate	common	moderate
19H-CC	abundant	good	barren		barren		few	moderate	common	moderate
20X-CC	abundant	good	barren		rare	moderate	few	moderate	common	moderate
21X-CC	abundant	good	barren		rare	poor	few	moderate	few	moderate
22X-CC	abundant	good	barren		barren		rare	poor	common	good
23X-CC	abundant	moderate	barren		barren		barren		common	moderate
24X-CC	common	moderate	barren		barren		rare	moderate	abundant	good
25X-CC	few	moderate	barren		rare	poor	few	moderate	abundant	moderate
26X-CC	abundant	good	barren		barren		rare	poor	abundant	good
27X-CC	abundant	moderate	barren		barren		rare	poor	abundant	good
28X-CC	common	moderate	barren		barren		rare	poor	abundant	moderate to good
29X-CC										
30X-CC	common	moderate	barren		barren		rare	poor	abundant	moderate
31X-CC	common	moderate	barren		abundant	good	abundant	good	abundant	good
32X-CC	few	moderate	barren		barren		rare	poor	few	moderate
33X-CC	rare	poor	barren		rare	poor	few	moderate	few	poor
34X-CC	barren		barren		barren		rare	poor	rare	moderate
35X-CC	barren		barren		few	poor	few	moderate	few	poor
36X-CC	barren		barren		rare	poor	few	moderate	few	poor
37X-CC	few	moderate	barren		barren		few	poor	few	poor
38X-CC	barren		barren		barren		barren		rare	poor
39X-CC	barren		barren		barren		barren		few	poor
40X-CC			few	moderate to poor	barren		barren		rare	poor
41X-CC			rare	poor	barren		barren		few	poor
42X-CC			barren		barren		barren		rare	poor
43X-CC			barren		barren		barren		rare to few	poor
44X-CC			barren		barren		barren		rare	poor
45X-CC			barren		barren		barren		rare	poor
46X-CC			rare	poor	barren		barren		rare	poor
47X-CC			few	moderate	barren		few	moderate	rare	poor
48X-CC			barren		barren		few	moderate	barren	
49X-CC			barren		rare	poor	rare	poor	barren	
50X-CC			barren		barren		barren		barren	
51X-CC			rare	moderate to poor	common	poor	abundant	good	barren	
52X-CC			barren		few	poor	abundant	poor	barren	
53X-CC			barren							

moderately to well preserved. As at Site 794, the *Emiliania huxleyi* Zone, marking the uppermost part of the Pleistocene and the Holocene, was not recognized at Site 797 because of the absence of nannofossils. Cores 127-797B-3H through 127-797B-5H are assigned to the *Umbilicosphaera sibogae* Zone (Fig. 24) based on the presence of the two marker species *Gephyrocapsa oceanica* and *Pseudoemiliania lacunosa*, which have concurrent ranges that define this zone. The other species found in this zone are *Coccolithus pelagicus*, *Gephyrocapsa caribbeanica*, small *Gephyrocapsa*, *Calcidiscus leptoporus*, *Pontosphaera* sp., and small *Reticulofenestra*. Small *Reticulofenestra* is extremely abundant in Sample 127-797B-5H-CC. The overwhelming dominance of small *Reticulofenestra* over other species in the lower part of the *Umbilicosphaera sibogae* Zone probably has some paleocean-

ographic implication for the southern part of the Japan Sea, and remains to be investigated. Sample 127-797B-8H-CC belongs to the undifferentiated *Calcidiscus leptoporus* Zone and the *Gephyrocapsa caribbeanica–Calcidiscus macintyrei* Zone based on the presence of *G. caribbeanica* and the absence of *G. oceanica*. Also contained in the sediments of this zone are *C. pelagicus*, small *Reticulofenestra*, and small *Gephyrocapsa*. As at Sites 794 and 796, the absence of *C. macintyrei* precludes demarcation between the *Gephyrocapsa caribbeanca–Calcidiscus macintyrei* Zone and the *Calcidiscus leptoporus* Zone. The nannofossil assemblages of Samples 127-797B-9H-CC and 127-797B-14H-CC are composed of small *Reticulofenestra*, *C. pelagicus*, *C. leptoporus*, and small *Gephyrocapsa*. These samples could not be assigned to any zone because of the absence of marker
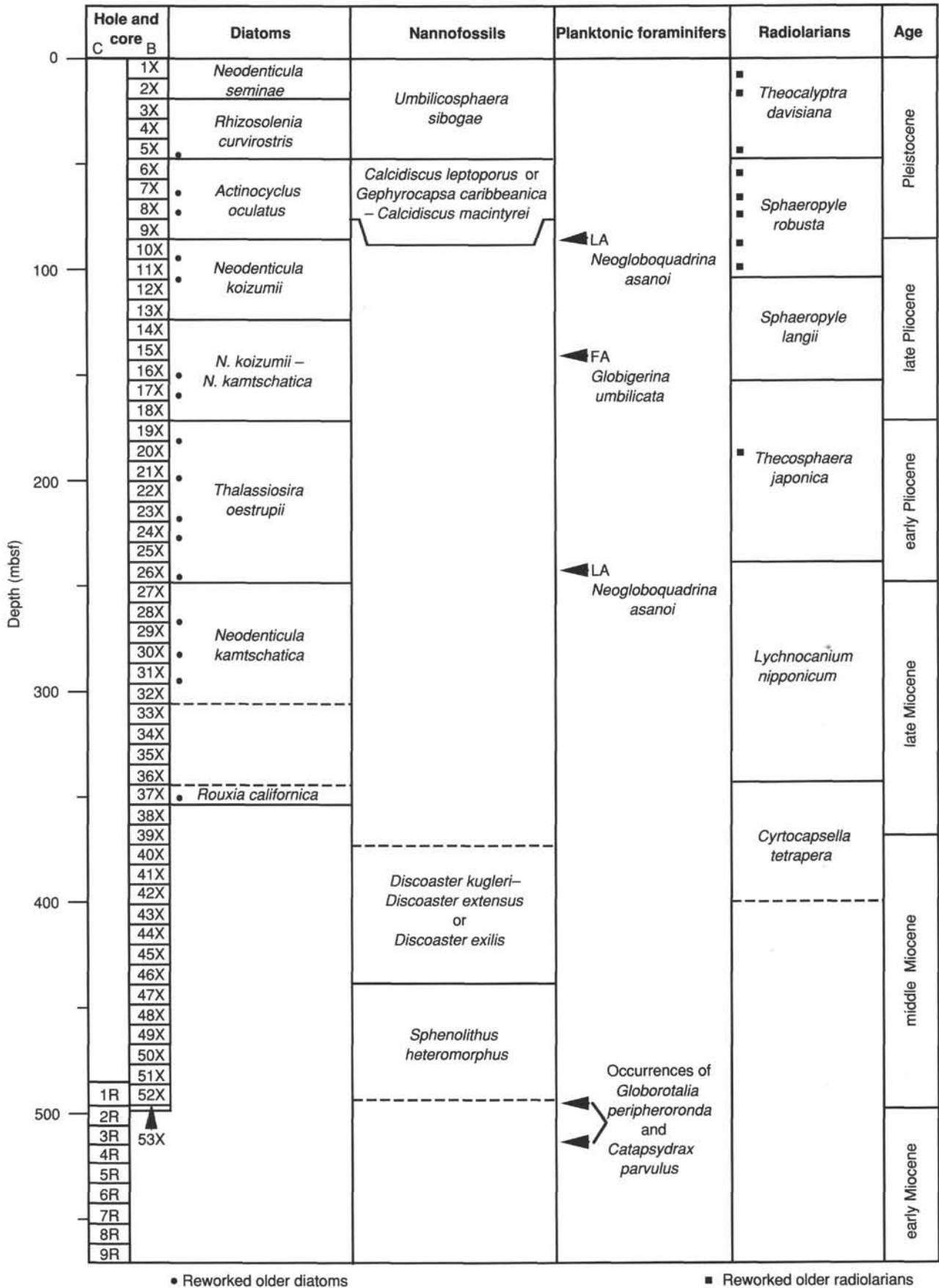
Figure 24. Planktonic-microfossil zones in Holes 797B and 797C. FA = first appearance; LA = last appearance.

Table 3. Abundance and preservation of microfossils in Hole 797C.

Core	Diatoms		Nannofossils		Planktonic foraminifers		Benthic foraminifers		Radiolarians	
	Abundance	Preservation	Abundance	Preservation	Abundance	Preservation	Abundance	Preservation	Abundance	Preservation
127-797C-										
1R-CC			rare	moderate to poor	barren		barren		barren	
2R-CC			barren		rare	poor	few	poor	barren	
3R-CC			barren		rare	good	few	moderate	barren	
4R-CC			barren						barren	
5R-CC			barren						barren	
6R-CC			barren		barren		common	moderate	barren	
7R-CC			barren		barren		barren		barren	
8R-CC			barren		barren		abundant	moderate		
9R-CC			barren							
10R-CC			barren							
11R-CC			barren							
12R-CC			barren							
13R-CC			barren							
14R-CC			barren							
15R-CC			barren							
16R-CC			barren							
17R-CC			barren							
18R-CC			barren							
18R-1, 88-90					barren		barren			
19R-CC			barren							
20R-CC			barren							
20R-2, 42-44					barren		barren			
21R-CC			barren							
22R-CC			barren		barren		barren		barren	
23R-CC			barren		barren		barren		rare	poor
24R-CC										
25R-CC										
25R-6, 33-35					barren		barren			
26R-CC										
27R-CC			barren		barren		barren		barren	
28R-CC										
29R-CC										
30R-CC			barren							
31R-CC										
32R-CC										
33R-CC										
33R-3, 42-44					barren		barren			
34R-CC			few	moderate to poor	barren		barren		barren	

species. The presence of small *Gephyrocapsa* and the absence of *G. caribbeanica*, however, indicate an age between 1.68 and 3.6 Ma (Berggren et al., 1985; Rahman and Roth, 1989). This age range agrees with the diatom biostratigraphy. Nannofossils are absent from Cores 127-797B-39X through 127-797B-46X. Samples 127-797B-40X-1, 26-27 cm to 127-797B-46X-CC are assigned to the undifferentiated *Discoaster kugleri–Discoaster extensus* Zone and the *Discoaster exilis* Zone. This zonal assignment is based on the presence of *Cyclicargolithus floridanus* and the absence of *Sphenolithus heteromorphus*. The last-occurrence datum level of the former species lies in the *Discoaster kugleri–Discoaster extensus* Zone and is dated at 11.6 Ma (Berggren et al., 1985b). The two zones could not be differentiated because of the rare and sporadic occurrence of *Discoaster kugleri*, and the presence of strong overgrowths on discoasters in general makes its distinction difficult from other discoasters having a large central area. The nannofossil assemblages found in the undifferentiated *Discoaster kugleri–Discoaster extensus* Zone and the *Discoaster exilis* Zone consist of *Reticulofenestra pseudoumbilica*, *C. pelagicus*, *Sphenolithus abies*, *Dictycoccites antarcticus*, *Helicosphaera carteri*, *Helicosphaera scissura*, *Discoaster brouweri*, *Discoaster exilis*, *Discoaster deflandre*, *D. kugleri*, small *Reticulofenestra*, *Triquetrorhabdulus rugosus*, and several other poorly preserved specimens of discoasters and *Helicosphaera*. There are some malformed discoasters in this interval, a characteristic often seen in the nannofossil assemblages of marginal seas (Okada and Honjo, 1975). The last-occurrence datum level of *C. floridanus* lies within the middle Miocene

claystones, where other microfossils are either absent or poorly preserved. The exact position of this datum level, however, could not be precisely determined because nannofossils are absent from Samples 127-797B-15H-CC through 127-797B-39X-CC. The very low sedimentation rate above the observed last occurrence of *C. floridanus* (see "Sediment Accumulation Rates," this chapter) suggests that the datum level should not be more than one core above the observed occurrence. The diverse assemblage; the presence of warm water taxa such as *Sphenolithus*, *Discoaster*, and *Helicosphaera* (Perch-Nielsen, 1985); and the rare occurrence of the cold-water species *C. pelagicus* (Roth and Coulbourn, 1982) reveal a subtropical aspect to the nannofossil assemblage in the undifferentiated *Discoaster kugleri–Discoaster extensus* and *Discoaster exilis* Zones and the *Sphenolithus heteromorphus* Zone. The subtropical nature of the nannofossil assemblages may be related to climatic warming in the middle Miocene as inferred from fossil micro- and macrofaunas of the Japanese Islands (Saito, 1963).

Samples 127-797B-47X-2, 41–42 cm, through 127-797B-51X-CC are assigned to the middle Miocene *Sphenolithus heteromorphus* Zone. The nannofossil assemblages in this zone are composed of *Sphenolithus heteromorphus*, *Sphenolithus moriformis*, *Coccolithus miopelagicus*, *Coccolithus pelagicus*, *Discoaster deflandre*, *Cyclicargolithus floridanus*, *Dictycoccites antarcticus*, small *Reticulofenestra*, *Discoaster variabilis*, *Braarudosphaera bigelowii*, *Helicosphaera carteri*, *Discoaster sanmiguelensis*, unidentified discoasters, and *Helicosphaera*. The last-occurrence datum level of *S. heteromorphus*, dated at 14.4 Ma

(Berggren et al., 1985), is placed slightly above Sample 127-797B-47X-2, 134–135 cm.

From Hole 797C, most of the core-catcher samples are barren of nannofossils. Nannofossils are few to rare where present and have good to poor preservation. Sample 127-797C-1R-CC contains *Dictyococcites antarcticus, Coccolithus pelagicus, Sphenolithus neoabies, Helicosphaera,* and *Sphenolithus heteromorphus* and is assigned to the *Sphenolithus heteromorphus* Zone (Fig. 24). The first occurrence of *S. heteromorphus,* dated at 17.1 Ma (Berggren et al., 1985), lies below and probably close to Sample 127-797C-1R-CC, as suggested by the sedimentation curve (see "Sediment Accumulation Rates," this chapter). Samples 127-25R-2, 142–143 cm, 127-33R-3, 67–68 cm, and 127-797C-34R-CC contain *D. antarcticus,* small *Reticulofenestra,* discoasters with strong overgrowth, *Calcidiscus leptoporus,* and a very small unidentifiable species related to *C. leptoporus.* The presence of nannofossils in these samples suggests that marine conditions existed in the Japan Sea as early as during the deposition of sediment in Core 127-797C-34R. Owing to lack of age-diagnostic nannofossils, it was not possible to assign a precise age to this core. *C. leptoporus* has ranged from early Miocene to Holocene and has been used for age determination in poorly preserved assemblages (Perch-Nielsen, 1985). The presence of this species in Sample 127-797C-34R-CC, therefore, provides an estimate of maximum possible age. The age of the first appearance of *C. leptoporus* within the lower Miocene is not known.

Foraminifers

The abundance and preservation of calcareous foraminifers at Site 797 exceeded those of all other sites cored during Leg 127 (Table 2). Planktonic foraminifers are found in all core-catcher samples of the Quaternary banded silty clays of lithologic Subunit IA. They occur abundantly in four of nine samples and are common to rare in the remainder. Preservation is moderate to poor, and most samples contain some specimens with preservation different from the majority of specimens, a condition which suggests minor reworking. Calcareous benthic foraminifers are few to common in number in upper Quaternary sediments and absent from lower Quaternary sediments. Agglutinated foraminifers are absent from the entire Quaternary sequence.

Planktonic foraminifers are common in the upper Pliocene ashy diatom silty clay, lithologic Subunit IB. They occur sporadically in 11 of 23 samples and are rare to abundant throughout the underlying diatom silty clay and ooze, the silty clay, and the silty clay and claystone of lithologic Units II and III and Subunit IVA. Agglutinated or calcareous with agglutinated benthic foraminifers occur in all but one sample from lithologic Subunits IA to IVA of the upper Pliocene to upper Miocene. Abundant neritic diatoms and rare occurrences of the shallow-water benthic foraminifers *Elphidium* and *Discorbis* occur only in Unit III of the uppermost Miocene and lowermost Pliocene of Site 797. The shallow-water fossils indicate transport from a shallow source.

The occurrence of the opal-A/opal-CT transition between Cores 127-797B-31X and 127-797B-33X has no observable effect on the preservation of foraminifers. In contrast, the interval that bears chert and porcellanite in siliceous claystone, lithologic Subunit IVB, is barren of both calcareous and agglutinated foraminifers. The barren zone extends from Cores 127-797B-37X to 127-797B-48X among planktonic foraminifers and from Cores 127-797B-38X to 127-797B-46X among benthic foraminifers. The underlying siliceous claystone of lithologic Unit V contains planktonic foraminifers in its midsection and benthic foraminifers throughout its length. The underlying sandstones, siltstones, and claystones bedded among the igneous sills of lithologic Unit VI are barren of foraminifers.

Quaternary assemblages of planktonic foraminifers are composed of species typical of subarctic waters, *Globigerina bulloides, Globigerina quinqueloba, Globigerina umbilicata, Globigerinita glutinata, Globigerinita* cf. *uvula,* and sinistral- and dextral-coiling forms of *Neogloboquadrina pachyderma.* Assemblages bear different proportions of sinistral and dextral *Nq. pachyderma,* a condition which reflects alternation between warm and cold surface waters characteristic of Pleistocene and late Pliocene glacial cycles.

Pliocene assemblages of planktonic foraminifers consist of species typical of warm subpolar conditions, *Globigerina bulloides, Globigerina quinqueloba, Globigerina umbilicata,* and predominantly dextral-coiling forms of *Neogloboquadrina pachyderma.* The section bears species and datum levels expected in the Pliocene. *Neogloboquadrina asanoi* makes its first and last appearances at the top and bottom of the Pliocene unit in Samples 127-797B-9H-CC and 127-797B-25X-CC respectively. *Ga. umbilicata* makes its first appearance in Sample 127-797B-15X-CC. *Ga. woodi* makes its last appearance near the top of the Pliocene unit in Sample 127-797B-11H-CC. *Neogloboquadrina kagaensis* appears in the Pliocene sequence but does not appear in core-catcher samples of the overlying Pleistocene interval. Examination of additional samples may reveal its presence in the lower Pleistocene.

Late Miocene assemblages bear cool-water, high-latitude species including *Globigerina bulloides, Globigerina falconensis, Globigerinita uvula, Globigerinita* cf. *uvula, Neogloboquadrina humerosa, Neogloboquadrina* cf. *kagaensis,* and dextral morphs of *Neogloboquadrina pachyderma.* Middle Miocene assemblages contain species of warmer water affinities than do younger assemblages of the Japan Sea, including *Catapsydrax parvulus, Globorotalia peripheroronda,* and *Globoquadrina* cf. *venezuelana.* Other species with a tolerance for warm to cool conditions include *Globigerina woodi, Globigerina praebulloides,* and *Neogloboquadrina continuosa.* The occurrences of *Catapsydrax parvulus* and *Globorotalia peripheroronda* in Samples 127-797B-52X-CC and 127-797C-3R-CC are consistent with assignment of this part of the hole to the middle Miocene based on nannofossils, because *Ct. parvulus* ranges from Zones N7 to N15 (Kennett and Srinivasan, 1983) about 17.6 to 10.2 Ma (Berggren et al., 1985) and *Gr. peripheroronda* ranges from Zones N4B to N10 (Kennett and Srinivasan, 1983) about 23 Ma to 14.6 Ma (Berggren et al., 1985).

Benthic foraminiferal assemblages of the Quaternary sequence consist of calcareous taxa almost exclusively and include *Bolivina, Cassidulina, Epistominella pacifica, Fursenkoina, Globobulimina, Globocassidulina,* lagenids, *Melonis pompilioides, Nonion, Pyrgo, Quinqueloculina, Stainforthia, Trifarina,* and costate *Uvigerina.* A single specimen of *Cyclammina cancellata* represents the suborder Textulariina.

The Pliocene assemblage of benthic foraminifers includes both textularids and calcareous genera. Agglutinated species occur in 15 of 18 samples and consist of *Miliammina echigoensis, Martinottiella communis, Eggerella, Trochammina,* and *Haplophragmoides.* Calcareous genera occur in 11 of 18 samples of the Pliocene sequence and include *Bolivina, Cassidulina, Chilostomella, Cibicides, Elphidium, Fissurina, Fontbotia wuellerstorfi, Globobulimina, Globocassidulina, Gyroidina, Gyroidinoides,* lagenids, *Melonis pompilioides, Nonion, Oridorsalis,* and *Quinqueloculina.* The association is typical of lower middle bathyal depths greater than 1500 m.

The latest Miocene assemblage of benthic foraminifers found in lithologic Unit III and Subunit IVA is similar to that of the overlying Pliocene sequence except for the addition of six taxa, *Valvulineria,* a papillate *Uvigerina, Pullenia bulloides, Nonionella, Lenticulina,* and *Hanzawaia nipponica,* and the absence

of four taxa, *Fontbotia wuellerstorfi*, *Fissurina*, *Quinqueloculina*, and *Bolivina*. The assemblage ranges from 1500 to 2000 m water depth. The textularid assemblage in the deepest foraminifer-bearing sample of the upper Miocene, Sample 127-797B-37X-CC, is more similar to that of the middle Miocene in that it contains *Cyclammina* and *Ammodiscus*.

The middle Miocene assemblage of benthic foraminifers includes the textularids *Cyclammina*, *Ammodiscus*, *Eggerella*, *Haplophragmoides*, *Martinottiella communis*, *Saccammina*, *Spirosigmoilinella*, and other textularids. Calcareous benthic foraminifers include *Chilostomella*, *Fissurina*, *Globobulimina*, *Gyroidina*, *Gyroidinoides*, *Hanzawaia nipponica*, *Lenticulina*, *Melonis pompilioides*, *Nonion*, *Nonionella*, *Oridorsalis*, *Pullenia bulloides*, *Pyrgo*, *Quinqueloculina*, *Sphaeroidina bulloides*, *Valvulineria*, and other genera. The assemblage is typical of water depths of 1500 to 2000 m.

Radiolarians

Radiolarians recovered from Site 797 sediments are, in general, found in common abundance with moderate to good preservation (Table 2). Again, as at Sites 794, 795, and 796, poorly preserved radiolarians survive the opal-A/opal-CT transition. Reworking of older radiolarians is restricted to upper Pliocene and Quaternary samples and one core-catcher sample of early Pliocene age (Fig. 24). The assemblage compositions of core-catcher samples from Site 797 are slightly different from samples examined from Sites 794, 795, and 796 but need to be quantified in order to outline and determine the reasons for the differences. Variations in water mass properties, such as temperature and nutrients, are the most likely cause. Several tropical and North Pacific zonal indicators, including *Eucyrtidium matuyamai*, *Eucyrtidium calvertense*, and *Spongaster tetras*, are present in Quaternary and Pliocene samples but unfortunately do not permit zonal correlations with other Pacific sites. The radiolarian zonation for Site 797 is summarized in Figure 24.

As at the three previous sites, Quaternary radiolarian assemblages show striking changes in assemblage composition, abundance, and preservation that probably reflect climatic changes caused by Northern Hemisphere glaciation. Radiolarian datum levels found in Quaternary sediments of Site 797 include the FAD of *Lychnocanium* sp. cf. *L. grande* (between Samples 127-797B-3H-CC and 127-797B-4H-CC), the LAD of *Clathrocyclas cabrilloensis* (between Samples 127-797B-4H-CC and 127-797B-5H-CC), and the LAD of *Druppatractus acquilonius* (between Samples 127-797B-8H-CC and 127-797B-9H-CC). The LAD of *Sphaeropyle robusta*, which defines the top of the *Sphaeropyle robusta* Zone, is placed between Samples 127-797B-5H-CC and 127-797B-6H-CC. This datum level is not very reliable because it is based on a single specimen of *Sphaeropyle robusta* in Sample 797B-6H-CC. *Sphaeropyle robusta* becomes abundant in Pliocene and Miocene sediments below Core 127-797B-11H.

The Quaternary radiolarian assemblages from the Site 797 silty clays contain few to common euchitonids, *Amphirhopalum ypsilon*, *Didymocyrtis tetrathalamus*, and *Spongaster tetras*, which are absent in all but one sample examined from Sites 794, 795, and 796. Euchitonids, *Amphirhopalum ypsilon*, *Didymocyrtis tetrathalamus*, and *Spongaster tetras* are seen in Pliocene sediments of the Pacific but are absent from the Pliocene diatom-rich silty clays and oozes recovered in Hole 797B. Their appearance at the Pliocene/Pleistocene boundary seems to indicate strong changes in water-mass properties above Site 797 at this time. Since these species have subtropical and tropical distributions in the Pacific Ocean (Lombari and Boden, 1985), their occurrence in Quaternary sediments at Site 797 may indicate that warmer or deeper waters from the Kuroshio Current were not able to enter the Japan Sea through the Korea Strait until Quaternary time.

Common to abundant Pliocene radiolarian assemblages found in Site 797 sediments are moderately to well preserved. Radiolarian datum levels found in the Pliocene sediments of Site 797 include the FAD of *Theocalyptra davisiana* (between Samples 127-797B-11H-CC and 127-797B-12H-CC), the LAD of *Thecosphaera japonica* (between Samples 127-797B-11H-CC and 127-797B-12H-CC), the LAD of *Stylacontarium* sp. cf. *S. acquilonarium* (between Samples 127-797B-16H-CC and 127-797B-17H-CC), the FAD of *Druppatractus acquilonius* (between Samples 127-797B-17H-CC and 127-797B-18H-CC), the LAD of *Sethocyrtis japonica* (between Samples 127-797B-20X-CC and 127-797B-21X-CC), the LAD of *Lychnocanium nipponicum* (between Samples 127-797B-24X-CC and 127-797B-25X-CC), and the FAD of *Thecosphaera japonica* (between Samples 127-797B-25X-CC and 127-797B-26X-CC). *Thecosphaera akitoensis* and *Lipmanella* sp. aff. *Theocyrtis redondoensis* are not as abundant at Site 797 as they are at some of the other sites cored during Leg 127. These species occur sporadically in Site 797 sediments, however, and range between Samples 127-797B-12H-CC and 127-797B-23X-CC, and Samples 127-797B-14H-CC and 127-797B-22X-CC, respectively.

Other more problematic datum levels found in the Pliocene sediments of Site 797 include the FAD of *Sphaeropyle langii* and the LAD of *Stichocorys peregrina*. The base of the *Sphaeropyle langii* Zone is placed at the first occurrence of *Sphaeropyle langii* which was found in Sample 127-797B-16H-CC. This datum level may not be reliable because, like the closely related species *Sphaeropyle robusta*, its appearance throughout the Pliocene and Quaternary sediments is sporadic. *Stichocorys peregrina* is more abundant in Site 797 sediments than in Site 794, 795, and 796 sediments. Its LAD, however, is difficult to define at Site 797 because near the top of its range *Stichocorys peregrina* occurs sporadically and ranges into the Quaternary sediments. The LAD of *Stichocorys peregrina* is estimated to occur between Samples 127-797B-18H-CC and 127-797B-19H-CC, its last abundant appearance. Any occurrence of *Stichocorys peregrina* found above Core 797-18H is attributable to upward sediment reworking.

The base of the *Thecosphaera japonica* Zone at Site 797, defined by the FAD of *Thecosphaera japonica*, occurs in lower Pliocene sediments of the *Thalassiosira oestrupii* (diatom) Zone. At Sites 794, 795, and 796, the base of the *Thecosphaera japonica* Zone falls within sediments belonging to the Miocene *Neodenticula kamtschatica* (diatom) Zone. This implies that the FAD of *Thecosphaera japonica* may be diachronous within the Japan Sea. Other species (*Sethocyrtis japonica* and *Lychnocanium nipponicum*) last appear in the Pliocene of Site 797 instead of in the Miocene as at Sites 794, 795, and 796, probably indicating differences in late Miocene and early Pliocene environmental conditions between Site 797 and Sites 794, 795, and 796.

Miocene radiolarians are abundant and moderately preserved in the silty clays above the opal-A/opal-CT boundary at Site 797. Below this boundary, in the silty clays and siliceous claystones, radiolarians are found in low abundances (rare to few) and are poorly preserved (Tables 2 and 3). Below Sample 127-797B-47X-CC (445.9 mbsf) radiolarians are barren from the core-catcher samples examined, except for Sample 127-797C-23R-CC in which completely re-silicified spumellarians were observed. *Tholospyris anthopora*, the zonal indicator for the top of the *Cyrtocapsella terapera* Zone, was not found, so another criterion, the last-abundant-appearance datum (LAAD) of *Cyrtocapsella terapera* (Nakaseko and Sugano, 1973), was used. This was possible at Site 797 because *Cyrtocapsella terapera* was present in higher abundances than it was at the other sites. The LAAD at *Cyrtocapsella terapera* is found between Samples 127-797B-36X-CC and 127-797B-37X-CC. One specimen of *Lithop-*

era renzae was found in Sample 127-797B-39X-CC. This species was not found at any other site.

Paleoenvironment

Marine waters filled the southern Yamato Basin as long ago as early Miocene time, based on the presence of calcareous nannofossils in mudstones intercalated between sandstones and siltstones at the base of Hole 797C.

By the middle Miocene, the basin floor had subsided to lower middle bathyal depths between 1500 and 2000 water depth, based on assemblages of benthic foraminifers. Surface waters were warm, based on the presence of temperate species of planktonic foraminifers and several subtropical species in a diverse assemblage of calcareous nannofossils.

Paleodepth remained between 1500 and 2000 m water depth in the late Miocene based on assemblages of benthic foraminifers. Surface waters had cooled significantly since the middle Miocene based on the presence of planktonic foraminifers and diatoms typical of the high-latitude North Pacific Ocean. Sedimentation rates slowed to 5 m/m.y. between 350 and 374 mbsf at the top of an interval barren of all microfossils. The cause of this slow sedimentation is unclear. A hiatus may be indicated by the LAAD of *Cyrtocapsella tetrapera*, which occurs between Samples 127-797B-36X-CC and 127-797B-37X-CC. The interval forms a boundary between moderate sedimentation rates of 25 m/m.y. in the middle Miocene sequence and fast sedimentation rates in upper Miocene and younger units. Reworking of shallow-water and older Miocene diatoms, radiolarians, and benthic foraminifers, perhaps from the Yamato Rise, into sediments of latest Miocene and earliest Pliocene age coincided with periods of low sea level during the Messinian crisis.

Pliocene paleodepth was greater than 1500 m and likely greater than 2000 m, based on assemblage changes in benthic foraminifers. Cool surface-water conditions persisted from the late Miocene through the Pliocene, based on assemblages of planktonic foraminifers and diatoms. High productivity of diatoms persisted in the Japan Sea from 5.3 to 2.6 Ma, based on the presence of diatom silty clays and oozes.

In the Quaternary, deep-water conditions changed drastically. The early Quaternary was unfavorable to benthic foraminifers based on their absence from units in which more delicate carbonate fossils are preserved. A calcareous assemblage of benthic foraminifers returned to the Yamato Basin in the late Quaternary. This unusual assemblage contains species more characteristic of depths shallower than the present seafloor, an indication that isolation of deep waters was in progress (Matoba, 1984).

Surface-water conditions appear cooler in the Pleistocene than in the Pliocene based on planktonic foraminifers, and surface and intermediate waters were warmer in the Pleistocene than in the Pliocene based on calcareous nannofossils and radiolarians. Surface and intermediate waters were warmer at Site 797 in the Quaternary than at the more northerly sites of Leg 127 based on radiolarians and calcareous nannofossils. Quaternary surface and intermediate waters alternated between two or more different modes in response to glacial cycles based on variability in assemblage composition, abundance, and preservation of planktonic foraminifers and radiolarians. In contrast to other sites cored during Leg 127, the CCD apparently lay below Site 797 throughout most of the Neogene and Quaternary.

PALEOMAGNETISM

Introduction

Magnetic measurements with the pass-through cryogenic magnetometer were carried out on all the recovered cores except those which are completely disrupted by the drilling. All the APC cores, after Core 127-797A-1H, were oriented with the multishot camera system, but because of some uncertainty in the directions after the corrections, we prefer to plot the results in the core coordinates. Peak fields of 8 and 15 mT were used to demagnetize the split sections of the cores from Hole 797B. Further steps of 4 and 12 mT were used for both sedimentary and igneous rocks recovered from Hole 797C in order to obtain more information about the magnetic behavior of the rocks. Owing to a lack of time and to the weak magnetization of the sediments, shipboard measurements of discrete samples were carried out only on samples from Hole 797C. Declination, inclination, and intensity of magnetization after alternating field (AF) cleaning with 15 mT are plotted vs. depth in Figure 25.

At this site we observed a problem that did not occur at previous sites but which had been reported on other legs (Leg 101, Sager 1986; Leg 115). The tops of several of the cores showed an abrupt increase in magnetic intensity followed by a decreasing trend downcore (Fig. 25A, B; i.e., Core 127-797B-10H, 81.95 mbsf). We suspect that several of the cores probably were contaminated by rust particles as reflected by the pattern of the intensity of magnetization. This contamination was not visually observed, but the consistent position of the spikes in the measurements of the magnetic susceptibility in several cores confirms this hypothesis (Fig. 26).

As noted at previous sites, XCB drilling produces a deformation of the cores that disturb the paleomagnetic signature. An example of this effect is given in Table 4, which shows the results of the measurements of a section (127-797C-51X-4) which is only slightly disturbed by drilling. Coherent directions are present only in individual samples measured separately (Table 4). The scattering of the results from the whole section measurement make it impossible to recognize a polarity, whereas the results of the individual undeformed sedimentary samples are consistent.

Results

Hole 797B

As at the previous sites, the intensity of magnetization of the sediments is quite weak, with an estimated mean value around 1 mA/m, except in the upper part of the section where it exhibited values above 10 m/Am.

In order to obtain some quantitative and qualitative information about the natural remanent magnetization (NRM) carriers of the recovered sediments, one sample from each section (about 250 samples destined for shore-based paleontological study) was collected and magnetically saturated with a peak field of 500 mT using the pulse magnetizer available on the *JOIDES Resolution*. Subsequently the isothermal remanent magnetization (IRM) acquired by the sediments was progressively demagnetized with the Schonstedt AF demagnetizer in peak fields of 5, 15, and 55 mT. IRM results clearly reflect the NRM pattern with higher values in the upper part of the hole where the intensity in some cases exceeds the value of 1 A/m. A downhole plot of the results for the IRM is shown in Figure 27.

Hole 797C

Sedimentary and igneous rocks were recovered from Hole 797C. The occurrence of sediments and basalts in the same sections made it difficult to make the measurements with the cryogenic magnetometer because of the large intensity differences. The range of measurement is chosen by the computer according to the intensity of the stronger rocks, with the consequence that the sediments appear to be much stronger than their real value, and with directions meaningless. To avoid this problem, the two lithologies were measured separately. The NRM of the basalts is generally too strong for the cryogenic magnetometer. However,
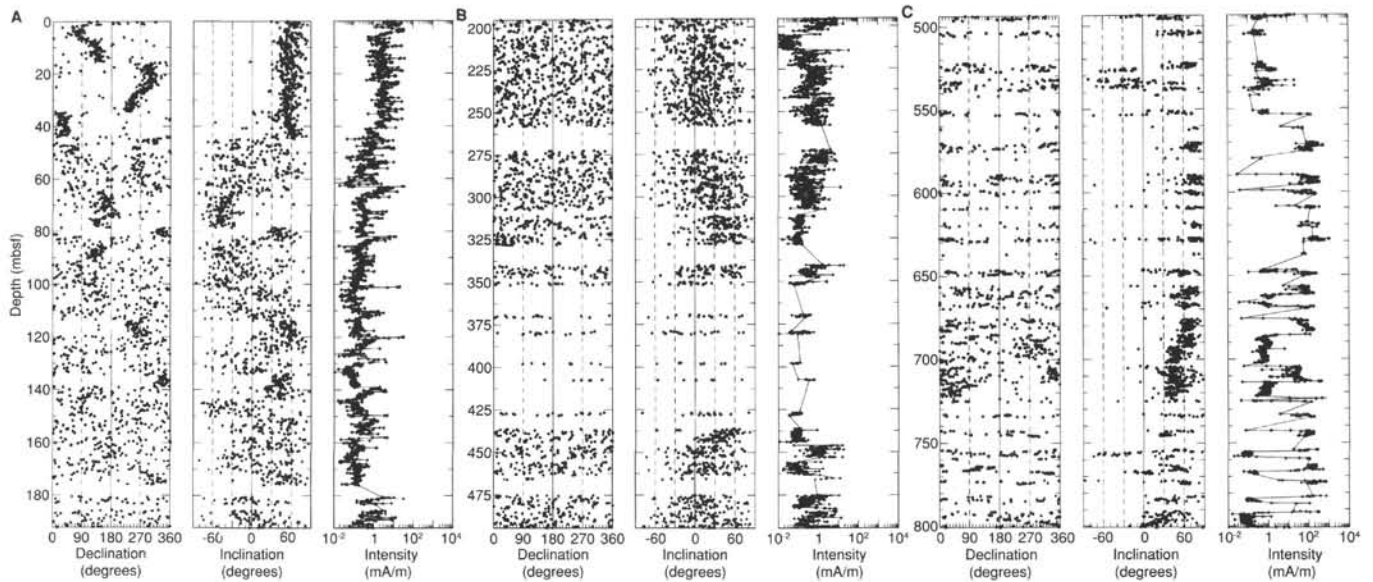
Figure 25. Downhole plots of declination, inclination, and intensity of magnetization after demagnetization with peak field of 15 mT. **A, B.** Results from Hole 797B. **C.** Results from Hole 797C.
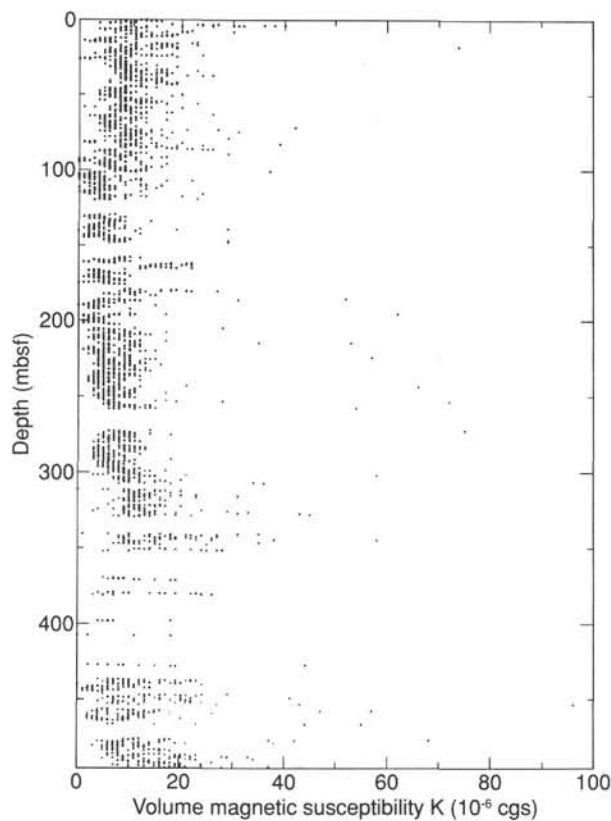
Figure 26. Magnetic susceptibility plotted vs. depth for Hole 797B.

Table 4. Paleomagnetic results from Section 127-797B-51X-4 measured as a whole section (A) and as individual samples (B). The effect of XCB drilling disturbance is dramatically shown in the inclinations.

Depth (cm)	Declination (°)	Inclination (°)	Intensity (mA/m)
	(A)		
5.0	313.9	+ 64.4	0.1303
15.0	160.0	+ 3.7	0.2662
25.0	350.0	− 35.2	0.3848
35.0	341.6	− 15.8	0.4228
45.0	227.5	+ 2.5	0.5284
55.0	58.6	+ 17.3	0.1173
65.0	74.8	+ 73.8	0.1891
	(B)		
5.0	343.1	+ 74.8	0.0660
15.0	136.7	+ 52.8	0.1018
25.0	106.1	+ 49.0	0.0837
35.0	174.3	+ 49.9	0.0813
45.0	264.9	+ 53.0	0.0653
55.0	172.3	+ 60.4	0.0604
65.0	31.0	+ 39.6	0.0638

the rock exhibited a low coercivity, with a median destructive field of about 5 mT, so after AF cleaning the intensity decreased to a value acceptable for measurements with this magnetometer.

The NRM of 21 discrete samples (12 from the basalts and 9 from the sedimentary rocks) was measured with the Molspin magnetometer before and after progressive AF demagnetizations

in peak fields up to 90 mT. Orthogonal projections for the sediments and the igneous rocks are plotted in Figure 28A,B, respectively. The rock did not always exhibit a stable magnetization during AF treatment; even some basalts showed the existence of a higher coercivity component which was not revealed by AF cleaning. It is possible that thermal treatment will give different results.

The magnetic susceptibility of the basalts (Fig. 29) is generally below 2000 × 10-6 cgs units down to Core 127-797C-26R (720 mbsf), where the range increases up to 8000 × 10^{-6} cgs units. The magnetic susceptibility reflects the content and the grainsize of the magnetic minerals. These parameters clearly must be different between these two populations, possibly representing two different kinds of basalts or two very different stages of alteration. X-ray-fluorescence (XRF) analysis of these
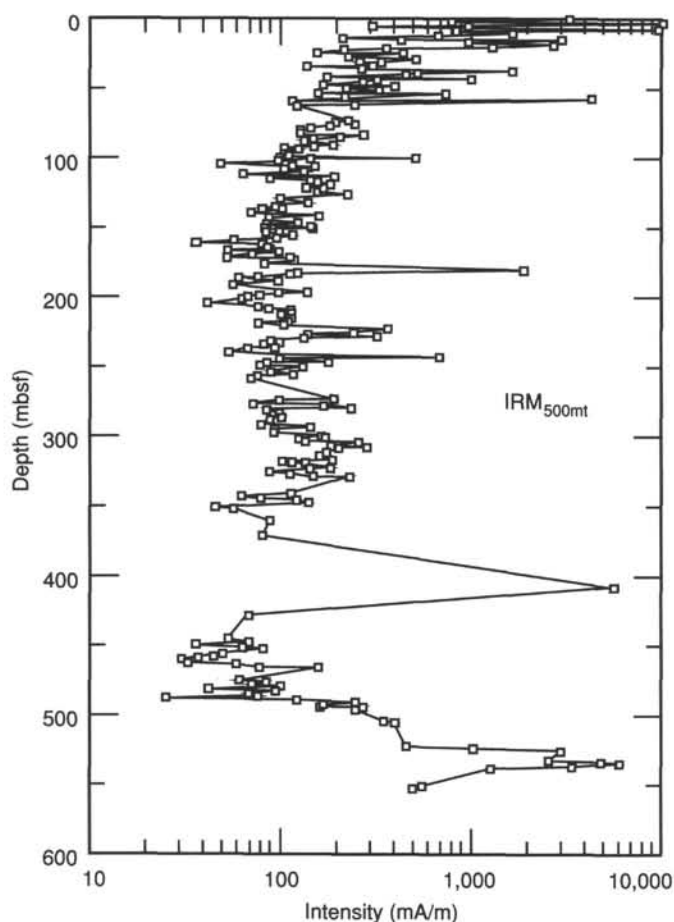
Figure 27. Isothermal remanent magnetization plotted vs. depth for Hole 797B.

basalts indicates that this change in magnetic properties correlates with a change in rock chemistry from high-Al basaltic to alkalic.

The sediments recovered from Hole 797C showed a good paleomagnetic record. Normal and reverse intervals were identified. The upper part of this hole to Section 127-797C-5R-3 (463–525 mbsf) exhibited a normal polarity followed by a consistent reverse polarity to Section 127-797C-6R-4 at 537 mbsf. Below this depth, a long interval of normal polarity was observed to Section 127-797C-30R-2 at 755.5 mbsf. The few discrete samples demagnetized from this part of the hole confirm this polarity. In spite of the incomplete recovery of some cores, no large gaps occur in the section. Moreover, sedimentological evidence suggests that these sediments were deposited in a relatively short period of time (see "Lithostratigraphy" section, this chapter).

The sediments are interbedded with basaltic sills and in several cores the effect of the baking was observed near the contacts. This observation suggests a possible remagnetization induced by intrusion. The best example of this effect comes from the sediments recovered in Core 127-797C-30R. These sediments yield a normal polarity in the NRM, but AF cleaning with 15 mT changed their inclinations except in the part closest to the basalt. Near the basalt contact, these sediments maintained the NRM direction clearly acquired during the baking (Fig. 30).

From Cores 127-797C-31R through -37R (824 mbsf), the sediments still showed an overprint of normal polarity which could

not always be completely removed by AF cleaning with 15 mT. However the magnetic behavior of the rock, observed on the Zijderveld plots, seems to indicate a reverse polarity. Below 824 mbsf poor recovery hampered the results; however, sedimentary rocks recovered with Core 127-797C-41R exhibited a consistent normal polarity without indications of different components after AF demagnetization with 15 mT.

All basaltic rocks showed consistently positive inclinations except the last two cores (127-797C-44R and -45R). These exhibited a reverse polarity, attesting to a different emplacement time for these units.

Magnetostratigraphy

Paleomagnetic measurements from the sediments recovered at Hole 797B provide a recognizable polarity for the cores drilled using the APC (from Cores 127-797B-1H through 127-797B-19H). The polarity pattern is not always obvious. Intervals with normal polarity yield consistent directions but intervals interpreted as reverse on the basis of both magnetic behavior and paleontological age exhibit scattered directions (Fig. 25A,B). The peak field of 15 mT was probably insufficient to completely remove an overprint in the present field. Despite these uncertainties a polarity pattern has been defined for the upper 175 m of Hole 797B. A reasonable correlation with the Geomagnetic Reference Time Scale (GRTS) for Quaternary–Middle Pliocene time is shown in Figure 31.

An example of the importance of good biostratigraphic control for detailed magnetostratigraphic correlations is given by the interpretation of the Jaramillo Subchron at 56.8 mbsf. Two short but consistent normal polarity intervals exist in the interval from 44.8 through 66.6 mbsf. The LAD of *A. oculatus* (0.9 Ma) in Sample 127-797B-6H-CC at about 53 mbsf constrains this interpretation of normal polarity at 56.8 mbsf.

Below 170 mbsf, erratic directions predominate. Systematic variation of inclination within sections, and discontinuities coinciding with section boundaries, suggest that mechanical effects during drilling, and probably also during the splitting of the core, disturbed the magnetization. Clearly, it is impossible to recognize a polarity pattern from the shipboard measurements below this depth. It is hoped that shore-based measurements will provide a clearer picture.

In comparing the results of Site 797 with those at Site 794 (Fig. 28), it is evident that the two sites, which are both in the Yamato Basin, are characterized by different sedimentation rates. Site 797 yielded the highest sedimentation rates for the last million years with respect to all the sites drilled during Leg 127.

A polarity pattern was recognized at Hole 797C but cannot be correlated with the GRTS because of a lack of biostratigraphic control.

SEDIMENT ACCUMULATION RATES

Sedimentation rates for Site 797 were estimated on the basis of four diatom and three nannofossil datum levels (Table 5). Magnetostratigraphy provides depths and ages of three reversals in upper Pliocene and Pleistocene sediments and is in excellent agreement with the diatom datum levels. From the age vs. depth relationship, a sedimentation rate was estimated for each of the sedimentary intervals between adjacent datum levels (Table 5 and Fig. 32).

Sedimentation rates at Site 797 ranged from 5 to 56 m/m.y. The fastest rates are indicated from the Pleistocene to uppermost Miocene sequence, whereas the slowest rate is from the upper Miocene. Middle Miocene and lower Miocene sediments were deposited at an intermediate rate of about 20 m/m.y. Trends in sediment accumulation rates expressed in g/cm²/k.y. (Table 5 and Fig. 32) closely mimic the sedimentation rate trends. From

A

Sample 127-797C-20R-2, 60cm
(0 - 75 mT)
Scale: 0.5 mA/m per div.
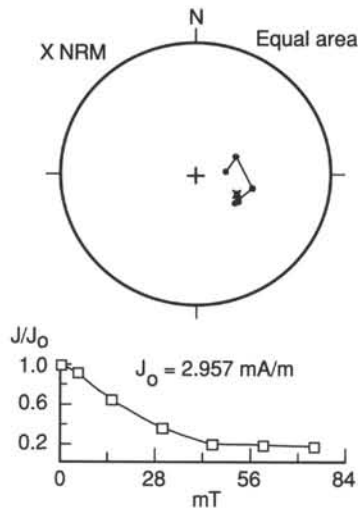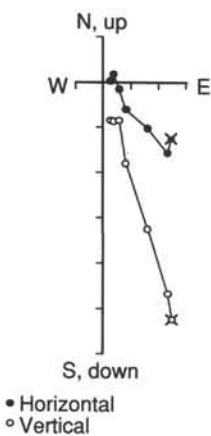
Sample 127-797C-23R-4, 37cm
(0 - 60 mT)
Scale: 0.2 mA/m per div.
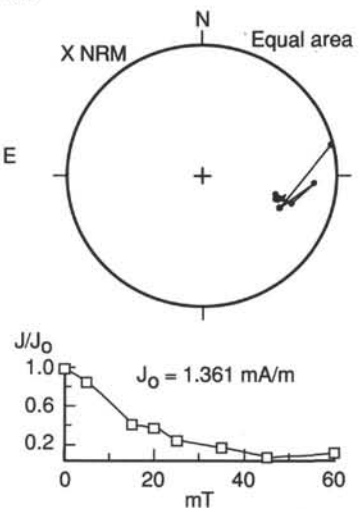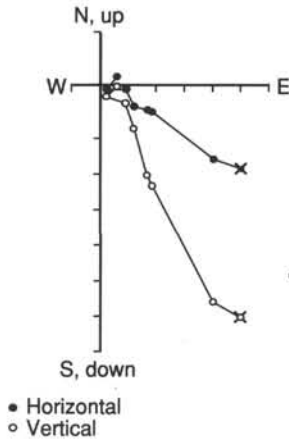
Sample 127-797C-34R-4, 142cm
(0 - 40 mT)
Scale: 0.03 mA/m per div.
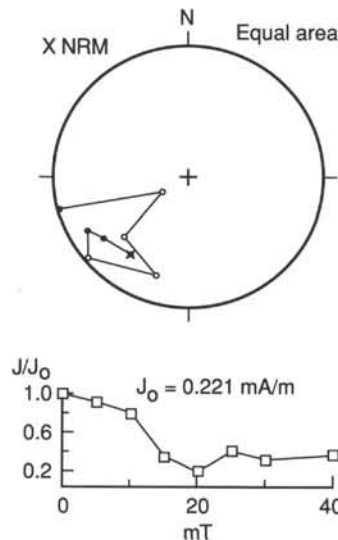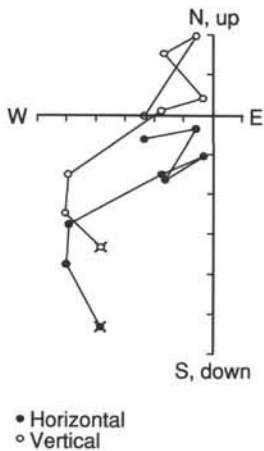
Sample 127-797C-33R-2, 63cm
(0 - 50 mT)
Scale: 0.1 mA/m per div.
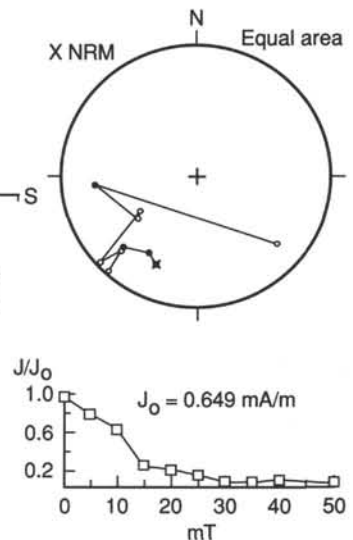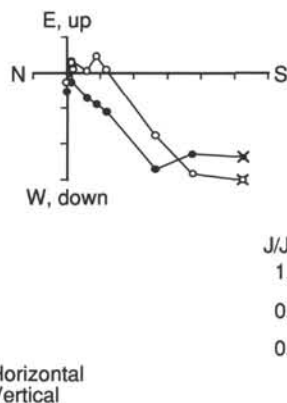
Figure 28. Zijderveld, equal-area and intensity-decay plots as functions of AF demagnetization for sedimentary rocks (**A**) and basalts (**B**) recovered from Hole 797C.

the middle Miocene to the early part of the late Miocene, sediment accumulation rates increased in a relative sense, suggesting that compaction has affected the resulting sediments.

The sedimentation rate of 5 m/m.y. is the slowest rate we have estimated for all sites. The interval of slow sedimentation may be a disconformity because stratigraphic uncertainities owing to barren intervals suggest that the estimated rate is a maximum value. This estimated rate is based on the age and depth relationship between the base of the *Rouxia californica* Interval Zone and the last occurrence of *Cyclicargolithus floridanus*, both of which merit detailed discussion because of their importance. The top of the *Rouxia californica* Zone is defined by the first occurrence of *Neodenticula kamtschatica* at 6.4 Ma, and the base of the zone is defined by the last occurrence of *Thalassionema schraderi* at 7.2 Ma. Samples 127-797B-37X-1, 84–85 cm,

and 127-797B-37X-5, 8–9 cm, which are carbonate nodules from the interval otherwise barren of diatoms below the opal-A/opal-CT boundary, are placed in the *Rouxia californica* Interval Zone, based on the absence of the two marker species and the acme of *Rouxia californica* (see "Biostratigraphy" section, this chapter). The uncertainty owing to the absence of diatoms above the *Rouxia californica* Zone does not affect the placement of the base of this zone. Barren intervals below Sample 127-797B-37X-5, 8–9 cm, suggest that the base of this zone could occur between 341.2 and 369.6 m. Deepening the base of the *Rouxia californica* Zone reduces the sedimentation rate to less than 5 m/m.y. The present position of the base of the *Rouxia californica* Zone is consistent with the sedimentation rate above. A calcareous nannofossil, *Cyclicargolithus floridanus*, marks the lower boundary of the interval of slow sedimentation. *C. flori-*
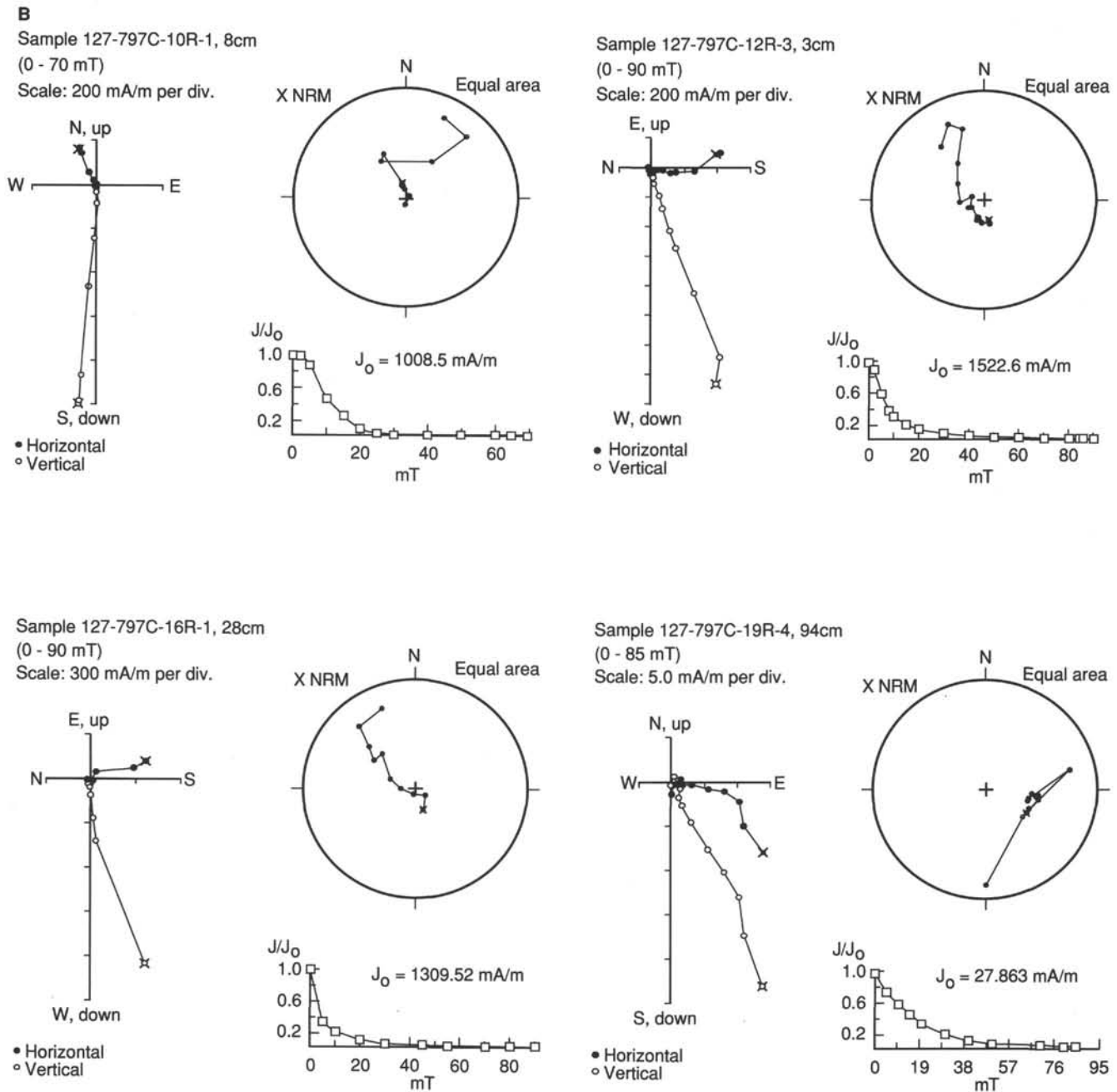
Figure 28 (continued).

danus was last observed in Sample 127-797B-40X-1, 26–27 cm, and its last occurrence is assigned to this point in the section. Samples above Sample 127-797B-40X-1, 26–27 cm, however, are barren of calcareous nannofossils and introduce uncertainty as to the proper stratigraphic placement of the LAD. The datum event can be shallower in the section, a condition which reduces the estimated sedimentation rate in the interval of slow sedimentation. The sedimentation-rate estimate of 5 m/m.y. is a maximum, and a hiatus may lie in the interval. A hiatus may be indicated by the LAAD of *Cyrtocapsella tetrapera*, which occurs between Samples 127-797B-36X-CC and 127-797B-37X-CC.

Extrapolation of the sedimentation rate between the last and first occurrences of *Sphenolithus heteromorphus* to the contact between the sedimentary and shallowest igneous rocks in Core 127-797C-8R (553.5 mbsf) provides an age of about 20 Ma. This extrapolated age is consistent with the presence of two plank-

tonic foraminifers, *Globorotalia peripheroronda* and *Catapsydrax parvulus*, in Sample 127-797B-52X-CC (Fig. 32). These two species have overlapping ranges between Zones N7 and N10 from 14.5 to 17.5 Ma. The age of 20 Ma for the contact between the igneous and sedimentary rocks should be considered a maximum age, because sediments below the observed first occurrence of *S. heteromorphus* are barren of nannofossils. The minimum age bracket is 16 Ma, based on extrapolation between the last occurrence of *Cyclicargolithus floridanus* and the top of the overlap in the ranges of *G. peripheroronda* and *C. parvulus* in Sample 127-797B-52X-CC. This minimum estimate requires a very high sedimentation rate, several times higher than the average sedimentation rate of all the sites, a condition which is highly unlikely based on the lithologic characteristics. The presence of *S. heteromorphus* in Sample 127-797B-47X-2, 135–136 cm, suggests an age estimate of 19 Ma, based on extrapolation
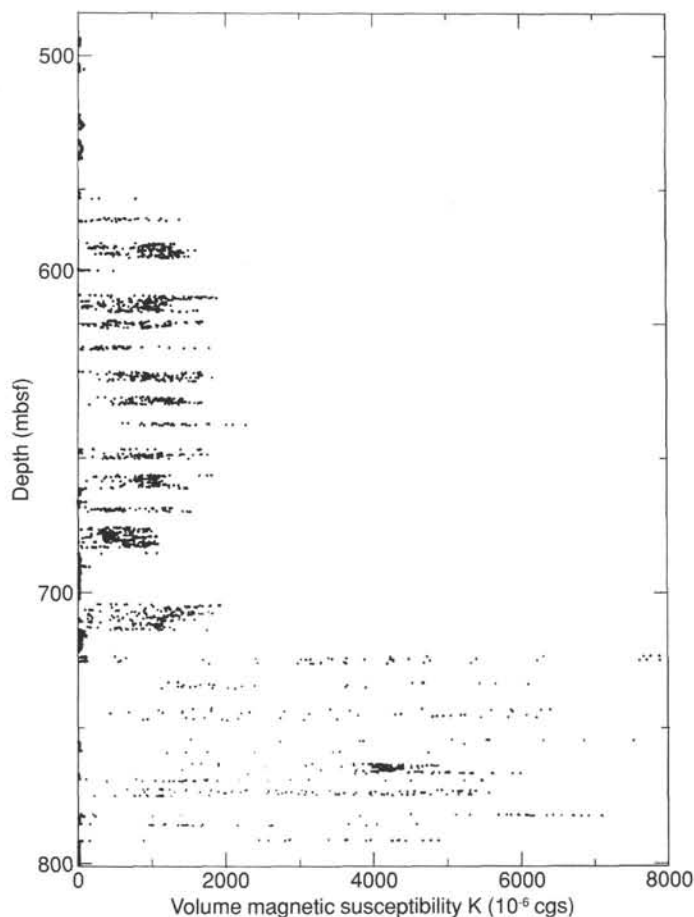
Figure 29. Magnetic susceptibility plotted vs. depth for Hole 797C.

between the last occurrences of this species and *C. floridanus*. This age is the most likely estimate of the shallowest sedimentary/igneous rock contact. By taking into account the uncertainty of the last occurrence of *C. floridanus* in the worst possible case—i.e., if this datum level extends up to and immediately below the base of the *Rouxia californica* Zone, and extrapolating it through the last occurrence of *S. heteromorphus*—we get an estimate of 18 Ma. This age is consistent with the previous estimate.

The sediments interlayered with the igneous rocks do not contain age-diagnostic fossils. Therefore, no attempt is made to estimate their sedimentation rates.

INORGANIC GEOCHEMISTRY

Interstitial water samples were obtained at Site 797 from 2.9 to 525 mbsf, using both the standard ODP stainless-steel squeezer (Manheim and Sayles, 1974) and the new plastic-lined squeezer (Brumsack et al., in preparation). Detailed sampling of the first 10 cores (2.9 to 87.9 mbsf) and near the opal-A/opal-CT transition (272 to 314.2 mbsf) contributed to the total collection of 43 interstitial water samples from 25 different cores. The Barnes *in-situ* water sampler was not used. Major ion data from both squeezers are presented in Table 6.

As at other Leg 127 sites, most notably Site 795, the opal-A/opal-CT transition marks a primary division in the interstitial water profiles. Chemical behavior above the transition, in this case from 0 to 300 mbsf, is dictated by both organic and inorganic diagenetic reactions within the sediment column. Below

the opal-A/opal-CT transition, where diffusion rates are probably considerably slower owing to the decrease in porosity and permeability, the chemical profiles of virtually all constituents indicate significant influence by basement-alteration reactions.

Sulfate, Alkalinity, Ammonia, and Phosphate

Sulfate decreases rapidly from a near-surface value of 24.0 mmol/L to a minimum of 0.1 mmol/L at 370 mbsf (Fig. 33). Sulfate concentrations increase from the 370-mbsf minimum to 9.0 mmol/L at 525 mbsf.

Alkalinity also shows a steep gradient in the upper interstitial waters, increasing to 19.3 mmol/L at 78 mbsf (Fig. 33). Concentrations then gradually decrease to approximately 15 mmol/L at 288 mbsf. Through the opal-A/opal-CT transition from 288 to 314 mbsf, the alkalinity decreases more rapidly to approximately 9 mmol/L. From 314 mbsf to the deepest sample at 525 mbsf, the alkalinity decreases to 1.4 mmol/L.

The ammonia profile exhibits many of the same characteristics as the sulfate and alkalinity profiles. The concentration gradient over the upper 78 m is steep, with ammonia increasing from 160 to 1470 μmol/L (Fig. 33). Below 78 mbsf, ammonia concentrations increase slightly to approximately 1650 at 191 mbsf and subsequently stay essentially constant to 370 mbsf. Ammonia then decreases consistently to 970 μmol/L at 525 mbsf, indicating incorporation into diagenetically formed clay minerals.

Phosphate (Fig. 33) rapidly increases from 25 μmol/L at 3 mbsf to 40 μmol/L at 12 mbsf, before falling to 0 μmol/L at 370 mbsf owing to removal into authigenic sedimentary phases.

The concentrations of sulfate, alkalinity, and ammonia in the uppermost interstitial waters of Site 797 are strongly related to bacterial degradation of organic matter. The most intense consumption of organic matter is occurring in the upper 90 m, resulting in sulfate depletion and the buildup of alkalinity and ammonia. The continued depletion of sulfate to values approaching, but not equal to, 0 mmol/L over 280 to 370 mbsf reflects the presence but low availability of organic matter for bacterial degradation. This is also manifested in the low levels of methane at the site ("Organic Geochemistry" section, this chapter).

The sulfate increase from 370 to 525 mbsf is perhaps due to a sedimentation-rate decrease that occurred during the middle and late Miocene (380 to 340 mbsf; see "Sediment Accumulation Rates," this chapter). The inferred low sedimentation rate over this interval also marked by an increase in the total organic carbon ("Organic Geochemistry section," this chapter), may have allowed deeper diffusive penetration of sulfate from the sediment/water interface at that time; the sulfate now found at depth may represent trapped sulfate that has not yet been totally consumed by bacterial degradation.

The overall decrease of alkalinity throughout the entire sediment column reflects the consumption of HCO$_3^-$ during dolomitization. This will be discussed in the context of the Ca, Mg, and Sr concentration gradients.

Silica

Silica concentrations at Site 797 increase from 540 μmol/L at 2.9 mbsf to 770 μmol at 78 mbsf (Fig. 34). From 88 mbsf to 288 mbsf, Si further increases from 1030 to 1460 μmol/L. Through the opal-A/opal-CT transition from 288 mbsf to 314 mbsf, Si abruptly decreases to approximately 620 μmol/L. Si decreases further through the opal-CT zone, resulting in a minimum of 160 μmol/L at 525 mbsf.

The consistent Si increase over the uppermost 78 m correlates to the relatively organic-rich Quaternary Unit IA ("Lithostratigraphy," this chapter). In this interval, diatoms are a relatively minor constituent, and the interstitial water chemistry re-
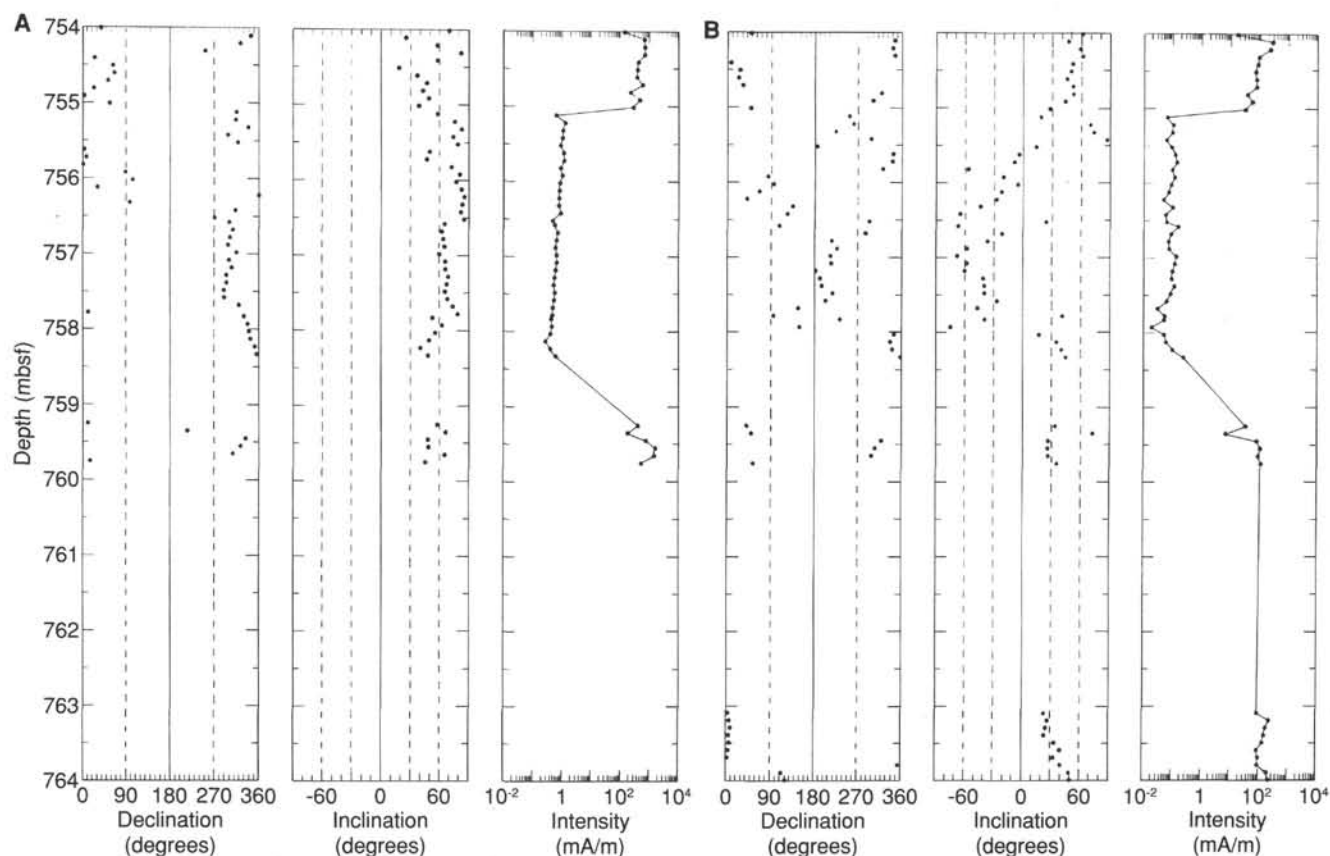
Figure 30. Paleomagnetic results for Core 127-797C-30R before (A) and after (B) AF cleaning with 15 mT. Basalts and sediments can be distinguished by the different intensities of magnetization.

flects the low availability of biogenic Si. Dissolved Si increases through Unit II ("Lithostratigraphy," this chapter), indicating progressive diatom dissolution.

Dissolved silica is removed from interstitial waters across the opal-A/opal-CT transition. As mentioned before, this opal-A/opal-CT transition affects all chemical profiles by the porosity and permeability decrease associated with opal-CT formation. Further depletion of Si from pore waters occurs throughout the opal-CT zone during precipitation of progressively ordered silica phases. There is no distinct concentration change in Si across the opal-CT/quartz transition at 428 to 438 mbsf.

Calcium, Magnesium, and Strontium

Calcium concentrations initially decrease from 10.1 mmol/L at 3.0 mbsf to 7.6 mmol/L at 59 mbsf, and subsequently stay constant to 314 mbsf, just below the opal-A/opal-CT transition (Fig. 35). From 314 mbsf to the deepest sample at 525 mbsf, Ca exhibits a large and consistent increase to 38.3 mmol/L.

Magnesium concentrations also change relatively rapidly in the uppermost interstitial waters, decreasing from 49.8 mmol/L at 3 mbsf to approximately 45.7 mmol/L at 31 mbsf (Fig. 35). Magnesium then decreases slightly yet consistently to a relative minimum of 38.4 mmol/L at 296 mbsf and then increases through the opal-A/opal-CT transition to 41.6 mmol/L at 314 mbsf. Below the opal-A/opal-CT transition, Mg decreases to a final minimum value of 20.2 mmol/L at 525 mbsf.

Strontium concentrations (Fig. 35) remain at approximately 85 μmol/L from 3 to 192 mbsf and then gently increase to 105 μmol/L at 296 mbsf, just below the opal-A/opal-CT transition.

From 1925 to 304 mbsf, Sr increases to 125 μmol/L. Beneath the opal-A/opal-CT transition, from 304 mbsf to the deepest sample at 525 mbsf, Sr further increases to 205 μmol/L.

The sequential downhole variations of Ca and Mg, summarized in Figure 35, indicate different mechanisms of dolomite formation and/or alteration of volcanic-ash layers. Carbonate formation and ash alteration similarly affect the relative concentrations of Ca and Mg and cannot always be exclusively differentiated.

The Ca and Mg decrease in the upper sediments, coupled with the higher alkalinity (Figs. 33 and 35), may indicate precipitation from solution of dolomite according to the reaction:

$$Ca + Mg + 4HCO_3 = CaMg(CO_3)_2 + 2CO_2 + 2H_2O$$
(from Baker and Burns, 1985).
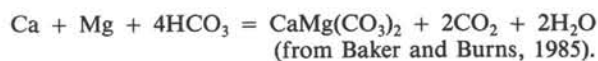
The interstitial water data records this process as it occurs presently; indeed, the youngest carbonate observed at Site 797 is a dolomite layer at approximately 24 mbsf (Core 127-797B-4H; "Lithostratigraphy" section, this chapter). This interpretation of primary dolomite formation agrees with the essentially constant Sr concentration from 3 to 196 mbsf, which suggests that carbonate is not forming at the expense of a biogenic precursor calcite or aragonite phase.

From 30 to 300 mbsf, through which Ca is constant and Mg and alkalinity both decrease, dolomite formation may be occurring at the expense of calcite, according to:

$$CaCO_3 + Mg + 2HCO_3 = CaMg(CO_3) + CO_2 + H_2O$$
(from Baker and Burns, 1985).

Magnetic polarity
time scale
(after Berggren et al., 1985)
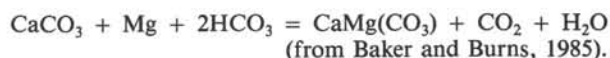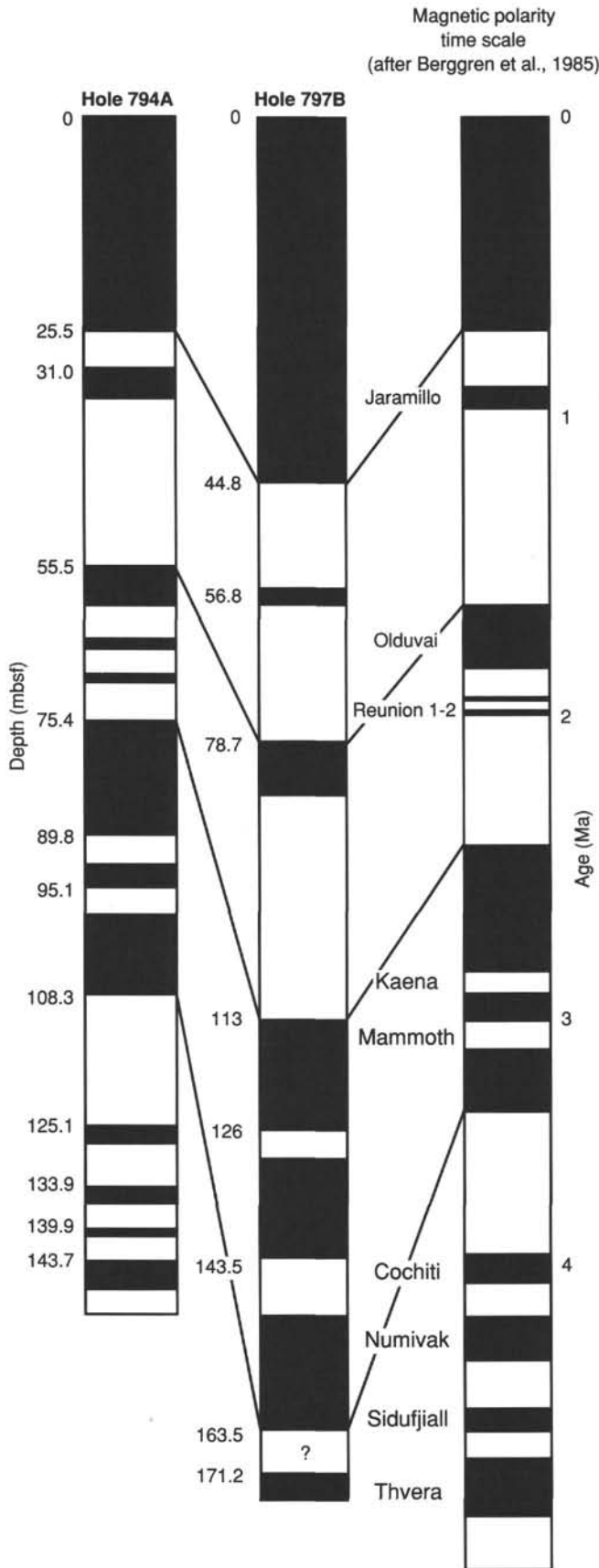
Figure 31. Polarity interpretation of the paleomagnetic results from Hole 797B (0–170 mbsf), correlated with Hole 794A and the magnetostratigraphic time scale of Berggren et al. (1985). Reversed intervals are blank.

Again, this agrees with the Sr increase from 192 to 296 mbsf, as Sr is released from carbonate during recrystallization.

Below the opal-A/opal-CT transition at 300 mbsf, the Ca, Mg, and Sr profiles both indicate interaction with basement, with Ca and Sr increasing owing to release during silicate mineral alteration and Mg decreasing because of uptake into clay-mineral alteration products. Note that these deeper trends also may be consistent with large-scale dolomitization of a calcium carbonate precursor; as a result, the relative contributions of basement alteration and dolomite formation again cannot be differentiated.

Potassium, Rubidium, and Lithium

Potassium and rubidium behave similarly at Site 797. Both alkali metals are enriched relative to seawater in the uppermost sediments (at 3 mbsf K = 11.3 mmol/L; Rb = 2.29 μmol/L) and decrease linearly to the opal-A/opal-CT transition at 304 mbsf (Fig. 36). From 304 to 525 mbsf, the concentration gradient for both K and Rb lessens, resulting in concentrations at 525 mbsf of 1.9 mmol/L and 0.40 μmol/L, respectively.

The enrichment of K and Rb relative to seawater in the uppermost sediments may indicate release by clay minerals, or it might be a squeezing artifact (Manheim and Sayles, 1974). The consistently decreasing concentrations indicate an overall seawater source and basement sink, with diffusion being restricted below the opal-A/opal-CT transition.

Lithium increases from essentially seawater concentrations near the surface to a maximum of 94 μmol/L at the opal-A/opal-CT transition at 300 mbsf and decreases to 29 μmol/L at 525 mbsf (Fig. 36). The profile indicates the release of Li during diatom dissolution and silica transformation, and, like K, Rb, and Mg, uptake into basement-alteration products.

pH, Sodium, Chlorine, and Salinity

Several constituents of the interstitial waters at Site 797 present simple and consistent profiles. pH is essentially constant throughout the entire sediment column (Fig. 37). A slight perturbation between 255 and 304 mbsf may relate to the opal-A/opal-CT transition, but any interpretation of pH data is restricted by sampling artifacts such as outlined in Gieskes and Peretsman (1986).

Na and Cl show little change with depth (Fig. 37) indicating no significant freshwater or brine input at depth. Salinity (Fig. 37) decreases from 35 g/kg at 3 mbsf to minimum values of 30.1 g/kg from 370 to 441 mbsf and then increases to a relative maximum of 31.7 g/kg at 525 mbsf. The decrease through the upper 441 is due to the removal of sulfate, alkalinity, Mg, and K; the increase below this level is caused by the trapped sulfate and the Ca increase associated with basalt alteration.

Summary

As at the other Leg 127 sites, the chemistry of the interstitial waters at Site 797 is controlled by the availability of organic matter for bacterial degradation, silica diagenesis, and pore water interaction with basement during alteration reactions. Sulfate is never completely depleted and in fact increases with depth, which perhaps is related to a middle to late Miocene decrease in sedimentation rate.

The opal-A/opal-CT transition at approximately 300 mbsf restricts communication between the upper and lower sediments, developing two different diffusive regimes. Above the opal-A/opal-CT transition zone, concentration gradients are controlled by diffusion from and into the sediment/water interface and, most notably in the cases of Ca and Mg, by reaction with sediments. Below the opal-A/opal-CT transition, basement alteration serves as the primary sink or source for the various dissolved chemical constituents.

Table 5. Biostratigraphic datum planes and estimates of sedimentation rates for Site 797. The depths of zonal boundaries and datums in core-catcher samples are taken from the top or bottom of the cored interval rather than from the base of the recovered sediment.

Datum	Age (Ma)	Depth (mbsf)	Sedimentation rate m/m.y.	Sedimentation rate cm/k.y.	Mean dry bulk density (g/cm^3)	Accumulation rate (g/cm^2/k.y.)
Seafloor	0	0				
			46	4.6	0.88	4.1
1. FAD of *A. oculatus*	1.80	81.9				
			50	5.0	0.86	4.3
2. FAD of *N. koizumii*	3.50	166.4				
			43	4.3	0.85	3.7
3. Base of *T. oestrupii* Zone	5.30	243.4				
			56	5.6	1.02	5.7
4. Base of *R. californica* Zone	7.20	350.0				
			5	0.5	1.47	0.7
5. LAD of *C. floridanus*	11.60	369.6				
			25	2.5	1.47	3.7
6. LAD of *S. heteromorphus*	14.40	439.1				
			20	2.0	1.48	3.0
7. FAD of *S. heteromorphus*	17.10	493.5				

Note: LAD = last-appearance datum; FAD = first-appearance datum.

ORGANIC GEOCHEMISTRY

The shipboard organic geochemical analyses of sediment samples from Holes 797B and 797C included inorganic carbon, total carbon, nitrogen, sulfur, Rock-Eval, and volatile hydrocarbon analyses. The procedures used for these determinations are outlined in the "Explanatory Notes" chapter of this volume, while a background and detailed descriptions are given in Emeis and Kvenvolden (1986).

Carbon, Nitrogen, and Sulfur

The concentrations of inorganic, total, and organic carbon in the sediments recovered from Site 797 are presented in Table 7. The percentage of calcium carbonate (CaCO$_3$) was calculated from the inorganic carbon concentrations by assuming that all carbonate is in the form of calcite. Nitrogen and some sulfur concentrations are also given in Table 7. Sedimentary carbonates range from 0.1% to 83.4%, although most of the samples contain less than 1% CaCO$_3$. The generally low values and the poor preservation of biogenic carbonate detritus (see "Biostratigraphy," this chapter) suggest that sediment deposition generally occurred below the carbonate compensation depth (CCD) or that subsurface carbonate dissolution occurred. However, the overall concentrations of carbonate appear to be higher at Site 797 than at the previous sites of Leg 127. The concentrations of organic carbon (%C$_{org}$) in the whole sediments range from 0.18% to 8.53%, with most of the sediments containing about 1.0% on a dry weight basis. The total nitrogen contents range from 0% to 0.59% of whole sediments on the same basis. The ratio of organic carbon to total nitrogen (C/N) ranges from 5.70 to 33, with most of the sediments having values between 7 and 15.

The %CaCO$_3$, %C$_{org}$, and C/N ratio values are plotted against the sub-bottom depth in Figure 38. Carbonates are generally present at less than 1%, but there are occurrences of increased carbonate content (5% to 58%) over narrow intervals in the top 300 m. These occurrences may be authigenic in nature, as dolomites were present even in the uppermost cores, although increased preservation of biogenic carbonate must also be considered. There is very little carbonate preservation below 300 mbsf (approximately the middle of the upper Miocene) except for Sample 797B-50X-CC, 7–9 cm (middle Miocene), which contained 83% carbonate. Conditions were generally unfavorable for carbonate preservation in the Miocene.

The sediments at Site 797 are characterized by moderate to low values of organic carbon (generally less than 1.5%). As with the previous sites of Leg 127, high organic contents are found in the Quaternary in the darkest colored sediments, many of which contain pyrite (see below) or are rich in foraminifers.

The latter are often concentrated at the bases of dark layers. Organic carbon concentrations vary markedly (0.3%–7.4%) in the silty clays of the Quaternary and the uppermost Pliocene (0–100 mbsf). TOC levels are generally low (about 0.6%) in the Pliocene silty clays (100–250 mbsf). TOC levels increase markedly (up to 8.53%) in the silty clays and the siliceous claystones of the upper Miocene (250–350 mbsf; 290 m is approximately the beginning of the opal-A/opal-CT transition). A similar increase in TOC levels was also seen in upper Miocene sediments at Site 794. Organic carbon concentrations are lower (about 0.8%) in the siliceous claystones of the upper and middle Miocene (approximately 350–550 mbsf). The oldest claystones recovered (early and uppermost middle Miocene; 550–800 mbsf) are interbedded with igneous rocks and consistently show TOC levels of about 0.6%.

The occurrence of the dark, organic-rich layers, particularly in the Quaternary and upper Miocene, represents conditions in which productivity was enhanced and/or that conditions for the preservation of organic matter were more favorable. Such a situation may be due to the short-term formation of anoxic bottom waters associated with the restriction of deep-water circulation in the Japan Sea during the Quaternary and the late Miocene. Alternatively, these sediments may derive from organic-rich sediments originally deposited upslope in an oxygen-minimum zone and transported downslope by slumping and turbidity flows, with rapid burial preventing oxidative degradation of the organic matter. The generally low organic content in the lighter colored sediments at Site 797 attests to conditions which were generally unfavorable for the deposition and/or preservation of organic matter. The mottling of sediments from bioturbation was commonly observed at Site 797, which implies oxygenated conditions at the sediment/water interface.

The ratio of organic carbon to total nitrogen in the sediments is also plotted in Figure 38. The nitrogen component includes both organic and inorganic nitrogen. Nitrogen concentrations (Table 7) are generally high (up to 0.38%) in the silty clays of the Quaternary (0–90 mbsf). However, the Quaternary also contains very low concentrations of nitrogen, particularly in the organic-poor sediments. Nitrogen levels are generally low (about 0.05%) in the Pliocene diatom oozes and silty clays (90–225 mbsf), increase (0.08%–5.9%) in the silty clays and siliceous claystones of upper Miocene sediments (225–425 mbsf) and fall (about 0.06%) in the lower and middle Miocene sediments (425–800 mbsf).

In the Quaternary, several pairs of light and dark bands which are immediately adjacent to each other have been analyzed. There is no consistent difference in the C/N ratios between the light and the dark sediments at Site 797. Organic carbon commonly increases by an order of magnitude from a light- to a
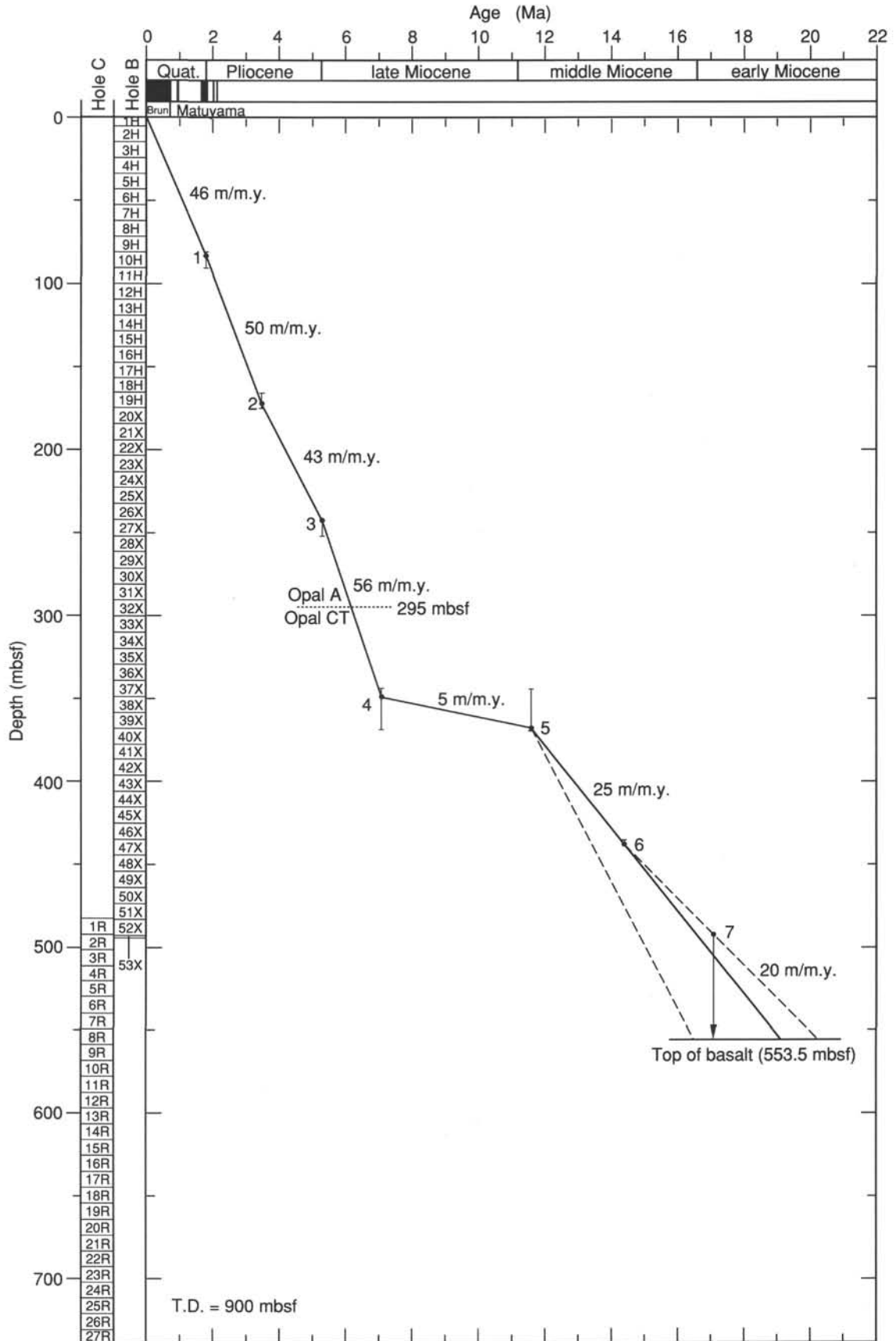
Figure 32. Age vs. depth relationship at Site 797. Error bars indicate uncertainties in age and depth of datum levels. Double-headed arrow shows the depth and age range of overlap between *Globorotalia peripheroronda* and *Catapsydrax parvulus*. Datum level 7 is the apparent first occurence of *Sphenolithus heteromorphus*.

Table 6. Interstitial water geochemistry data, Site 797.

Core, section, interval (cm)	Depth (mbsf)	Vol. (mL)	pH	Alkalinity (mM)	Salinity (g/kg)	Mg (mM)	Ca (mM)	Cl (mM)	SO$_4$ (mM)	PO$_4$ (μM)	NH$_4$ (μM)	SiO$_2$	Mg^{2+}/Ca^{2+}
127-797A-													
1H-4, 140–145	9.30	20	7.64	8.888	35.0								
127-797B-													
1H-2, 140–145	2.90	36	7.41	5.134	35.0	49.8	10.1	543	24.0	25	160	540	4.93
2H-4, 145–150	11.85	5	7.58	10.507	34.0	47.6	9.5	553	18.6	40	710	605	5.01
3H-5, 140–145	22.80	5				46.2	8.6	544	12.1			950	5.37
3H-5, 145–150	22.85	65	7.29	14.139	34.0	45.9	8.6	539	15.6	40	945	735	5.34
4H-4, 145–150	30.85	5	7.53	15.806	33.8	45.7	8.2	532	13.9	35	1005	700	5.57
5H-4, 145–150	40.35	5	7.65	17.461	33.5	44.9	8.0	538	12.5	40	1215	720	5.61
6H-4, 140–145	49.80	5			44.5		7.9			37	1365	770	5.63
6H-4, 145–150	49.85	5	7.49	18.530	33.5	44.6	7.9	548	10.7	34	1330	1015	5.65
7H-4, 145–150	59.35	5	7.56	19.223	33.5	43.9	7.6	531	9.4	35	1290	815	5.78
8H-4, 145–150	68.85	5	7.56	19.223	33.0	43.7	7.7	541	8.7	30	1350	835	5.68
9H-4, 140–145	78.30	22	7.59	19.266	33.0	43.0	7.9	543	7.6	12	1470	650	5.44
9H-4, 140–145	78.30	5				43.0	7.6		7.5		1475	770	5.66
10H-4, 140–145	87.80	5	7.53	18.420	33.0	42.5	7.6	539	6.1	26	1470	1030	5.59
12H-4, 140–145	106.80	65	7.41	19.049	33.5	42.5	7.4	539	6.1	18	1470	1150	5.74
15H-4, 140–145	135.30	56	7.43	18.623	32.3	41.3	7.4	538	4.5	13	1585	1245	5.58
18H-4, 140–145	163.80	43	7.40	17.925	32.2	40.4	7.4	541	3.7	10	1560	1285	5.46
18H-4, 145–150	163.85	5				40.4	7.4	510	3.3		1630		5.46
21X-4, 140–145	191.40	5				39.1	7.5	536	2.7		1680		5.21
21X-4, 145–150	191.45	64	7.40	17.276	32.0	39.7	7.5	540	2.7	10	1615	1340	5.29
24X-5, 140–145	221.70	5				38.9	7.5	537	2.3		1775	1310	5.19
24X-5, 145–150	221.75	61	7.50	16.460	32.0	39.2	7.5	542	2.0	7	1700	1510	5.23
27X-6, 140–145	252.30	5									1720		
27X-6, 145–150	252.35	64	7.58	15.445	31.7	39.0	7.5	533	1.7	5	1695	1325	5.20
28X-1, 145–150	254.55	5	7.72	13.089	31.5	39.4	7.7	535	3.5	6	1710		5.12
30X-1, 145–150	273.95	5	7.46	13.883	31.0	38.6	7.5	540	0.9	9	1735	1340	5.15
31X-4, 140–145	288.10	12	7.40	14.824	32.0	39.3	7.8	530	0.3	6	1635	1460	5.04
32X-3, 145–150	296.35	5	7.51	12.988	31.0	38.4	7.8	538	0.6	5	1640	1180	4.92
33X-2, 140–145	304.40	8	7.52	8.832	32.0	40.9	8.3	533	2.0	2	1600	900	4.93
33X-2, 145–150	304.45	5									1865		
34X-2, 145–150	314.15	5	7.69	8.773	30.3	41.6	7.1	533	1.1	2		615	5.86
37X-4, 140–145	346.20	5				39.7	8.3		2.9				4.78
37X-4, 145–150	346.25	36	7.69	7.107	31.5	40.3	8.4	536	4.0	2	1615	630	4.80
40X-1, 56–61	369.86	5							0.1		1605		
40X-1, 61–66	369.91	20	7.69	4.980	30.1	37.3	9.5	524	0.6	0	1520	480	3.93
47X-3, 140–145	440.60	3			30.5	27.7	21.2	530	2.9			365	1.31
49X-3, 145–150	459.95	5	7.55	2.377	30.3	24.8	23.1	539	3.5		1340	320	1.07
51X-4, 140–145	480.80	5							4.9		1200	320	
51X-4, 145–150	480.85	18	7.35	1.541	31.0	23.5	26.9	537	5.0	0	1255	255	0.87
127-797C-													
5R-2, 140–145	524.90	5											
5R-2, 145–150	524.95	15	7.62	1.417	31.7	20.2	38.3	521	9.0	0	970	160	0.53

dark-colored band, but nitrogen increases also. The C/N ratio tends to be highly variable; the highest ratios are generally to be seen in those samples which are very low in nitrogen. It is generally accepted that C/N values are higher for organic matter from a terrestrial rather than from a marine source (e.g., Calvert, 1983). However, modern marine sediments have C/N ratios in the range of 9 to 18 (Müller, 1977; Stevenson and Cheng, 1972) and diagenesis can alter C/N values (Müller, 1977; Waples and Sloan, 1980) which is in keeping with most of the C/N ratios observed at Site 797. Ratios outside this range at Site 797 are usually from sediments which are very low in nitrogen.

Total sulfur was routinely measured in samples from Cores 127-797B-1H through -3H and then on selected samples. The concentration of total sulfur is highly variable in these samples. Sulfate in pore waters is never depleted at this site (see "Inorganic Chemistry," this chapter) and methanogenesis (see volatile hydrocarbons, below) was minor. This scenario is similar to that seen at Site 794, also in the Yamato Basin, but unlike that at Sites 795 and 796 of the Japan Basin, where sulfate was rapidly depleted in the Quaternary sediments.

Rock-Eval Analysis

Samples from Site 797 were analyzed for total organic carbon (TOC), source character, and thermal maturity and hydrocarbon potential using the Rock-Eval instrument. The resulting values are presented in Table 8. The measurement of several parameters is inconsistent (see discussion in the Site 794 chapter) and repeatability was poor, except for TOC. Hence, interpretations regarding source, maturation and potential would be speculative. The TOC values were generally in very good agreement with those values determined by difference (cf. Tables 7 and 8). A van Krevelen-type diagram of the hydrogen index (HI) vs. the oxygen index (OI) for Site 797 is shown in Figure 39. Many samples exhibit OI values above 300 and are not included on this plot. Based on the sample distributions in this plot, the organic contents of these sediments are primarily mixtures of type II and type III organic matter. The samples which are low in organic carbon tend to plot more in the type II region while the samples which are richer in organic matter tend to plot in the type II/III region.
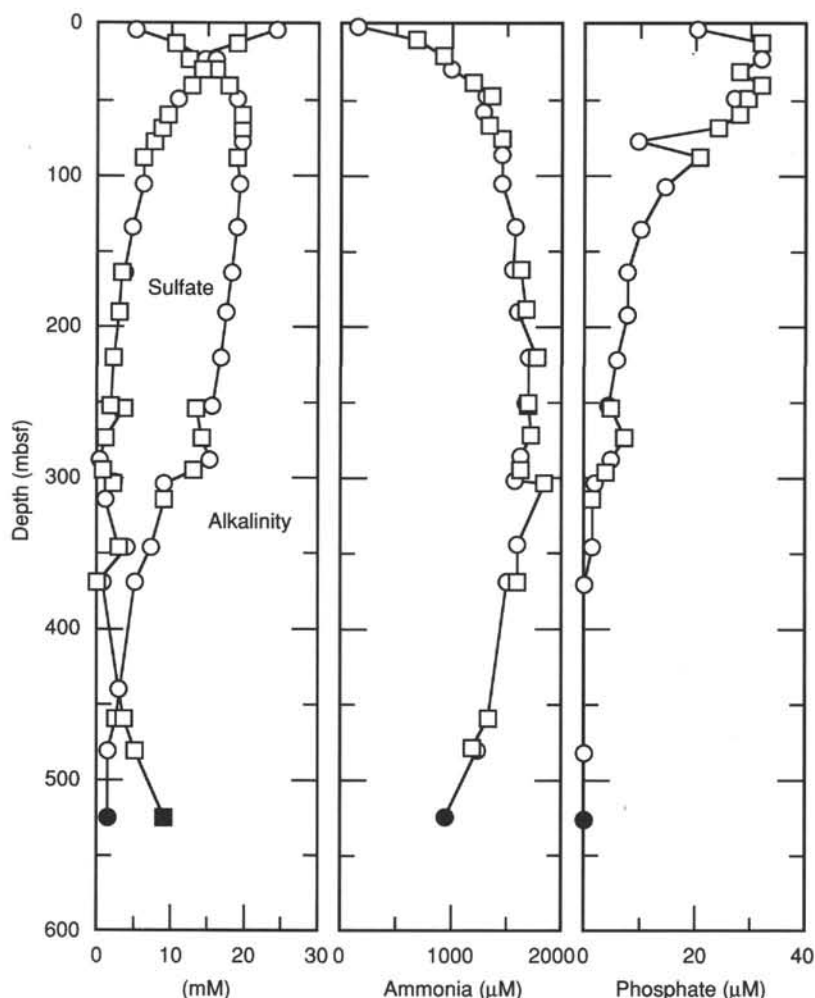
Figure 33. Sulfate, alkalinity, ammonia, and phosphate profiles with depth, Holes 797B and 797C. Circles: ODP squeezer. Squares: Brumsack squeezer. Open symbols for Hole 797B, solid symbols for Hole 797C.

Volatile Hydrocarbons

As part of the shipboard safety and pollution monitoring program, the hydrocarbon gases were continuously measured in the sediments at Site 797 using the headspace technique. Minor concentrations of volatile hydrocarbons, predominantly methane, were detected. The results are presented in Table 9. Methane concentrations in the headspace volumes ranged between 3 and 200 ppm. Traces of ethane and propane were present, particularly in the deeper sediments of Hole 797B. Sulfate is never depleted at Site 797 (see "Inorganic Chemistry," this chapter) but decreases gradually with depth to a minimum at about 290 m and then gradually increases with depth down to 525 m. The low overall content of methane in the sediments, coupled with the observed sulfate levels, suggests that methanogenesis was minor at Site 797. It is interesting that the minimum sulfate concentrations at Site 797 (see "Inorganic Geochemistry") approximately coincide with maxima in organic-rich sediments observed between 290 and 350 mbsf (Fig. 38). The necessary conditions to initiate and sustain methanogenesis are significant concentrations of organic matter in oxygen-poor sedimentary environments, particularly when the available sulfate has been utilized (Oremland and Taylor, 1978). The situation at Site 797 is similar to that at Site 794, which is also in the Yamato Basin. The extent of sulfate reduction and methanogenesis is minor at both sites

and is strikingly different from that at Sites 795 and 796, both in the Japan Basin, where sulfate was rapidly depleted with depth and methane concentrations were significant.

The concentrations of total organic carbon at Sites 794, 795, 796, and 797 are similar, in that the organic contents are generally low but numerous thin, dark, organic-rich sediments occur periodically, particularly in the Quaternary. The lack of significant sulfate reduction and methanogenesis at Sites 794 and 797 may be due to higher concentrations of dissolved oxygen in the bottom waters at the time of deposition in the Yamato Basin than at Sites 795 and 796 in the Japan Basin. In other words, the generally low organic levels at Sites 794 and 797 are due to the degradation of the organic matter by mainly aerobic processes, while at Site 795 significant organic matter survived aerobic degradation, which was then degraded anaerobically.

Conclusions

Preservation of organic matter at Site 797 is generally poor to moderate. The sediments may have been initially laid down in oxic bottom waters, which allowed the organic matter to be recycled by aerobic respiration. Subsequent sulfate reduction was moderate, and methanogenesis was minor. Deposition of thin, dark, organic-rich sediments occurred periodically, particularly during the Quaternary and in the late Miocene (290–350 mbsf). The similarity in the profiles of organic carbon at Sites 797 and
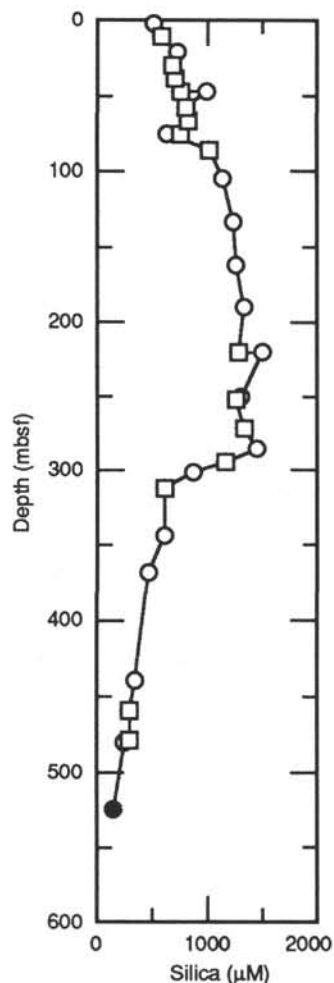
Figure 34. Silica profile with depth, Holes 797B and 797C. Symbols as in Figure 33.

794 suggests that the factors which determine organic productivity and preservation were basin-wide in operation. These sediments may have been laid down during short periods of time when the bottom waters were anoxic owing to restricted or sluggish water circulation in the Yamato Basin. Another scenario for their formation could be by the deposition of downslope turbidites. The material making up these turbidites would have been deposited in shallower water, perhaps where the oxygen-minimum layer impinged upon the slope, which should have enhanced the preservation of organic matter. Deposition in the Yamato Basin at Sites 794 and 797 may have occurred in bottom waters which were more oxic than those in the Japan Basin at Sites 795 and 796.

BASEMENT ROCKS

Introduction

Hole 797C encountered basement composed of interlayered igneous and sedimentary rocks at 553.5 mbsf. A total of 347 m of this basement was cored with a total recovery of 40%, or 140 m. The lithology of the interlayered sedimentary rocks varies with increasing depth, from claystone to laminated sandstone, siltstone, and claystone (see "Lithostratigraphy," this chapter). The total recovery of igneous rocks was 80 m. This section describes the lithologic and petrographic characteristics of the igneous rocks and presents their whole-rock major- and trace-

element chemistry. We were able to identify 21 units, based on (1) the presence of the intercalated sedimentary rocks, (2) significant structural change, and (3) the presence of chilled marginal facies. In this summary, each igneous rock unit is named according to the dominant rock type.

Lithology and Petrography

The lithologic and petrographic characteristics of each unit are described below. Figure 40 shows a graphic presentation of the lithology of the igneous- and sedimentary-rock sequence from Hole 797C. Established and uncertain unit boundaries are shown by full and dashed lines, respectively. Visual core descriptions and thin-section descriptions are given in the appendixes.

Unit 1. Sparsely plagioclase olivine phyric basalt (Section 127-797C-8R-2, 105 cm, to Section 127-797C-9R-1, Piece 25; 553.5 to 562.1 mbsf)

This unit is composed mainly of highly fractured and brecciated basalt, with sporadic pieces of conglomerate. The top of the unit is bounded by overlying sedimentary rock. The base of the unit is defined by a change to less fractured and brecciated basalt without conglomerate. The basalt contains sparse phenocrysts of plagioclase and olivine, which sometimes form glomeroporphyritic clusters. The groundmass consists of plagioclase, mesostasis, and greatly subordinate magnetite and Cr-spinel. The rock is highly altered, with mafic silicates and the mesostasis totally altered to clay and with plagioclase highly to moderately altered to clay. The fractures are filled with clay, carbonate minerals, and minor pyrite. Vesicles are sparse (<1%) and filled with clay minerals.

Unit 2. Sparsely plagioclase olivine phyric basalt (Section 127-797C-9R-2, Piece 1, to Section 127-797C-10R-4, Piece 10; 562.1 to 579.5 mbsf)

The lower limit of the unit is defined by the appearance of sedimentary rock in Section 127-797C-11R-1. The unit is composed of fractured, sparsely plagioclase olivine phyric basalt. This unit is petrographically similar to Unit 1 but is distinguished by being less fractured and by the absence of conglomerate.

Unit 3. Aphyric basalt (Section 127-797C-11R-1, Piece 9, to Section 127-797C-14R-1, Piece 5; 580.2 to 608.6 mbsf)

This unit is bounded at the top and base by sedimentary rocks and has both upper and lower chilled borders. The interior of the unit is only slightly altered, but fractures are developed throughout and are filled by clay and carbonate minerals and by subordinate pyrite. The unit is composed dominantly of fine- to medium-grained aphyric basalt with an interstitial texture developed by plagioclase, clinopyroxene, olivine, magnetite, and mesostasis. Olivine is partially altered and the mesostasis is totally altered to clay minerals. Interstitial clinopyroxenes show radiating textures from rapid growth, suggesting that the cooling rate at the final crystallization stage of the interior of the unit have might exceeded a few tens of degrees per hour (Lofgren, 1980). The upper and lower chilled marginal facies are characteristically bleached, highly altered, and have a cryptocrystalline, spherulitic groundmass.

Unit 4. Aphyric basalt (Section 127-797C-14R-1, Piece 8, to Section 127-797C-14R-2, Piece 1; 608.8 to 609.4 mbsf)

The top of the unit is defined by the occurrence of sedimentary rock in Section 797C-14R-1, Pieces 6 and 7. The base of the unit is poorly constrained between the lower end of Section 127-797C-14R-2 and the sedimentary rock at the top of Section 127-797C-15R-1. No chilled margins were observed. This unit is characterized by an extremely fractured and partially brecciated structure (Fig. 41). Fractures are interconnected and filled with
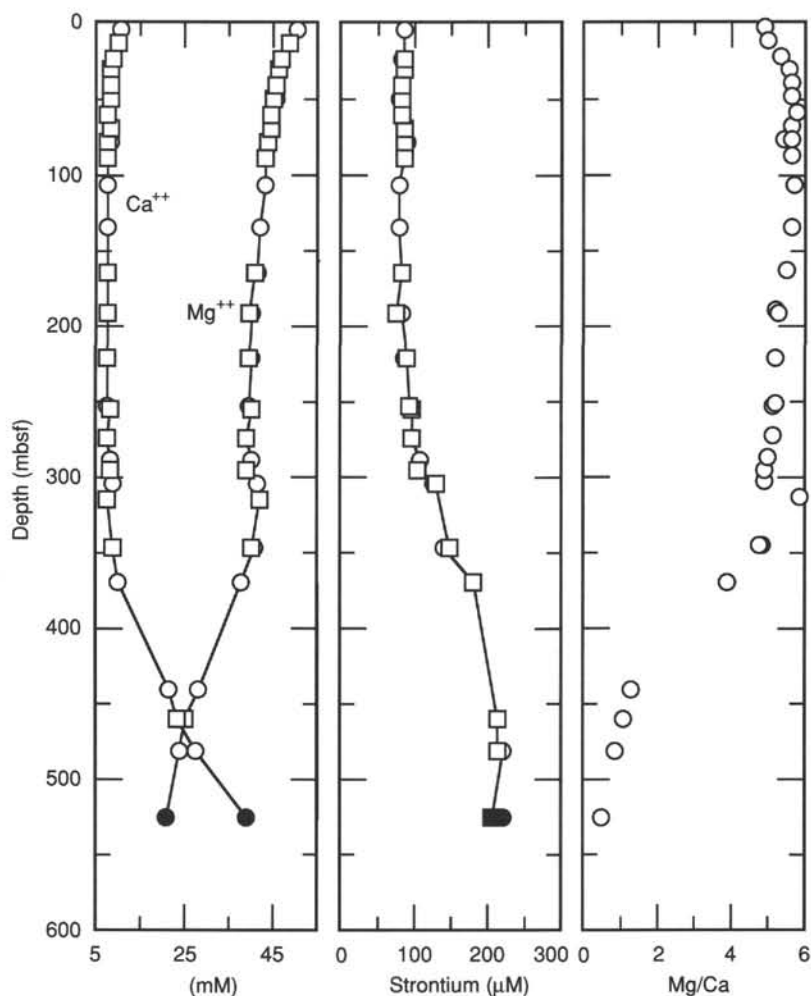
Figure 35. Calcium, magnesium, strontium, and magnesium/calcium profiles with depth, Holes 797B and 797C. Symbols as in Figure 33.

clay minerals and minor amounts of pyrite. The bulk of the unit is composed of cryptocrystalline to microcrystalline aphyric basalt with trace amounts of plagioclase and olivine phenocrysts. The unit is very highly altered, with the olivine and the mesostasis totally replaced by clay minerals and the plagioclase slightly to highly altered to clay minerals. Vesicles are sparse (< 1%) and are filled with clay minerals.

Unit 5. Aphyric basalt (Section 127-797C-15R-1, Piece 2, to Section 127-797C-18R-1, Piece 7; 618 to 646.9 mbsf)

The unit is bounded by sedimentary rocks at the top and base. The bulk of the unit is composed of aphyric basalt with fractures that are filled with clay minerals, carbonate minerals, and pyrite. The rock has a fine- to medium-grained interstitial to subophitic texture developed by plagioclase, clinopyroxene, olivine, magnetite, and mesostasis. The unit is moderately to highly altered with the olivine and mesostasis totally replaced by clay minerals and the plagioclase and clinopyroxene partially altered to clay minerals. This unit was divided into four subunits (Subunits 5A, 5B, 5C, and 5D) based on variations in grain size. Subunit 5A is fine grained and was defined from Section 127-797C-15R-1, Piece 6 to Section 127-797C-15R-1, Piece 9. This subunit is extremely fractured in some places. Subunit 5B is coarser grained than Subunit 5A and was defined from Section

127-797C-15R-1, Piece 10, to Section 127-797C-15R-2, Piece 11. Subunit 5C is the center of Unit 5 and is characterized by the presence of subophitic texture and by a lesser degree of alteration than Subunit 5B. Subunit 5C was defined from Section 127-797C-15R-2, Piece 11, to Section 127-797C-17R-1, Piece 8. The lowermost Subunit 5D is finer grained than overlying Subunits 5B and 5C and was defined from Section 127-797C-17R-1, Piece 9, to Section 127-797C-18R-1, Piece 7. The finer grained nature of the uppermost and lowermost subunits relative to the central subunits indicates that they represent chilled margins.

Unit 6. Sparsely plagioclase phyric basalt (Section 127-797C-18R-2, Piece 5 to Section 127-797C-19R-1, Piece 4; 648.3 to 656.4 mbsf)

This unit is overlain by sediment which appears to be baked (see "Lithostratigraphy," this chapter), suggesting that this unit is intrusive. The top and basal parts of the unit are finer grained relative to the inner part, suggesting that they represent chilled margins. The base of the unit was defined by an abrupt change in grain size to an underlying coarser grained unit, but no direct contact was observed. Unit 6 is composed of massive, sparsely plagioclase phyric basalt with a fine- to medium-grained interstitial groundmass. A small proportion of vesicles (<3%) is present. The rock is highly altered, with the mafic silicates and
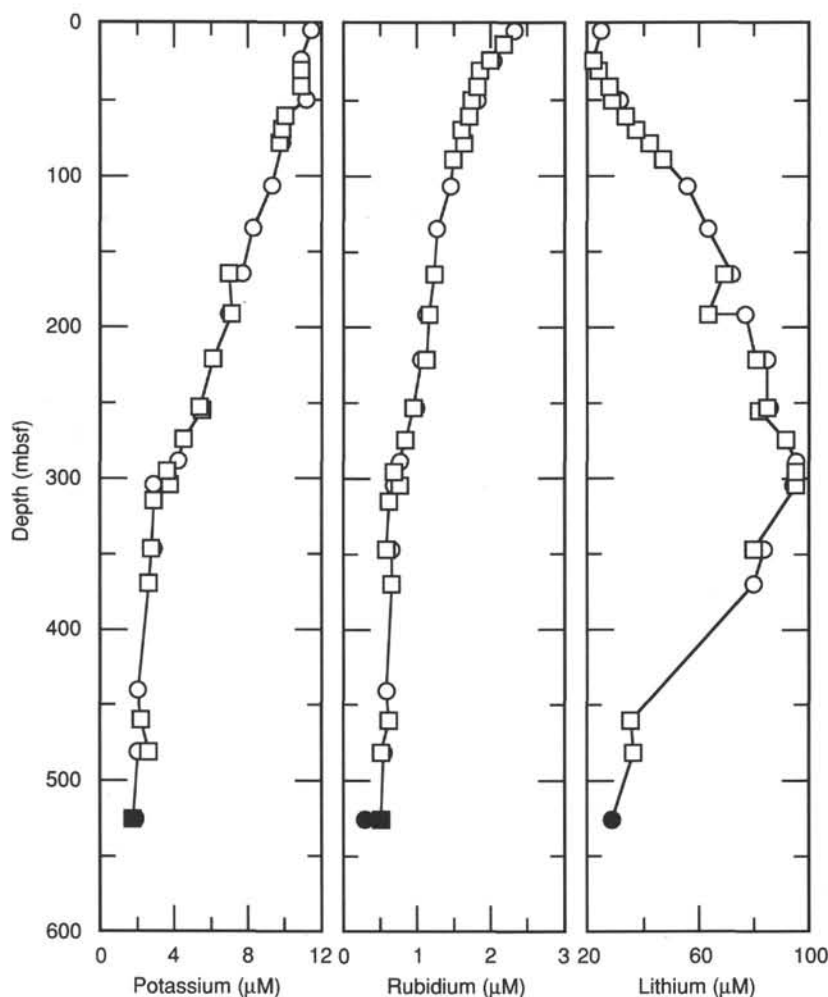
Figure 36. Potassium, rubidium, and lithium profiles with depth, Holes 797B and 797C. Symbols as in Figure 33.

mesostasis totally altered to clay minerals and plagioclase moderately altered to clay minerals. Vesicles are filled with carbonate and clay minerals and minor pyrite.

Unit 7. Sparsely plagioclase phyric dolerite (Section 127-797C-19R-1, Piece 5 to Section 127-797C-19R-4, Piece 8; 656.4 to 661.4 mbsf)

The top of this unit is marked by a change from the chilled margin of Unit 6 to medium-grained dolerite. The base of the unit was defined by a chilled margin and by a baked sediment contact in Section 127-797C-19R-4, Piece 8 (Fig. 42). The lowermost part of the unit just above the baked sediment is bleached and highly altered and shows a cryptocrystalline, spherulitic texture. The interior of the unit is composed dominantly of massive, moderately plagioclase phyric dolerite. A small amount (<2%) of plagioclase phenocrysts is scattered in a medium- to fine-grained subophitic to intergranular groundmass consisting of plagioclase, clinopyroxene, olivine, magnetite, and mesostasis. Vesicles are present in trace amounts (<1%). The rock is moderately to highly altered, with most of the mafic silicate minerals and all of the mesostasis replaced by clay minerals. Plagioclase is slightly to highly altered to clay minerals. In the chilled marginal part of the unit, secondary carbonate minerals occur, replacing plagioclase and filling veins and vesicles along with clay minerals.

Unit 8. Aphyric Dolerite (Section 127-797C-20R-2, Piece 1a, to Section 127-797C-22R-1, 35 cm; 668.3 to 685.5 mbsf)

The top and base of the unit are defined by the presence of sedimentary rocks. Although no direct contacts were observed, the sediments just below this unit exhibit color changes which suggest baking. A reduction in the grain size of the igneous rock immediately adjacent to the sediments suggests a chilled margin. Fractures filled with clay, carbonate minerals, and minor pyrite are scattered throughout the unit. The interior of the unit is massive aphyric dolerite (Fig. 43). Trace amounts of plagioclase phenocrysts (<1%), which rarely occur with olivine in glomeroporphyritic clusters, are contained in a medium-grained, subophitic to intergranular groundmass. The groundmass consists of plagioclase, clinopyroxene, olivine, magnetite, and mesostasis. The unit interior is moderately to highly altered with the olivine and the mesostasis totally replaced by clay minerals. Plagioclase and clinopyroxene are slightly altered to clay minerals. Trace amounts (<1%) of secondary biotite are present. The chilled marginal facies are microcrystalline and very highly altered, with secondary carbonate minerals as well as clay minerals.

Unit 9. Sparsely plagioclase phyric dolerite (Section 127-797C-23R-CC to Section 127-797C-25R-1, Piece 1; 702 to 713.8 mbsf)

This unit is bounded at both the top and bottom by sedimentary rocks. The upper and lower parts of the unit are finer

Table 7. Concentrations of inorganic and organic carbon, and total nitrogen and sulfur at Site 797.

Core, section, interval (cm)	Depth (mbsf)	Total carbon (%)	Inorganic carbon (%)	Organic carbon (%)	$CaCO_3$ (%)	Nitrogen (%)	Sulfur (%)	C_{org}/N	C_{org}/S
127-797B-									
1H-1, 33–35	0.33	0.57	0.04	0.53	0.3	0.07	0.19	7.6	2.80
1H-1, 131–134	1.31	1.90	0.32	1.58	2.7	0.12	2.57	13.1	0.62
1H-2, 99–101	2.49	2.26	0.38	1.88	3.2	0.14	0.73	13.4	2.57
1H-2, 140–145	2.90	0.66	0.15	0.51	1.2	0.06	0.19	8.5	2.70
1H-3, 0–3	3.00	1.50	0.17	1.33	1.4	0.11	0.31	12.1	4.29
1H-4, 76–82	5.26	3.51	0.17	3.34	1.4	0.28	1.42	11.9	2.35
2H-1, 71–77	6.61	5.25	0.50	4.75	4.2	0.37	4.69	12.8	1.01
2H-1, 77–83	6.67	0.86	0.27	0.59	2.2	0.03	0.42	19.0	1.40
2H-2, 100–102	8.40	0.59	0.24	0.35	2.0	0.02	0.15	17.0	2.30
2H-3, 111–113	10.01	0.45	0.15	0.30	1.2	0.03	1.31	10.0	0.23
2H-3, 115–117	10.05	2.66	0.18	2.47	1.5	0.16	0.92	15.4	2.68
2H-3, 118–120	10.08	0.51	0.15	0.36	1.2	0.02	0.15	18.0	2.40
2H-5, 0–5	11.90		0.13		1.1				
3H-2, 100–10	17.90	1.03	0.61	0.42	5.1	0.02	0.29	21.0	1.40
3H-4, 53–55	20.43	5.87	0.97	4.90	8.1	0.33	9.10	14.8	0.54
3H-4, 56–58	20.46	1.63	0.34	1.29	2.8	0.10	1.19	12.9	1.08
3H-4, 59–61	20.49	0.53	0.19	0.34	1.6	0.03	0.30	11.0	1.10
3H-4, 83–85	20.73	0.68	0.07	0.61	0.6	0.06	0.38	10.0	1.60
3H-4, 86–88	20.76	3.05	0.07	2.98	0.6	0.23	0.92	12.9	3.24
3H-4, 90–92	20.80	5.04	0.07	4.97	0.6	0.36	2.66	13.8	1.87
3H-4, 94–96	20.84	2.78	0.14	2.64	1.2	0.16	1.40	16.5	1.88
3H-4, 99–101	20.89	5.55	0.27	5.28	2.2	0.38	2.77	13.9	1.90
3H-4, 109–111	20.99	0.44	0.11	0.33	0.9	0.01	0.66	33.0	0.50
3H-4, 122–128	21.12	5.58	0.79	4.79	6.6	0.31	3.05	15.4	1.57
3H-4, 128–134	21.18	0.71	0.10	0.61	0.8	0.05	0.74	12.0	0.82
3H-6, 0–5	22.90		0.03		0.2				
4H-2, 8–14	26.48	1.43	0.08	1.35	0.7	0.11		12.3	
4H-2, 14–17	26.54	0.47	0.0	0.40	0.6	0.00			
4H-2, 17–20	26.57	1.75	0.39	1.36	3.2	0.08		17.0	
4H-2, 100–102	27.40	1.14	0.04	1.10	0.3	0.05		22.0	
4H-4, 126–128	30.66	6.19	2.72	3.47	22.7	0.17		20.4	
4H-5, 0–5	30.90		1.38		11.5				
4H-6, 86–88	33.26	1.41	0.13	1.28	1.1	0.06		21.3	
4H-6, 109–111	33.49	4.81	2.22	2.59	18.5	0.14		18.5	
4H-6, 131–133	33.71	4.14	2.24	1.90	18.7	0.07		27.1	
5H-2, 4–6	35.94	2.02	0.16	1.86	1.3	0.12		15.5	
5H-2, 8–14	35.98	4.75	1.88	2.87	15.7	0.20		14.3	
5H-2, 14–16	36.04	0.74	0.18	0.56	1.5	0.04		14.0	
5H-2, 100–102	36.90	1.43	0.05	1.38	0.4	0.05		27.6	
5H-2, 107–114	36.97	1.80	0.18	1.62	1.5	0.14		11.6	
5H-5, 0–5	40.40		0.18		1.5				
5H-6, 87–89	42.77	1.45	0.21	1.24	1.8	0.05		24.8	
6H-1, 10–12	44.00	0.63	0.17	0.46	1.4	0.06		7.6	
6H-1, 122–127	45.12	2.27	0.26	2.01	2.2	0.15		13.4	
6H-2, 100–102	46.40	1.47	0.33	1.14	2.7	0.10		11.4	
6H-5, 0–5	49.90		0.42		3.5				
7H-2, 100–101	55.90	7.56	0.13	7.43	1.1	0.30		24.7	
7H-5, 0–5	59.40		0.11		0.9				
8H-2, 100–101	65.40	0.52	0.19	0.33	1.6	0.05		6.6	
8H-5, 0–5	68.90		0.15		1.2				
8H-6, 133–135	71.73	9.22	6.92	2.30	57.6	0.11		20.9	
9H-1, 61–63	73.01	0.39	0.02	0.37	0.2	0.06		6.1	
9H-1, 80–86	73.20	4.70	0.96	3.74	8.0	0.29		12.9	
9H-1, 97–99	73.37	0.45	0.18	0.27	1.5	0.04		6.7	
9H-2, 100–101	74.90	1.32	0.93	0.39	7.7	0.03		13.0	
9H-5, 0–5	78.40		0.02		0.2				
10H-2, 99–101	84.39	0.67	0.06	0.61	0.5	0.08		7.6	
10H-5, 0–5	87.90		0.06		0.5				
10H-5, 128–130	89.18	0.59	0.17	0.42	1.4	0.06		7.0	
10H-5, 135–141	89.25	3.34	2.32	1.02	19.3	0.05		20.4	
11H-1, 130–136	92.70	0.64	0.08	0.56	0.7	0.06		9.3	
11H-2, 100–102	93.90	0.39	0.05	0.34	0.4	0.05		6.8	
11H-5, 0–5	97.40		0.09		0.7				
11H-7, 44–50	100.84	2.07	0.28	1.79	2.3	0.14		12.8	
11H-7, 51–56	100.91	2.16	0.27	1.89	2.2	0.16		11.8	
12H-2, 100–101	103.40	0.24	0.01	0.23	0.1	0.02		11.0	
12H-5, 0–3	106.90		0.83		6.9				
13H-2, 100–102	112.90	0.83	0.07	0.76	0.6	0.06		12.0	
13H-5, 0–3	116.40		0.09		0.7				
14H-2, 99–101	122.39	0.21	0.01	0.20	0.1	0.03		6.6	
14H-5, 0–3	125.90		0.04		0.3				
15H-2, 99–101	131.89	0.28	0.03	0.25	0.2	0.04		6.2	
15H-5, 0–3	135.40		0.05		0.4				
16H-2, 56–58	140.96		0.08		0.7				

Table 7 (continued).

Core, section, interval (cm)	Depth (mbsf)	Total carbon (%)	Inorganic carbon (%)	Organic carbon (%)	CaCO$_3$ (%)	Nitrogen (%)	Sulfur (%)	C$_{org}$/N	C$_{org}$/S
127-797B- (Cont.)									
16H-2, 99–101	141.39	0.93	0.12	0.81	1.0	0.07		11.0	
16H-5, 0–3	144.90		0.34		2.8				
17H-2, 20–22	150.10	0.66	0.05	0.61	0.4	0.05		12.0	
17H-5, 0–3	152.27		0.06		0.5				
18H-2, 99–100	160.39	0.56	0.03	0.53	0.2	0.04		13.0	
18H-3, 50–53	161.40	0.81	0.06	0.75	0.5	0.07		11.0	
18H-5, 0–3	163.90		1.70		14.2				
19H-2, 100–102	168.90	0.50	0.03	0.47	0.2	0.04		12.0	
19H-5, 0–3	172.40		0.03		0.2				
20X-4, 0–3	180.40	0.59	0.12	0.47	1.0	0.04		12.0	
20X-4, 99–100	181.39	1.07	0.66	0.41	5.5	0.05		8.2	
21X-1, 61–63	186.11	0.98	0.36	0.62	3.0	0.03		20.0	
21X-2, 100–101	188.00	0.49	0.03	0.46	0.2	0.05		9.2	
21X-5, 0–5	191.50	0.46	0.05	0.41	0.4	0.06		6.8	
22X-2, 99–100	197.69	0.27	0.04	0.23	0.3	0.04		5.7	
22X-3, 0–5	198.20	0.20	0.02	0.18	0.2	0.03		6.0	
23X-2, 100–101	207.30	0.53	0.04	0.49	0.3				
24X-2, 100–101	216.80	0.45	0.03	0.42	0.3				
24X-6, 0–3	221.80		0.02		0.2				
25X-2, 0–3	225.50		0.70		5.8				
25X-2, 100–101	226.50	0.38	0.02	0.36	0.2	0.04		9.0	
26X-2, 100–102	236.20	0.53	0.02	0.51	0.2	0.05		10.0	
26X-2, 120–126	236.40	0.86	0.05	0.81	0.4	0.08	0.69	10.0	1.20
26X-3, 127–129	237.97	1.89	0.04	1.85	0.3				
26X-4, 95–97	239.15	0.64	0.03	0.61	0.2				
26X-5, 0–3	239.70		0.06		0.5				
26X-7, 10–12	242.80		0.04		0.3				
27X-2, 100–102	245.90	1.79	0.12	1.67	1.0	0.13		12.80	
27X-3, 14–20	246.54	2.67	0.20	2.47	1.7	0.19	3.39	13.0	0.73
27X-3, 22–24	246.62	1.57	0.59	0.98	4.9	0.08		12.0	
27X-6, 73–75	251.63		0.22		1.8				
27X-6, 76–78	251.66	2.05	0.06	1.99	0.5	0.14		14.2	
27X-6, 79–81	251.69	1.85	0.72	1.13	6.0	0.08		14.1	
27X-6, 147–150	252.37		0.03		0.2				
28X-1, 147–150	254.57		0.04		0.3				
28X-2, 100–102	255.60	1.61	0.04	1.57	0.3	0.09		17.4	
28X-3, 89–91	256.99		0.02		0.2				
28X-4, 15–17	257.75	3.45	2.19	1.26	18.2	0.09	0.99	14.0	1.27
30X-2, 114–116	275.14	2.62	0.40	2.22	3.3	0.15		14.8	
30X-2, 117–119	275.17	1.79	0.18	1.61	1.5	0.11		14.6	
30X-2, 147–149	275.47	1.46	1.06	0.40	8.8				
31X-2, 12–18	283.82	2.86	0.07	2.79	0.6				
31X-5, 0–3	288.20	2.14	0.06	2.08	0.5				
31X-5, 18–20	288.38		0.05		0.4				
31X-7, 34–36	291.54	7.61	0.07	7.54	0.6	0.51	1.90	14.8	3.97
32X-5, 0–3	297.90		0.07		0.6				
32X-5, 20–23	298.10		0.07		0.6				
33X-3, 0–3	304.50		0.04		0.3				
34X-2, 115–117	313.85		0.06		0.5				
34X-5, 0–3	317.20		0.07		0.6				
34X-5, 16–18	317.36		0.05		0.4				
34X-5, 70–72	317.90	4.14	0.04	4.10	0.3	0.31	1.65	13.2	2.48
34X-5, 116–118	318.36	8.60	0.07	8.53	0.6	0.59	2.52	14.4	3.38
35X-2, 73–75	323.13		0.09		0.7				
35X-4, 147–150	326.87		0.09		0.7				
36X-CC, 0–3	330.60		0.11		0.9				
37X-2, 69–71	342.49		0.10		0.8				
37X-4, 147–150	346.27		0.13		1.1				
38X-1, 91–93	350.91	1.16	0.04	1.12	0.3	0.11	1.04	10.2	1.07
40X-2, 0–3	369.96	1.00	0.26	0.74	2.2	0.09	1.09	8.2	0.68
41X-1, 116–118	380.16	1.88	0.30	1.58	2.5				
42X-1, 0–3	387.90		0.14		1.2				
42X-1, 16–18	388.06	1.16	0.12	1.04	1.0	0.10	1.37	10.4	0.76
44X-1, 0–3	407.30	0.62	0.02	0.60	0.2	0.04	0.53	15.0	1.10
46X-1, 0–3	426.60	2.48	0.02	2.46	0.2	0.15	1.45	16.4	1.69
46X-1, 97–99	427.57	0.50	0.01	0.49	0.1				
46X-1, 140–142	428.00		0.02		0.2				
47X-2, 62–64	438.32		0.06		0.5				
47X-3, 0–3	439.20		0.06		0.5				
48X-2, 98–100	448.38		0.09		0.7				
48X-5, 0–3	451.90	0.95	0.01	0.94	0.1	0.06	1.17	15.0	0.80
49X-2, 100–102	458.00		0.02		0.2				
50X-CC, 7–9	465.85	10.01	83.4						
51X-1, 111–113	476.01	0.84	0.05	0.79	0.4				
51X-1, 139–141	476.29	4.45	0.05	4.40	0.4				

Table 7 (continued).

Core, section, interval (cm)	Depth (mbsf)	Total carbon (%)	Inorganic carbon (%)	Organic carbon (%)	CaCO$_3$ (%)	Nitrogen (%)	Sulfur (%)	C$_{org}$/N	C$_{org}$/S
127-797B- (Cont.)									
51X-2, 99–101	477.39		0.09		0.7				
51X-4, 147–150	480.87	1.46	0.27	1.19	2.2	0.08	1.16	14.9	1.02
52X-2, 112–114	487.12		0.80		6.7				
52X-4, 0–3	489.00		0.30		2.5				
53X-CC, 8–10	494.42		0.39		3.2				
127-797C-									
2R-2, 0–3	495.00	0.99	0.24	0.75	2.0	0.05	1.39	15.0	0.54
3R-2, 0–3	504.50	0.72	0.03	0.69	0.2	0.05	1.49	14.0	0.46
5R-2, 147–150	524.97		0.20		1.7				
11R-1, 0–3	579.50	1.09	0.15	0.94	1.3				
22R-2, 140–150	687.94	0.56	0.04	0.52	0.3				
22R-3, 0–3	688.04		0.10		0.8				
22R-3, 113–115	689.17	0.79	0.03	0.76	0.3				
23R-3, 0–3	697.60		0.05		0.4				
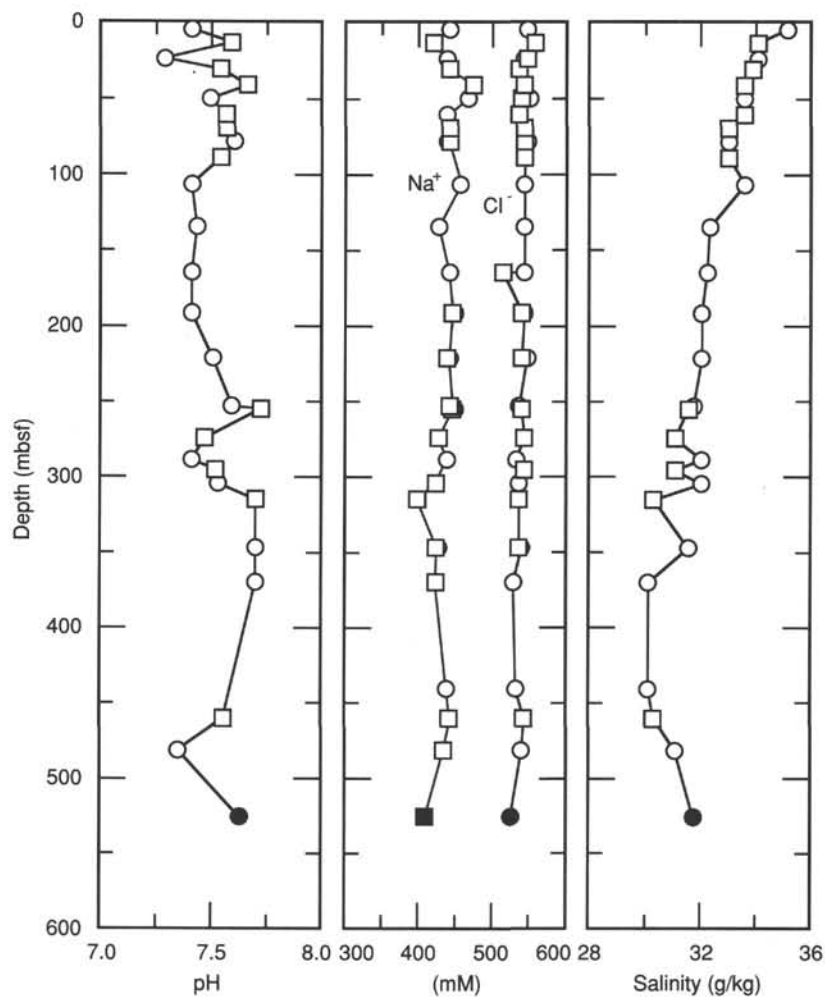
Figure 37. pH, sodium, chlorine, and salinity profiles with depth, Holes 797B and 797C. Symbols as in Figure 33.
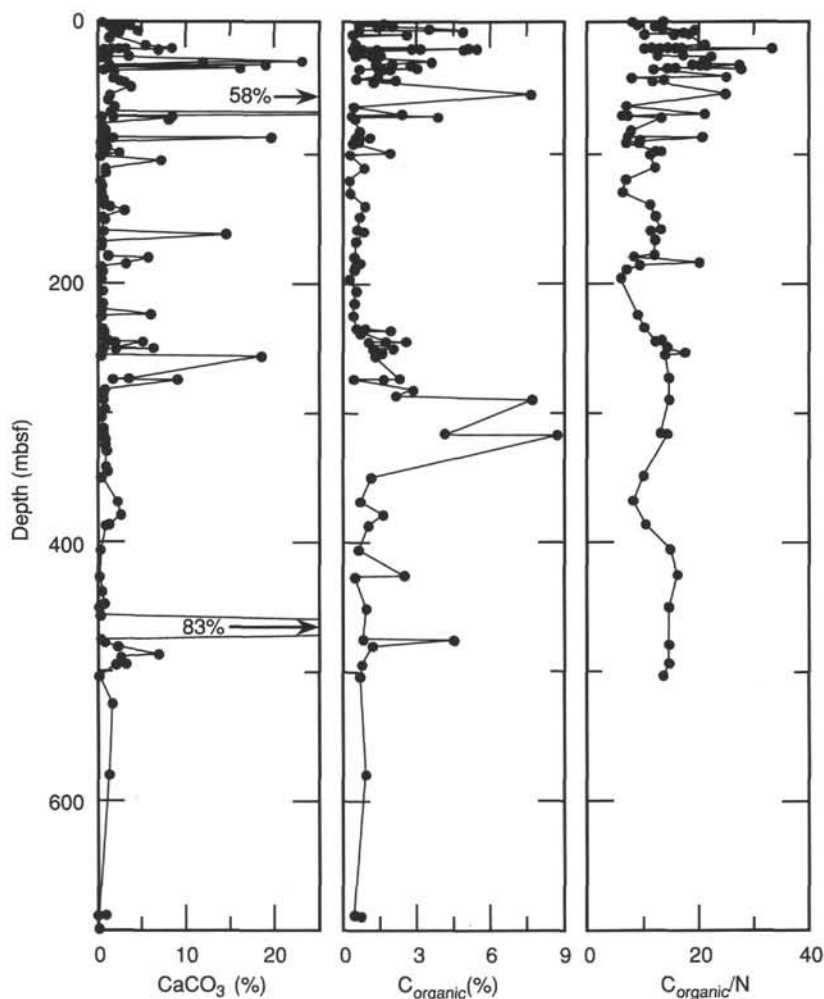
Figure 38. Downhole distributions of calcium carbonate and organic carbon concentrations as percentages of whole dry sediments and ratio of organic carbon to total nitrogen in sediments at Site 797.

grained relative to the interior of the unit, suggesting that they are chilled margins. A few fractures, filled with clay and carbonate minerals, are observed throughout the unit. The interior of the unit is composed dominantly of massive, sparsely plagioclase phyric dolerite. Plagioclase phenocrysts (about 1%), which sporadically formed glomeroporphyritic clusters with olivine, are scattered in a medium-grained, subophitic to intergranular groundmass. The groundmass consists of plagioclase, clinopyroxene, olivine, and magnetite. The rock is slightly to moderately altered, with the olivine partially replaced by clay minerals and the plagioclase slightly sericitized.

Unit 10. Aphyric basalt (Section 127-797C-26R-1, Piece 3 to Section 127-797C-26R-1, Piece 19; 723.4 to 724.7 mbsf)

This unit is bounded by sedimentary rocks at both the top and bottom. The unit is mostly massive except for the upper part, which contains common fractures filled with carbonate minerals and pyrite. The uppermost and lowermost parts of the unit are finer grained relative to the interior and show a spherulitic texture indicating a chilled margin. This unit is dominantly composed of very highly altered microcrystalline aphyric basalt in which the mafic silicate minerals and the mesostasis are totally replaced by clay minerals, and plagioclase is highly altered to clay minerals. The basalt contains less than 2% vesicles, which are filled with clay minerals and pyrite.

Unit 11. Aphyric Basalt (Section 127-797C-26R-2, Piece 6 to Section 127-797C-27R-1, Piece 7; 725.3 mbsf to 734 mbsf)

The top of the unit is bounded by overlying sedimentary rock and the base is defined by the chilled margin at the top of Unit 12. The uppermost and lowermost parts of the unit show a reduction in grain size relative to the interior and probably represent chilled margins. Only a few fractures occur throughout the unit and these are filled with clay, carbonate minerals, and pyrite. This unit is composed predominantly of massive, fine-grained aphyric basalt with trace amounts (<1%) of plagioclase phenocrysts set in an interstitial groundmass. A small amount of vesicles (<1%) is present throughout the unit. The rock is highly altered with mafic silicates and the mesostasis totally replaced by clay minerals. Plagioclase is highly to totally altered to clay minerals. The uppermost chilled margin is characterized by a high vesicularity (up to about 15%).

Unit 12. Aphyric basalt (Section 127-797C-27R-1, Piece 8 to Section 127-797C-30R-1, Piece 7; 734 to 755.1 mbsf)

The top and base of the unit are defined by the presence of chilled margins. Sedimentary rock underlies the unit, which is composed of massive aphyric basalt with only a few fractures. These fractures are filled with clay minerals and pyrite. Scattered plagioclase phenocrysts (<1%) occur in a fine-grained,

Table 8. Results of Rock-Eval analysis for Site 797.

Core, section, interval (cm)	Depth (mbsf)	S_1 (mg/g)	S_2 (mg/g)	S_3 (mg/g)	TOC (%)	PC	HI	OI	T_{max} (°C)	PI	S_2/S_3
127-797B-											
1H-1, 33–5	0.33	0.22	4.55	9.66	0.54	0.39	842	1788	549	0.05	0.47
1H-1, 131–134	1.31	0.69	3.28	3.48	1.39	0.33	235	250	379	0.17	0.94
1H-2, 99–101	2.49	0.64	2.91	5.57	1.63	0.29	178	341	380	0.18	0.52
1H-2, 140–145	2.90	0.08	0.78	0.98	0.40	0.07	195	245	484	0.09	0.79
1H-3, 0–3	3.00	0.51	2.99	2.78	1.19	0.29	251	233	518	0.15	1.07
1H-4, 76–82	5.26	1.13	6.96	12.70	3.20	0.67	217	396	398	0.14	0.54
2H-1, 71–77	6.61	2.79	10.31	18.14	4.15	1.09	248	437	396	0.21	0.56
2H-1, 77–83	6.67	0.30	2.76	1.33	0.61	0.25	452	218	590	0.10	2.07
2H-2, 100–102	8.40	0.06	3.09	4.37	0.51	0.26	605	856	578	0.02	0.70
2H-3, 111–113	10.01	0.07	2.11	0.00	0.37	0.18	570	0	588	0.03	
2H-3, 115–117	10.05	0.42	3.56	9.67	2.09	0.33	170	462	415	0.11	0.36
2H-3, 118–120	10.08	0.01	1.89	0.11	0.44	0.15	429	25	590	0.01	17.18
2H-5, 0–5	11.90	1.05	9.24	13.05	3.63	0.85	254	359	404	0.10	0.70
3H-2, 100–101	17.90	0.12	1.71	3.15	0.29	0.15	589	1086	589	0.07	0.54
3H-4, 53–5	20.43	1.38	10.52	17.84	4.08	0.99	257	437	413	0.12	0.58
3H-4, 56–58	20.46	0.39	2.48	4.24	1.18	0.23	210	359	404	0.14	0.58
3H-4, 59–61	20.49	0.06	2.89	0.00	0.46	0.24	628	0	590	0.02	
3H-4, 83–85	20.73	0.17	3.52	0.83	0.70	0.30	502	118	587	0.05	4.24
3H-4, 86–88	20.76	0.84	7.33	10.93	2.89	0.68	253	378	404	0.10	0.67
3H-4, 90–92	20.80	1.11	11.56	18.48	4.56	1.05	253	405	414	0.09	0.62
3H-4, 94–96	20.84	0.65	6.08	8.81	2.53	0.56	240	348	405	0.10	0.69
3H-4, 99–101	20.89	1.40	11.21	21.44	4.84	1.05	231	442	407	0.11	0.52
3H-4, 109–111	20.99	0.06	2.21	0.11	0.44	0.18	502	25	557	0.03	20.09
3H-4, 122–128	21.12	1.39	8.54	22.40	4.11	0.82	207	545	408	0.14	0.38
3H-4, 128–134	21.18	0.10	2.55	0.96	0.62	0.22	411	154	581	0.04	2.65
3H-6, 0–5	22.90	0.01	1.95	0.11	0.45	0.16	433	24	583	0.01	17.72
4H-2, 8–14	26.48	0.32	4.58	1.29	1.36	0.40	336	94	404	0.07	3.55
4H-2, 14–17	26.54	0.64	4.99	0.36	0.74	0.46	674	48	388	0.11	13.86
4H-2, 17–20	26.57	0.39	2.71	3.72	1.10	0.25	246	338	522	0.13	0.72
4H-2, 100–101	27.40	0.45	3.96	0.71	1.09	0.36	363	65	401	0.10	5.57
4H-4, 126–128	30.66	0.76	5.54	8.68	2.34	0.52	236	370	412	0.12	0.63
4H-5, 0–5	30.90	0.06	0.19	3.84	0.26	0.02	73	1476	373	0.25	0.04
4H-6, 86–88	33.26	0.30	3.25	0.60	1.16	0.29	280	51	408	0.08	5.41
4H-6, 109–111	33.49	0.57	4.19	4.42	2.42	0.39	173	182	419	0.12	0.94
4H-6, 131–133	33.71	0.19	1.36	2.49	1.31	0.12	103	190	413	0.12	0.54
5H-2, 4–6	35.94	0.33	4.38	2.18	1.87	0.39	234	116	413	0.07	2.00
5H-5, 0–5	40.40	0.16	2.90	1.57	1.01	0.25	287	155	588	0.05	1.84
5H-5, 8–14	40.48	0.46	3.64	11.04	2.61	0.34	139	422	421	0.11	0.32
5H-5, 14–16	40.54	0.03	1.16	1.60	0.55	0.09	210	290	591	0.03	0.72
5H-5, 87–89	41.27	0.11	1.63	0.47	0.81	0.14	201	58	417	0.06	3.46
5H-5, 100–101	41.40	0.21	1.49	1.74	0.79	0.14	188	220	549	0.12	0.85
5H-5, 107–114	41.47	0.29	3.77	1.88	1.54	0.33	244	122	413	0.07	2.00
6H-1, 10–12	44.00	0.01	1.22	0.27	0.45	0.10	271	60	542	0.01	4.51
6H-1, 122–127	45.12	0.44	4.38	1.88	1.75	0.40	250	107	404	0.09	2.32
6H-2, 100–102	46.40	0.22	2.36	1.72	1.07	0.21	220	160	410	0.09	1.37
6H-5, 0–5	49.90	0.35	4.02	9.14	2.07	0.36	194	441	420	0.08	0.43
7H-2, 0–5	54.90	0.94	40.34	8.08	7.03	3.44	573	114	431	0.02	4.99
7H-5, 100–101	60.40	0.14	3.12	0.20	0.72	0.27	433	27	586	0.04	15.60
8H-2, 100–101	65.40	0.07	1.57	0.43	0.49	0.13	320	87	584	0.04	3.65
8H-5, 0–5	68.90	0.11	2.78	1.24	0.63	0.24	441	196	569	0.04	2.24
8H-6, 133–135	71.73	0.18	2.33	6.93	1.89	0.20	123	366	427	0.07	0.33
9H-1, 61–63	73.01	0.10	3.46	0.00	0.53	0.29	652	0	531	0.03	
9H-1, 80–86	73.20	0.49	5.87	12.50	3.16	0.53	185	395	425	0.08	0.46
9H-1, 97–99	73.37	0.02	1.86	0.38	0.35	0.15	531	108	587	0.01	4.89
9H-2, 100–101	74.90	0.04	0.46	2.05	0.20	0.04	230	1025	499	0.08	0.22
9H-5, 0–5	78.40	0.15	2.79	0.14	0.68	0.24	410	20	581	0.05	19.92
10H-2, 99–101	84.39	0.15	3.10	0.17	0.85	0.27	364	20	588	0.05	18.23
10H-5, 0–5	87.90	0.01	1.46	1.82	0.39	0.12	374	466	583	0.01	0.80
10H-5, 128–130	89.18	0.06	0.48	7.14	0.55	0.04	87	1298	484	0.11	0.06
10H-5, 135–141	89.25	0.48	18.82	1.00	2.39	1.60	787	41	433	0.02	18.82
11H-1, 130–136	92.70	0.10	2.35	0.01	0.50	0.20	470	2	584	0.04	
11H-2, 100–102	93.90	0.03	1.66	0.42	0.35	0.14	474	120	575	0.02	3.95
11H-5, 0–5	97.40	0.00	0.23	0.01	0.02	0.01	1150	50	574	0.00	23.00
11H-7, 44–50	100.84	0.14	2.72	10.85	1.86	0.23	146	583	414	0.05	0.25
11H-7, 51–56	100.91	0.19	2.70	10.98	1.78	0.24	151	616	408	0.07	0.24
12H-2, 100–101	103.40	0.34	2.74	0.24	0.49	0.25	559	48	404	0.11	11.41
12H-5, 0–3	106.90	0.16	2.03	17.03	1.11	0.18	182	1534	529	0.07	0.11
13H-2, 100–102	112.90	0.29	2.67	0.16	0.89	0.24	300	17	530	0.10	16.68
13H-5, 0–3	116.40	0.32	2.75	2.06	1.06	0.25	259	194	582	0.10	1.33
14H-2, 99–101	122.39	0.21	2.86	0.20	0.42	0.25	680	47	557	0.07	14.30
14H-5, 0–3	125.90	0.13	3.30	0.00	0.60	0.28	550	0	513	0.04	
15H-2, 99–101	131.89	0.33	2.55	0.00	0.39	0.24	653	0	551	0.11	
15H-5, 0–3	135.40	0.08	2.16	0.56	0.66	0.18	327	84	578	0.04	3.85
16H-2, 56–58	140.96	0.15	2.52	2.12	0.65	0.22	387	326	583	0.06	1.18
16H-2, 99–101	141.39	0.20	2.69	3.06	0.84	0.24	320	364	581	0.07	0.87

Table 8 (continued).

Core, section, interval (cm)	Depth (mbsf)	S_1 (mg/g)	S_2 (mg/g)	S_3 (mg/g)	TOC (%)	PC	HI	OI	T_{max} (°C)	PI	S_2/S_3
127-797B- (Cont.)											
16H-5, 0–3	144.90	0.17	1.72	6.07	0.70	0.15	245	867	586	0.09	0.28
17H-2, 20–22	150.10	0.13	3.25	0.00	0.79	0.28	411	0	566	0.04	
17H-5, 0–3	152.27	0.14	2.32	0.10	0.53	0.20	437	18	575	0.06	23.20
18H-2, 99–101	160.39	0.27	2.33	0.33	0.69	0.21	337	47	558	0.10	7.06
18H-3, 50–53	161.40	0.28	2.36	2.80	0.86	0.22	274	325	572	0.11	0.84
18H-5, 0–3	163.90	0.04	0.61	20.66	0.27	0.05	225	7651	492	0.06	0.02
19H-2, 100–102	168.90	0.09	2.48	0.04	0.62	0.21	400	6	563	0.04	62.00
19H-5, 0–3	172.40	0.26	1.92	0.16	0.35	0.18	548	45	541	0.12	12.00
20X-4, 0–3	180.40	0.27	1.90	3.62	0.47	0.18	404	770	574	0.12	0.52
20X-4, 99–100	181.39	0.12	1.37	9.89	0.38	0.12	360	2602	585	0.08	0.13
21X-1, 61–63	186.11	0.07	1.46	8.85	0.56	0.12	260	1580	588	0.05	0.16
21X-2, 100–101	188.00	0.16	2.67	0.13	0.45	0.23	593	28	554	0.06	20.53
21X-5, 0–5	191.50	0.15	2.24	0.85	0.40	0.19	560	212	585	0.06	2.63
22X-2, 99–100	197.69	0.77	2.80	0.03	0.41	0.29	682	7	576	0.22	93.33
22X-3, 0–5	198.20	0.54	2.92	0.00	0.38	0.28	768	0	572	0.16	
23X-2, 100–101	207.30	0.07	3.00	0.00	0.47	0.25	638	0	573	0.02	
24X-2, 100–101	216.80	0.08	2.55	0.01	0.44	0.21	579	2	490	0.03	
24X-6, 0–5	221.80	0.31	2.51	0.00	3.88	0.23	64	0	573	0.11	
25X-2, 0–3	225.50	0.56	2.04	2.06	0.37	0.21	551	556	464	0.22	0.99
25X-2, 100–101	226.50	0.14	2.10	0.14	0.45	0.18	466	31	578	0.06	15.00
26X-2, 100–102	236.20	0.34	2.55	0.07	0.59	0.24	432	11	582	0.12	36.42
26X-2, 120–126	236.40	0.18	2.90	0.00	0.96	0.25	302	0	483	0.06	
26X-3, 127–129	237.97	0.14	2.30	0.74	0.60	0.20	383	123	562	0.06	3.10
26X-4, 95–97	239.15	0.78	3.12	0.00	0.71	0.32	439	0	575	0.20	
26X-5, 0–3	239.70	0.51	2.29	0.00	0.45	0.23	508	0	579	0.18	
27X-2, 100–102	245.90	0.21	3.80	3.39	1.57	0.33	242	215	402	0.05	1.12
27X-3, 14–20	246.54	0.29	5.01	8.09	2.24	0.44	223	361	412	0.05	0.61
27X-3, 22–24	246.62	0.11	1.70	9.82	0.89	0.15	191	1103	474	0.06	0.17
27X-6, 73–75	251.63	0.14	2.16	3.90	1.04	0.19	207	375	408	0.06	0.55
27X-6, 76–78	251.66	0.23	5.26	2.80	2.05	0.45	256	136	415	0.04	1.87
27X-6, 79–81	251.69	0.15	2.27	7.24	1.09	0.20	208	664	404	0.06	0.31
27X-6, 147–150	252.37	0.12	2.73	0.08	1.07	0.23	255	7	399	0.04	34.12
27X-7, 10–12	252.50	0.22	4.23	2.35	1.64	0.37	257	143	409	0.05	1.80
28X-1, 147–150	254.57	0.15	3.21	0.98	1.37	0.28	234	71	406	0.04	3.27
28X-2, 100–102	255.60	0.36	4.85	1.46	1.69	0.43	286	86	407	0.07	3.32
28X-3, 89–91	256.99	0.14	3.36	0.00	0.77	0.29	436	0	522	0.04	
28X-4, 15–17	257.75	0.14	1.55	21.28	0.99	0.14	156	2149	418	0.08	0.07
30X-2, 114–116	275.14	0.22	5.12	5.58	2.06	0.44	248	270	418	0.04	0.91
30X-2, 117–119	275.17	0.42	4.23	3.99	1.62	0.38	261	246	405	0.09	1.06
30X-2, 147–149	275.47	0.00	0.85	0.98	0.52	0.07	163	188	420	0.00	0.86
31X-2, 12–18	283.82	0.28	5.32	0.85	1.90	0.46	280	44	411	0.05	6.25
31X-5, 0–3	288.20	0.18	4.72	1.90	1.85	0.40	255	102	411	0.04	2.48
31X-5, 18–20	288.38	0.28	5.87	3.96	2.14	0.51	274	185	412	0.05	1.48
31X-7, 34–36	291.54	0.88	26.09	14.06	6.72	2.24	388	209	416	0.03	1.85
32X-5, 0–3	297.90	0.63	13.54	7.47	4.11	1.18	329	181	412	0.04	1.81
32X-5, 20–23	298.10	0.00	0.05	0.00	0.01	0.00	500	0	451	0.00	
33X-3, 0–3	304.50	0.04	2.17	0.09	1.19	0.18	182	7	425	0.02	24.11
34X-5, 0–3	317.20	0.08	3.45	0.98	1.84	0.29	187	53	429	0.02	3.52
34X-5, 16–18	317.36	0.12	4.81	0.91	2.00	0.41	240	45	428	0.02	5.28
34X-5, 70–72	317.90	0.31	10.46	4.06	3.79	0.89	275	107	423	0.03	2.57
34X-5, 116–118	318.36	0.91	33.78	11.60	8.35	2.89	404	138	417	0.03	2.91
35X-4, 147–150	326.87	0.03	2.08	0.07	1.00	0.17	208	7	497	0.01	29.71
36X-C, 0–3	330.60	0.08	2.80	0.26	1.35	0.24	207	19	431	0.03	10.76
37X-4, 147–150	346.27	0.09	3.57	1.95	1.52	0.30	234	128	431	0.02	1.83
38X-1, 91–93	350.91	0.07	2.06	0.00	0.95	0.17	216	0	423	0.03	
40X-2, 0–3	369.96	0.08	1.39	0.15	0.69	0.12	201	21	443	0.05	9.26
41X-1, 116–118	380.16	0.03	1.05	0.59	0.54	0.09	194	109	594	0.03	1.77
42X-1, 0–3	387.90	0.09	1.46	0.33	0.77	0.12	189	42	410	0.06	4.42
42X-1, 16–18	388.06	0.05	1.57	0.42	0.90	0.13	174	46	409	0.03	3.73
44X-1, 0–3	407.30	0.05	1.19	0.00	0.55	0.10	216	0	408	0.04	
46X-1, 0–3	426.60	0.15	6.14	0.00	2.22	0.52	276	0	415	0.02	
46X-1, 97–99	427.57	0.00	0.50	0.00	0.32	0.04	156	0	458	0.00	
47X-3, 0–3	439.20	0.21	5.38	0.39	1.75	0.46	307	22	415	0.04	13.79
48X-5, 0–3	451.90	0.06	3.08	0.00	0.87	0.26	354	0	427	0.02	
51X-1, 111–113	476.01	0.00	1.57	0.00	0.28	0.13	560	0	557	0.00	
51X-1, 139–141	476.29	0.12	4.31	0.00	1.44	0.36	299	0	425	0.03	
51X-4, 147–150	480.87	0.04	2.71	0.10	1.02	0.22	265	9	424	0.01	27.10
52X-4, 0–3	489.00	0.08	8.63	1.66	2.58	0.72	334	64	434	0.01	5.19
127-797C-											
2R-2, 0–3	495.00	0.00	1.58	0.00	0.69	0.13	228	0	420	0.00	
3R-2, 0–3	504.50	0.00	2.02	0.00	0.68	0.16	297	0	421	0.00	
5R-2, 147–150	524.97	0.00	1.12	0.00	0.40	0.09	280	0	431	0.00	
11R-1, 0–3	579.50	0.00	1.06	1.19	0.63	0.08	168	188	596	0.00	0.89

Table 8 (continued).

Core, section, interval (cm)	Depth (mbsf)	S_1 (mg/g)	S_2 (mg/g)	S_3 (mg/g)	TOC (%)	PC	HI	OI	T_{max} (°C)	PI	S_2/S_3
127-797C- (Cont.)											
18R-1, 94–96	647.44	0.05	1.25	0.00	0.76	0.10	164	0	509	0.04	
18R-1, 137–139	647.87	0.05	0.46	0.00	0.62	0.04	74	0	442	0.10	
22R-2, 140–150	687.94	0.00	0.76	0.00	0.39	0.06	194	0	495	0.00	
22R-3, 0–3	688.04	0.00	0.38	0.00	0.48	0.03	79	0	550	0.00	
22R-3, 113–115	689.17	0.01	0.00	0.00	0.53	0.00	0	0	436		
23R-3, 0–3	697.60	0.00	1.17	0.00	0.63	0.09	185	0	522	0.00	
30R-4, 0–3	758.03	0.00	0.62	0.00	0.35	0.05	177	0	543	0.00	

Note: TOC = total organic carbon; PC = petroleum potential; HI = hydrogen index; OI = oxygen index; PI = productivity index.
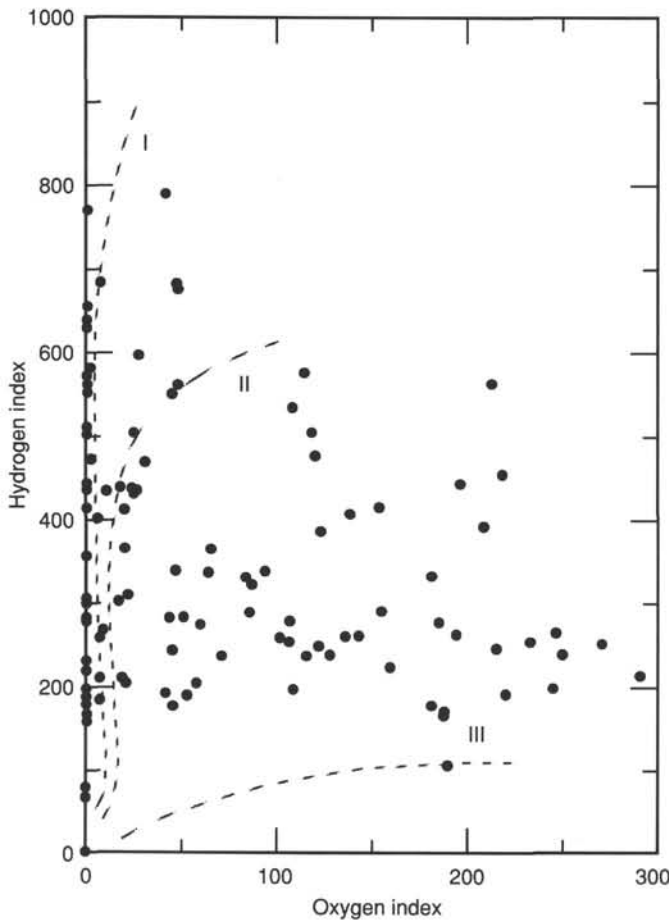
Figure 39. van Krevelen-type diagram of the hydrogen (HI) versus oxygen (OI) indices of sediments from Site 797.

sparsely vesicular, interstitial groundmass consisting of plagioclase, clinopyroxene, olivine, magnetite, and mesostasis. The rock is highly altered, with the olivine and the mesostasis totally altered to clay minerals, and the plagioclase and the clinopyroxene partially altered to clay. The chilled margin at the top of the unit is also highly altered and has a microcrystalline to cryptocrystalline groundmass with a spherulitic texture that indicates rapid cooling.

Unit 13. Aphyric basalt (Section 127-797C-30R-4, Piece 2 to Section 127-797C-31R-3, Piece 2c; 759.8 to 766.9 mbsf)

The unit is bounded by sedimentary rocks at the top and base. The uppermost and lowermost parts of the unit show a re-

Table 9. Hydrocarbon gas data for Site 797.

Core, section, interval (cm)	Depth (mbsf)	C_1 (ppm)	C_2 (ppm)	C_3 (ppm)	C_1/C_2
127-797B-					
1H-3, 0–3	3.00	57			
2H-5, 0–5	11.90	25			
3H-6, 0–5	22.90	200	1		200.00
4H-5, 0–5	30.90	7			
5H-5, 0–5	40.40	5			
6H-5, 0–5	49.90	6			
7H-5, 0–5	59.40	12			
8H-5, 0–5	68.90	5			
9H-5, 0–5	78.40	5			
10H-5, 0–5	87.90	20			
11H-5, 0–5	97.40	7			
12H-5, 0–3	106.90	9			
13H-5, 0–3	116.40	10			
14H-5, 0–3	125.90	13			
15H-5, 0–3	135.40	9			
16H-5, 0–3	144.90	5			
17H-5, 0–3	152.27	5			
18H-5, 0–3	163.90	5			
19H-5, 0–3	172.40	5			
20X-4, 0–3	180.40	5			
21X-5, 0–5	191.50	7			
22X-3, 0–5	198.20	5			
24X-6, 0–3	221.80	3			
25X-2, 0–3	225.50	12			
26X-5, 0–3	239.70	20			
27X-6, 147–150	252.37	9			
28X-1, 147–150	254.57	12	1		12.00
31X-5, 0–3	288.20	15	1		15.00
32X-5, 0–3	297.90	13	1		13.00
33X-3, 0–3	304.50	25	1		25.00
34X-5, 0–3	317.20	13			
35X-4, 147–150	326.87	13			
36X-CC, 0–3	330.60	12			
37X-4, 147–150	346.27	39	1		39.00
38X-1, 0–3	350.00	7	1	1	7.00
40X-2, 0–3	369.96	23	1		23.00
42X-1, 0–3	387.90	6			
44X-1, 0–3	407.30	11			
44X-CC, 0–3	407.89	27	7		3.86
46X-1, 0–3	426.60	7	1		7.00
47X-3, 0–3	439.20	10			
49X-6, 0–3	463.00	7	1		7.00
51X-4, 147–150	480.87	4			
52X-4, 0–3	489.00	8	1		8.00
127-797C-					
3R-2, 0–3	504.50	7			
5R-2, 147–150	524.97	5			
11R-1, 0–3	579.50	7			
22R-3, 0–3	688.04	11			
23R-3, 0–3	697.60	7			
30R-4, 0–3	757.78	17			
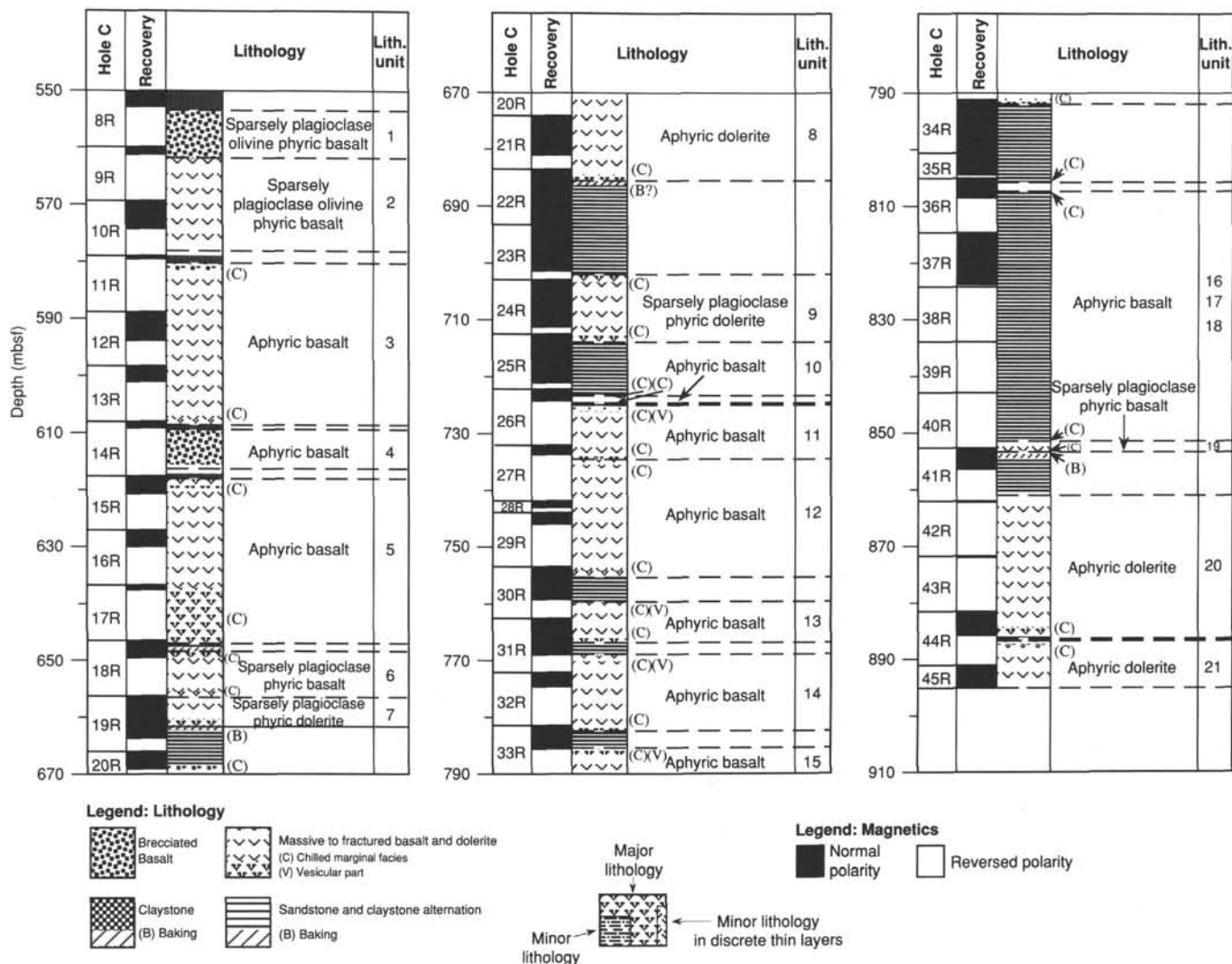
Figure 40. Graphic presentation of the basement lithology and core recovery from Hole 797C. Uncertain unit boundaries are denoted by dashed lines and are highly schematic. Thicknesses of the intervening sedimentary units are likely underestimated, owing to the relatively poor recovery of sediments in cores with igneous rocks.

duction in grain size relative to the interior, suggesting the presence of chilled margins. This unit is dominated by massive aphyric basalt. The few fractures that occur are filled with clay minerals, pyrite, silica, and zeolite(?). The interior of the unit is composed of fine- to medium-grained aphyric basalt with a subophitic to intergranular texture developed by plagioclase, clinopyroxene, magnetite, and mesostasis. Trace amounts (<1%) of plagioclase phenocrysts and a small amount of vesicles (a few percent) are scattered throughout the unit interior. The rock is highly altered, with the mesostasis totally replaced and plagioclase and clinopyroxene partially replaced by clay minerals. The uppermost part of the unit is characterized by more abundant and larger vesicles as compared to the interior of the unit.

Unit 14. Aphyric basalt (Section 127-797C-31R-5, Piece 1, to Section 127-797C-33R-1, Piece 3; 769.1 to 782.5 mbsf)

The unit is bounded by sedimentary rocks at the top and the base. The uppermost and lowermost parts of the unit are finer grained than the interior, suggesting that they are chilled borders. The unit is composed of massive aphyric basalt with a fine-grained, interstitial texture developed by plagioclase, clinopyroxene, olivine, magnetite, and mesostasis. The rock is highly altered, with the olivine and mesostasis totally altered to clay

minerals and the plagioclase and clinopyroxene slightly to moderately altered to clay minerals. The uppermost part of the unit is highly vesicular with some vesicles filled with clay minerals.

Unit 15. Aphyric basalt (Section 127-797C-33R-3, Piece 1 to Section 127-797C-34R-1, Piece 4; 785.3 to 791.8 mbsf)

This unit is bounded by sedimentary rocks at its top and base. The uppermost and lowermost parts of the unit show a reduction in grain size relative to the unit interior, suggesting the presence of chilled margins. The interior of the unit is composed of massive, fine-grained aphyric basalt with an interstitial texture. The rock is highly altered with the mesostasis and mafic silicates totally replaced and the plagioclase highly replaced by clay minerals. The uppermost and lowermost chilled margins are very highly altered and bleached. A microcrystalline, spherulitic texture, and abundant vesicles (to 10%) filled with carbonate and clay minerals, characterize these margins.

Unit 16. Aphyric basalt (Section 127-797C-36R-1, 78 cm, to Section 127-797C-36R-2, Piece 2; 805.6 to 806.5 mbsf)

The unit is bounded by sedimentary rock and a chilled margin at the top. The bottom of the unit is defined by a chilled contact against Unit 17 in Section 127-797C-36R-2, Piece 2. The

cm
78

79

80

81

82

83

84

85

86
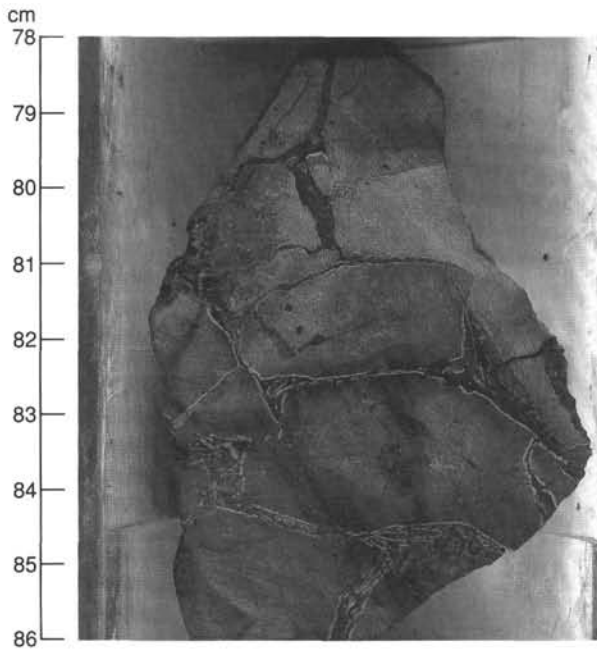
Figure 41. Brecciated basalt of Unit 4. Section 127-797C-14R-1, 78–86 cm.

interior of the unit is composed of massive, fine-grained aphyric basalt with trace amounts (<1%) of vesicles filled with clay and carbonate minerals. The rock is highly to moderately altered and contains sparse fractures filled with clay and carbonate minerals. The chilled marginal facies is cryptocrystalline aphyric basalt and is highly altered and bleached. The top chilled marginal facies is characterized by a higher vesicularity than the interior of the unit.

Unit 17. Aphyric basalt (Section 127-797C-36R-2, Piece 2 to Section 127-797C-36R-3, 10 cm; 806.5 to 806.9 mbsf)

The top of the unit is bounded by the chilled margin of Unit 16. The base of the unit is bounded by the chilled margin of Unit 18. The bulk of the unit is massive, fine-grained, aphyric basalt. The rock is moderately to highly altered.

Unit 18. Aphyric basalt (Section 127-797C-36R-3, 10 cm, to Section 127-797C-37R-1, 35 cm; 806.9 to 807.1 mbsf)

The top of the unit is defined by a chilled contact against the overlying unit. The bottom of the unit is defined by sedimentary rocks. The unit is massive and moderately altered, fine-grained, aphyric basalt.

Unit 19. Sparsely plagioclase phyric basalt (Section 127-797C-41R-1, 0 cm, to Section 127-797C-41R-1, 80 cm; 852.4 to 853.2 mbsf)

The top of the unit is bounded by sedimentary rock, while the bottom is defined by the presence of a chilled margin with the adjacent baked sediment. The unit is composed of massive, sparsely plagioclase, phyric basalt with a fine-grained groundmass containing sparse vesicles filled with carbonate minerals and pyrite. The rock is moderately altered. The chilled margin at the bottom of the unit is cryptocrystalline and highly altered.

Unit 20. Aphyric dolerite (Section 127-797C-42R-CC, 0 cm, to Section 127-797C-44R-3, Piece 4e; 861.9 to 885.7 mbsf)

The unit is bounded by sedimentary rock at the top and the bottom. The unit bottom is marked by a chilled margin suggested by a reduction in grain size. The interior of the unit is

cm
70

75

80

85

90

Figure 42. Piece in center includes contact between chilled marginal facies of Unit 7 and baked sediments at the base of the unit. Section 127-797C-19R-4 (Piece 8).

composed of massive, medium-grained aphyric dolerite with a subophitic texture. A small amount (3%–5%) of vesicles is present throughout the unit, and these are filled with clay and carbonate minerals. The rock is highly altered.

Unit 21. Aphyric dolerite (Section 127-797C-44R-4, Piece 1, to Section 127-797C-45R-4, Piece 2; 885.8 to 895.2 mbsf)

The unit is bounded by sedimentary rocks and a chilled margin at the top of the unit. The bottom of the unit is unknown owing to termination of drilling. The unit is predominantly composed of massive, fine-grained aphyric basalt. Sparse vesicles (<1%) are present throughout the unit and are filled with clay and carbonate minerals and pyrite. The rock is highly altered.
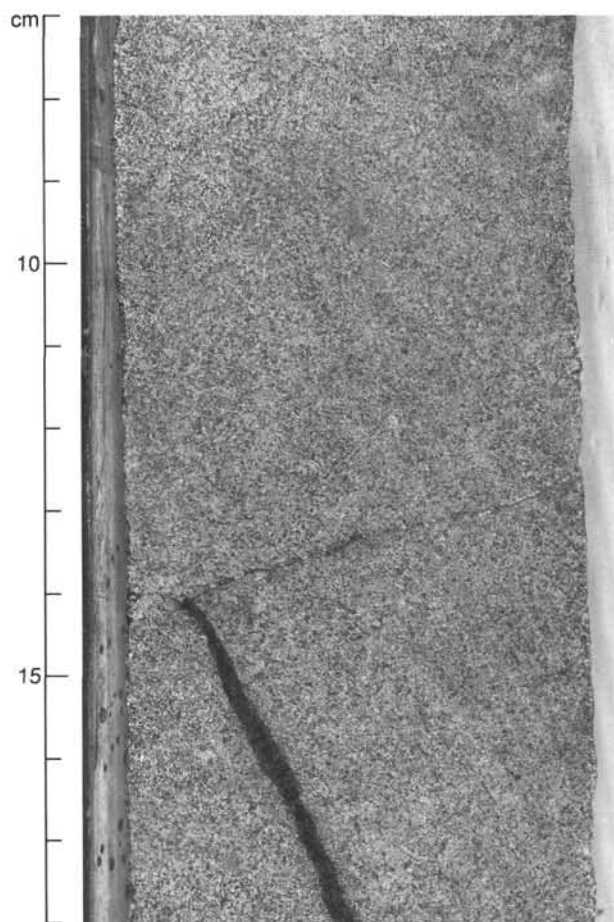
Figure 43. Massive, aphyric dolerite of Unit 8. Section 127-797C-21R-2.

Emplacement of Igneous Rocks

The igneous-rock units can be divided into two major groups in terms of whether or not they have chilled margins. The upper group consists of Units 1, 2, and 4 and lacks chilled margins. The lower group of units consists of Units 3 and 5–21, and has chilled margins. The units of the upper group are also highly fractured and brecciated. In contrast, the units of the lower group are predominantly massive. These contrasting characteristics suggest that the two groups have different means of emplacement.

The highly fractured and brecciated nature and the lack of chilled margins suggests that the upper group of units underwent autobrecciation associated with eruption as lava flows. Unit 1 includes scattered volcanic conglomerates, indicating that it may represent a talus pile. The compositional and petrographic similarity of the clasts of Unit 1 to the lava of Unit 2 suggests that they may have resulted from the same eruptive episode. On the other hand, the predominantly massive character, the presence of chilled marginal facies, and the sporadic presence of adjacent baked sediments indicate that units of the lower group were emplaced either as sills or dikes. This conclusion is supported by the observation that some of the adjacent sediments exhibited magnetic reversals as compared with the same lithology further away from the unit contact (see "Paleomagnetism"). This was best exhibited by Core 127-797C-30R, where reversals in the sedimentary-rock magnetization were observed above Unit 13 and below Unit 12 ("Paleomagnetism," this chapter, Fig. 30). In order to better constrain the emplacement history, radiometric age determinations of the igneous-rock units from Hole 797C and evaluation of the diagenetic mineralogy of the intercalated sedimentary rocks are needed.

Whole-Rock Chemistry

A variety of basaltic rocks, including high-Al basalts, alkali basalts, and incompatible-elements-enriched theoleiites, were recovered from the basement of Hole 797C. Because the basaltic rocks from Hole 797C are aphyric to sparsely phyric, the chemical characteristics of the least altered basaltic rocks may approximate those of the original magma. X-ray-fluorescence whole-rock analyses are given in Table 10. The loss on ignition (LOI) ranges from 2 wt% to over 7 wt%, consistent with the petrographic observations of alteration. For rocks of similar chemistry, the Al_2O_3 content is positively correlated with LOI and the CaO content is negatively correlated with LOI. These observations suggest that samples with high LOI content have undergone extensive compositional change owing to alteration. Therefore, samples with high LOI are not considered to reflect their original magmatic composition. As a result, we have used only samples with about 3% or less LOI for petrologic interpretation.

Most of the basalts and dolerites from Hole 797C resemble high-Al basalt in composition. Some of these are primitive, with high MgO (>9%), Ni (>150 ppm), and Cr (>300 ppm). Others are more evolved, with low MgO (<7%). All of the high-Al basalts have low Ce, Rb, K_2O, and Ba, moderate amounts of Sr, and very low Nb (Table 10 and Fig. 44). They are distinguished from tholeiitic basalt by the lack of iron enrichment and aluminum depletion trends. All of these basalts have high Al_2O_3 contents, ranging from 18 wt% in the relatively primitive samples to 20 wt% in the more evolved ones. When normalized to N-type mid-ocean-ridge-basalt composition (Pearce et al., 1981), these basalts exhibit a significant negative Nb anomaly relative to the large-ion lithophile elements. This anomaly is a common feature of arc volcanic rocks (e.g., Gill, 1981; Sakuyama and Nesbitt, 1986; Pearce, 1983).

The relatively high Al_2O_3 content of the more evolved high-Al basaltic rocks may result from fractional crystallization under high P_{H2O} that suppressed the onset of plagioclase crystallization (e.g., Baker and Eggler, 1987). Tatsumi et. al. (1986) explained the trace-element signature of arc volcanic rocks by differential transport of large-ion lithophile elements (LILE) and high-field-strength elements (HFSE) by metasomatic fluids from the subducting slab into the overlying wedge mantle. The MORB-normalized Nb depletion and Sr enrichment of the Hole 797C high-Al basaltic rocks suggest that these high-Al basaltic rocks originated from such a hydrous, metasomatized mantle-source material.

The lowermost analyzed units (Unit 10 and below) are mildly alkaline basalts and LILE- and HFSE-enriched tholeiites with relatively high alkalies, TiO_2, Zr, Y, Rb, Ba, and Ce (Table 10). These lavas plot within the alkaline field of Kuno (1968) but lack normative nepheline (perhaps owing to alteration). Petrographically, they are characterized by greater vesicularity than the high-Al basalts, consistent with having greater magmatic volatile contents. These units lack the relative depletion of HFSE relative to the LILE that the high-Al basaltic rocks exhibit but contain substantially higher contents of TiO_2 and other incompatible elements than do N-type MORB (Fig. 44). Their higher TiO_2 contents are reflected by their fourfold-higher magnetic susceptibility as compared to the high-Al basalts (see "Paleomagnetism" and Fig. 29). They were derived from a source much richer in both LILE and HFSE elements than the high-Al basalts; the similar Sr contents of the two groups of rocks preclude differing amounts of melting from a common source as a petrogenetic possibility. Rocks from the lower units show a mild iron-enrichment trend; this, together with their higher HFSE

Table 10. Whole rock chemical analyses of igneous rocks from Hole 797C. Total iron as FeO. Mg# refers to molecular $Mg/(Mg + Fe^{2+})$, where Fe^{2+} is assumed to be $Fe^{Total} \cdot 0.9$. $(Nb/Zr)_N$ represents the chondrite-normalized ratio of these elements (Sun et al., 1979). ND represents element not detected.

Hole	797C	797C	797C	797C	797C	797C	797C	797C	797C	797C	797C	797C	797C
Core/sec	8R-2	9R-1	10R-1	10R-4	11R-1	12R-2	12R-4	13R-2	14R-1	14R-1	15R-1	16R-2	18R-3
Interval (cm)	126–130	90–92	90–92	109–11	72–74	81–83	35–37	70–72	70–72	134–136	77–79	70–72	60–62
Unit	1	1	2	2	3	3	3	3	4	4	5	5	6
SiO$_2$	49.81	49.36	50.16	48.64	50.63	47.33	47.48	48.67	48.36	51.38	48.99	48.14	48.89
TiO$_2$	1.27	1.25	1.12	1.06	1.13	0.95	0.94	0.98	1.24	1.51	1.22	1.11	0.89
Al$_2$O$_3$	21.17	21.07	19.08	19.07	19.49	17.61	17.70	18.26	20.96	20.66	21.11	19.32	17.97
FeO	6.28	6.54	6.75	6.51	5.63	7.46	7.37	7.24	6.98	5.27	6.50	6.83	6.89
MnO	0.21	0.26	0.41	0.35	0.08	0.17	0.16	0.31	0.43	0.11	0.37	0.44	0.33
MgO	7.25	7.89	6.21	7.49	10.63	9.76	9.91	7.48	8.96	9.54	9.05	8.37	7.87
CaO	7.51	7.47	10.85	10.85	6.34	11.13	11.05	11.70	6.17	4.51	7.09	10.02	11.44
Na$_2$O	4.32	4.10	3.75	3.53	3.55	3.15	3.03	3.28	3.86	3.63	3.67	3.48	3.36
K$_2$O	0.32	0.23	0.11	0.09	1.03	0.06	0.05	0.04	0.17	1.39	0.18	0.05	0.06
P$_2$O$_5$	0.17	0.15	0.14	0.13	0.12	0.11	0.12	0.10	0.12	0.15	0.12	0.12	0.09
Totals	98.31	98.30	98.58	97.72	98.63	97.73	97.81	98.06	98.01	98.15	98.30	97.88	98.19
LOI	4.16	4.49	2.39	2.82	4.78	1.94	1.98	2.33	5.26	5.80	5.02	3.61	2.82
Nb	1	1	1	ND	1	ND	ND	ND	ND	ND	ND	1	ND
Zr	110	107	97	89	92	77	75	73	89	108	87	80	54
Y	22	20	21	22	18	19	19	21	19	22	19	18	20
Sr	314	308	302	275	242	239	238	229	229	180	252	237	215
Rb	3	2	1	1	8	1	ND	ND	1	11	2	ND	ND
Zn	95	84	63	58	40	53	53	59	89	101	96	71	59
Cu	98	95	89	86	92	81	79	88	110	90	89	85	84
Ni	143	162	150	169	160	163	165	145	172	140	140	158	102
Cr	315	303	272	247	277	216	218	245	323	375	325	284	309
V	220	230	214	192	192	166	158	166	248	238	250	214	200
Ce	16	18	13	17	19	10	8	6	15	18	9	13	10
Ba	23	24	25	23	31	14	10	11	12	21	25	22	2
Mg #	0.70	0.71	0.65	0.70	0.79	0.72	0.73	0.67	0.72	0.78	0.73	0.71	0.69
(Nb/Zr)$_N$	0.1	0.1	0.1		0.2							0.2	

contents, may indicate that they lack characteristic compositional signatures of arc volcanic rocks (e.g., Gill, 1981; Pearce, 1983). Instead, except for their moderate Nb contents, they are similar in composition to what has generally been described as "intra-plate" volcanics. Because of the intrusive nature of the alkaline basalts, their temporal relation to the high-Al basalts is unknown.

PHYSICAL PROPERTIES

Introduction

A full program of physical-property measurements was conducted on Site 797 cores that included magnetic susceptibility, GRAPE density and P-wave velocity measurements on the multisensor track (MST), index properties, thermal conductivity, P-wave velocity using the Hamilton Frame, and the formation factor. All of the physical-property results for discrete samples and selected values from the P-wave logger are presented in Table 11 for Holes 797A, 797B, and 797C.

Methods and Data Quality

To allow cross-correlation of the results, index properties, thermal conductivity, and the formation factor were measured at a single location in each section, usually 100 cm from the top. In addition, two of the index-property samples from each APC core and one for each XCB and rotary core were analyzed for grain size, carbonate content, and total organic carbon content. The P-wave logger (PWL) on the MST could be used reliably only on APC cores—i.e., to a depth of about 170 mbsf. In addition, the PWL periodically malfunctioned and, in the process of reestablishing the PWL operation, some of the measurement settings were improperly done. This required that the data for Sections 127-797A-1H-7 and 127-797B-1H-1 through 127-797B-

9H-3 be corrected. The corrections were, of necessity, based on local averages, and the PWL velocities thus are not as reliable as at previous sites. The PWL velocities are included in Figure 45 but are not included in any of the data tables. Deeper in the section (>300 mbsf), where the strength of the cored material allowed, a sample from each section was cut into a cube and the velocity measured using the Hamilton Frame apparatus. As a consequence, almost no velocity measurements were made between 180 and 350 mbsf.

As described in the Site 794 physical-properties summary, the cores taken at Site 797 using the extended core barrel (XCB) are disturbed to such a degree that some of the physical properties are altered from their in-situ condition. The XCB disturbance appears to decompact the sediments by the formation of small fractures throughout the cores (also see "Lithostratigraphy," this chapter). The effects on the physical properties are to bias the bulk density and thermal conductivity toward lower values, and the water content toward higher values. As for the previous Sites 795 and 796, the accuracy of the thermal conductivity values in Table 11 is estimated to be ±5%.

The index-property measurements remained problematic. The ship's motion was greater during much of the drilling at Site 797 than at previous sites, so the error in the weights was estimated to be 0.01 as opposed to 0.005 g. The errors in the wet and dry volumes, estimated to be 0.05 cm^3, caused difficulties with measurements of the least porous basement rocks. Initially, dry volume measurements on a few samples were greater than the wet volume values, though they are within the error bounds established for the volume measurements. We were able to rectify the problem by thoroughly cleaning the pycnometer cells before each volume reading and by taking multiple readings.

The formation-factor determinations involve measurements of the resistivity of the sediments parallel and perpendicular to

Table 10 (continued).

797C 19R-2 42–44 7	797C 19R-4 61–64 7	797C 20R-2 104–108 8	797C 21R-1 82–85 8	797C 24R-6 38–40 9	797C 26R-1 76–78 10	797C 26R-2 61–64 11	797C 27R-1 30–32 11	797C 28R-1 49–51 12	797C 29R-1 69–70 12	797C 31R-2 36–38 13	797C 32R-2 15–17 14	797C 33R-1 63–65 14	797C 33R-4 5.–7. 15	797C 34R-1 33–35 15
49.14	45.37	46.39	47.86	47.98	51.43	47.69	49.35	52.53	52.31	50.24	49.16	52.10		
0.88	1.06	1.10	0.88	0.92	2.99	2.25	1.87	2.18	2.02	1.65	1.75	2.00	2.01	1.94
17.97	20.69	20.53	18.06	17.40	15.03	17.93	15.91	14.34	14.62	14.91	16.51	15.59		
6.47	7.09	8.20	7.05	7.67	10.47	10.50	9.66	9.46	9.36	9.25	8.96	10.36		
0.28	0.74	0.45	0.19	0.18	0.32	0.28	0.20	0.18	0.18	0.19	0.31	0.49		
8.12	8.41	12.65	8.80	8.75	5.64	8.79	7.85	6.19	5.89	6.13	7.10	8.52		
11.57	10.45	4.60	10.30	11.59	3.88	2.95	6.57	5.27	6.53	10.04	8.78	1.35		
3.09	3.55	2.81	3.40	2.80	4.48	4.49	3.90	4.42	4.14	3.55	3.72	3.75		
0.07	0.08	0.40	0.13	0.12	1.03	1.18	0.38	1.17	1.07	0.52	0.48	2.42		
0.08	0.09	0.10	0.09	0.10	0.43	0.32	0.25	0.33	0.29	0.24	0.24	0.33		
97.63	97.53	97.23	97.44	98.12	96.84	97.54	96.99	97.10	97.44	97.72	98.01	98.03		
2.40	7.86	8.44	4.17	2.12	3.06	4.35	3.42	2.53	2.08	1.64	2.54	4.37		
ND	ND	ND	1	1	11	8	6	8	8	6	6	9	7	6
54	62	67	61	67	283	211	162	231	207	160	159	224	180	168
21	21	15	20	20	53	43	39	45	39	34	33	38	37	33
179	189	138	189	218	305	191	298	265	275	276	329	110	295	297
ND	1	9	1	1	7	6	2	15	14	3	2	32	11	9
61	65	68	59	57	126	166	89	109	99	87	87	92	86	87
83	86	76	67	73	39	62	62	46	45	59	69	42	50	57
101	106	153	143	94	11	33	39	14	18	36	60	29	31	43
317	396	314	272	293	14	178	169	11	26	134	195	85	87	122
200	260	215	183	187	409	370	328	306	303	266	293	283	304	295
9	14	15	5	10	57	31	31	41	38	40	32	44	43	36
17	12	15	26	4	217	104	127	242	242	181	145	282	159	167
0.71	0.70	0.75	0.71	0.69	0.52	0.62	0.62	0.56	0.56	0.57	0.61	0.62		
			0.2	0.2	0.54	0.55	0.51	0.51	0.55	0.49	0.53	0.55	0.54	0.51

the axis of the core, preceded and followed closely by a resistivity measurement of surface seawater. The seawater was contained in half a core liner to duplicate the geometry of the sediment measurements. Unlike the previous sites, the seawater resistivity measurements gave stable and consistent results. The variation in the resistivity of the seawater reference was about 2%, and we estimate the overall error in the formation factor to be of the order of 5%. Resistivity measurements could be made only in unconsolidated sediments in the interval from 0 to 180 mbsf.

Physical Properties of the Sedimentary Section

In this section, we use the lithostratigraphic units as a framework for discussing the magnitude and variation of the physical-property measurements. Plots of the principal physical properties vs. depth are presented in Figure 45, and in Figure 46 for the formation factor. The first-order statistics for each of the major lithostratigraphic units are presented in Tables 12 through 17. The general patterns and trends in the physical-property data are remarkably similar to those observed at Site 794, as will be discussed in more detail.

Unit I (0–119.9 mbsf) is composed of an unconsolidated silty clay with alternating dark and light bands (Subunit IA), and an ashy, diatomaceous silty clay (Subunit IB). The index properties, thermal conductivity, and formation factor show some variability in this unit (Table 12). There is a small linear decrease in the porosity and water content in the upper 40 m and an associated increase in the wet and dry bulk densities, the thermal conductivity, and the formation factor. The acoustic velocity exhibits low scatter and values close to that of seawater (Fig. 45).

Diatomaceous silty clays and oozes make up Unit II (119.9–224 mbsf), with increasing diatom content with depth. All of
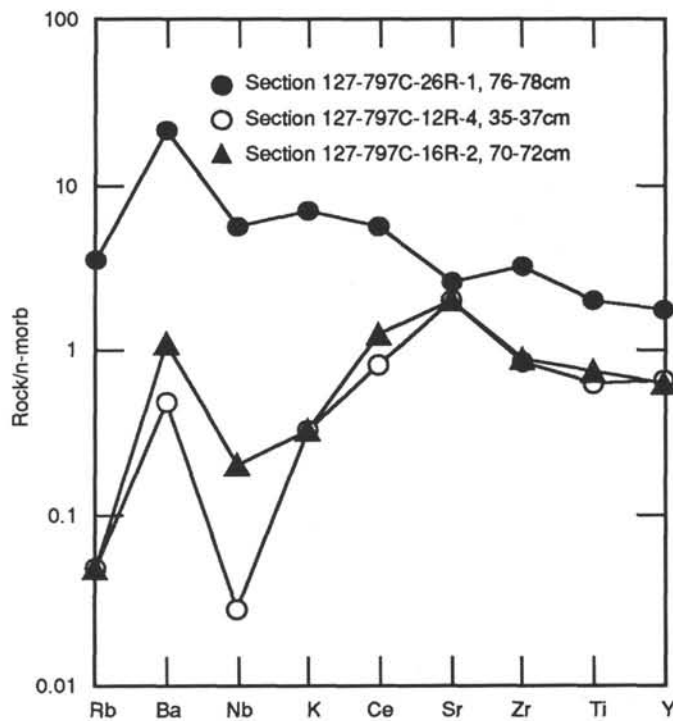
Figure 44. Compositions of selected basalts from Hole 797C normalized to N-type MORB (Pearce et al., 1981). The order of elements is of relative incompatibility, following Sun et al. (1979).

Table 11. Summary of Site 797 physical property data.

Core, section, interval (cm)	Depth (mbsf)	Wet bulk (g/cm³)	Dry bulk (g/cm³)	Grain (g/cm³)	Porosity (%)	Water content (%)	Void ratio	Water ratio	A	B	C	Thermal conductivity (W/m · K)	H	V	Mean	Anistropy
127-797A-																
1H-1, 100–102	4.40	1.46	0.64	2.75	79.4	55.8	3.85	1.26				0.840	1.66	1.75	1.70	1.03
1H-2, 100–102	5.90	1.38	0.51	2.67	85.5	63.2	5.88	1.72				0.896	1.59	1.76	1.67	1.05
1H-3, 100–102	7.40	1.36	0.50	2.60	84.7	63.6	5.52	1.75				0.745	1.53	1.60	1.56	1.02
1H-4, 100–102	8.90	1.36	0.47	2.77	86.9	65.7	6.66	1.91				0.783	1.47	1.61	1.54	1.05
1H-5, 100–102	10.40	1.58	0.84	2.60	72.5	47.1	2.64	0.89				0.998	1.86	2.06	1.96	1.05
1H-6, 100–102	11.90	1.47	0.73	2.60	72.8	50.7	2.67	1.03				0.954	1.75	1.81	1.78	1.02
1H-7, 40–41	12.80											0.844				
127-797B-																
1H-1, 100–101	1.00											0.830				
1H-2, 100–102	2.50	1.42	0.59	2.71	81.6	58.7	4.42	1.42				0.774	1.61	1.70	1.65	1.03
1H-3, 100–102	4.00	1.40	0.57	2.58	81.0	59.3	4.27	1.46				0.903	1.65	1.71	1.68	1.02
1H-4, 90–92	5.40	1.35	0.47	2.56	85.7	65.2	5.98	1.88					1.44	1.65	1.54	1.07
2H-1, 100–102	6.90	1.33	0.45	2.48	86.5	66.5	6.41	1.98				0.808	1.51	1.59	1.55	1.03
2H-2, 100–102	8.40	1.40	0.57	2.71	81.3	59.4	4.34	1.46				0.882	1.65	1.77	1.71	1.04
2H-3, 100–102	9.90	1.43	0.60	2.60	81.3	58.3	4.36	1.40				0.810	1.74	1.76	1.75	1.01
2H-4, 100–102	11.40	1.39	0.53	2.61	83.9	61.9	5.19	1.62				0.796	1.60	1.66	1.63	1.02
2H-5, 100–102	12.90	1.42	0.58	2.03	82.0	59.1	4.56	1.45				0.942	1.63	1.77	1.70	1.04
2H-6, 100–102	14.40	1.45	0.64	2.58	79.8	56.2	3.94	1.28				0.876	1.84	1.81	1.82	0.99
2H-7, 50–52	15.40	1.30	0.41	2.44	87.0	68.3	6.69	2.16				0.744	1.52	1.60	1.56	1.03
3H-1, 100–102	16.40	1.35	0.48	2.67	84.9	64.2	5.62	1.79				0.892	1.54	1.61	1.57	1.02
3H-2, 100–102	17.90	1.46	0.64	2.78	80.2	56.4	4.05	1.29				0.937	1.69	1.76	1.72	1.02
3H-3, 100–102	19.40	1.54	0.77	2.75	75.4	50.2	3.07	1.01				0.959	1.96	2.00	1.98	1.01
3H-4, 100–102	20.90	1.41	0.55	2.56	83.5	60.8	5.06	1.55				0.772	1.71	1.81	1.76	1.03
3H-5, 100–102	22.40	1.35	0.47	2.51	86.2	65.3	6.26	1.89				0.867	1.59	1.67	1.63	1.02
3H-6, 100–102	23.90	1.54	0.76	2.80	75.9	50.6	3.15	1.02				0.940	2.20	2.10	2.15	0.98
3H-7, 40–42	24.80	1.58	0.81	2.77	74.8	48.6	2.97	0.95				0.937	2.08	2.19	2.13	1.03
4H-1, 99–100	25.89	1.35	0.47	2.70	86.2	65.3	6.23	1.88				0.880	1.66	1.76	1.71	1.03
4H-2, 99–100	27.39	1.41	0.58	2.45	81.1	58.9	4.28	1.44				0.788	1.86	2.06	1.96	1.05
4H-3, 99–100	28.89	1.44	0.62	2.54	79.9	56.7	3.98	1.31				0.865	1.88	1.95	1.91	1.02
4H-4, 99–100	30.39	1.49	0.69	2.55	78.3	53.7	3.60	1.16				1.002	1.92	2.09	2.00	1.04
4H-5, 99–100	31.89	1.44	0.55	2.66	86.8	61.9	6.57	1.62				0.868	1.68	1.77	1.72	1.03
4H-6, 99–100	33.39	1.55	0.77	2.82	76.7	50.6	3.29	1.03				0.870	2.08	2.09	2.08	1.00
4H-7, 40–42	34.30	1.49	0.68	2.51	78.6	54.2	3.67	1.18								
5H-1, 100–100	35.40	1.62	0.88	2.88	72.8	46.0	2.68	0.85				1.032	2.21	2.24	2.22	1.01
5H-2, 100–100	36.90	1.50	0.71	2.51	76.9	52.4	3.33	1.10				0.844	1.99	2.00	1.99	1.00
5H-3, 100–100	38.40	1.42	0.57	2.70	83.2	60.0	4.94	1.50				0.807	1.77	1.80	1.78	1.01
5H-4, 88–90	39.78	1.96	1.32	2.63	62.0	32.4	1.63	0.48								
5H-4, 100–100	39.90	1.41	0.56	2.46	83.3	60.4	4.98	1.52				1.012	1.78	1.87	1.82	1.02
5H-5, 100–100	41.40	1.51	0.74	2.57	75.2	51.1	3.04	1.05				0.864	1.72	1.83	1.77	1.03
5H-6, 100–100	42.90	1.53	0.80	2.52	71.6	47.8	2.52	0.92				0.970	2.01	2.18	2.09	1.04
5H-7, 40–40	43.80	1.43	0.63	2.62	77.8	55.9	3.50	1.27					1.82	1.90	1.86	1.02
6H-1, 100–100	44.90	1.44	0.58	2.79	83.5	59.4	5.07	1.47				0.923	1.86	1.92	1.89	1.02
6H-2, 100–100	46.40	1.44	0.60	2.59	81.4	58.1	4.39	1.38				0.816	1.87	1.98	1.92	1.03
6H-3, 100–100	47.90	1.47	0.66	2.55	79.4	55.4	3.86	1.24				0.894	1.89	2.19	2.03	1.08
6H-4, 100–100	49.40	1.44	0.61	2.47	81.2	57.6	4.33	1.36				0.907	1.96	2.00	1.98	1.01
6H-5, 100–100	50.90	1.53	0.76	2.65	75.2	50.3	3.04	1.01					2.15	2.07	2.11	0.98
6H-6, 100–100	52.40	1.53	0.76	2.65	75.2	50.3	3.04	1.01				0.992	2.28	2.75	2.50	1.10
6H-7, 40–40	53.30	1.52	0.74	2.62	76.3	51.4	3.23	1.06					2.03	2.18	2.10	1.04
7H-1, 100–100	54.40	1.63	0.89	2.77	72.0	45.2	2.57	0.83				1.057	2.26	2.21	2.23	0.99
7H-2, 100–102	55.90	1.36	0.49	2.47	84.5	63.8	5.46	1.76				0.800	1.81	1.88	1.84	1.02
7H-3, 100–102	57.40	1.37	0.51	2.65	83.6	62.5	5.09	1.67				0.803	1.91	2.01	1.96	1.03
7H-4, 100–102	58.90	1.47	0.64	2.72	81.3	56.7	4.33	1.31				0.840	2.01	1.87	1.94	0.96
7H-5, 100–102	60.40	1.41	0.59	2.49	80.2	58.2	4.06	1.39				0.865	1.91	1.99	1.95	1.02
7H-6, 100–102	61.90	1.62	0.88	2.78	72.6	45.9	2.65	0.85				0.958	2.20	2.30	2.25	1.02
7H-7, 40–42	62.80	1.39	0.55	2.48	81.9	60.3	4.53	1.52				0.871	1.83	1.93	1.88	1.03
8H-1, 100–102	63.90	1.39	0.54	2.54	83.2	61.4	4.96	1.59				0.825	1.79	1.90	1.84	1.03
8H-2, 100–101	65.40	1.57	0.83	2.59	72.0	46.9	2.57	0.88				0.905	2.26	2.25	2.25	1.00
8H-3, 100–101	66.90	1.54	0.76	2.55	76.2	50.8	3.20	1.03				0.894	2.22	2.35	2.28	1.03
8H-4, 100–102	68.40	1.38	0.52	2.49	84.1	62.2	5.28	1.65					1.84	1.87	1.85	1.01
8H-5, 100–102	69.90	1.36	0.50	2.69	84.4	63.4	5.40	1.73					2.10	2.16	2.13	1.01
8H-6, 100–102	71.40	1.38	0.52	2.57	84.2	62.5	5.31	1.67				0.755	1.76	1.85	1.80	1.03
8H-7, 50–52	72.40	1.52	0.73	2.63	77.3	52.2	3.40	1.09					2.00	2.07	2.03	1.02
9H-1, 100–102	73.40	1.51	0.71	3.01	77.9	52.9	3.53	1.12				0.998	2.08	2.11	2.09	1.01
9H-2, 100–102	74.90	1.69	0.97	2.76	69.8	42.4	2.32	0.74					2.51	2.57	2.54	1.01
9H-3, 100–102	76.40	1.44	0.61	2.72	81.3	57.9	4.35	1.38				0.809	1.90	1.98	1.94	1.02
9H-4, 100–102	77.90	1.40	0.53	2.64	84.6	62.1	5.51	1.64				0.806	1.73	1.84	1.78	1.03
9H-5, 100–102	79.40	1.54	0.77	2.68	74.9	49.8	2.98	0.99				1.041	2.31	2.46	2.38	1.03
9H-6, 100–102	80.90	1.48	0.65	2.64	80.8	56.1	4.22	1.28				0.845	1.86	1.95	1.90	1.02
10H-1, 100–102	82.90	1.41	0.54	2.63	84.3	61.4	5.38	1.59				0.867	1.81	1.86	1.83	1.01
10H-2, 100–102	84.40	1.48	0.67	2.67	78.8	54.6	3.71	1.20				0.886	2.07	2.21	2.14	1.03
10H-3, 100–102	85.90	1.43	0.59	2.63	81.4	58.5	4.37	1.41					1.91	2.01	1.96	1.03
10H-4, 100–102	87.40	1.39	0.54	2.48	83.1	61.3	4.90	1.58				0.827	1.85	1.93	1.89	1.02
10H-5, 100–102	88.90	1.55	0.77	2.66	75.9	50.2	3.15	1.01				1.043	2.23	2.32	2.27	1.02
10H-6, 100–102	90.40	1.51	0.72	2.69	77.5	52.7	3.44	1.11				0.947	2.26	2.42	2.34	1.03
11H-1, 100–102	92.40	1.41	0.56	2.62	82.9	60.3	4.86	1.52				0.853	1.91	2.04	1.97	1.03
11H-2, 100–102	93.90	1.47	0.65	2.62	80.4	56.1	4.09	1.28				0.779	2.00	2.16	2.08	1.04
11H-3, 100–102	95.40	1.57	0.76	2.76	79.1	51.5	3.79	1.06				0.878	2.34	2.97	2.64	1.13
11H-4, 100–102	96.90	1.42	0.59	2.47	80.9	58.2	4.24	1.39				0.865	2.03	2.07	2.05	1.01
11H-5, 100–102	98.40	1.28	0.59	2.43	67.9	54.2	2.12	1.18					1.95	2.13	2.04	1.05
11H-6, 100–102	99.90	1.42	0.58	2.45	81.4	58.9	4.39	1.43				0.881	1.91	2.04	1.97	1.03

Table 11 (continued).

Core, section, interval (cm)	Depth (mbsf)	Wet bulk (g/cm³)	Dry bulk (g/cm³)	Grain (g/cm³)	Porosity (%)	Water content (%)	Void ratio	Water ratio	A	B	C	Thermal conductivity (W/m · K)	H	V	Mean	Anistropy
127-797B- (Cont.)																
11H-7, 50–52	100.90	1.59	0.83	2.72	73.9	47.6	2.83	0.91					2.34	2.85	2.58	1.10
12H-1, 100–102	101.90	1.39	0.54	2.52	82.9	61.2	4.86	1.58					1.86	1.99	1.92	1.03
12H-2, 100–102	103.40	1.37	0.51	2.48	84.1	62.8	5.29	1.69				0.761	1.85	2.01	1.93	1.04
12H-3, 100–102	104.90	1.40	0.54	2.51	83.8	61.4	5.17	1.59				0.811	1.90	2.10	2.00	1.05
12H-4, 100–102	106.40	1.71	1.03	2.70	66.8	40.0	2.01	0.67				1.001	2.66	2.80	2.73	1.03
12H-5, 100–102	107.90	1.38	0.52	2.46	83.6	62.2	5.12	1.65				0.828	1.85	1.95	1.90	1.03
12H-6, 100–102	109.40	1.36	0.51	2.28	82.7	62.2	4.77	1.64				0.835	1.85	1.95	1.90	1.03
12H-7, 50–52	110.40	1.42	0.61	2.60	79.2	57.2	3.82	1.34					1.94	2.05	1.99	1.03
13H-1, 100–102	111.40	1.34	0.46	2.39	86.2	65.9	6.24	1.94				0.795	2.05	2.56	2.29	1.12
13H-2, 100–102	112.90	1.52	0.74	2.55	76.5	51.5	3.26	1.06				0.871	2.17	2.33	2.25	1.04
13H-3, 100–102	114.40	1.35	0.49	2.50	83.4	63.5	5.02	1.74				0.817	1.95	2.12	2.03	1.04
13H-4, 100–102	115.90	1.35	0.51	2.39	82.2	62.5	4.63	1.67				0.753	1.90	2.04	1.97	1.04
13H-5, 100–102	117.40	1.36	0.51	2.40	82.8	62.5	4.82	1.67				0.805	1.87	1.99	1.93	1.03
13H-6, 100–102	118.90	1.41	0.58	2.50	80.4	58.6	4.11	1.42				0.876	2.01	2.17	2.09	1.04
13H-7, 40–41	119.80											0.832				
14H-1, 100–102	120.90	1.42	0.57	2.58	82.7	59.6	4.79	1.47				0.884	2.36	2.99	2.66	1.13
14H-2, 100–102	122.40	1.39	0.54	2.41	83.1	61.2	4.91	1.58				0.778	2.12	2.21	2.16	1.02
14H-3, 100–102	123.90	1.44	0.61	2.47	81.7	57.9	4.47	1.38				0.925	2.01	2.05	2.03	1.01
14H-4, 100–102	125.40	1.46	0.61	2.70	82.9	58.1	4.85	1.39				0.841	1.97	2.15	2.06	1.04
14H-5, 100–102	126.90	1.46	0.62	2.61	82.4	57.8	4.67	1.37				0.827	2.00	2.08	2.04	1.02
15H-1, 100–102	130.40	1.43	0.56	2.60	84.3	60.6	5.38	1.54				0.854	1.84	1.99	1.91	1.04
15H-2, 100–102	131.90	1.40	0.52	2.53	85.3	62.6	5.81	1.67				0.809	1.83	2.04	1.93	1.06
15H-3, 100–102	133.40	1.50	0.69	2.71	78.5	53.7	3.65	1.16				0.898	2.14	2.20	2.17	1.01
15H-4, 100–102	134.90	1.46	0.60	2.68	83.7	58.9	5.13	1.43				0.829	1.96	2.06	2.01	1.03
15H-5, 100–102	136.40	1.41	0.56	2.59	82.9	60.2	4.84	1.51				0.828	1.87	1.99	1.93	1.03
15H-6, 100–102	137.90	1.41	0.59	2.50	80.1	58.2	4.02	1.39				0.866	2.08	2.15	2.11	1.02
15H-7, 50–52	138.90	1.40	0.54	2.56	83.8	61.3	5.15	1.59				0.820	1.91	2.03	1.97	1.03
16H-1, 100–102	139.90	1.40	0.49	2.57	88.7	64.7	7.86	1.84				0.824	1.82	1.94	1.88	1.03
16H-2, 100–102	141.40	1.46	0.59	2.41	84.8	59.3	5.60	1.46				0.829	1.99	2.15	2.07	1.04
16H-3, 90–92	142.80	1.56	0.71	2.82	82.5	54.3	4.71	1.19				0.804	1.85	1.97	1.91	1.03
16H-4, 100–102	144.40	1.41	0.54	2.50	84.9	61.8	5.62	1.62				0.795	1.91	1.94	1.92	1.01
16H-5, 100–102	145.90	1.46	0.66	2.50	78.2	54.8	3.59	1.21				0.835	2.18	2.27	2.22	1.02
16H-6, 100–102	147.40	1.47	0.59	2.62	86.0	59.9	6.15	1.49				0.882	1.99	2.07	2.03	1.02
16H-7, 20–22	148.10	1.39	0.50	2.45	86.9	63.8	6.61	1.77				0.856	1.86	1.92	1.89	1.02
17H-1, 100–102	149.40	1.38	0.51	2.65	84.8	63.0	5.59	1.70					1.91	1.98	1.94	1.02
17H-2, 20–22	150.10	1.40	0.51	2.65	87.4	63.8	6.94	1.76					2.41	2.38	2.39	0.99
17H-4, 110–112	151.87	1.43	0.57	2.51	84.5	60.5	5.45	1.53					2.03	2.16	2.09	1.03
17H-5, 100–102	153.27	1.45	0.57	2.69	85.7	60.6	6.00	1.54					2.11	2.31	2.21	1.05
17H-6, 100–102	154.77	1.42	0.60	2.31	80.7	58.0	4.17	1.38					2.02	2.12	2.07	1.02
17H-7, 100–102	156.27	1.42	0.55	2.58	85.4	61.6	5.83	1.60					2.06	2.01	2.03	0.99
18H-1, 100–102	158.90	1.40	0.56	2.49	82.4	60.1	4.67	1.51				0.827	2.02	2.09	2.05	1.02
18H-2, 100–102	160.40	1.37	0.51	2.43	83.9	62.6	5.20	1.68				0.751	1.91	2.00	1.95	1.02
18H-3, 100–102	161.90	1.45	0.63	2.36	80.1	56.6	4.03	1.30				0.818	1.92	2.00	1.96	1.02
18H-4, 100–102	163.40	1.46	0.64	2.54	80.5	56.4	4.13	1.29				0.862	1.91	1.98	1.94	1.02
18H-5, 100–102	164.90	1.44	0.60	2.59	81.9	58.3	4.53	1.40				0.832	1.82	1.92	1.87	1.03
18H-6, 50–52	165.90	1.43	0.57	2.63	83.8	60.1	5.16	1.51				0.823				
19H-1, 100–102	167.40	1.34	0.47	2.21	84.5	64.6	5.45	1.83				0.832	1.81	1.87	1.84	1.02
19H-2, 100–102	168.90	1.38	0.51	2.48	85.2	63.0	5.74	1.70				0.734	1.86	2.03	1.94	1.04
19H-3, 100–102	170.40	1.34	0.50	2.06	81.5	62.5	4.40	1.67				0.774	1.91	2.04	1.97	1.03
19H-4, 100–102	171.90	1.36	0.52	2.26	82.4	62.0	4.67	1.63				0.835	1.97	2.08	2.02	1.03
19H-5, 100–102	173.40	1.36	0.51	2.32	83.1	62.4	4.90	1.66				0.778	1.97	2.06	2.01	1.02
19H-6, 100–102	174.90	1.38	0.50	2.34	85.3	63.5	5.82	1.74				0.816	2.02	2.12	2.07	1.02
19H-7, 50–52	175.90	1.40	0.63	2.42	75.4	55.2	3.06	1.23					1.81	1.92	1.86	1.03
20X-3, 100–101	179.90											0.760				
20X-4, 100–102	181.40	1.35	0.45	2.56	87.7	66.7	7.13	2.00				0.729				
20X-5, 110–112	183.00	1.33	0.48	2.19	82.7	63.8	4.79	1.76				0.750	1.86	1.83	1.84	0.99
21X-1, 100–102	186.50	1.35	0.46	2.40	87.1	66.1	6.75	1.95				0.798				
21X-2, 100–102	188.00	1.36	0.45	2.61	88.8	66.9	7.93	2.02				0.737				
21X-3, 100–102	189.50	1.32	0.46	2.29	84.4	65.4	5.40	1.89				0.764				
21X-4, 100–102	191.00	1.39	0.49	2.36	88.1	65.0	7.40	1.86								
21X-5, 20–22	191.70	1.39	0.52	2.33	84.9	62.7	5.61	1.68								
22X-1, 100–102	196.20	1.35	0.44	2.21	89.1	67.6	8.15	2.09								
22X-2, 100–102	197.70	1.40	0.50	2.52	87.9	64.5	7.25	1.82				0.753				
22X-3, 100–102	199.20	1.37	0.48	2.16	87.0	65.3	6.67	1.88				0.741				
22X-4, 100–102	200.70	1.35	0.45	2.32	87.6	66.5	7.09	1.99				0.757				
22X-5, 100–102	202.20	1.42	0.52	2.44	87.4	63.1	6.93	1.71				0.736				
23X-1, 100–102	205.80	1.36	0.47	2.55	87.3	65.6	6.89	1.90				0.749				
23X-2, 100–102	207.30	1.40	0.52	2.42	85.7	62.9	6.01	1.69				0.773				
23X-3, 100–102	208.80	1.37	0.50	2.72	84.9	63.5	5.63	1.74				0.726				
23X-4, 100–102	210.30	1.35	0.46	2.50	86.6	65.8	6.44	1.92				0.768				
23X-5, 100–102	211.80	1.36	0.49	2.23	84.9	63.8	5.61	1.76				0.787				
23X-6, 100–102	213.30	1.49	0.68	2.37	78.7	54.3	3.70	1.19				0.875				
24X-1, 100–102	215.30	1.42	0.61	2.24	78.9	57.0	3.74	1.33				0.834				
24X-2, 100–102	216.80	1.47	0.60	2.62	85.0	59.4	5.68	1.47				0.753				
24X-3, 100–102	218.30	1.33	0.48	2.18	83.0	64.0	4.87	1.78				0.764				
24X-4, 100–102	219.80	1.45	0.58	2.50	85.1	60.3	5.72	1.52				0.788				
24X-5, 100–102	221.30	1.38	0.55	2.42	81.0	60.1	4.28	1.51				0.832				
24X-6, 100–102	222.80	1.46	0.62	2.91	82.0	57.4	4.56	1.35				0.807				
24X-7, 30–32	223.60	1.42	0.54	2.36	86.1	62.0	6.18	1.63								
25X-1, 100–102	225.00	1.47	0.60	1.92	84.3	58.9	5.36	1.43				0.866				
25X-2, 100–102	226.50	1.35	0.48	2.05	84.9	64.5	5.63	1.81				0.692				
25X-3, 100–102	228.00	1.39	0.53	2.41	84.3	62.2	5.35	1.65				0.765				

Table 11 (continued).

Core, section, interval (cm)	Depth (mbsf)	Densities Wet bulk (g/cm³)	Dry bulk (g/cm³)	Grain (g/cm³)	Porosity (%)	Water content (%)	Void ratio	Water ratio	Velocity (m/s) A	B	C	Thermal conductivity (W/m·K)	Formation factors H	V	Mean	Anistropy
127-797B- (Cont.)																
25X-4, 100–102	229.50	1.39	0.50	2.55	86.5	64.0	6.43	1.77				0.832				
25X-5, 100–102	231.00	1.47	0.60	2.47	84.6	59.1	5.50	1.45				0.807				
25X-6, 100–102	232.50	1.41	0.54	2.36	84.9	61.8	5.61	1.62				0.802				
25X-7, 30–32	233.30	1.43	0.59	2.34	82.0	58.9	4.55	1.43				0.839				
26X-1, 100–102	234.70	1.38	0.53	2.32	83.7	61.9	5.12	1.63				0.798				
26X-2, 100–102	236.20	1.35	0.45	2.50	87.9	66.5	7.25	1.98								
26X-3, 100–102	237.70	1.37	0.49	2.34	86.6	64.6	6.46	1.82				0.753				
26X-4, 100–102	239.20	1.38	0.50	2.41	86.1	63.9	6.21	1.77								
26X-5, 100–102	240.70	1.40	0.56	2.42	81.5	59.8	4.41	1.49				0.797				
26X-6, 100–102	242.20	1.37	0.47	2.47	87.3	65.5	6.85	1.90				0.857				
27X-1, 100–102	244.40	1.31	0.43	2.38	86.0	67.5	6.13	2.07				0.760				
27X-2, 100–102	245.90	1.35	0.47	2.52	85.9	65.1	6.07	1.87				0.803				
27X-3, 100–102	247.40	1.37	0.52	2.44	82.8	61.9	4.81	1.63				0.824				
27X-4, 100–102	248.90	1.40	0.56	2.52	82.1	60.3	4.60	1.52				0.889				
27X-5, 100–102	250.40	1.32	0.42	2.53	87.4	67.9	6.93	2.11								
27X-6, 100–102	251.90	1.33	0.45	2.49	85.7	65.9	5.98	1.94								
28X-1, 100–102	254.10	1.30	0.42	2.42	85.6	67.3	5.96	2.06				0.819				
28X-2, 100–102	255.60	1.29	0.39	2.38	87.8	69.5	7.22	2.28				0.775				
28X-3, 100–102	257.10	1.34	0.44	2.46	87.8	67.3	7.21	2.05				0.786				
28X-4, 50–52	258.10	1.36	0.45	2.54	89.2	67.0	8.25	2.03				0.726				
30X-1, 100–102	273.50	1.39	0.53	2.59	84.1	61.8	5.29	1.62				0.945				
30X-2, 100–102	275.00	1.38	0.49	2.48	86.9	64.7	6.64	1.83				0.877				
30X-3, 100–102	276.50	1.58	0.81	2.68	75.0	48.7	3.00	0.95				0.987				
30X-4, 100–102	278.00	1.39	0.54	2.27	82.8	60.8	4.80	1.55				1.026				
30X-5, 100–102	279.50	1.36	0.47	2.38	86.5	65.3	6.39	1.88								
30X-6, 50–52	280.50	1.37	0.50	2.54	85.1	63.6	5.71	1.75								
31X-1, 100–102	283.20	1.44	0.57	2.69	85.5	60.7	5.88	1.54				0.748				
31X-2, 100–102	284.70	1.42	0.58	2.39	81.5	58.8	4.40	1.43				0.842				
31X-3, 100–102	286.20	1.42	0.59	2.36	81.5	58.6	4.41	1.42				0.775				
31X-4, 100–102	287.70	1.37	0.49	2.40	85.6	63.9	5.96	1.77				0.845				
31X-5, 100–102	289.20	1.52	0.73	2.81	77.4	52.2	3.42	1.09								
31X-6, 100–102	290.70	1.48	0.66	2.75	79.7	55.3	3.94	1.24								
31X-7, 30–32	291.50	1.45	0.66	2.41	77.6	54.8	3.46	1.21								
32X-1, 100–102	292.90	1.39	0.51	2.70	86.0	63.6	6.16	1.75				0.775				
32X-2, 100–102	294.40	1.38	0.54	2.30	82.6	61.1	4.74	1.57				0.781				
32X-3, 100–102	295.90	1.42	0.56	2.66	83.9	60.7	5.21	1.54				0.765				
32X-4, 100–102	297.40	1.43	0.60	2.49	80.8	57.9	4.20	1.37				0.855				
32X-5, 100–102	298.90	1.54	0.73	2.61	78.4	52.4	3.64	1.10								
32X-6, 100–102	300.40	1.64	0.90	2.47	72.6	45.2	2.65	0.83								
33X-1, 100–102	302.50	1.52	0.73	2.54	77.0	51.9	3.35	1.08				0.902				
33X-2, 100–102	304.00	1.61	0.86	2.56	72.7	46.3	2.66	0.86				0.827				
33X-3, 2–64	305.12								1864	2024	2084					
33X-3, 100–102	305.50	1.67	0.97	2.53	68.2	41.9	2.15	0.72				1.013				
33X-4, 100–102	307.00	1.72	1.05	2.56	65.1	38.8	1.86	0.63				0.984				
34X-1, 97–99	312.17	1.82	1.16	2.80	64.6	36.3	1.82	0.57				1.108				
34X-2, 100–101	313.70											0.985				
34X-2, 115–117	313.85	1.85	1.20	2.72	63.6	35.2	1.74	0.54	1633			1.085				
34X-3, 93–95	315.13	1.81	1.15	2.63	63.9	36.2	1.77	0.57				1.044				
34X-4, 102–104	316.72	1.76	1.12	2.45	62.5	36.3	1.66	0.57				1.037				
34X-5, 8–10	317.28	1.82	1.14	2.53	66.7	37.5	2.00	0.60	1615	1644	1643	1.098				
34X-6, 20–22	318.90	1.76	1.09	2.62	65.3	38.0	1.88	0.61								
35X-1, 136–138	322.26	1.69	1.00	2.65	67.3	40.9	2.06	0.69								
35X-2, 73–75	323.13	1.64	0.93	2.49	68.8	43.1	2.21	0.76								
35X-2, 100–101	323.40											0.884				
35X-3, 95–97	324.85	1.68	0.98	2.53	68.6	41.9	2.18	0.72				0.860				
35X-4, 88–90	326.28	1.89	1.24	2.73	63.8	34.5	1.76	0.53				0.954				
35X-5, 97–99	327.87	1.64	0.97	2.76	65.3	40.7	1.88	0.69				0.948				
37X-1, 48–50	340.78	1.76	1.09	2.51	65.0	38.0	1.86	0.61				0.975				
37X-1, 100–101	341.30											0.906				
37X-2, 68–70	342.48	1.75	1.07	2.49	66.6	38.9	1.99	0.64								
37X-2, 100–101	342.80											0.960				
37X-3, 70–72	344.00	1.77	1.01	2.82	74.5	43.1	2.92	0.76				0.942				
37X-4, 88–90	345.68	1.73	0.99	2.75	72.3	42.8	2.61	0.75				1.008				
37X-5, 68–70	346.98	1.67	0.98	2.55	66.9	41.0	2.02	0.70								
37X-5, 100–101	347.30											1.002				
38X-1, 99–101	350.99	1.63	0.93	2.67	68.0	42.7	2.13	0.75				0.991				
38X-1, 132–134	351.32	2.10	1.74	2.37	35.5	17.4	0.55	0.21	2788	3088	3015					
39X-CC, 41–43	360.40	1.89	1.37	2.4	50.7	27.5	1.03	0.38								
40X-1, 25–26	369.55											1.037				
40X-1, 32–34	369.62	1.64	1.01	2.64	61.6	38.6	1.61	0.63	1618	1673	1676	0.993				
40X-2, 40–41	370.36											0.914				
40X-2, 100–102	370.96	1.83	1.10	2.58	71.4	39.9	2.49	0.66				1.000				
41X-1, 5–7	379.05	1.77	1.11	2.61	64.8	37.5	1.84	0.60	1614	1668	1667	1.020				
41X-1, 50–51	379.50											0.993				
41X-1, 100–101	380.00											1.067				
41X-2, 41–42	380.91											1.025				
42X-1, 46–47	388.36	1.90	1.41	2.30	47.4	25.5	0.90	0.34								
43X-1, 1–3	397.61	2.38	2.05	2.77	32.4	13.9	0.48	0.16	2570	2934	2747	1.866				
44X-1, 29–31	407.59	1.96	1.58	2.31	37.5	19.6	0.60	0.24	2535	2811	2778					
46X-1, 40–42	427.00	1.88	1.27	2.44	59.3	32.2	1.46	0.48	1979	2087	2072	1.082				
46X-1, 140–142	428.00	1.91	1.38	2.52	51.9	27.8	1.08	0.39	1911	1984	1991	1.218				
47X-1, 107–109	437.27	1.87	1.24	2.62	61.6	33.8	1.60	0.51	1688	1753	1754	1.098				

Table 11 (continued).

Core, section, interval (cm)	Depth (mbsf)	Wet bulk (g/cm³)	Dry bulk (g/cm³)	Grain (g/cm³)	Porosity (%)	Water content (%)	Void ratio	Water ratio	A	B	C	Thermal conductivity (W/m · K)	H	V	Mean	Anistropy
127-797B- (Cont.)																
47X-2, 62-63	438.32	1.87	1.26	3.19	59.7	32.7	1.48	0.49								
47X-3, 25-27	439.45	1.81	1.18	2.51	61.6	34.9	1.61	0.54	1665	1730	1725	1.076				
47X-4, 99-100	441.69	1.83	1.20	2.60	61.8	34.6	1.62	0.53								
47X-5, 101-103	443.21	2.02	1.55	2.57	46.2	23.4	0.86	0.31	2197	2351	2355	1.276				
47X-5, 137-139	443.57	1.66	0.86	2.44	78.4	48.4	3.64	0.94	1776	1830	1830					
48X-1, 100-102	446.90	1.85	1.29	2.66	54.6	30.3	1.20	0.44								
48X-2, 35-37	447.75								1899	2041	2024					
48X-2, 100-102	448.40	1.86	1.32	2.62	53.1	29.3	1.13	0.41								
48X-3, 100-101	449.90	1.92	1.36	2.74	55.1	29.4	1.23	0.42				1.175				
48X-4, 133-135	451.73	1.89	1.26	2.61	61.1	33.1	1.57	0.50	1700	1738	1729	1.172				
48X-5, 51-53	452.41	1.94	1.40	2.56	52.5	27.7	1.10	0.38	1825	1943	1942	1.263				
49X-1, 132-134	456.82	2.74	2.57	2.84	16.8	6.3	0.20	0.07	4157	4259	4228	1.977				
49X-3, 82-84	459.32	1.89	1.26	2.63	61.5	33.3	1.60	0.50	1711	1737	1726	1.261				
49X-4, 47-49	460.47	2.00	1.42	2.72	56.8	29.1	1.31	0.41	1793	1862	1864	1.317				
49X-5, 124-126	462.74	2.05	1.52	2.51	52.0	26.0	1.08	0.35	1956	2040	2052	1.250				
50X-CC, 7-9	465.85	2.81	2.68	2.84	12.9	4.7	0.15	0.05	4504	4803	4785	2.124				
51X-1, 66-68	475.56	1.91	1.34	2.66	55.5	29.8	1.25	0.42	1708	1785	1773	1.179				
51X-2, 99-101	477.39	1.99	1.44	2.64	53.7	27.5	1.16	0.38	1850	1989	1957	1.330				
51X-3, 124-126	479.14	2.03	1.46	2.61	55.8	28.2	1.26	0.39	1788	1873	1840	1.306				
51X-4, 46-48	479.86	1.94	1.37	2.63	56.3	29.6	1.29	0.42	1722	1786	1730	1.285				
51X-4, 63-65	480.03	2.04	1.48	2.64	55.0	27.6	1.22	0.38	1744	1961	1811					
51X-5, 95-97	481.85	2.02	1.44	2.62	56.9	28.9	1.32	0.41	1716	1765	1749					
51X-6, 62-64	483.02	1.97	1.42	2.56	53.2	27.7	1.14	0.38	1748	1801	1773	1.356				
52X-1, 121-123	485.71	2.04	1.48	2.67	55.1	27.7	1.23	0.38								
52X-2, 112-114	487.12	1.95	1.36	2.62	57.2	30.1	1.34	0.43								
52X-3, 20-22	487.70	1.92	1.36	2.64	54.9	29.2	1.22	0.41								
52X-4, 88-90	489.88								1672	1746	1714					
52X-5, 64-66	491.14	1.88	1.26	2.6	60.7	33.0	1.55	0.49								
52X-6, 124-126	493.24	1.91	1.31	2.56	58.9	31.6	1.43	0.46								
52X-7, 16-18	493.66	1.95	1.35	2.72	58.7	30.9	1.42	0.45	1688	1717	1705	1.174				
53X-CC, 10-12	494.44	1.97	1.38	2.62	57.1	29.8	1.33	0.42	1666	1725	1730	1.139				
127-797C-																
2R-1, 144-146	494.94	1.95	1.34	2.82	59.7	31.4	1.48	0.46	1692	1755	1740	1.230				
2R-2, 100-102	496.00	1.75	1.03	2.77	70.2	41.2	2.36	0.70	1875	1891	1887	1.032				
2R-CC, 5-7	496.49	1.99	1.42	2.78	55.4	28.6	1.24	0.40	1694	1750	1749					
3R-1, 45-47	503.45	1.96	1.35	2.81	59.9	31.4	1.50	0.46	1683	1719	1727	1.184				
3R-2, 112-114	505.62	1.96	1.35	2.81	59.9	31.4	1.50	0.46	1712	1758	1742	1.215				
5R-1, 101-103	523.01	1.97	1.33	2.88	62.1	32.4	1.64	0.48	1698	1740	1705	1.142				
5R-2, 114-116	524.64	1.93	1.34	2.79	58.0	30.8	1.38	0.45	1719	1779	1817	1.183				
5R-3, 123-125	526.23	1.89	1.32	2.89	55.5	30.1	1.25	0.43	1712	1769	1749	1.167				
6R-1, 28-30	531.88	1.73	0.96	3.16	75.2	44.4	3.03	0.80	1672	1779	1781	1.140				
6R-1, 94-96	532.54	1.95	1.40	2.81	53.5	28.1	1.15	0.39	1778	1822	1821	1.387				
6R-2, 18-20	533.28	1.73	0.99	3.06	72.6	42.9	2.65	0.75	1777	1794	1780	1.045				
6R-3, 28-30	534.88								1721	1773	1749					
6R-3, 58-60	535.18	1.96	1.36	2.78	58.2	30.4	1.39	0.44	1715	1780	1772	1.182				
6R-3, 58-60	535.18								1705	1756	1760					
6R-5, 80-82	538.40	1.94	1.34	2.77	58.4	30.7	1.40	0.44	1705	1753	1744	1.185				
8R-1, 22-24	551.12	2.06	1.53	2.71	52.1	25.9	1.09	0.35	1719	1829	1808	1.223				
8R-2, 41-43	552.62	2.05	1.50	2.76	53.9	26.9	1.17	0.37	1742	1856	1850	1.282				
9R-1, 90-92	561.50	2.59									4526	1.375				
9R-2, 7-9	562.17	2.68	2.52	2.73	16.0	6.1	0.19	0.07	4468	4527	4462	1.420				
10R-1, 16-18	570.16	2.65	2.56	2.59	8.8	3.4	0.10	0.04			4720	1.437				
10R-4, 109-111	575.25	2.73	2.69	2.75	4.2	1.6	0.04	0.02			5437	1.665				
11R-1, 29-31	579.79	2.20	1.76	2.69	43.2	20.1	0.76	0.25	2113	2157	2108	1.748				
12R-2, 81-83	591.48	2.89	2.89	2.90	0.2	0.1	0.00	0.00			6623	1.752				
12R-4, 35-37	593.92	2.89	2.89	2.91	0.2	0.1	0.00	0.00			6598	1.720				
13R-1, 119-121	599.99	2.61	2.50	2.67	10.2	4.0	0.11	0.04			4737	1.433				
13R-2, 70-72	601.00	2.84	2.82	2.84	1.9	0.7	0.02	0.01			5990	1.595				
14R-1, 49-51	608.79	2.52	2.38	2.62	13.3	5.4	0.15	0.06			4147	1.443				
14R-1, 81-83	609.11	2.32	2.03	2.68	28.6	12.7	0.40	0.15			3205	1.309				
15R-1, 74-76	618.54	2.53	2.36	2.70	16.5	6.7	0.20	0.07			4366	1.416				
15R-3, 43-45	621.09	2.80	2.73	2.75	6.3	2.3	0.07	0.02			5143	1.547				
16R-1, 28-30	627.58	2.81	2.76	2.77	4.7	1.7	0.05	0.02	5664	5636	5851	1.618				
16R-2, 73-75	629.43	2.68	2.59	2.71	9.0	3.5	0.10	0.04	5103	4981	5007	1.482				
17R-1, 35-37	637.25	2.56	2.39	2.76	16.5	6.6	0.20	0.07	4231	4307	4063	1.389				
18R-1, 94-96	647.44	2.11	1.62	2.75	48.3	23.4	0.94	0.31	1888	1988	1980	1.216				
18R-2, 71-73	648.66	2.69	2.56	2.76	12.9	4.9	0.15	0.05	4610	4517	4394	1.454				
18R-3, 60-62	650.05	2.85	2.81	2.85	3.9	1.4	0.04	0.01	5488	5535	5669	1.565				
19R-1, 67-69	656.77	2.61	2.59	2.84	2.3	0.9	0.02	0.01	5817	5925	5782	1.618				
19R-3, 22-24	659.20	2.91	2.91	2.98	0.0	0.0	0.00	0.00	6298	6194	6638	1.830				
19R-4, 67-69	661.06	2.72	2.64	2.69	8.4	3.1	0.09	0.03	4699	4772	4837	1.500				
19R-4, 84-86	661.23	2.37	2.06	2.55	30.4	13.1	0.44	0.15	3082	3387	3374	2.024				
19R-4, 94-96	661.33	2.29	1.97	2.67	31.6	14.1	0.46	0.16	2959	3376	3304					
19R-5, 48-50	662.03	2.08	1.64	2.63	43.3	21.3	0.76	0.27	1939	2104	2037	1.318				
19R-6, 37-39	663.42	1.89	1.47	2.68	41.3	22.4	0.70	0.29	1863	1958	1942	1.226				
20R-2, 61-63	668.01	2.23	1.87	2.72	35.0	16.1	0.54	0.19	2322	2538	2531	1.533				
20R-3, 74-76	669.64	2.72	2.65	2.75	6.9	2.6	0.07	0.03				1.461				
21R-1, 94-96	676.54	2.75	2.71	2.73	4.0	1.5	0.04	0.02				1.664				
21R-3, 75-77	679.09	2.80	2.77	2.77	2.7	1.0	0.03	0.01				1.659				
21R-5, 102-104	682.32	2.84	2.82	2.82	2.0	0.7	0.02	0.01				1.691				

Table 11 (continued).

Core, section, interval (cm)	Depth (mbsf)	Densities Wet bulk (g/cm³)	Dry bulk (g/cm³)	Grain (g/cm³)	Porosity (%)	Water content (%)	Void ratio	Water ratio	Velocity (m/s) A	B	C	Thermal conductivity (W/m · K)	Formation factors H	V	Mean	Anistropy
127-797B- (Cont.)																
22R-1, 124–126	686.34	2.18	1.77	2.68	40.4	19.0	0.68	0.24	2034	2193	2192	1.451*				
22R-1, 124–126	686.34											1.340**				
22R-2, 119–121	687.73	2.18	1.79	2.71	38.6	18.1	0.63	0.22	2142	2304	2285	1.409*				
22R-2, 119–121	687.73											1.512**				
22R-3, 147–149	689.51	2.10	1.67	2.67	42.3	20.6	0.73	0.26	2074	2207	2186	1.335				
22R-4, 70–72	690.24	2.20	1.77	2.78	41.7	19.4	0.72	0.24	2460	2491	2457	1.512				
22R-6, 6–8	692.60	2.13	1.74	2.67	38.3	18.5	0.62	0.23	2044	2213	2149	1.241*				
22R-6, 6–8	692.60											1.489**				
23R-1, 27–29	694.87	2.16	1.76	2.73	38.8	18.4	0.63	0.23	2080	2266	2238	1.429				
23R-3, 79–81	698.39	2.22	1.80	2.73	41.4	19.1	0.71	0.24	2100	2276	2248	1.444				
23R-5, 97–99	701.57	2.17	1.76	2.76	40.3	19.0	0.67	0.24	2410	2680	2597	1.481				
24R-1, 86–88	704.96	2.87	2.85	2.88	1.9	0.7	0.02	0.01	5813	5618	6094	1.724				
24R-2, 8–10	705.47	2.87	2.85	2.87	1.6	0.6	0.02	0.01	5895	5755	5766	1.736				
24R-3, 21–23	707.10	2.86	2.80	2.83	5.4	2.0	0.06	0.02	5079	4958	5258	1.692				
24R-4, 8–10	708.32	2.87	2.86	2.86	0.6	0.2	0.01	0.00			6193	1.717				
24R-5, 38–40	710.12	2.89	2.89	2.89	0.2	0.1	0.00	0.00			6361	1.799				
24R-6, 29–31	711.37	2.89	2.89	2.90	0.3	0.1	0.00	0.00			6263	1.788				
24R-7, 80–82	713.38	2.64	2.59	2.62	5.1	2.0	0.05	0.02			4957	1.436				
25R-1, 144–146	715.04	2.17	1.74	2.69	42.2	19.9	0.73	0.25	2135	2310	2205	1.671				
25R-2, 145–147	716.55	2.20	1.77	2.60	42.2	19.7	0.73	0.25	2059	2235	2150	1.403				
25R-3, 138–140	717.98	2.25	1.82	2.72	41.9	19.1	0.72	0.24	2039	2128	2182	1.380				
25R-4, 66–68	718.76	2.24	1.82	2.76	41.0	18.7	0.69	0.23	2105	2275	2202					
25R-5, 61–62	720.21											1.468				
25R-5, 109–111	720.69	2.22	1.77	2.59	43.8	20.3	0.78	0.25	2166	2304	2321	1.464				
26R-1, 77–79	723.97	2.54	2.36	2.76	17.6	7.1	0.21	0.08			3474	1.509				
26R-2, 48–50	725.18	2.52	2.28	2.67	23.0	9.3	0.30	0.10	2751	2938	2917	2.064				
26R-2, 75–77	725.45	2.44	2.21	2.78	22.1	9.3	0.28	0.10			3271	1.430				
27R-1, 26–28	733.16	2.62	2.47	2.79	14.2	5.6	0.17	0.06			4421	1.502				
27R-1, 126–128	734.16	2.47	2.26	2.73	20.9	8.7	0.26	0.10			3535	1.504				
28R-1, 47–49	743.07	2.59	2.48	2.73	10.7	4.2	0.12	0.04			4520	1.561				
29R-1, 70–72	745.30	2.71	2.60	2.74	11.0	4.1	0.12	0.04			4343	1.782				
30R-1, 60–62	754.60	2.55	2.37	2.61	17.2	6.9	0.21	0.07			3781	1.561				
30R-2, 143–145	756.46	2.28	1.91	2.74	36.2	16.2	0.57	0.19	2337	2504	2334	1.572				
30R-3, 121–123	757.74	2.31	1.95	2.84	34.9	15.5	0.54	0.18	2273	2442	2354					
30R-4, 47–49	758.25	2.24	1.89	2.73	34.7	15.8	0.53	0.19	2377	2547	2500	1.652				
30R-4, 119–120	758.97											1.444				
31R-1, 73–75	763.73	2.72	2.62	2.80	9.5	3.6	0.10	0.04			4735	1.507				
31R-2, 83–85	765.05	2.81	2.76	2.76	5.2	1.9	0.06	0.02			5538	1.553				
31R-3, 105–107	766.44	2.74	2.64	2.86	9.6	3.6	0.11	0.04			4660	1.519				
31R-4, 77–79	767.66	2.41	2.16	2.65	24.2	10.3	0.32	0.12	2745	2912	2912	1.659				
31R-5, 51–53	768.70	2.53	2.28	2.75	24.7	10.0	0.33	0.11	3034	3282	3270	1.600				
32R-2, 15–17	773.79	2.68	2.56	2.82	11.1	4.3	0.13	0.05			4390	1.539				
33R-1, 63–65	782.23	2.80	2.69	2.59	10.5	3.8	0.12	0.04	4518	4535	4401	1.884				
33R-1, 84–86	782.44	2.66	2.47	2.72	18.1	7.0	0.22	0.08	3434	3400	3555	1.852				
33R-1, 103–105	782.63	2.50	2.18	2.70	31.2	12.7	0.45	0.15	2413	2651	2635	1.826				
33R-2, 63–65	783.73	2.27	1.96	2.61	30.1	13.6	0.43	0.16	2279	2558	2501	1.613				
33R-4, 5–7	786.04	2.71	2.62	2.75	9.1	3.5	0.10	0.04			4585	1.610				
34R-1, 33–35	791.33	2.70	2.61	2.80	8.8	3.4	0.10	0.04			4442	1.574				
34R-2, 40–42	792.63	2.22	1.90	2.71	30.8	14.2	0.45	0.17	2337	2550	2522	1.499				
34R-3, 143–145	795.16	2.27	1.92	2.77	34.1	15.4	0.52	0.18	2286	2506	2503	1.471				
34R-4, 143–145	796.66	2.34	1.99	2.74	34.0	14.9	0.51	0.18	2271	2455	2393	1.428				
34R-6, 7–9	798.30	2.25	1.89	2.74	34.9	15.9	0.54	0.19	2310	2492	2498	1.657				
35R-2, 54–56	802.34	2.31	1.96	2.75	34.3	15.2	0.52	0.18	2165	2366	2325	1.446				
35R-3, 4–6	803.34	2.34	1.96	2.76	36.6	16.0	0.58	0.19	2125	2254	2252	1.629				
36R-1, 23–25	805.03	2.15	1.79	2.75	34.6	16.5	0.53	0.20	2183	2330	2190	1.588				
36R-3, 86–88	807.63	2.45	2.10	2.76	33.9	14.2	0.51	0.17	2332	2592	2573	1.569				
37R-1, 98–100	815.38	2.31	1.97	2.74	33.1	14.7	0.49	0.17	2328	2444	2426	1.549				
37R-2, 5–7	815.95	2.33	1.99	2.58	32.7	14.4	0.49	0.17	2396	2539	2422	1.710				
37R-3, 92–94	818.32	2.35	2.03	2.64	30.9	13.4	0.45	0.16	2680	2915	2874	1.892				
37R-5, 50–52	820.90	2.33	2.01	2.64	31.4	13.8	0.46	0.16	2349	2621	2581	1.626				

Note: *Readings taken parallel to bedding. **Readings taken perpendicular to bedding.

the physical parameters we measured are highly uniform with depth and exhibit low variability, with the exception of the grain density, which is highly variable (Table 13). There are small but notable offsets in the physical-property values near the APC/XCB changeover. Whether this is a real phenomenon or an artifact of the XCB coring is uncertain. The mean grain density appears to change (Fig. 45), but the variability also appears to increase.

Unit III (224–301.5 mbsf) sediments are silty clays with traces of diatoms. The grain density increases slightly with depth through the unit, possibly reflecting a decrease in diatom content with depth. The water content and porosity first increase and then decrease with depth, with concomitant decreasing then

increasing wet and dry bulk densities. The thermal conductivity increases slightly with depth.

As at previous sites, Site 794 in particular, the most remarkable feature of the section from the seafloor to 300 mbsf (Units I, II, and III) is the uniformity of all parameters that depend on water content. The profile at Site 797 is similar to that at Site 794 and suggests that there is virtually no consolidation of the sediments with depth of burial over this interval. As we proposed for the Site 794 and Site 795 observations, this behavior is attributable to the extraordinary strength of sediments whose framework contains a significant amount of diatoms.

The boundary between Units III and IV at 301.5 mbsf is near the transition from opal-A to opal-CT. All of the measured

physical properties, with the exception of grain density, show an abrupt and relatively large change at this boundary. Porosity and water content decrease, and there are complementary increases in the bulk densities and the thermal conductivity. There are no velocity measurements on discrete samples across the opal-A/opal-CT transition.

Unit IV (301.5–426.6 mbsf) is silty clay and siliceous claystone with chert and porcellanite zones. The variability of all properties in Unit IV is greater than in the two overlying units, but the sparseness of the data reflects the low core recovery in this interval. The water content and porosity decrease, and the bulk densities and thermal conductivities increase across the unit. The acoustic-velocity data are too sparse for analysis.

Unit V (426.6–627.3 mbsf) is a siliceous claystone with minor tuffs, overlying and interbedded with brecciated and fractured basalt. The physical properties are variable in the upper 30 m of Unit V but are relatively uniform in the middle part of the unit above the contact with the basement rocks. The claystones that are interbedded with the basalts are much lower in water content and higher in density, probably reflecting some thermal interaction with the basalts.

The lowermost unit, Unit VI (646.9–800.3 mbsf), is a sequence of sandstone, siltstone, and claystone, interbedded with basalt (Fig. 47). The water contents range from 10% to 24%, much lower than the units overlying the basalts, which is indicative of a higher degree of consolidation and/or thermal alteration and dewatering through interaction with the basalts.

Physical Properties of the Basement Units

The basement rocks consist of a series of basalts of variable alteration and brecciation interbedded with sedimentary units. Twenty-one separate units have been defined (see "Basement Rocks," this chapter), so a detailed statistical analysis and discussion for each basement unit is precluded. We have collected physical properties data for samples from the upper fifteen units. The wet bulk density, grain density, water content, porosity, thermal conductivity, and acoustic velocity are plotted vs. depth for the interbedded section in Figure 47. We note a qualitative correlation of the lowest water content, essentially zero, and the highest acoustic velocity, about 6600 m/s, with the freshest basalts, at about 591 to 594 mbsf. The more vesicular basalts of the lower units, Units 13 and 14 in particular (approximately 731 to 755 mbsf), are conversely more porous and have lower acoustic velocities. The statistical properties of the basement rocks for Units 1 through 9 (558 to 715 mbsf) (Table 18A), and for Units 10 through 15 (725 to 792 mbsf) (Table 18B), have been calculated together. These are approximately representative of the fresher and more vesicular units, respectively, though there are specific units within each grouping that are not characteristic of the group. As an example, Unit 1, a brecciated basalt, has water contents that are similar to those of Units 14 and 15. Some of the samples from Unit 13 have water contents more akin to those of Unit 6.

Discussion

Physical-Property Correlations

Taken as a whole, the physical properties clearly delineate the igneous units from the interbedded sedimentary units. The water contents of the igneous units never exceed 10%, with coincident high acoustic velocities and wet bulk densities. The thermal conductivity is often lower in the igneous rocks than it is in the sediments, which is similar to results from Sites 794 and 795. This may reflect a higher terrigenous (i.e., quartz) content in the sediments and/or a higher carbonate content.

The wet bulk density is plotted vs. water content in Figure 48A. The error in the wet bulk density determinations is apparent when the data are compared with model curves for various grain densities. The matching model curve at high water contents requires an unreasonably high grain density. Note that for low porosities and water contents, for which there is likely to be less error in the wet and dry volume measurements, the wet bulk density vs. water content suggests a grain density near 2.9 g/cm³, not far off the average igneous grain density of about 2.8 g/cm³.

The same effect can be seen when we examine the acoustic velocity vs. porosity (Fig. 48B). Model curves for a grain density of 2.9 g/cm³ and grain velocity of 6600 m/s are plotted for comparison. The weighted Wood-Wyllie model curve (Nobes et al., 1986) follows the trend in the data well, but the grain density is anomalously high, especially for the sediments. Again, we suggest that the porosity is systematically high and point to the volume determination as a likely suspect.

Finally, the thermal conductivity in the basement units is commonly lower than in the overlying and the interbedded sediments. This can also be seen in the plot of thermal conductivity vs. porosity (Fig. 48C). The samples from the igneous rocks cluster about the model curve for a grain thermal conductivity of 1.7 W/m · K, which is typical for relatively fresh basaltic rocks (Hyndman et al., 1977). The thermal conductivities of the sediments, on the other hand, appear to require grain thermal conductivities as high as 4 W/m · K. Calcite has a grain thermal conductivity of about 5 W/m · K, and quartz has a grain thermal conductivity of 10 W/m · K. A significant component of carbonate and/or quartz is indicated. There is some evidence for higher carbonate content in both the lithostratigraphy (see "Lithostratigraphy") and in the inorganic-chemistry analysis.

Comparison with Site 794 Results

The variation of physical properties with depth at Site 797 mimics the major features of the Site 794 profiles quite closely. Figure 49 shows the wet bulk density, grain density, and water-content profiles from both sites. For clarity, the data for Site 794 have been offset by arbitrary amounts to the left; the data values for the two sites are quite similar. The uniformity of the bulk density in the upper 300 m and the pronounced effects of the opal-A/opal-CT transformation, which occurs at nearly the same depth, are clearly seen in both profiles. Along many sections of the profiles even the small-scale variations match. Both profiles have increasing wet bulk density, and decreasing water content, in the upper 40 m. Both have two small but notable excursions between 40 and 60 mbsf. The variations in the wet bulk density and water content between about 300 mbsf, the opal-A/opal-CT boundary, and the first encounter with basement, near 540 to 550 mbsf, follow quite closely in form and magnitude. The close correlation of the two profiles suggests similar sedimentation, diagenetic, and thermal histories. The two sites are from opposite ends of the Yamato Basin and indicate that the sediment physical properties are controlled by basinwide processes. We may be able to associate a number of the features identified in the physical-property profiles with reflectors in the seismic profiles, which could be traced across the Yamato Basin. These common basinal reflectors could then be tied to the results from Sites 794 and 797.

DOWNHOLE MEASUREMENTS

Operations

Downhole measurements were made in two of the holes drilled at Site 797. In Hole 797B, seven measurements of temperature ahead of the bit were made using the Barnes/Uyeda probe. Logging operations, including the full suite of Schlumberger logs and the borehole televiewer (BHTV) developed at Lamont-Doherty Geological Observatory (LDGO), were run in Hole 797C.
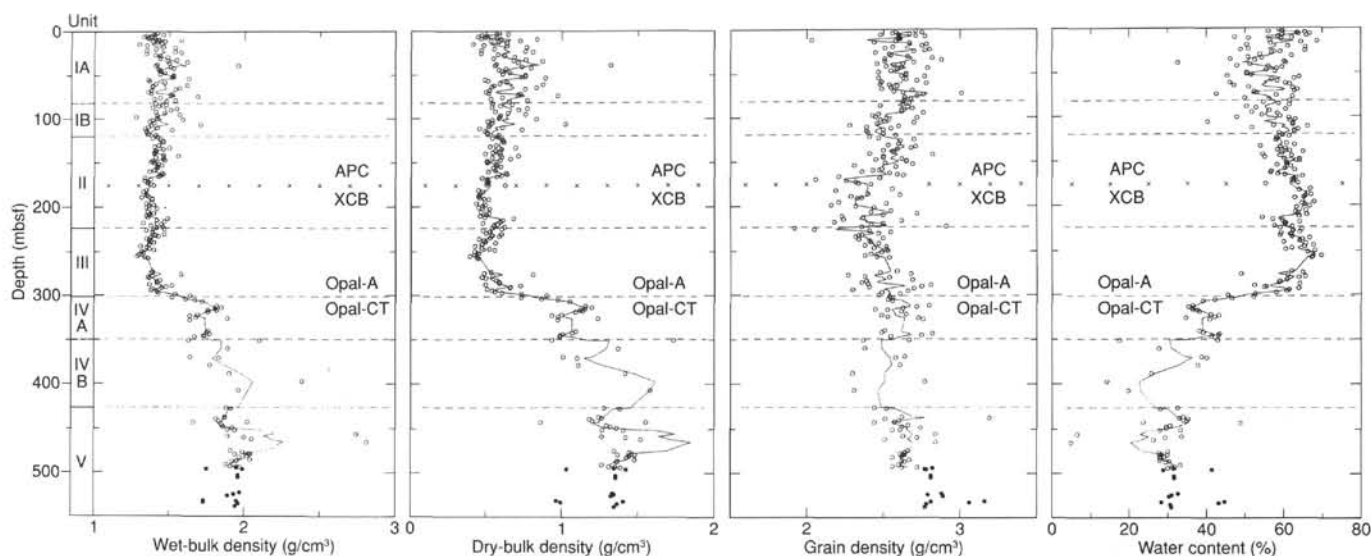
Figure 45. Plots of principal physical properties from the sedimentary section vs. depth for Site 797. For wet bulk density, dry bulk density, grain density, water content, porosity, and thermal conductivity, open circles and the solid curve represent data from Holes 797A and 797B; and solid circles, data from Hole 797C. The curve represents a five-point tapered running mean. Note the approximately constant dry bulk density in the upper 300 m, indicating an approximately constant mass-accumulation rate, and the sharp rise at the opal-A/opal-CT boundary. For acoustic velocity, the solid curve down to the APC/XCB changeover represents P-wave logger velocity; Hamilton Frame velocities given below the opal-A/opal-CT transition are as follows: barbed circles = A direction parallel to core; squares = B direction; triangles = C direction; horizontal line = range of values for a given discrete sample.

A rotatable packer was inserted into the BHA prior to logging, but severe and deteriorating hole conditions led to the decision to abandon the attempt to carry out the packer experiment. After pulling it out of the hole, it was seen that the outer layer of rubber on the inflatable element of the packer was completely abraded away while cleaning the hole for logging. A planned vertical seismic profile (VSP) was not run at this site because the hole was extremely out of gauge (more than 18 in.), precluding the good clamping needed for a VSP.

Temperature Measurements

Five of the seven runs with the Uyeda probe yielded valid formation temperatures. One run appears to have been partially retracted after penetration, and for another the data were lost. The virgin formation temperatures for all of the runs for which valid data were obtained are shown in Table 19 and plotted vs. depth in Figure 50. The temperatures describe a nearly uniform increase of the temperature with depth with a best-fit gradient of 121°C/km. A similar value was found at Site 794.

Equilibrium temperatures in the sediment for each run were estimated by extrapolating the temperature history after penetration to equilibrium using plots of temperature vs. 1/time. The temperature histories of all of the downhole runs spanning the time interval that the probe was in the sediment are shown in Figure 51. The trace for the run at 111.4 m (run 4) shows evidence of a strong disturbance. To be in accord with the other runs, the equilibrium temperature should be 13°–14°C; however, after rising sharply to about 8°C for the first two cycles the temperature dropped to a level close to that observed at 26 m. On this run the probe probably penetrated fill at the bottom of the hole and then was inadvertently partially retracted. This run did not yield a valid temperature. Run 1 showed an anomalous increase in temperature toward the end of the observation period, but the early part of the record permits extrapolation to a reasonable value. The temperatures recorded at the seafloor before penetration are 0.2°C, which agrees with hydrographic measurements of deep-water temperatures in the Japan Sea and in-

dicates that the thermistor probe held its calibration throughout all of the measurements made on Leg 127.

Thermal-conductivity measurements were made on cores from Holes 797A, 797B, and 797C using the needle-probe technique in unconsolidated and semiconsolidated sediments and the "half-space" technique for indurated sediments and igneous-rock samples. The values adjusted to in-situ conditions (Ratcliffe, 1960) are plotted vs. depth in Figure 52. More information on the conductivity measurements can be found in the section on physical properties. The heat flow associated with the thermal gradient measured in Hole 797B was determined by calculating the thermal resistance of the sedimentary section between the seafloor and the depth of each temperature measurement (Table 19). A plot of formation temperatures vs. thermal resistance is shown in Figure 53. The slope, $\Delta T/\Delta R$ of the linear regression to the temperature points, gives the best estimate of the heat flow through the upper 220 m of sediment at Site 797. The nearly linear increase of temperature with resistance seen in Figure 53 indicates a conductive thermal regime and a heat flow of 101 mW/m². The error associated with this heat-flow determination is estimated to be ±5%.

A seafloor heat-flow measurement made close to Site 797 obtained a value of 102 mW/m² (Yamano et al., 1987); thus the heat flow can be considered very well determined in the vicinity of the site. Both measurements are within the error of measurement of the mean for the Yamato Basin average (Tamaki, 1986). A line of seafloor stations roughly along the line of seamounts that lie near the central axis of the Yamato Basin yielded heat-flow values that are lower on average and more variable. These seamounts penetrate the sediment cover and may promote hydrothermal flux through the seafloor which will reduce the apparent conductive flux and increase the variability.

The thermal-conductivity profile in the section deeper than 220 m and the heat-flow value in Hole 797B allow temperatures at deeper, unsampled levels of the section to be estimated by extrapolation. The estimated temperature profile is shown in Figure 54. This profile yields the following estimated temperatures:
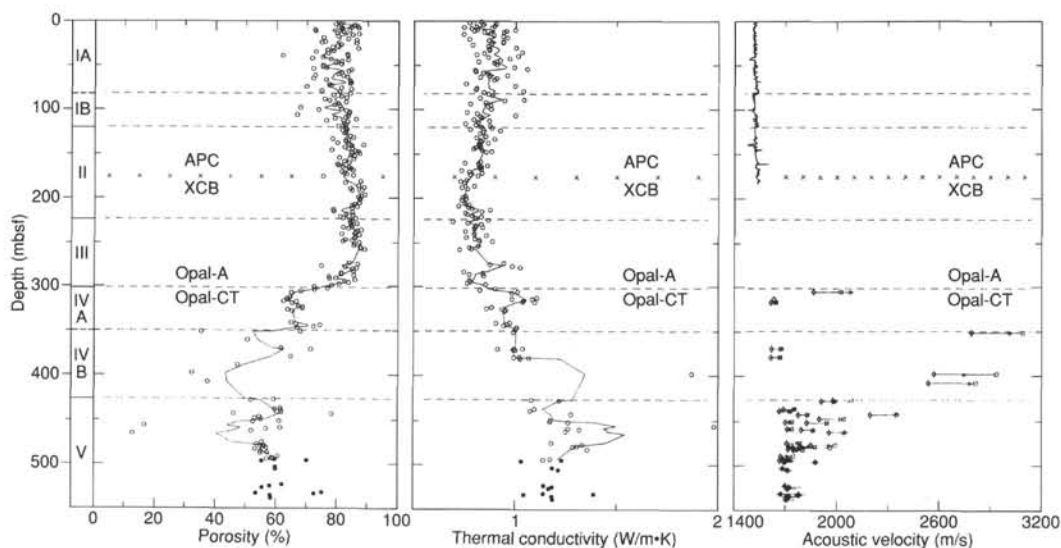
Figure 45 (continued).
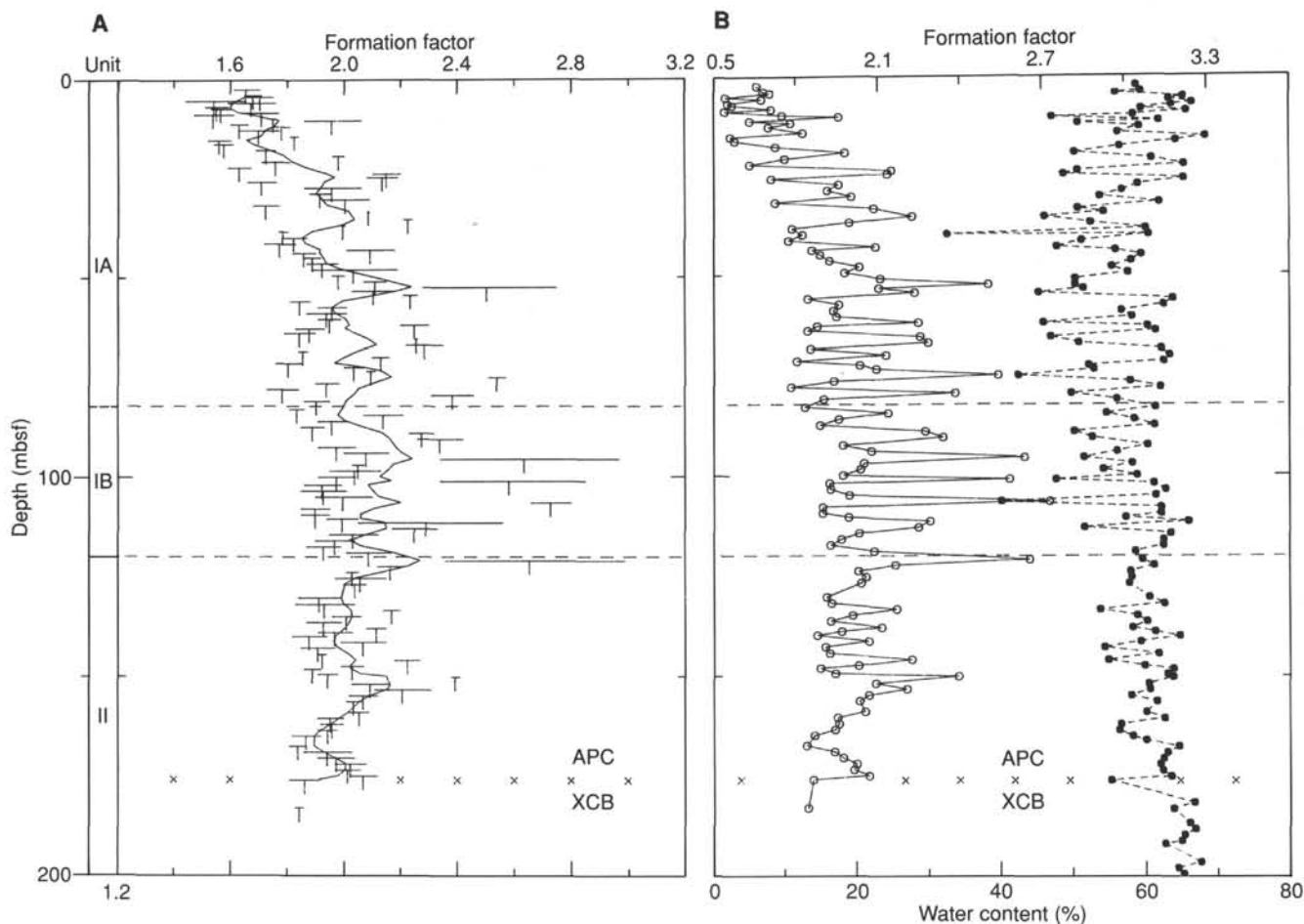
Figure 46. **A.** Formation factor vs. depth for Holes 797A and 797B. The horizontal lines connect values measured across the core axis and along the axis. The vertical barb indicates the geometric mean formation factor. The solid curve represents the five-point tapered running mean of the mean formation factor. **B.** Geometric mean formation factor (open circles) and water content (solid circles) vs. depth for Holes 797A and 797B. Note the similarity in the data; the formation factor is principally a measure of the water content, though a detailed examination shows that some scatter is evident in the correlation.

Table 12. Statistical characteristics of Unit I physical properties, Site 797.

	Units	Mean	Standard deviation	Minimum	Maximum
Unit I (0–119.9 mbsf, Holocene to Pliocene)					
Wet bulk density	g/cm^3	1.46	0.10	1.28	1.96
Dry bulk density	g/cm^3	0.64	0.15	0.41	1.32
Grain density	g/cm^3	2.60	0.14	2.03	3.01
Water content	%	56.6	6.6	32.4	68.3
Porosity	%	79.8	4.9	62.0	87.0
Thermal conductivity	W/m · K	0.873	0.077	0.744	1.057
Mean formation factor		1.96	0.25	1.54	2.73
Formation anisotropy		1.03	0.03	0.96	1.13

Table 13. Statistical characteristics of Unit II physical properties, Site 797.

	Units	Mean	Standard deviation	Minimum	Maximum
Unit II (119.9–224 mbsf, upper Pliocene)					
Wet bulk density	g/cm^3	1.41	0.05	1.32	1.56
Dry bulk density	g/cm^3	0.55	0.07	0.44	0.71
Grain density	g/cm^3	2.47	0.17	2.06	2.91
Water content	%	61.3	3.4	53.7	67.6
Porosity	%	84.0	2.9	75.4	89.1
Thermal conductivity	W/m · K	0.805	0.047	0.720	0.925
Mean formation factor		2.02	0.16	1.84	2.67
Formation anisotropy		1.03	0.02	0.99	1.13

at the opal-A/opal-CT boundary at 290 mbsf, 36°C; at the top of the basalt/sediment, 56°C; and at the bottom of the hole, 76°C.

Logging

Three Schlumberger tool strings were run in Hole 797C: the geophysical/lithodensity tool string, which was run once, the geochemical tool string, which was run once through the drill pipe with a 10-m interval in the open hole initially, and the formation microscanner (FMS), which was run three times. The temperature tool was run successfully on the bottom of the Schlumberger tool strings five times.

The first stage of logging operations in Hole 797C was conducted in the open hole between 100 and 534 mbsf. Both upgoing and downgoing runs were made for the geophysical/lithodensity tool string. However, because of a slower logging speed the upgoing logs are of higher quality and are the only logs displayed. Only upgoing runs were made with the FMS tool. The hole constriction at 540 mbsf precluded logging the basement in this first stage. Basement had been drilled at this time to a total depth of 800 mbsf.

For the second stage of logging operations in Hole 797C, the geophysical/lithodensity tool was rigged down and the pipe was lowered to try to break through the bridge at 540 mbsf. This was successful, but another more severe hole constriction in the basement was encountered at 567 mbsf. The FMS was run again from 568 mbsf up to 544 mbsf to provide an overlapping sequence. To keep the hole conditions from deteriorating further, it was decided to run the geochemistry tool string through the pipe from 567 mbsf to the seafloor. However, the first 10 m of this upgoing geochemistry run was conducted in the open hole. The geochemistry tool yields valuable data from behind drill pipe, but measurements suffer from drill-pipe attenuation and, more significantly, drill-collar attenuation.

A third stage of logging operations in Hole 797C began with rigging up of the side-entry-sub assembly. The side-entry-sub assembly is a device that allows the wireline to enter the drill pipe from the side so that pipe can be lowered up and down the hole while logging. The pipe cannot be rotated, but by lowering and raising the heavy drill pipe it is possible to break through some constrictions, thus keeping the hole clear. By utilizing the side-entry-sub assembly, another 35 m of FMS logs was acquired. The logs from 603 mbsf upward logged the contact between the sediment and the shallowest basalt at 554 mbsf.

A summary of logging depths reached is presented as Table 20.

Log Quality and Processing

The quality of the logging data acquired at this site was variable. The preliminary data from the FMS tool strings looked

Table 14. Statistical characteristics of Unit III physical properties, Site 797.

	Units	Mean	Minimum	Maximum	Gradient (/100 m)
Unit III (224–301.5 mbsf, lower Pliocene to upper Miocene)					
Wet bulk density	g/cm^3	1.40	1.29	1.64	0.14 ± 0.04
Dry bulk density	g/cm^3	0.54	0.39	0.90	0.21 ± 0.06
Grain density	g/cm^3	2.47	2.05	2.81	0.25 ± 0.08
Water content	%	61.5	45.2	69.5	− 10.9 ± 3.0
Porosity	%	83.8	72.6	89.2	− 7.5 ± 2.1
Thermal conductivity	W/m · K	0.820	0.692	1.026	0.06 ± 0.05

Table 15. Statistical characteristics of Unit IV physical properties, Site 797.

	Units	Mean	Minimum	Maximum	Gradient (/100 m)
Unit IV (301.5–426.6 mbsf, upper Miocene)					
Wet bulk density	g/cm^3	1.78	1.52	2.38	0.32 ± 0.09
Dry bulk density	g/cm^3	1.14	0.73	2.05	0.57 ± 0.02
Grain density	g/cm^3	2.58	2.30	2.82	
Water content	%	36.8	13.9	51.9	− 18.6 ± 4.3
Porosity	%	62.7	32.4	77.0	− 24.8 ± 5.6
Thermal conductivity	W/m · K	1.014	0.827	1.866	0.25 ± 0.11
Acoustic velocity, A	m/s	2029	1614	2788	
Acoustic velocity, B	m/s	2263	1644	3088	
Acoustic velocity, C	m/s	2230	1643	3015	

Table 16. Statistical characteristics of Unit V physical properties, Site 797.

	Units	Mean	Standard deviation	Minimum	Maximum
Unit V (426.6–627.3 mbsf, middle Miocene)					
Wet bulk density	g/cm³	1.97	0.20	1.66	2.81
Dry bulk density	g/cm³	1.40	0.31	0.86	2.68
Grain density	g/cm³	2.70	0.16	2.44	3.19
Water content	%	29.6	7.4	4.6	48.4
Porosity	%	55.6	11.2	12.9	78.4
Thermal conductivity	W/m · K	1.270	0.226	1.032	2.124
Acoustic velocity, A	m/s	1774	139	1705	2113
Acoustic velocity, B	m/s	1843	133	1753	2157
Acoustic velocity, C	m/s	1999	469	1744	3205

Table 17. Statistical characteristics of Unit VI physical properties, Site 797.

	Units	Mean	Standard deviation	Minimum	Maximum
Unit VI (627.3–800.3 mbsf)					
Wet bulk density	g/cm³	2.26	0.15	1.89	2.66
Dry bulk density	g/cm³	1.89	0.21	1.47	2.47
Grain density	g/cm³	2.70	0.06	2.55	2.84
Water content	%	16.6	3.9	7.0	23.4
Porosity	%	36.1	6.8	18.1	48.3
Thermal conductivity	W/m · K	1.522	0.198	1.216	2.064
Acoustic velocity, A	m/s	2336	366	1863	3434
Acoustic velocity, B	m/s	2515	389	1958	3400
Acoustic velocity, C	m/s	2484	406	1942	3555

particularly promising and provided valuable information over the zone of poor core recovery. The logs of the upper 350 m of the hole show very uniform properties owing to the high water content of the sediments. These logs are almost identical to logs from a similar interval at Site 794. Each log shows large changes at the opal-A/opal-CT diagenetic boundary at about 302 mbsf with no depth shift applied to the data.

The long-spaced sonic (LSS) log at Site 797 showed the most severe noise problems of any of the Leg 127 sites. These noise problems were limited to the interval from 350 to 460 mbsf. Sonic data consist of a collection of microseismograms. The source is an impulse generated at one end of the tool and recorded by receivers a fixed distance away from the receivers. For purposes of calculating velocities, the first break in the microseismogram or waveform, representing the *P*-wave arrival and called the traveltime, is detected. Noise in the interval from 350 to 460 mbsf can be attributed to the large number of thin (5–50 cm), low-porosity, high-velocity (up to 3000 m/s) layers interbedded between lower velocity siliceous claystones (up to 1700 m/s) in Units IV and V (see Fig. 55). These layers produce strong acoustic contrasts, causing most of the amplitude of incoming wavefronts to be reflected back toward the source instead of being transmitted to the receiver. Therefore, only a small fraction of the original impulse amplitude is preserved at the receiver location. A lack of high-amplitude coherent arrivals causes noise peaks and multiples to be picked as the first arrivals instead of the proper waveform, thus denying accurate velocity determinations.

An algorithm (Srivastava, Arthur, et al., 1987) to reduce noise was applied to the sonic data. This algorithm computes mean and median traveltimes by combining eight different source-receiver traveltime pairs and by editing poor values. In processing this sonic log, we removed approximately 5% of the traveltimes. The interval from 369 to 382 mbsf in particular contained so many spurious values that none of the eight traveltime values were valid, and no velocity could be determined.

The circuits used to count electrons at various energy levels and frequencies malfunctioned in the hostile-environment lithodensity tool (HLDT). Therefore, electron density logs, both from the long- and short-spacing detectors, and the photoelectric-effect logs were physically recorded, but the data from this site are not usable.

The geochemical log was run through the pipe, requiring corrections for the attenuation effects from the pipe and drill collars. This processing was not completed in time for this publication. Nevertheless, general trends are readily evident from the data and are discussed below.

Gamma Ray, Sonic, Resistivity

Figure 56 summarizes the gamma-ray, sonic, and resistivity logs. The gamma-ray log is from the compensated gamma-ray (CGR) log, and the resistivity is from the deep resistivity measurement and is plotted on a linear scale; the sonic-log velocity is from the processed sonic log measured in meters/seconds.

Lithologic Unit I consists of clay and silty clay from 0 to 120 mbsf. Diatom ooze represents a minor lithology, and interbeds of ash are present. Logging was performed from 80 to 120 mbsf in Unit I, but only the CGR log is displayed for this interval. The CGR measures the natural radioactivity of potassium, uranium, and thorium in the sediments. The uranium and thorium counts come almost exclusively from clay minerals, whereas the potassium counts reflect the distribution of both minerals and albitic feldspars. However, for the grain sizes and lithologies at this site we expect most of the potassium, and therefore most of the CGR response, to be due to clay minerals.

Lithologic Units II and III can be grouped together on the basis of their relatively uniform log responses. Both units consist dominantly of diatom ooze and clay. A positive gradient in velocity and a negative gradient in resistivity are readily discernible in Figure 56. The gradient in velocity may be associated with increasing strength of the sediment framework, and the negative gradient in resistivity is due to the increasing temperature with depth. Like Site 794, very high porosities are encountered at Site 797. Thus the physical properties of seawater dominate the log responses in these units. The gamma-ray log, however, is sensitive to clay mineralogy and chemistry and thus is more variable through Units I, II, and III. In Unit II, the gamma-ray log is highly variable, ranging from 10 to 45 American Petroleum Institute (API) units. Excellent core recovery by APC piston cores allows us to unravel the gamma-ray profile. From 120 to 145 mbsf the gamma ray varies between 20 and 30 API units. An increase is seen at 150 mbsf, the location of Core 127-797B-17H owing to a change in lithology to diatom clay from diatom ooze. The next core, Core 127-797B-18H, at 163 mbsf, shows calcareous cementation and possible dissolution of clays, and thus a gamma-ray minimum. The gamma-ray response from 170 to 185 mbsf decreases until the diatom/ooze contact at 185 mbsf. The clay content increases slightly at the Unit II/ Unit III boundary (200 to 224 mbsf) as the percentage of diatoms decreases.

The variability of the gamma-ray log decreases considerably in Unit III, ranging between 20 and 30 API units and reflecting the dominance of the clay and silty clay.

Lithologic Subunit IVA consists of silty clay and siliceous claystone, and Subunit IVB consists of siliceous claystone with chert and porcellanite. The total unit extends from 302 to 427 mbsf. A large change in the log responses and increased variability is seen at and below the opal-A/opal-CT boundary at about 302 mbsf. Here the resistivity increases to about 0.5 ohm-m, and the sonic velocity to about 1700 m/s. These changes are related to the 15%–20% decrease in porosity typically encountered across this diagenetic transition. Remarkable features of the logs through Unit IV include the sawtooth nature of the re-
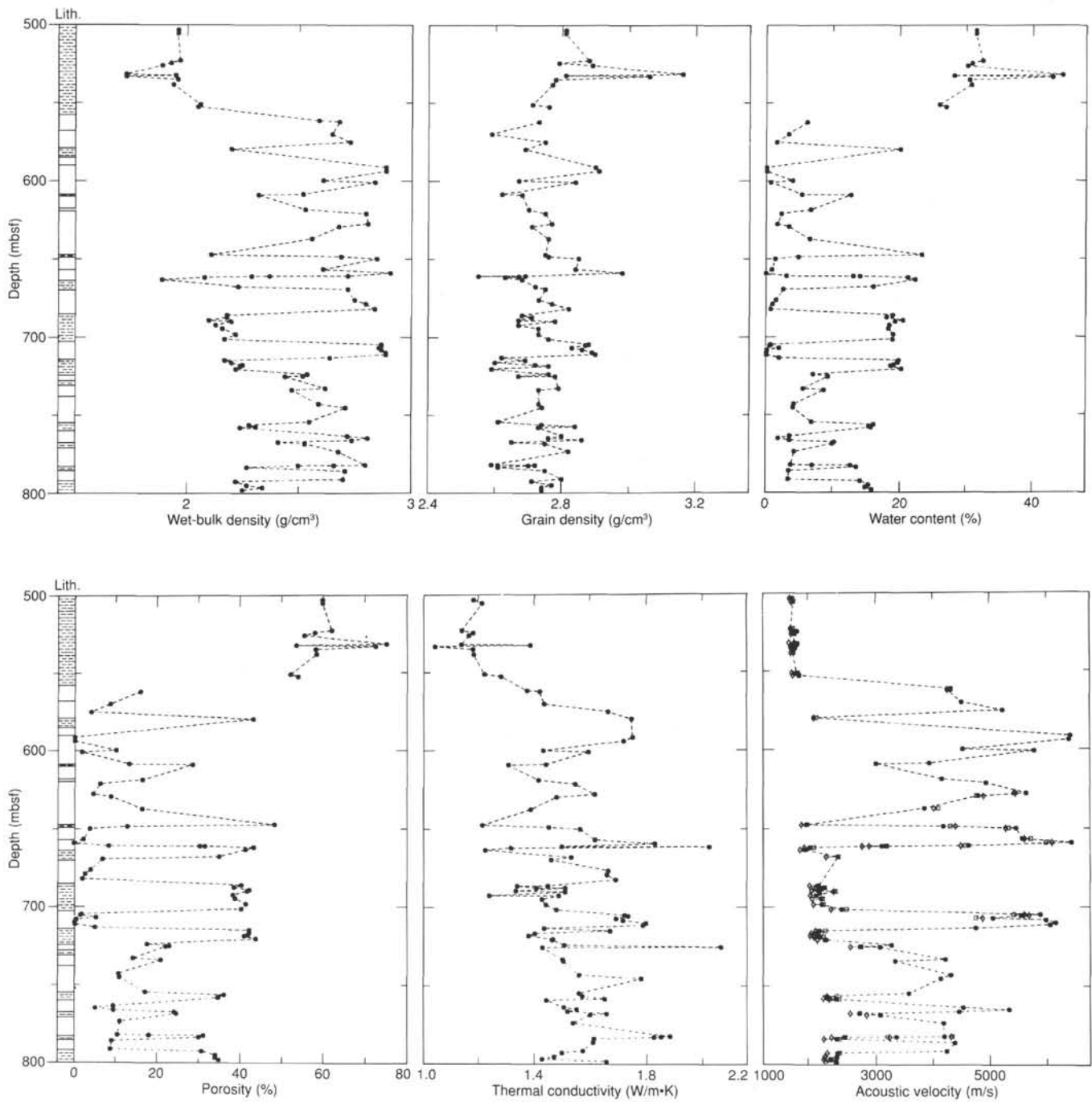
Figure 47. Plots showing wet bulk density, grain density, water content, porosity, thermal conductivity, and acoustic velocity vs. depth in the interbedded igneous/sediment section of Hole 797C. The lithology is also schematically presented. Shaded areas indicate sediments, and open areas, basalt. Unit boundaries are marked by horizontal lines.

sistivity profile in particular, which is also seen in the gamma-ray and sonic logs. This cyclic behavior is most likely due to the numerous chert and porcellanite layers between siliceous-claystone layers encountered from 350 to 410 mbsf. The FMS log and neutron-porosity log confirm these observations, as discussed below. The extreme variation in physical properties encountered in this zone played havoc with the sonic log and created numerous noise problems. Velocities vary by more than 500 m/s over 15-cm intervals. Velocities for the interval from

369 to 382 mbsf could not be salvaged with on-board processing.

The gamma-ray log in Unit IV begins at 302 mbsf, with the large increase due to opal-A/opal-CT diagenesis. The diagenetic process creates a porosity minimum and a concentration of clay, yielding a maximum reading of 70 API units. As the clay is replaced by siliceous claystone through 350 mbsf, the gamma-ray log values decrease. From 350 mbsf through the end of Unit IV at 420 mbsf, the gamma-ray profile becomes broadly

Table 18. Statistical characteristics of igneous unit physical properties, Site 797.

	Units	Mean	Standard deviation	Minimum	Maximum
		A. Units 1 through 9 (553.5–713.8 mbsf)			
Wet bulk density	g/cm³	2.75	0.12	2.52	2.91
Dry bulk density	g/cm³	2.70	0.17	2.36	2.91
Grain density	g/cm³	2.78	0.10	2.59	2.98
Water content	%	2.2	2.0	0.0	6.7
Porosity	%	5.7	5.1	0.0	16.5
Thermal conductivity	W/m · K	1.587	0.138	1.375	1.830
Acoustic velocity, A	m/s	5264	632	4231	6298
Acoustic velocity, B	m/s	5227	598	4307	6194
Acoustic velocity, C	m/s	5380	806	4063	6638
		B. Units 10 through 15 (723.4–791.8 mbsf)			
Wet bulk density	g/cm³	2.65	0.11	2.44	2.81
Dry bulk density	g/cm³	2.51	0.16	2.21	2.76
Grain density	g/cm³	2.75	0.07	2.59	2.86
Water content	%	5.1	2.17	1.9	9.3
Porosity	%	13.0	4.99	5.2	22.1
Thermal conductivity	W/m · K	1.593	0.136	1.430	1.884
Acoustic velocity, A	m/s	4518			
Acoustic velocity, B	m/s	4535			
Acoustic velocity, C	m/s	4243	606	3271	5538

cyclic, ranging from 10 to 45 API units. A gamma-ray minimum at 400 m corresponds to the greatest number of chert layers and the poorest XCB core recovery.

Lithologic Unit V is the final sedimentary unit logged and consists of a siliceous claystone with tuff interbeds. Logging in Unit V was accomplished to a total depth of 510 mbsf; Unit V extends to 554 mbsf, the first sediment/basement contact. The resistivity profile is uniform in Unit V and shows a negative gradient with depth as in Units II and III owing to increasing temperature. The sawtooth pattern so prevalent in the logs of Unit IV disappears in Unit V. A few chert layers encountered at 452–456 mbsf affect the sonic and resistivity logs, but these chert layers show less dramatic effects than those between 350 and 450 mbsf in Unit IV. The sonic log displays values of 1700 to 1800 m/s in general and are surprisingly low for these depths. This observation is confirmed by the physical-property data, indicating that high porosities are still maintained for the sediments in Unit V. The tuff unit from 485 to 490 mbsf is well delineated by high resistivities and sonic velocities at this depth. The gamma-ray log in Unit V is surprisingly variable, considering the uniformity of lithology and the sonic and resistivity log responses. The gamma-ray log varies between 30 and 50 API units. Core recovery was good through this interval, so it should be possible to resolve the source of variability.

Porosity and Caliper

Neutron-porosity (PORS, porosity divided by 100) and caliper (CALI, inches) logs extracted from the geophysical/lithodensity tool-string run are plotted in Figure 57. The porosity log is highly variable and shows porosity to be generally uniform, averaging 55% through 350 mbsf. Beginning at 350 mbsf and coinciding with the introduction of the numerous chert layers, the porosity shows many sharp decreases to as low as 30% porosity. This character lasts until 430 mbsf, where the porosity returns to an average of 50%. A short interval just below 450 mbsf also shows some low-porosity cherty zones and is confirmed by the FMS log.

The caliper log strongly reflects the washed-out conditions encountered at the top of the hole. As an example, from 100 to 290 mbsf the hole diameter is more than 16 in., the maximum typical value gauged on scales. With the increase in consolida-
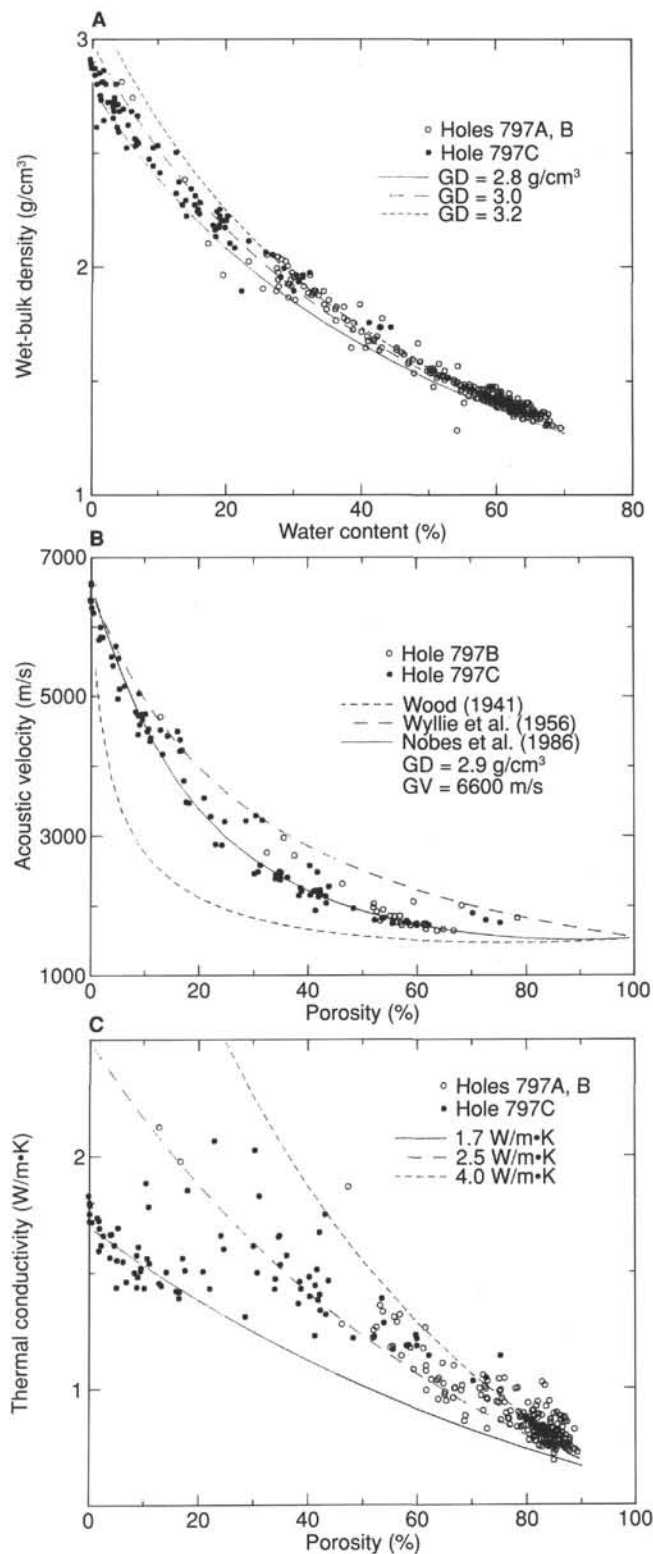
Figure 48. Physical-property plots for Site 797. **A.** Wet bulk density vs. water content. GD = grain density. **B.** Acoustic velocity vs. porosity. The Wood (1941) and Wyllie et al. (1956) curves bracket the data. GV = grain velocity. **C.** Thermal conductivity vs. porosity. Measurements in the igneous units cluster about the model curve for a grain thermal conductivity of 1.7 W/m K. The curves are derived from the geometric mean relation between conductivity and porosity. Curves for three different grain conductivities are shown.
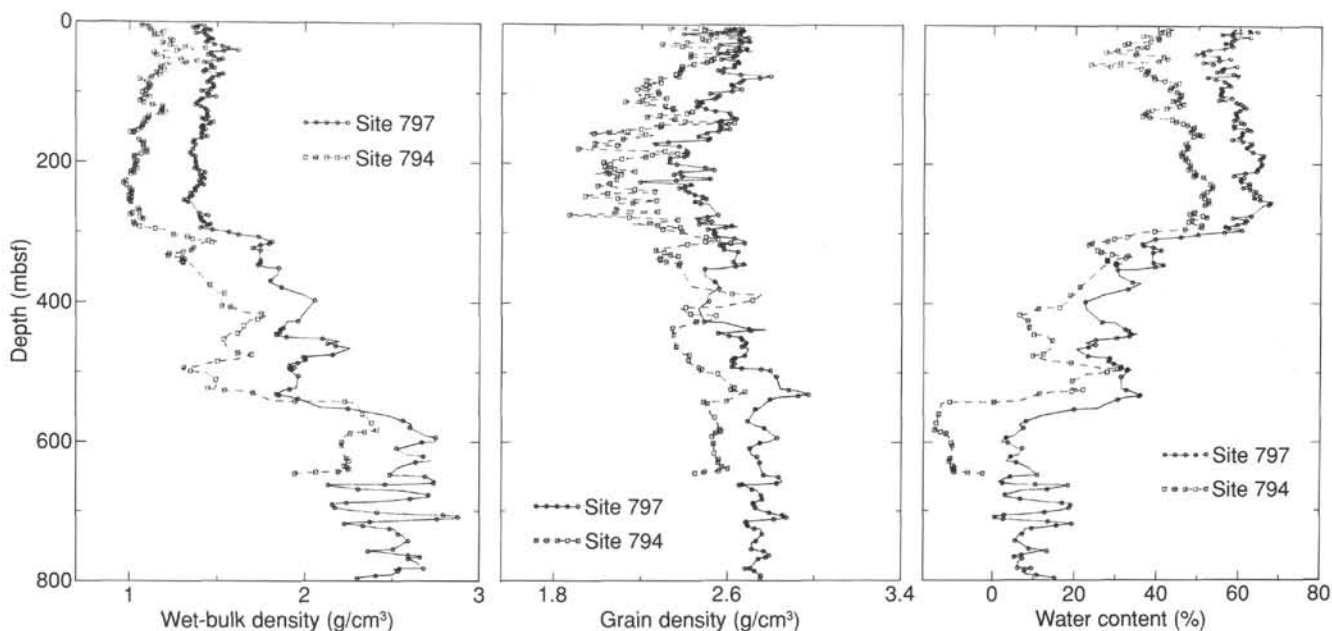
Figure 49. Comparison of five-point tapered running means for wet bulk density, grain density, and water content from Sites 797 and 794. For clarity, the data from Site 794 have been offset by approximately 0.3 unit to the left for wet bulk density and grain density, and 15 units to the left for water content. One of every two data points has been plotted; outliers have been filtered from the data.

Table 19. Downhole temperature measurements, Hole 797B.

Measurement no.	Next core no.	Depth (mbsf)	Temperature (°C)	Thermal resistivity (m^2 – K/W)
0	1	0.0	0.2	0.0
*1	4	25.9	3.1	31.44
2	7	54.4	7.00	63.95
3	10	82.9	10.37	97.83
**4	13	111.4	—	—
5	16	138.9	17.27	164.58
6	21	185.5	22.57	222.10

* This run shows an anomalous increase of temperature at the end of the observation period. Early part of record yields a reasonable value.

** The probe appears to have penetrated fill at the bottom of the hole.

tion and silica content, the well-bore diameter decreases to a value of 10 in. at 350 mbsf. A slight washed-out zone occurs from 350 to 380 mbsf. From 380 to 420 mbsf, the caliper response is extremely uniform, which is surprising, considering that this interval corresponds to the highest number of chert layers. From 420 to 450 mbsf the hole caliper becomes larger until 450 mbsf, where the maximum enlargement below 400 m is reached.

Geochemistry

The geochemical tool string measures the concentrations of aluminum, iron, calcium, chlorine, hydrogen, silicon, sulfur, potassium, thorium, and uranium. Figure 58 displays the uncorrected aluminum reading plus the uncorrected but normalized counts of silicon, calcium, iron, sulfur, hydrogen, and chlorine. The elemental percentages were normalized by dividing each element by the total number of counts.

The largest anomalies recorded by the geochemical logging tools are the effects of the drill collars, BHA, and pipe. Although these effects could not be removed on board, it is possible to discern broad geochemical trends. The most significant
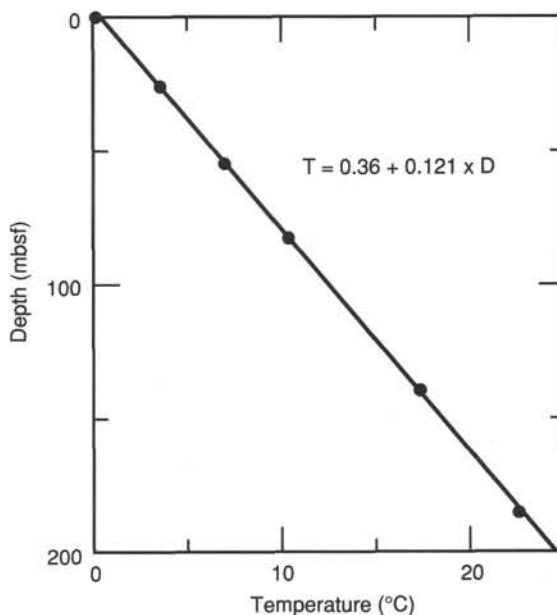
Figure 50. Downhole temperatures plotted vs. depth. The line is a linear regression showing a nearly uniform gradient of 121°/km. T = temperature; D = depth.

lithologic feature is the change in log responses at the opal-A/opal-CT transition zone, where the aluminum (ALUM) reading increases sharply. Since aluminum is primarily associated with clay mineralogy at this site, this observation should and does parallel a sharp increase in the gamma-ray reading at this same depth. In fact, the aluminum reading closely follows the gamma-ray trends for the entire interval of overlap as expected.

The opal-A/opal-CT transition zone also produces a discernible increase in normalized silica and a slight increase in normalized sulfur. Normalized calcium decreases only very slightly
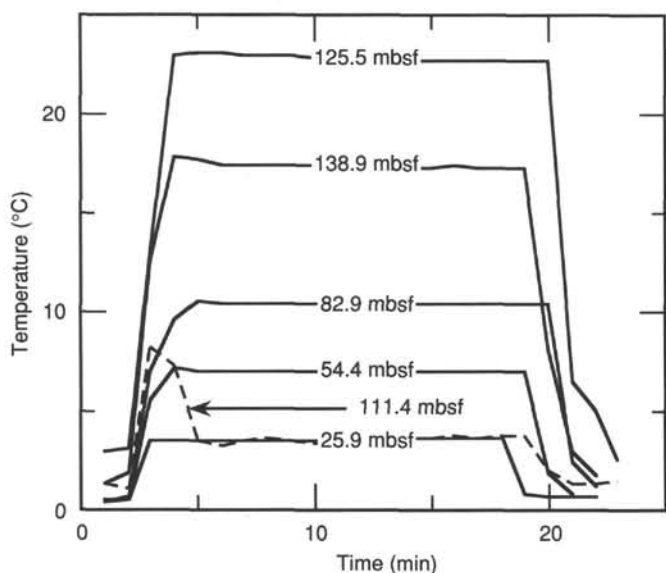
Figure 51. Multiple plot of six temperature records from Hole 797B showing the history just before, during, and after penetration. Run 4 (dashed trace) behaves as though the probe may have penetrated fill at the bottom of the hole and then inadvertently retracted.
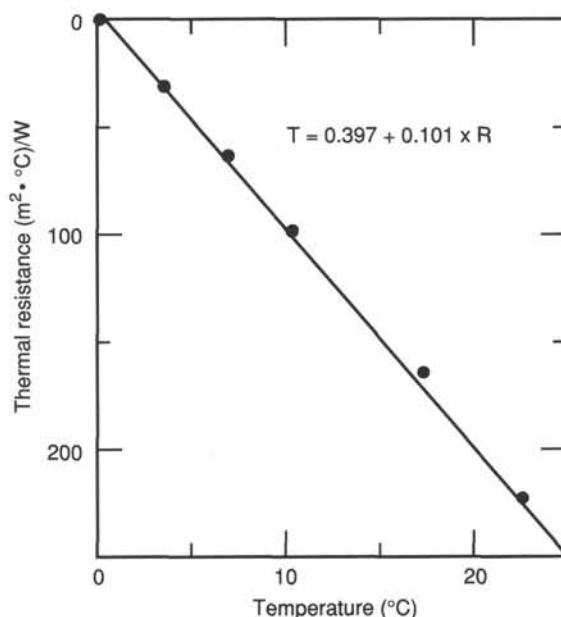
Figure 53. Downhole temperatures plotted vs. thermal resistance of the interval between the seafloor and the measurement for Site 797. The slope of the linear regression gives the heat flow as 0.101 W/m² (101 mW/m²). T = temperature; R = resistance.
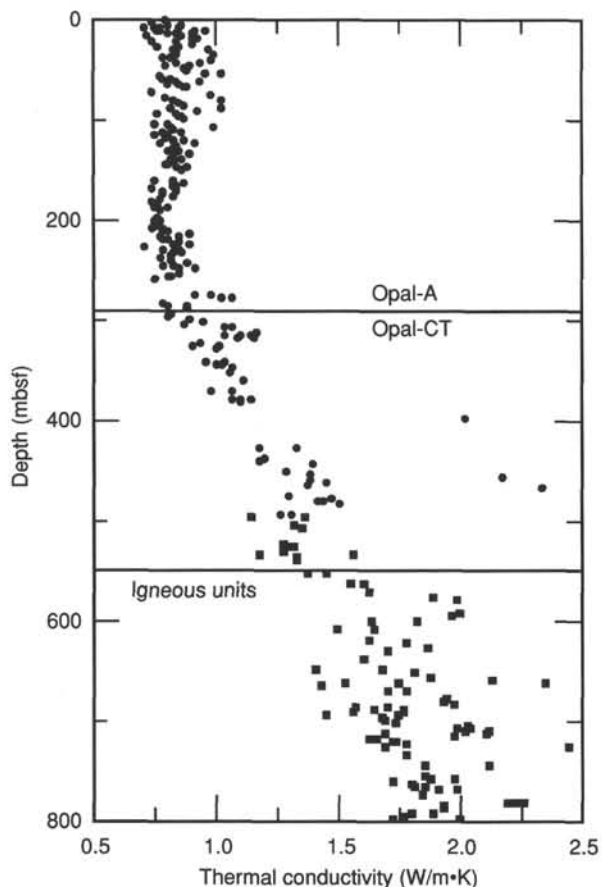
Figure 52. Thermal conductivity values vs. depth in Holes 797A, 797B, and 797C corrected to *in-situ* conditions.
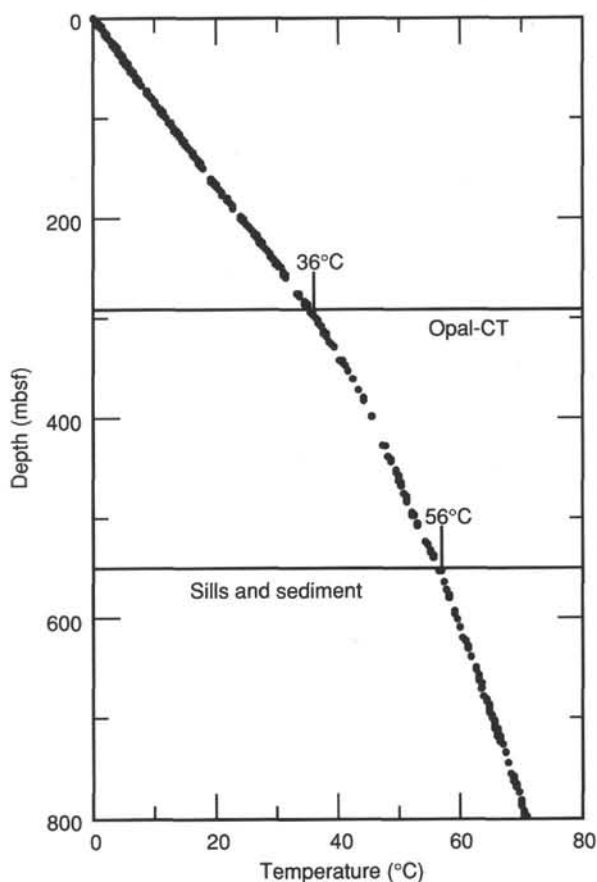
Figure 54. Extrapolated temperature profile for Site 797 based on the observed heat flow of 101 mW/m² and the conductivity profile of Figure 52.

397

Table 20. Summary of logging depths reached, Hole 797C.

Tool	Shallowest depths		Greatest depths		Upgoing	Nature of hole	KCl mud	Side-entry sub
	mbsf	fbrf	mbsf	fbrf				
FMS	83.2	9,705.7	516.0	11,125.7	Yes	Open	n/a	No
Geophysical	66.3	9,650.0	533.7	11,183.5	Yes	16-in. casing to 80 m, then open hole	No	No
Geochemistry	0.6	9,433.0	[a]633.1	11,509.7	Yes	16-in. casing to 80 m, drill pipe 80–623 m, open hole 623–633 m	4%	No
FMS	543.9	11,217.0	568.0	11,296.0	Yes	Open	n/a	No
FMS	485.0	11,027.0	599.9	11,401.0	Yes	Open	n/a	Yes
BHTV	549.0	11,233.8	603.0	11,411.0	Yes	Open	n/a	Yes

Note: fbrf = feet below rig floor; rig floor is calculated to be 11.4 m above sea level. FMS = formation microscanner; BHTV = borehole televiewer; n/a = not applicable. Basement depth = 554 mbsf; total drilled depth = 903 mbsf.
[a] Deepest log.
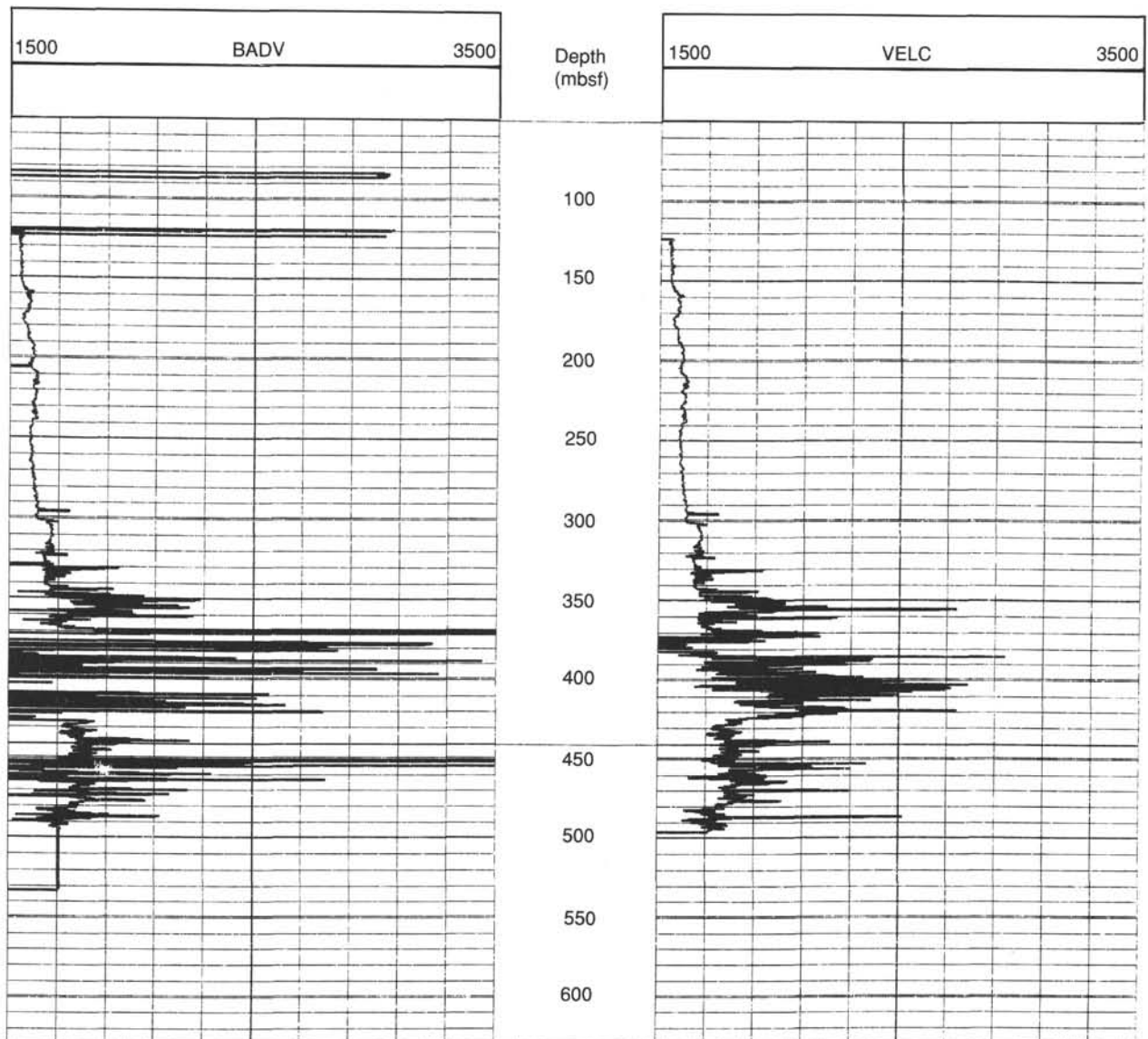
Figure 55. Sonic Log for Site 797 displayed before and after noise-removal algorithm (Srivastava, Arthur, et al., 1987) was applied. The left curve (BADV) is the sonic log before noise removal and is measured in m/s. The right curve (VELC) is the same log after noise removal and is also measured in m/s.

below 400 mbsf, and iron content fluctuates owing to the changes in drill-stem wall thickness.

Formation Microscanner

The formation microscanner (FMS) images and logs obtained during three logging runs of this tool at Hole 797C are of very good quality. The three runs represent overlapping sections covering a total logging interval from 84 to 597 mbsf.

The FMS tool string combines a general-purpose inclinometer tool (GPIT), a natural gamma-ray tool (NGT), and the FMS (see "Explanatory Notes," this volume). These sensors allow a comprehensive interpretation of the hole characteristics by correlating or various information from these tools. The caliper and inclinometer readings supply information about the hole size, shape, and orientation, while the NGT log is sensitive to clay content and is a good indicator of sedimentary intervals. The FMS images have been processed only in a preliminary way but show the distribution and the relative values of formation resistivities.

The two orthogonal calipers show that Hole 797C is elliptical, with the major axis trending northwest-southeast in the upper 300 m of the logged interval before it turns north-northeast-south-southwest from about 420 to 475 mbsf. The definition of a general orientation of the major axis below 475 mbsf is impossible owing to the rough hole conditions down to 554 mbsf. The igneous section, consisting of interbedded sediments and basaltic layers, begins at this depth. From 107 to 297 mbsf, the caliper log is completely off scale, indicating that large washout zones exist, resulting in a hole diameter of more than 16 in., the maximum physical extension of the calipers on the FMS tool. A double check done by monitoring the caliper readings of the geophysical tool string, which was deployed afterward, showed that the hole is larger than 20 in. over this interval.

The FMS images from 349 to 478 mbsf show a section dominated by sediments with interbedded, compacted, resistive layers that are probably chert and cherty porcellanite, although little chert was sampled during coring. In this section, about 100 resistive layers varying in thicknesses from about 2 to 70 cm were imaged as light bands (see Fig. 59). The location and abundance of these bands inversely correlates with core recovery, indicating the difficulties encountered in drilling these alternating beds of hard and soft material. These bands were numerous in some sections and appear as repeated sequences of variable resistivity.

The FMS images obtained in the basalt/sediment complex shows hole washouts that coincide with the sedimentary layers. Additionally there are uncommon sections in the igneous layers of almost cylindrical hole with a diameter of about 10 in. In places the hole diameter decreases to less than 6 in., but the hole cross section is still elliptical. The gamma-ray log indicated that these particular intervals were sedimentary. By using the side-entry-sub assembly, we found that the sediments that form these constrictions, tuffaceous sediments and clays, exhibited strong rebound properties. For example, after the 9¼-in.-diameter drill bit passed the constriction it immediately rebounded to a diameter of less than 6 in., according to the FMS caliper measurement.

The resolution of the images is good, and they permit clear distinctions between the different layers. The preliminary processing does not clearly image any characteristic features within the igneous units such as fractures, veins, or contacts.

Borehole Televiewer

The borehole televiewer (BHTV) was run in Hole 797C over the interval from 555 to 602 mbsf. This logged section is the lowermost part of the hole that could be reached for logging purposes and represents the uppermost 57-m interval of inter-

bedded igneous and sedimentary layers. In only a few sections within this interval were conditions favorable for good BHTV images of the hole walls. These sections are in the igneous layers that are cylindrical and true to gauge. Washouts of the sedimentary interfaces or a lack of a reflected signal owing to a large hole diameter made it extremely difficult to adjust the BHTV setting for optimum values during the run. Short sections in a thick igneous layer from 578 to 590 mbsf, where the hole was in gauge, shows some distinct features of the borehole wall, such as small-scale vertical and larger horizontal fractures as well as small, elliptically shaped areas of high reflectivity (Fig. 60).

A good signal was obtained throughout the whole logging run, so that digital processing at LDGO should produce much better images in sections of the hole where conditions are favorable.

SEISMIC STRATIGRAPHY

Available Data

The original proposal for Site 797 was made on the basis of a northwest-southeast multichannel record of the Japan National Oil Corporation (JNOC). One single-channel analog seismic line normal to this JNOC line was obtained by a research cruise of the Geological Survey of Japan in 1988. Two single-channel digital seismic reflection profiles were obtained during the approach of the *JOIDES Resolution* to Site 797, and three single-channel digital seismic reflection profiles were obtained by the *JOIDES Resolution* after drilling Site 797.

Seismic Stratigraphy

Site 797 is located in the southwestern margin of the Yamato Basin at the foot of the Yamato Bank and the Kita-Oki Bank. The seismic stratigraphic situation is quite similar to that of Site 794. The seismic stratigraphy of Site 797 differs from that of the central part of the Yamato Basin, where a thick, densely stratified layer prevails in the uppermost section of the sedimentary column. This densely stratified layer onlaps the margins of the Yamato Basin and corresponds to turbidites deposited on the abyssal plains (Fig. 10). As Site 797 is located on a gentle slope at the foot of the Yamato and Kita-Oki banks, the area is free from turbidite deposits and lacks the uppermost densely stratified layer that is widespread in the Yamato Basin.

Five seismic intervals (Intervals 1 to 5) and acoustic basement are recognized in the area around Site 797 (Figs. 10 and 61). From top to bottom, they are Interval 1, an uppermost moderately stratified interval; Interval 2, an upper transparent interval; Interval 3, a middle faintly stratified interval; Interval 4, a lower well-stratified interval; Interval 5, a lowermost irregularly stratified interval; and an acoustically opaque zone corresponding to acoustic basement. Each seismic interval does not necessarily correlate with the seismic intervals of the other sites of Leg 127, although the same nomenclature is used.

The thickness of Interval 1 in the area around the site varies slightly between 0.15 and 0.20 s (two-way traveltime; hereafter, this unit is used for the thickness of seismic intervals). The boundary between Interval 1 and Interval 2 is gradual and conformable. The thickness of Interval 2 in the area surrounding Site 797 is an almost constant 0.2 s. The reflectors in Interval 2 are nearly transparent, with some sparse, very faint and hummocky reflectors. Interval 3 is a faintly stratified interval with a constant thickness of 0.05 to 0.07 s. Interval 3 uniformly overlies Interval 4. Interval 4 is the most prominently stratified interval among the four intervals at this site. The reflectors of Interval 4 are parallel and horizontally continuous. The uppermost and lowermost parts of Interval 4 are characterized by strong reflectors and by discontinuous reflectors, respectively. The thickness of Interval 4 is in the range of 0.2–0.25 s, and the thickness
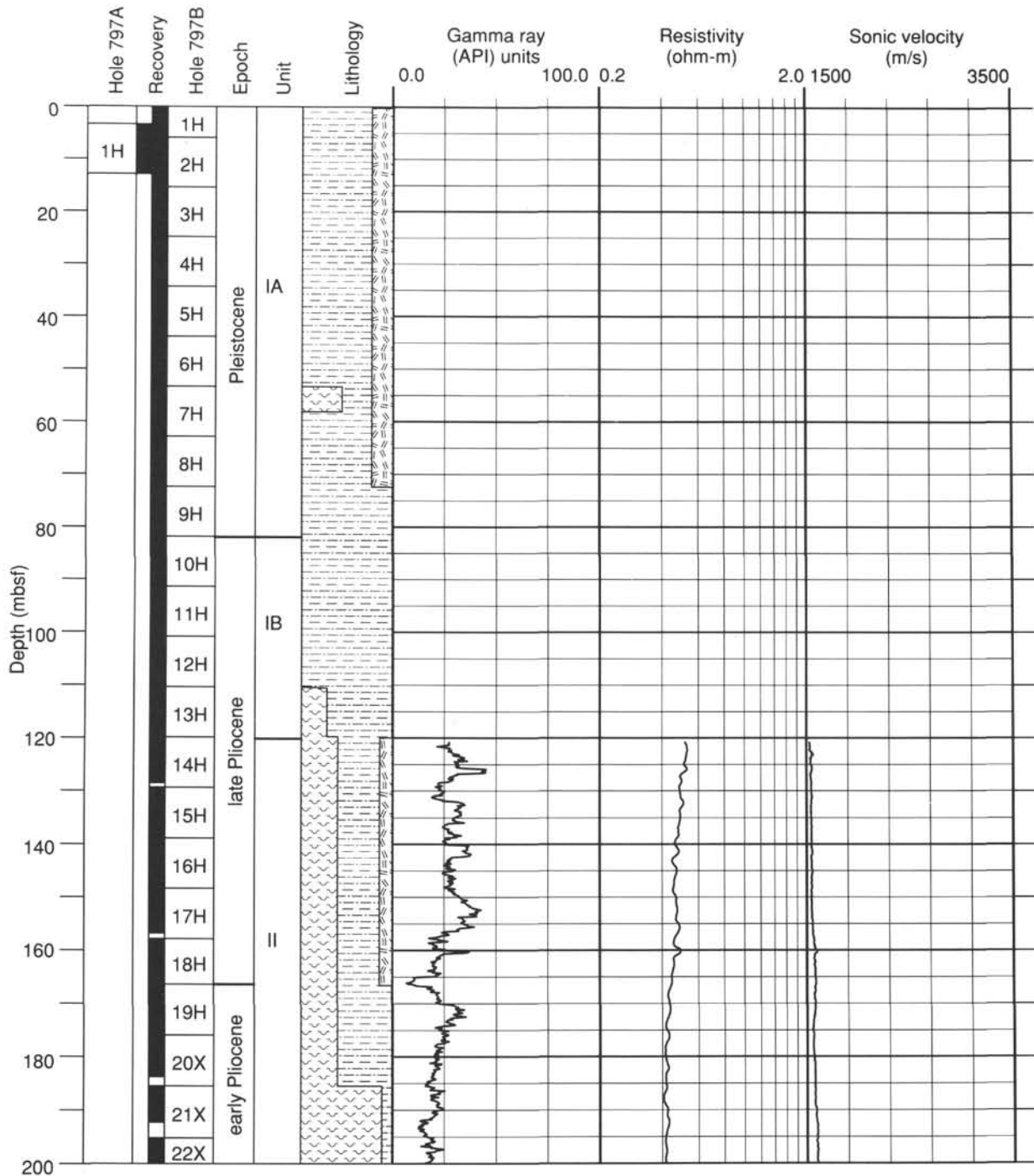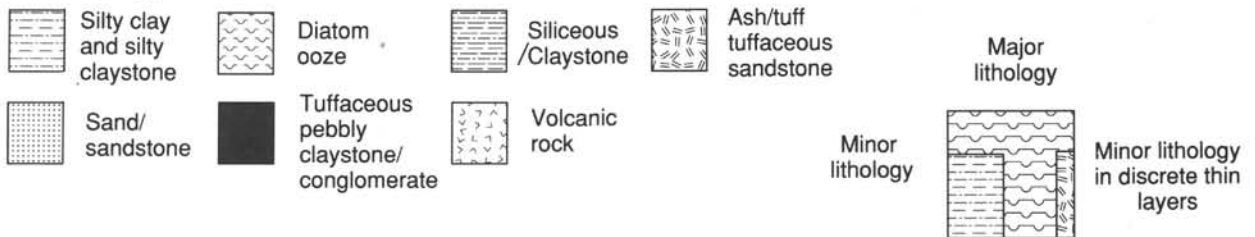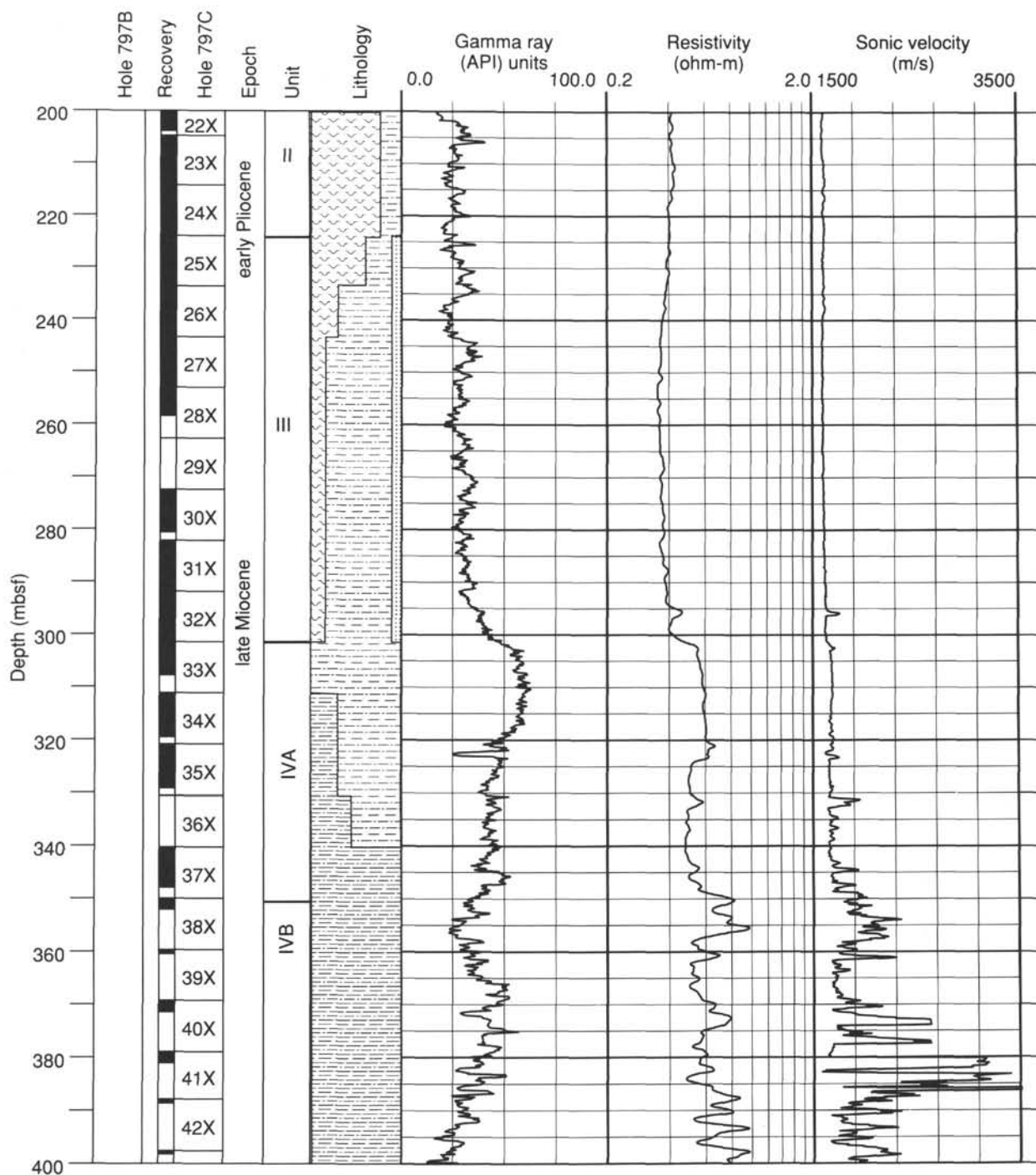
Figure 56. Lithostratigraphic column for Site 797 with corresponding logging measurements plotted of the compensated gamma-ray log measured in American Petroleum Institute (API) units, the resistivity in ohm-m, and the sonic velocity in m/s.
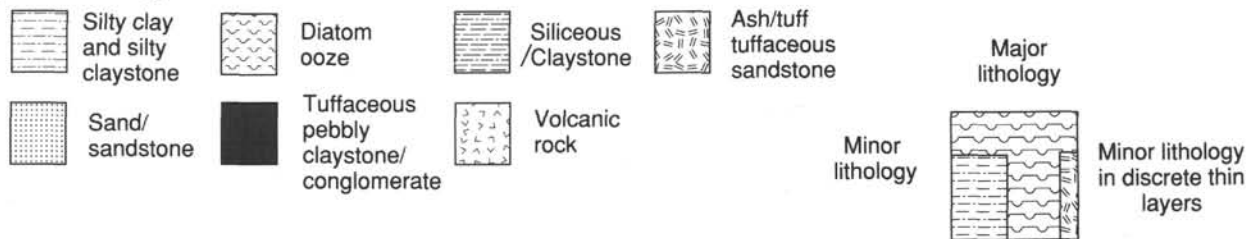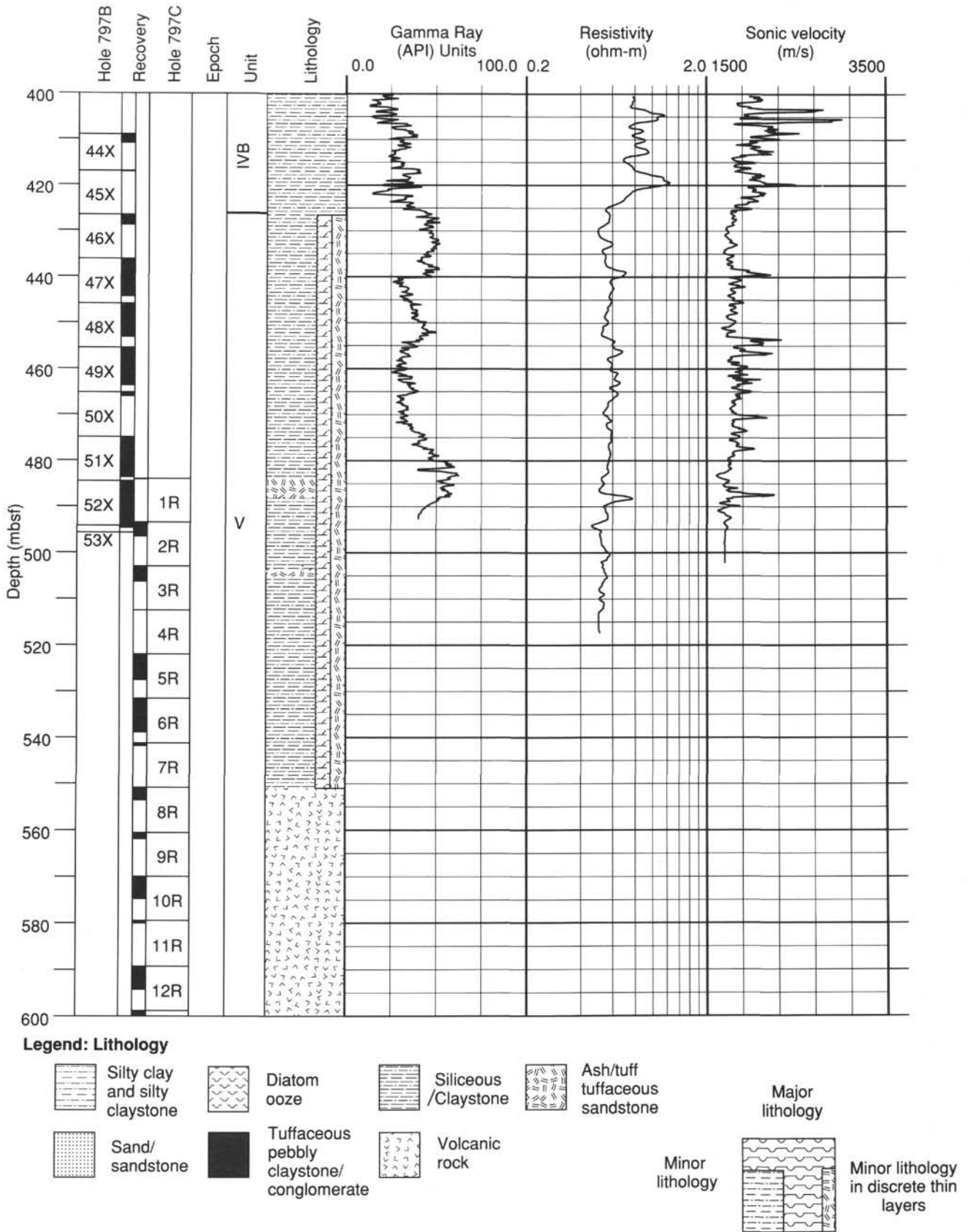
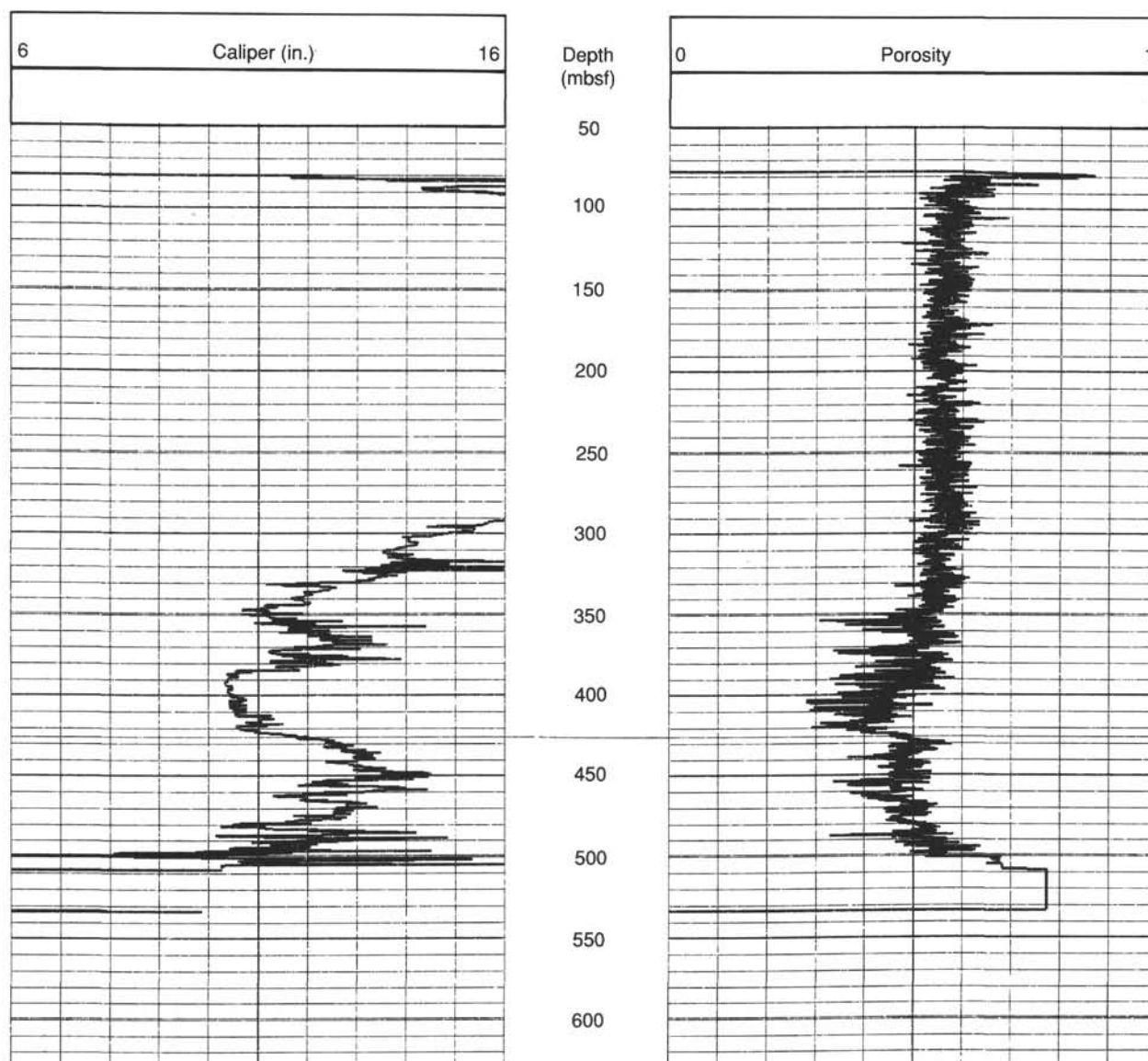Figure 56 (continued).

Figure 56 (continued).

Figure 57. Plot of porosity (PORS, porosity divided by 100) and caliper log (CALI, in.) for Site 797.

decreases toward the central part of the Yamato Basin (Fig. 10). Interval 5 is widely observed above the acoustic basement in this part of the Yamato Basin and probably covers acoustic basement throughout the Yamato Basin. Reflectors of Interval 5 are rather discontinuous and irregular. The thickness of Interval 5 is 0.1 s or less. The acoustic basement covered by Interval 5 is generally acoustically opaque, but some sparse, discontinuous reflectors occur at several horizons.

The following thicknesses of each interval at Site 797 were determined from the seismic reflection data acquired by the *JOIDES Resolution* during the site approach: 0.16 s for Interval 1; 0.22 s for Interval 2; 0.06 s for Interval 3; 0.23 s for Interval 4; and 0.06 s for Interval 5 (Fig. 62).

Correlation Between Seismic Stratigraphy and Lithology of Site 797

Correlation between seismic stratigraphy and lithostratigraphy was done using the physical-property velocity data and the logging sonic-velocity data. The sonic-velocity data were obtained by logging between 123 and 496 mbsf and were utilized

for the correlation of stratigraphy over this depth. Results of the correlation between the seismic stratigraphy and the lithostratigraphy are summarized in Figure 62.

Two sharp increases in the logging sonic velocity were used to determine the depth and thicknesses of the seismic intervals. The first sharp increase is at 295 mbsf, and the second at 345 mbsf. The first sharp increase of the logged velocity was correlated to a reflector at 0.38 sbsf at the top of Interval 3. As the opal-A/opal-CT boundary at this site is observed at 299 mbsf (see "Lithostratigraphy," this chapter), this reflector is not coincident with the exact opal-A/opal-CT lithologic boundary. The second sharp velocity increase seen in the sonic logging was correlated to a strong reflector at 0.46 sbsf at the top of Interval 4. This horizon is coincident with the boundary between Subunits IVA and IVB. The top of Interval 5 is apparently correlatable to the top of the shallowest basalt at 554 mbsf, and this correlation was used as a key marker for the correlation of the seismic stratigraphy with the lithologic units.

Interval 1 correlates to the alternating dark- and light-colored layers of the silty clay of Subunit IA and the ashy diatom
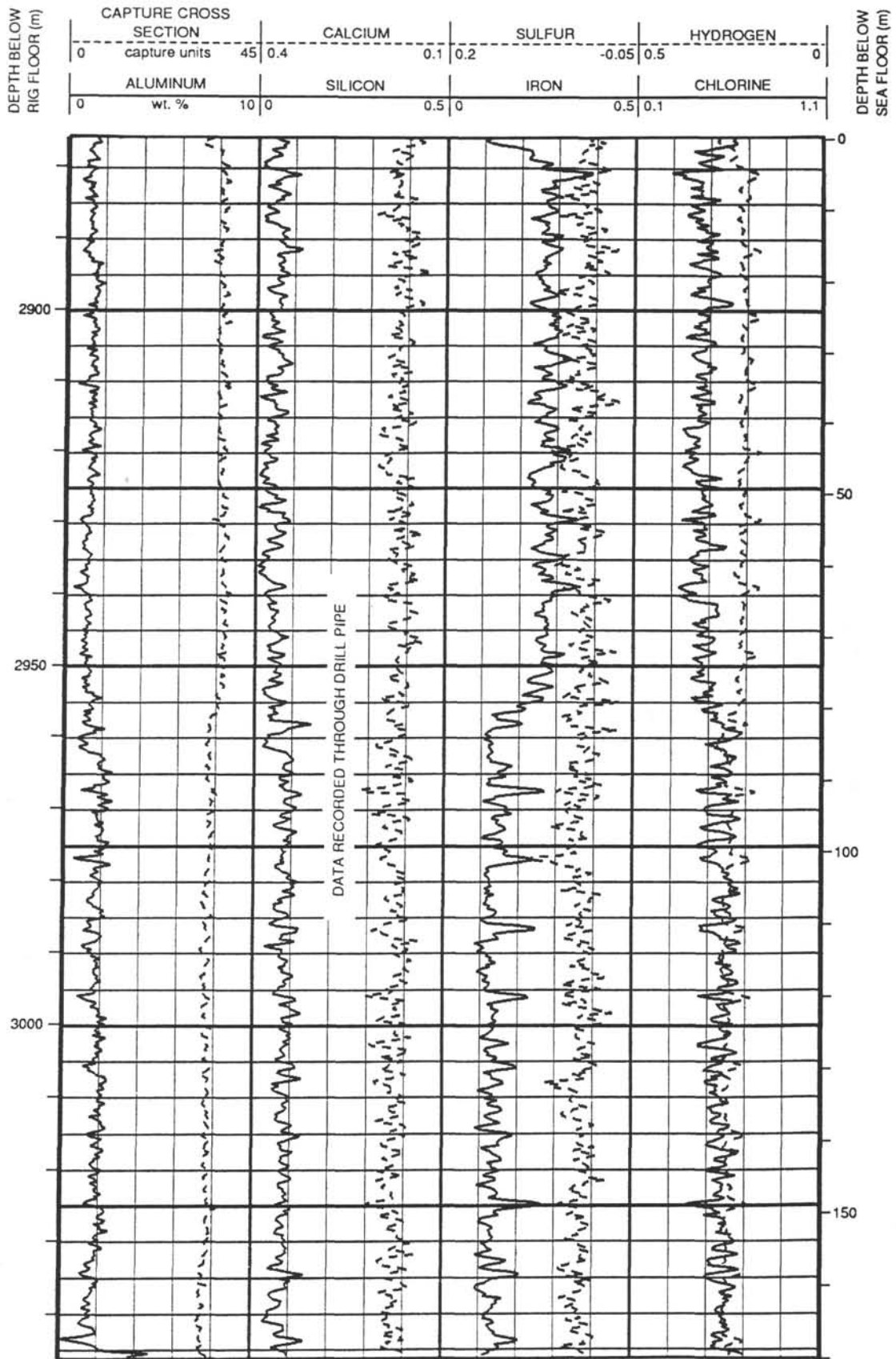
Figure 58. Geochemical logs from Hole 797C. Uncorrected elemental readings, capture cross section, and aluminum weight percent are displayed.
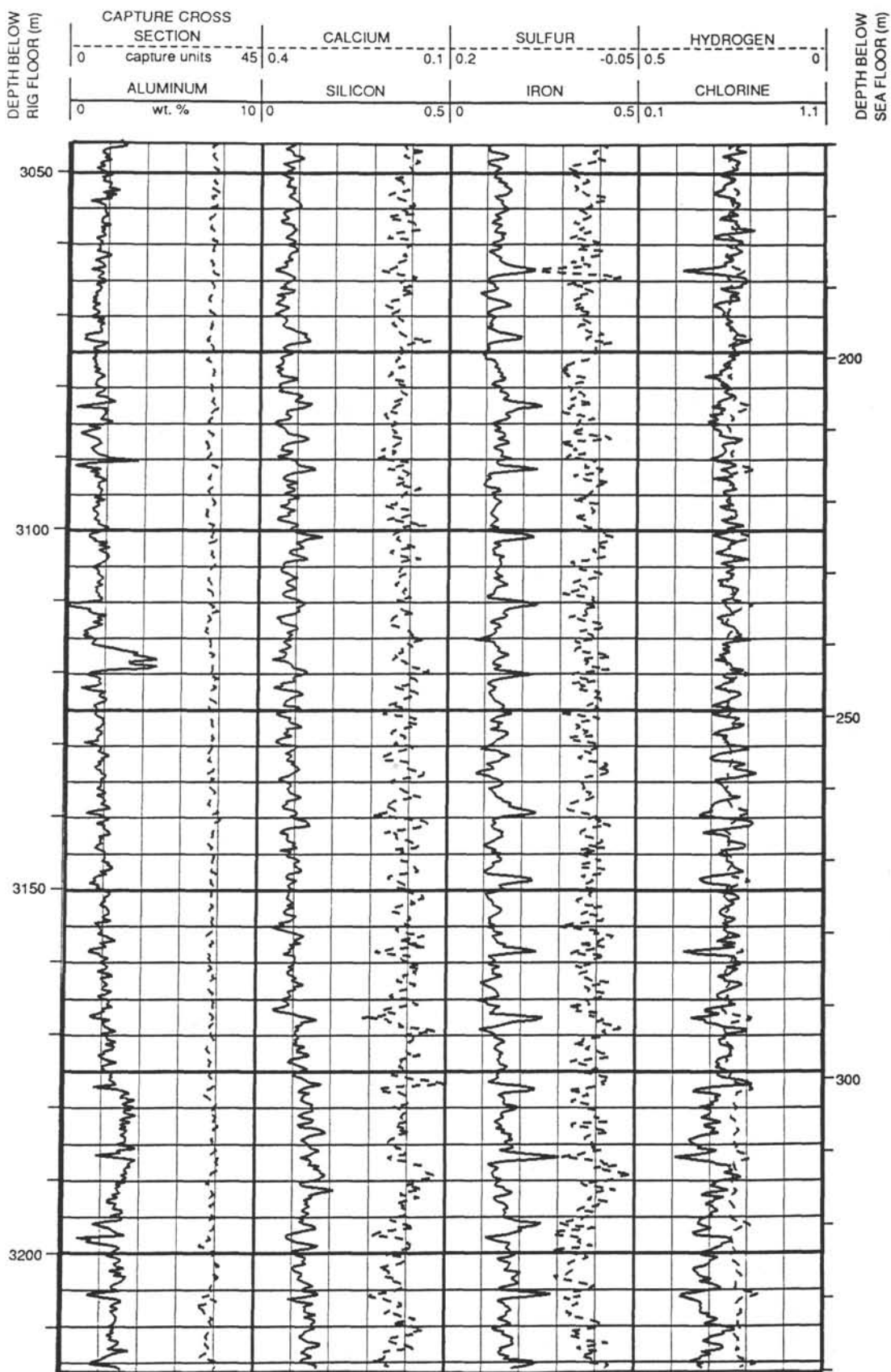
Figure 58 (continued).
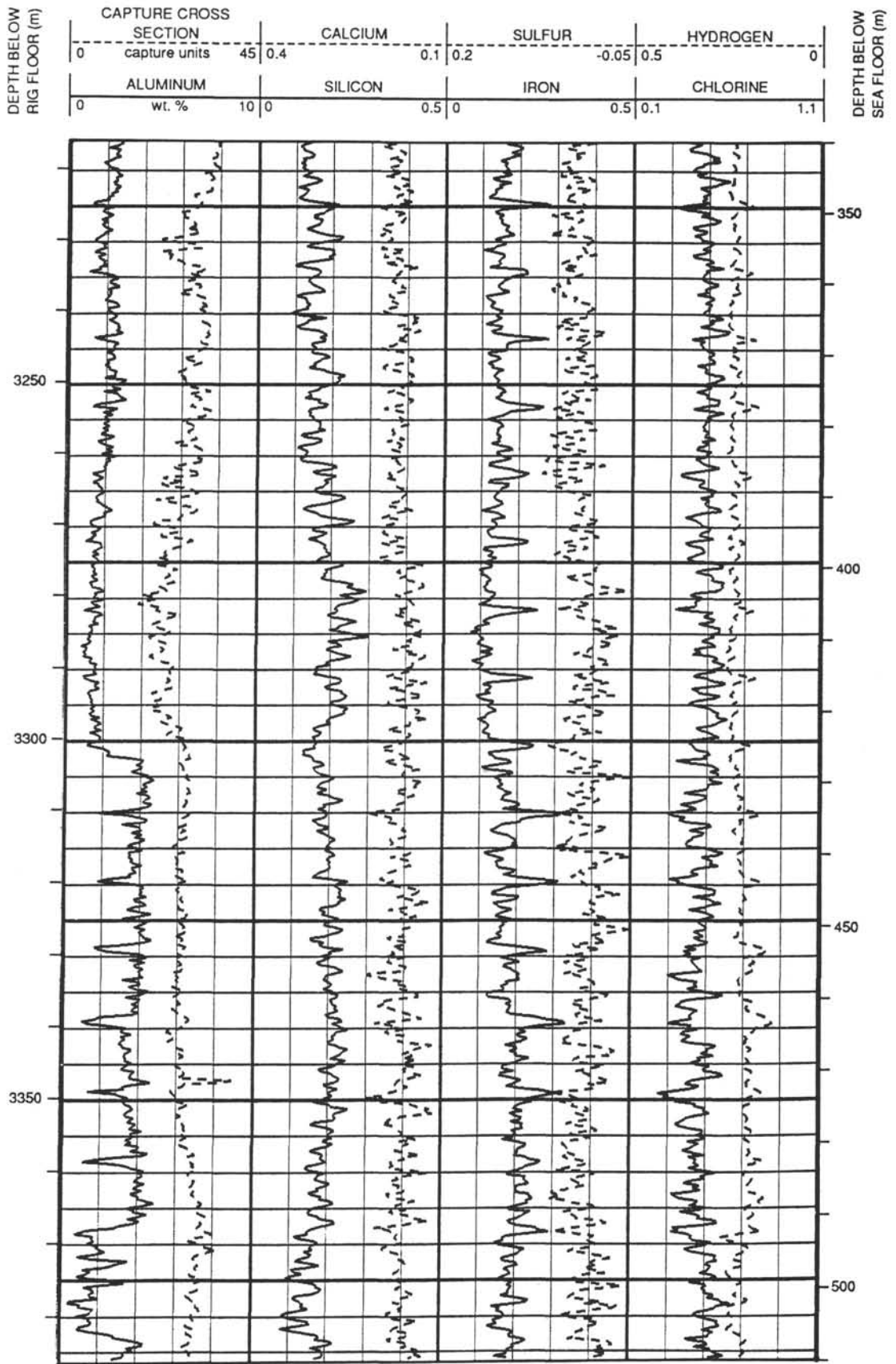
Figure 58 (continued).
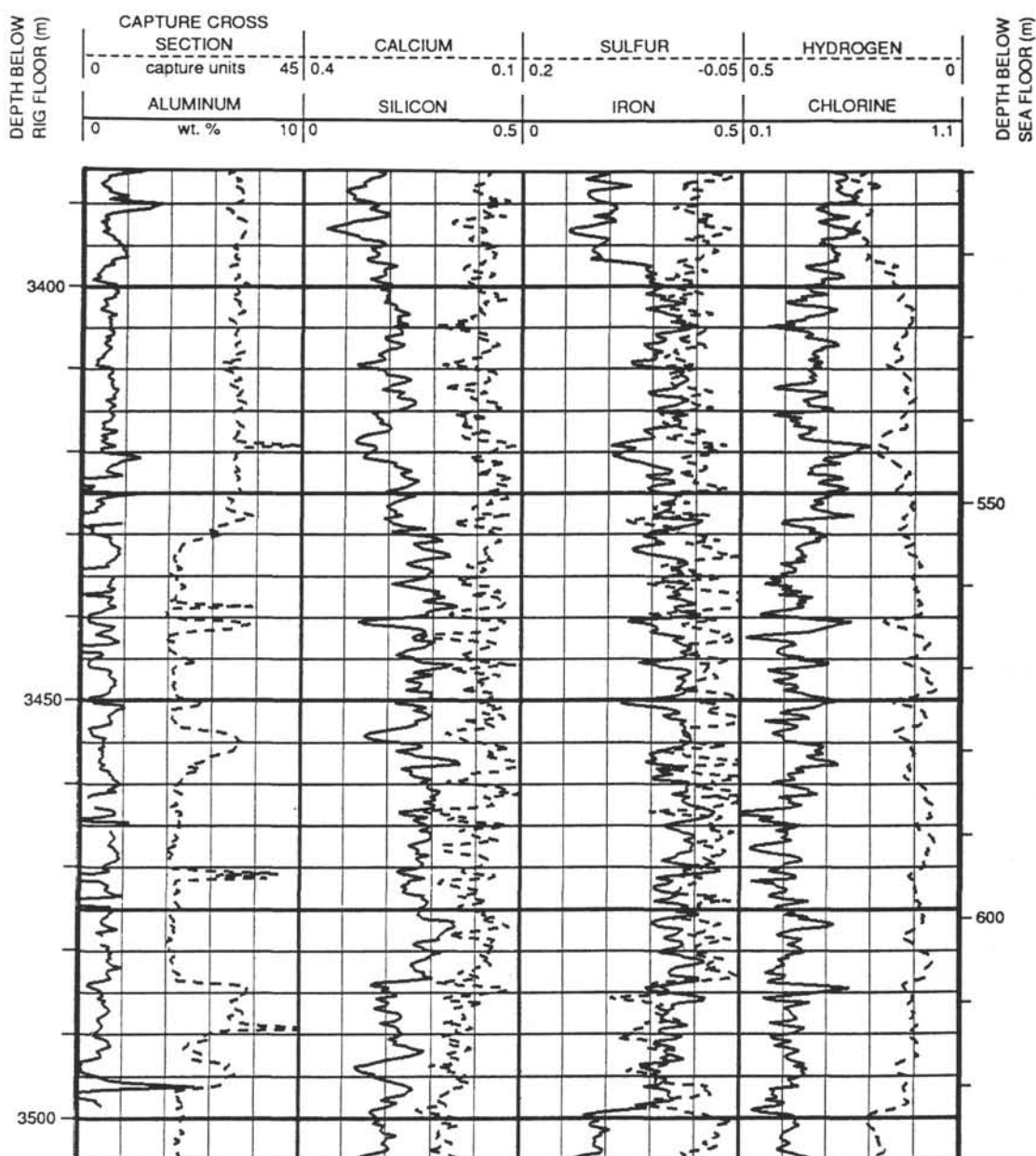
Figure 58 (continued).

silty clay of Subunit IB. The boundary between Intervals 1 and 2 at 120 mbsf coincides with the Unit I/Unit II boundary between the overlying diatom silty clay and the underlying more diatomaceous silty clay and diatomaceous ooze. The change of lithology from diatom silty clay to diatomaceous ooze appears to be consistent with the change from the stratified character of Interval 1 to the transparent character of Interval 2, the diatomaceous ooze or clay having a more transparent acoustic nature. The well-bedded structure of Subunit IA (0–81.9 mbsf) may account for the well-developed stratification of the upper part of Interval 1. The interval velocity of Interval 1 (1510 m/s) is an estimation based on P-wave-logger velocity data and is the same as the interval velocity of Interval 1 at Site 794.

Interval 2 correlates with the diatom silty clay and ooze of Unit II and with the silty diatomaceous clay of Unit III. The interval velocity of Interval 2 is estimated to be 1580 m/s, based on the assumption that the reflector at 0.38 sbsf is the same as

the sharp peak observed by velocity logging at 295 mbsf. This interval velocity is consistent with the velocity data of the sonic log and is comparable with the interval velocity of Interval 2 of Site 794.

Interval 3 corresponds to the silty clay and siliceous claystone of Unit III. The lithologically identified opal-A/opal-CT boundary is at 299 mbsf in the uppermost part of this interval. The logging data show a velocity increase that probably corresponds to the opal-A/opal-CT boundary at 299 mbsf and another sharp peak of velocity at 295 mbsf. This latter velocity peak was correlated to the reflector at the top of Interval 3. The interval velocity of Interval 3 is 1650 m/s, which is consistent with the sonic logging data.

Interval 4 corresponds to the siliceous claystone associated with chert and porcellanite of Subunit IVB and to the tuff and claystone of the upper part of Unit V. The strongly stratified character of Interval 4 reflects the abundant chert and porcel-

407
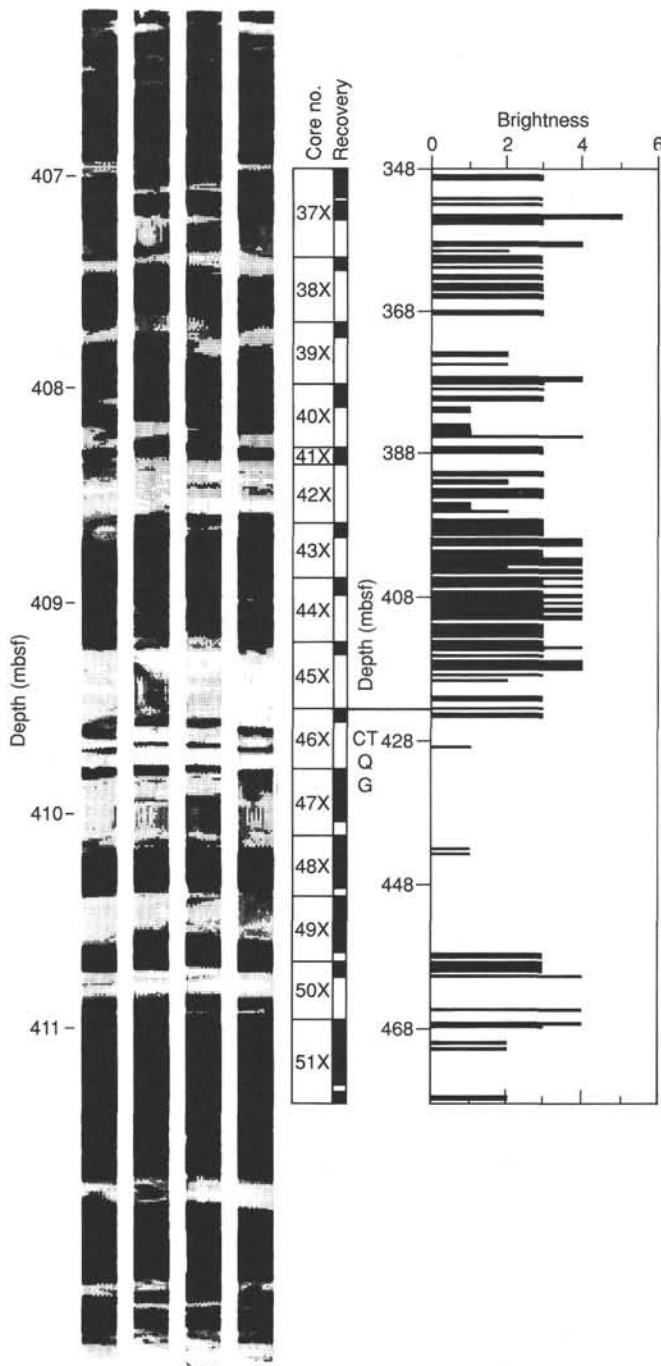
Figure 59. Formation microscanner (FMS) data from Hole 797C. The column at left shows images through a highly layered interval. The column at right shows the thickness, frequency, and relative resistivity of cherty layers from 348 to 468 mbsf. The middle column shows core recovery for this interval.

lanite layers within this unit. This is suggested by the sonic log, which shows correspondingly high variability, suggesting intercalation of layers with different physical properties. The interval velocity of Interval 4 was estimated using the constraint of the first encounter of igneous rock at 554 mbsf. The interval velocity is 1850 m/s, a figure similar to the equivalent horizon at Site 794 (Interval 4).

The top of Interval 5 is apparently correlatable to the top of the shallowest basalt. Interval 5 therefore corresponds to the intercalated basalts and siliceous claystones. The average sonic velocity of the basalts is 4500 m/s, and the average velocity of the siliceous rock is about 2000 m/s (see "Physical Properties," this chapter). Here, the interval velocity of Interval 5 is estimated to be 3500 m/s because a wide-angle reflection survey in the Yamato Basin suggests the velocity of 3500 m/s for this horizon (Ludwig et al., 1975). If this estimated interval velocity is applied, the thickness of Interval 5 is 88 m, and Interval 5 was unequivocally penetrated by the drilling of Hole 797C. As a sonic log over this interval was not obtained because of unsatisfactory hole conditions, the detailed correlation of this seismic interval and the lithology is difficult, and no successful solution for the correlation of Interval 5 and the lithology was obtained.

Acoustic basement beneath Interval 5 was penetrated by the drilling of Hole 797C. The boundary between lithologic Units V and VI is at 647 mbsf, within the intercalated basalts and sedimentary rocks. Unit VI is characterized by the introduction of sandy beds and shows slightly higher sonic velocity (see "Physical Properties," this chapter). The average velocity of the basaltic rocks is 4500 m/s in the upper part (554–710 mbsf) and 4000 m/s in the lower part (below 710 mbsf). This increase in the velocity of the sedimentary rocks and decrease in the velocity of the basaltic rocks may remove the acoustic-impedance contrast between igneous and sedimentary rocks below about 700 mbsf. The nonstratified opaque zone characterized as acoustic basement may be correlated with this stratigraphy. As the boundary between Interval 5 and the acoustic basement is ambiguous, more careful examination is needed for a detailed discussion. The acoustic basement is associated with spatially distributed deeper reflectors, which suggests that the thickness of the intercalated layer of igneous rocks and sedimentary rocks may be as thick as 1 to 2 km, in accordance with the wide-angle reflection data of Ludwig et al. (1975).

CONCLUSIONS

We accomplished two of our three main objectives at Site 797: (1) to gain information on the style and dynamics of rifting through a determination of the age and nature of basement, and (2) to characterize the sedimentation, subsidence, and oceanographic history of the southern Yamato Basin area. Because of hole problems, we were unable to reach our third goal, a measurement of the magnitude and direction of the present stress field. A detailed summary of the results and conclusions for Site 797 can be found at the beginning of this chapter. For emphasis, we highlight the key findings as they relate to our principal objectives in the sections below.

Style and Dynamics of Rifting

We were able to penetrate nearly 350 m below the top of interbedded basalts and sediments (seismic Interval 5 plus acoustic basement) at this site and found the rocks to consist of a complex of submarine basaltic flows and intrusive sills interlayered with volcaniclastic sandstones, siltstones, and silty claystones. Based on seismic ties, seismic character correlations, and drilling at Site 794, similar complexes probably make up uppermost acoustic basement throughout much of the Yamato Basin. The age of this complex at Site 797 is about 19 Ma or older, based on microfossils in the claystones, which overlie the shallowest basalt. The igneous rocks consist of an upper suite of high-Al basalt flows and intrusive sills or dikes, and a lower intrusive suite of mixed mildly alkaline and enriched tholeiitic basalts. The high-Al basalts probably represent volcanism associated with early rifting of a volcanic arc and, based on their chemistry, have interacted little with continental crust during
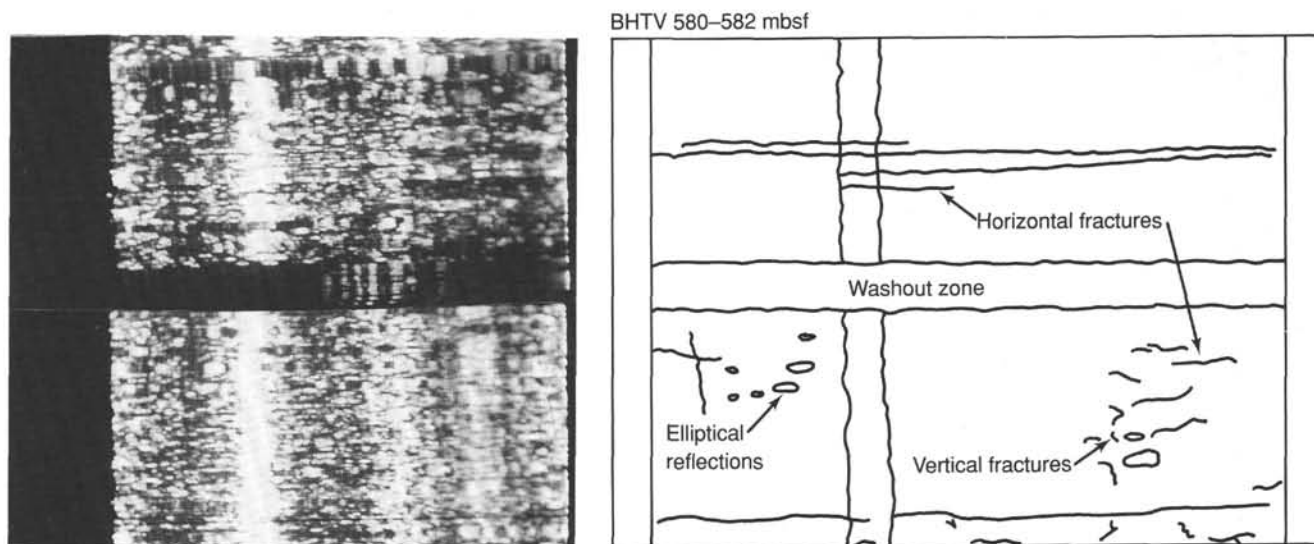
BHTV 580–582 mbsf

Figure 60. Example of borehole televiewer (BHTV) image and interpretation of fractures obtained during basement logging of Hole 797C.
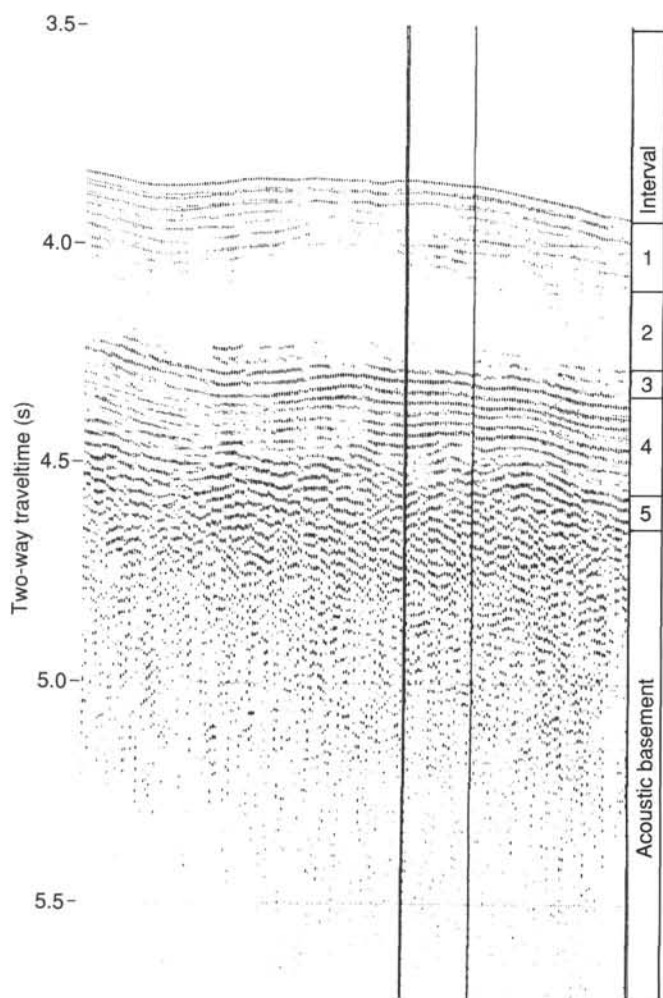

Figure 61. Northeast-southwest single-channel *JOIDES Resolution* seismic reflection record obtained during the approach to Site 797, with an assignment of acoustic intervals and the hole location (see Fig. 9 for track lines).

their formation and emplacement. The alkaline and enriched tholeiitic basaltic rocks are likely related to this same rifting event but show much less of an arc-related signature in their chemistry. Our preliminary paleodepth analysis suggests that this part of the Yamato Basin subsided rapidly during the early to early middle Miocene following or coincident with this volcanic activity.

Oceanographic and Sedimentation History

The vertical sequence of sedimentary facies encountered at Site 797 indicates at least four stages in the oceanographic and sedimentation history of this part of the Yamato Basin. The earliest stage for which we have data began with early Miocene submarine volcanism and deposition of graded and current-reworked volcaniclastic sands and silts on a shelf or slope, probably outboard of a delta on the flank of the proto-Yamato Basin. This facies constitutes a sedimentary unit which has never been penetrated before in the Japan Sea; it represents our first look at the sedimentary processes which operated in the early phase of basin formation. The second depositional phase was characterized by rapid subsidence of the area to lower middle bathyal depths during the late early to early middle Miocene. Calcareous and slightly phosphatic claystones were deposited in a poorly oxygenated basin during this stage. A period of initially slow sedimentation followed, which lasted to the middle of the late Miocene. During this time the climate cooled, and diatom productivity increased to high levels that culminated in the late Pliocene. The final stage spans the latest Pliocene to Holocene, a period characterized by a significant decrease in diatomaceous sedimentation, an increase in volcanic-ash production and terrigenous input, and oscillating climate. These conditions produced a distinctive sequence of interlayered light- and dark-colored silty clays having variable organic carbon contents. Throughout its sedimentary history, this site probably lay near or above the CCD, based on the nearly ubiquitous occurrence of calcareous benthic foraminifers.

As at other sites drilled on this leg, the sedimentary sequence at Site 797 has been significantly overprinted by diagenesis. The alteration of diatomaceous sediments to porcellanites and hard siliceous claystones containing opal-CT and quartz is the most pronounced diagenetic modification. The diagenetic transitions of opal-A to opal-CT and opal-CT to quartz are well docu-

Seismic interval	Acoustic character	Interval velocity (m/s)	Thickness (two-way traveltime, s)	Thickness (distance, m)	Simplified lithology	Lithologic unit	Age
1	Moderately stratified	1510	0.16	120	Alternating silty clay	IA	Pleistocene
					Ashy, diatom silty clay	IB	
2	Transparent partly hummocky reflectors	1580	0.22	175	Diatom silty clay and ooze	II	Pliocene
					Silty clay with traces of diatom	III	
3	Faintly stratified	1650	0.06	50	▬Opal-A/CT 299 mbsf▬ Silty clay and siliceous claystone	IVA	late Miocene
4	Well stratified	1850	0.23	209	Siliceous claystone, chert, porcellanite	IVB	
					Tuff and claystone	V	middle Miocene
5	Irregularly stratified	3500	0.06?	88?	Intercalated siliceous claystone and basalt/dolerite		

Two-way traveltime (s): 0, 0.16, 0.38, 0.46, 0.69

Depth (mbsf): 0, 120, 295, 345, 554

Figure 62. Summary of the seismic stratigraphy of Site 797 and its correlation with lithostratigraphy.

mented by a variety of data, including geochemical and physical-property profiles and downhole logs. Both alterations occur along diagenetic fronts which are parallel to the seafloor. The opal-A/opal-CT transition is manifested in seismic reflection records in this area of the Yamato Basin as a prominent bottom-simulating reflector.

REFERENCES

Baker, D. R., and Eggler, D. R., 1987. Compositions of anhydrous and hydrous melts coexisting with plagioclase, augite, and olivine or low-Ca pyroxene from 1 atm to 8 kbar: Application to the Aleutian volcanic center of Atka. *Am. Mineral.*, 72:12–28.

Baker, P. A., and Burns, S. J., 1985. Occurrence and formation of dolomite in organic-rich continental margin sediments. *AAPG Bull.*, 69: 1917–1930.

Berggren, W. A., Kent, D. V., Flynn, J. J., and Van Couvering, J. A., 1985. Cenozoic geochronology. *Geol. Soc. Am. Bull.*, 96:1407–1418.

Calvert, S. E., 1983. Geochemistry of Pleistocene sapropels and associated sediments from the Eastern Mediterranean. *Oceanol. Acta*, 6: 225–267.

Davis, E. E., and Lister, C.R.B., 1977. Heat flow measured over the Juan de Fuca Ridge: evidence for widespread hydrothermal circulation in a highly heat transportive crust. *J. Geophys. Res.*, 82:4845–4860.

Dott, R. H., and Bird, K. J., 1979. Sand transport through channels across an Eocene shelf and slope in southwestern Oregon, U.S.A. *Soc. Econ. Paleontol. Mineral. Spec. Publ.*, 27:327–342.

Emeis, K.-C., and Kvenvolden, K. A., 1986. Shipboard organic geochemistry on *JOIDES Resolution*. *ODP Tech. Note*, 7.

Geological Survey of Japan, 1982. Geologic atlas of Japan. *Geol. Surv. Japan*.

Gieskes, J. M., and Peretsman, G., 1985. Water chemistry procedures aboard *JOIDES Resolution*—some comments. *ODP Tech. Note*, 5.

Gill, J. B., 1981. *Orogenic Andesite and Plate Tectonics*: New York, Elsevier.

Hirata, N., Kinoshita, H., Suyehiro, K., Suyemasu, M., Matsuda, N., Ouchi, T., Katao, H., Koresawa, S., and Nagumo, S., 1987. Report on the DELP 1985 cruises in the Japan Sea, Part II: seismic refraction experiment conducted in the Yamato Basin, southeast Japan Sea. *Tokyo Daigaku Jishin Kenkyusho Iho*, 62:347–365.

Hirata, N., Tokuyama, H., and Chung, T. W., 1989. An anomalously thick layering of the crust of the Yamato Basin, southeastern Japan Sea: the final stage of back-arc spreading. *Tectonophysics*, 165:303–314.

Honza, E., (Ed.), 1979. Geological investigation of the Japan Sea. April-June 1978 (GH78-2 Cruise). *Cruise Rep.—Geol. Surv. Jpn.*, 13:1–99.

Hyndman, R. D., Von Herzen, R. P., Erickson, A. J., and Jolivet, J., 1977. Heat-flow measurements, DSDP Leg 37. *In* Aumento, F., Melson, W. G., et al., *Init. Repts. DSDP*, 37: Washington (U.S. Govt. Printing Office), 347–362.

Isezaki, N., 1986. A magnetic anomaly map of the Japan Sea. *J. Geomagn. Geoelectr.*, 38:403–410.

Kaneoka, I., 1986. Constraints on the time of the evolution of the Japan Sea based on radiometric ages. *J. Geomag. Geoelectr.*, 38:475–485.

Kaneoka, I., Hayashi, H., Iwaguchi, T., Yasuda, A., Takigami, Y., Fujioka, K., and Sakai, H., 1988. K-Ar dating of volcanic rocks dredged from the Yamato seamount chain in the Japan Sea. *Kazan*, 33:213–218.
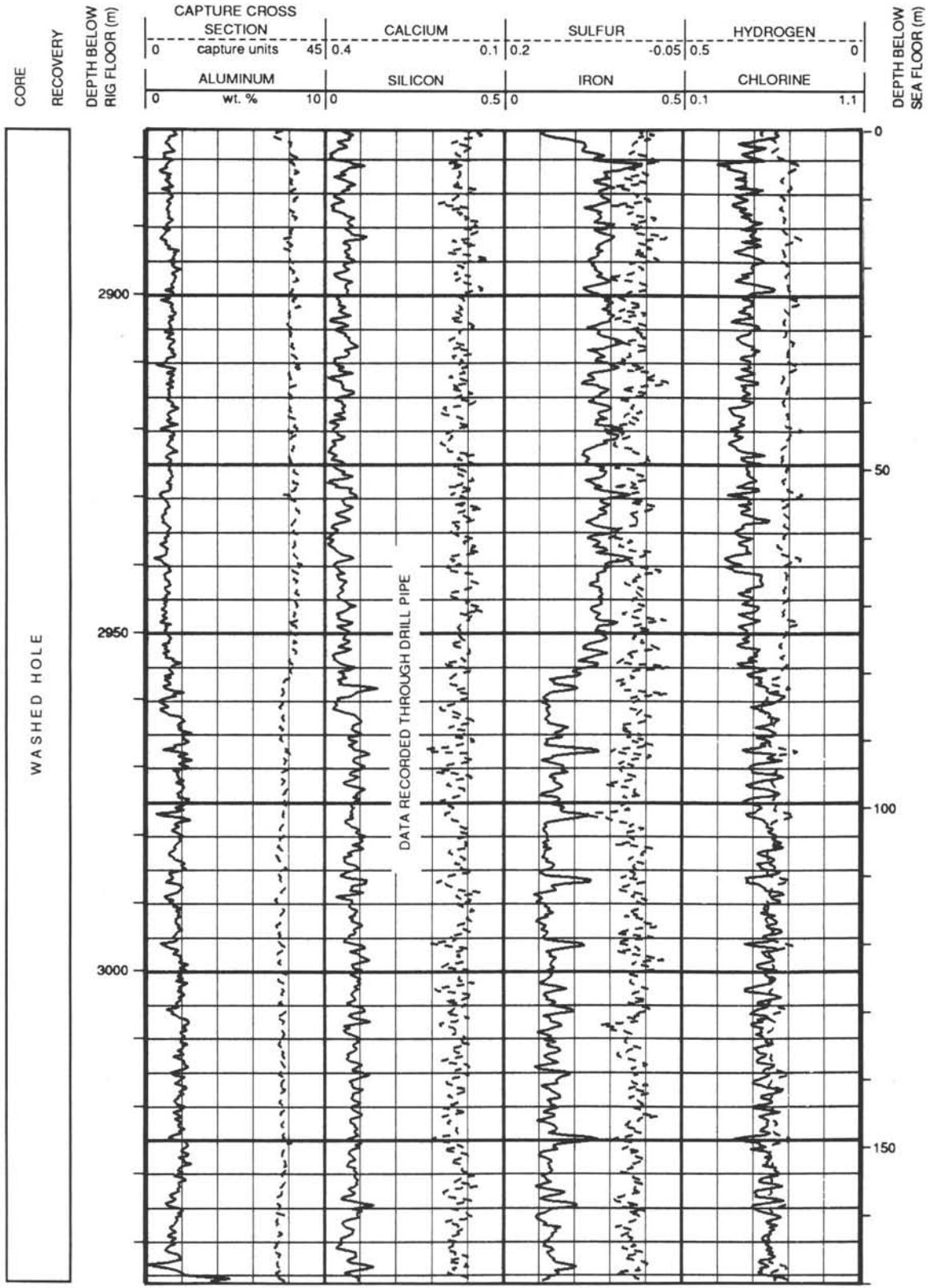
Kaneoka, I., Notsu, K., Takigami, Y., Fujioka, K., and Sakai, H., in press. Constraints on the evolution of the Japan Sea based on ^{40}Ar-^{39}Ar ages and Sr isotopic ratios for volcanic rocks of Yamato Seamount chain in the Japan Sea. *Earth Planet. Sci. Lett.*

Kaneoka, I., and Yuasa, M., 1988. ^{40}Ar-^{39}Ar Age studies on igneous rocks dredged from the central part of the Japan Sea during the GH78-2 cruise. *Geochem. J.*, 22:195–204.

Karig, D. E., Ingle, J. C., Jr., et al., 1975. *Init. Repts. DSDP*, 31: Washington (U.S. Government Printing Office).

Kennett, J. P., and Srinivasan, M. S., 1983. *Neogene Planktonic Foraminifera: A Phylogenetic Atlas*: Stroudsburg, PA (Hutchinson Ross).

Klein, G. D., Okada, H., and Mitsui, K., 1979. Slope sediments in small basins associated with a Neogene active margin, western Hokkaido Island, Japan: *Soc. Econ. Paleontol. Mineral. Spec. Publ.*, 27:359–374.

Kuno, H., 1968. Differentiation of basalt magmas. *In* Hess, H. H., and Poldervaart, A. (Eds.), *Basalts: The Poldervaart Treatise on Rocks of Basaltic Composition* (Vol. 2): New York (Wiley-Interscience), 623–688.

Lofgren, G., 1980. Experimental studies on the dynamic crystallization of silicate melts. *In* Hargraves, R. B. (Ed.), *Physics of Magnetic Processes*: Princeton (Princeton Univ. Press).

Lombari, G., and Boden, G., 1985. Modern radiolarian global distributions. *Spec. Publ. Cushman Found. Foraminiferal. Res.*, 16A.

Ludwig, W. J., Murauchi, S., and Houtz, R. E., 1975. Sediments and structure of the Japan Sea. *Geol. Soc. Am. Bull.*, 86:651–664.

Manheim, F. T., and Sayles, F. L., 1974. Composition and origin of interstitial waters of marine sediments based on deep sea drill cores. *In* Goldberg, E. D. (Ed.), *The Sea* (Vol. 5): New York (Wiley), 527–568.

Matoba, Y., 1984. Paleoenvironment of the Sea of Japan. *In* Oertli, H. J. (Ed.), *Benthos '83: 2nd Intern. Symp. Benthic Foraminifera*: 409–414.

Müller, P. J., 1977. C/N ratios in Pacific deep sea sediments: effect of inorganic ammonium and organic nitrogen compounds sorbed by clays. *Geochim. Cosmochim. Acta*, 41:765–776.

Nakaseko, K., and Sugano, K., 1973. Neogene radiolarian zonation in Japan. *Chishitsugaku Ronshu*, 8:23.

Nobes, D. C., Villinger, H., Davis, E. E., and Law, L. K., 1986. Estimation of marine sediment bulk physical properties at depth from seafloor geophysical measurements. *J. Geophys. Res.*, 91:14033–14043.

Okada, H., and Honjo, S., 1975. Distribution of coccolithophores in marginal seas along the western Pacific Ocean and in the Red Sea. *Mar. Biol.*, 31:271–285.

Oremland, R. S., and Taylor, B. F., 1978. Sulfate reduction and methanogenesis in marine sediments. *Geochim. Cosmochim. Acta*, 42:209–214.

Parsons, B., and Sclater, J. G., 1977. An analysis of the variation of oceanic bathymetry and heat flow with age. *J. Geophys. Res.*, 82:803–827.

Pearce, J. A., 1983. The role of sub-continental lithosphere in magma genesis at destructive plate margins. *In* Hawkesworth, C. J., and Norry, M. J. (Eds.), *Continental Basalts and Mantle Xenoliths*: Nantwich (Shiva), 230–250.

Pearce, J. A., Alabaster, T., Shelton, A. W., and Searle, M. P., 1981. The Oman ophiolite as a Cretaceous arc-basin complex: evidence and implications. *Philos. Trans. R. Soc. London*, A300:299–317.

Perch-Nielsen, K., 1985. Cenozoic calcareous nannofossils. *In* Bolli, H. M., Saunders, J. B., and Perch-Nielsen, K. (Eds.), *Plankton Stratigraphy*: Cambridge (Cambridge Univ. Press), 427–554.

Rahman, A., and Roth, P. H., 1989. Late Neogene calcareous nannofossil biostratigraphy of the Gulf of Aden region based on calcareous nannofossils. *Mar. Micropaleont.*, 15:1–27.

Ratcliffe, E. H., 1960. The thermal conductivities of ocean sediments. *J. Geophys. Res.*, 65:1535–1541.

Roth, P. H., and Coulbourn, W. T., 1982. Floral and solution patterns of coccoliths in surface sediments of the North Pacific. *Micropaleontology*, 7:1–52.

Sager, W. W., 1986. Magnetic-susceptibility measurements of metal contaminants in ODP Leg 101 cores. *In* Austin, J. A., Jr., Schlager, W., et al., *Proc. ODP, Init. Repts.*, 101: College Station, TX (Ocean Drilling Program), 39–46.

Saito, T., 1963. Miocene planktonic foraminifera from Honshu, Japan. *Tohoko Univ., Sci. Rept., 2nd Ser., (Geol.)*, 35:123–209.

Sakuyama, M., and Nesbitt, R. W., 1986. Geochemistry of the Quaternary volcanic rocks of the northeast Japan arc. *J. Volcanol. Geotherm. Res.*, 29:413–450.

Srivastava, S. P., Arthur, M., et al., *Proc. ODP, Init. Repts.*, 105: College Station, TX (Ocean Drilling Program), 61–418.

Stevenson, F. J., and Cheng, C. N., 1972. Organic geochemistry of the Argentine Basin sediments: carbon-nitrogen relationships and Quaternary correlations. *Geochim. Cosmochim. Acta*, 36:653–671.

Sun, S.-S., Nesbitt, R. W., and Sharaskin, A. Y., 1979. Geochemical characteristics of mid-ocean ridge basalts. *Earth Planet. Sci. Lett.*, 44:119–138.

Tamaki, K., 1986. Age estimation of the Japan Sea on the basis of stratigraphy, basement depth and heat flow data. *J. Geomagn. Geoelectr.*, 38:427–446.

_____, 1988. Geological structure of the Sea of Japan and its tectonic implications. *Chishitsu Chosasho Geppo*, 39:269–365.

Tamaki, K., Honza, E., Yuasa, M., Nishimura, K., and Murakami, F., 1981. Geological map of the central Japan Sea. Mar. Geol. Map Ser. 15, *Jpn. Geol. Surv.*, Scale 1:1,000,000.

Tatsumi, Y., Hamilton, D. L., and Nesbitt, R. W., 1986. Chemical characteristics of fluid phase from the subducted lithosphere: evidence from high pressure experiments and natural rocks. *J. Volcanol. Geotherm. Res.*, 29:293–309.

Tokuyama, H., Suyemasu, M., Tamaki, K., Nishiyama, E.-i., Kuramoto, S.-i., Suyehiro, K., Kinoshita, H., and Taira, A., 1987. Report on DELP 1985 cruises in the Japan Sea, Part II: seismic experiment conducted in the Yamato Basin, Southeast Japan Sea. *Tokyo Daigaku Jishin Kenkyusho Iho*, 62:347–365.

Waples, D. W., and Sloan, J. R., 1980. Carbon and nitrogen diagenesis in deep sea sediments. *Geochim. Cosmochim. Acta*, 44:1463–1470.

Wood, A. B., 1941. *A Textbook of Sound*: New York (MacMillan).

Wyllie, M.R.J., Gregory, A. R., and Gardner, L. W., 1956. Elastic wave velocities in heterogeneous and porous media. *Geophysics*, 21:41–70.

Yamano, M., Uyeda, S., Uyeshima, M., Kinoshita, M., Fujisawa, H., Nagihara, S., Boh, R., and Fujisama, H., 1987. Report on DELP 1985 cruises in the Japan Sea, Part V: heat flow measurements. *Tokyo Daigaku Jishin Kenkyusho Iho*, 62:417–432.

Yoshii, T., and Yamano, M., 1983. Digital heat flow data file around the Japan islands. Unpublished Data Files, Ocean Res. Inst., Univ. Tokyo.
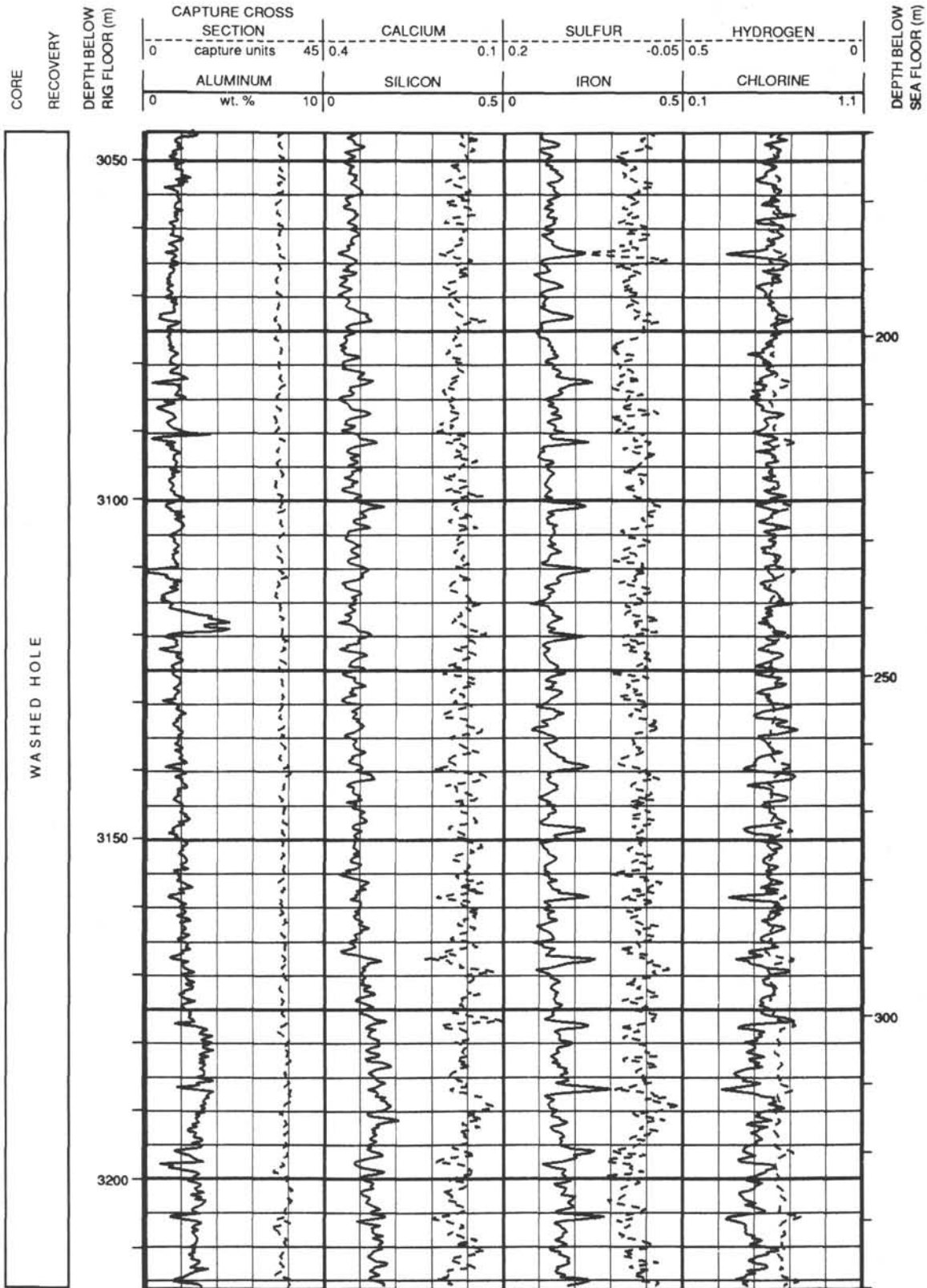
NOTE: All core description forms ("barrel sheets") and core photographs have been printed on coated paper and bound as Section 3, near the back of the book, beginning on page 425.
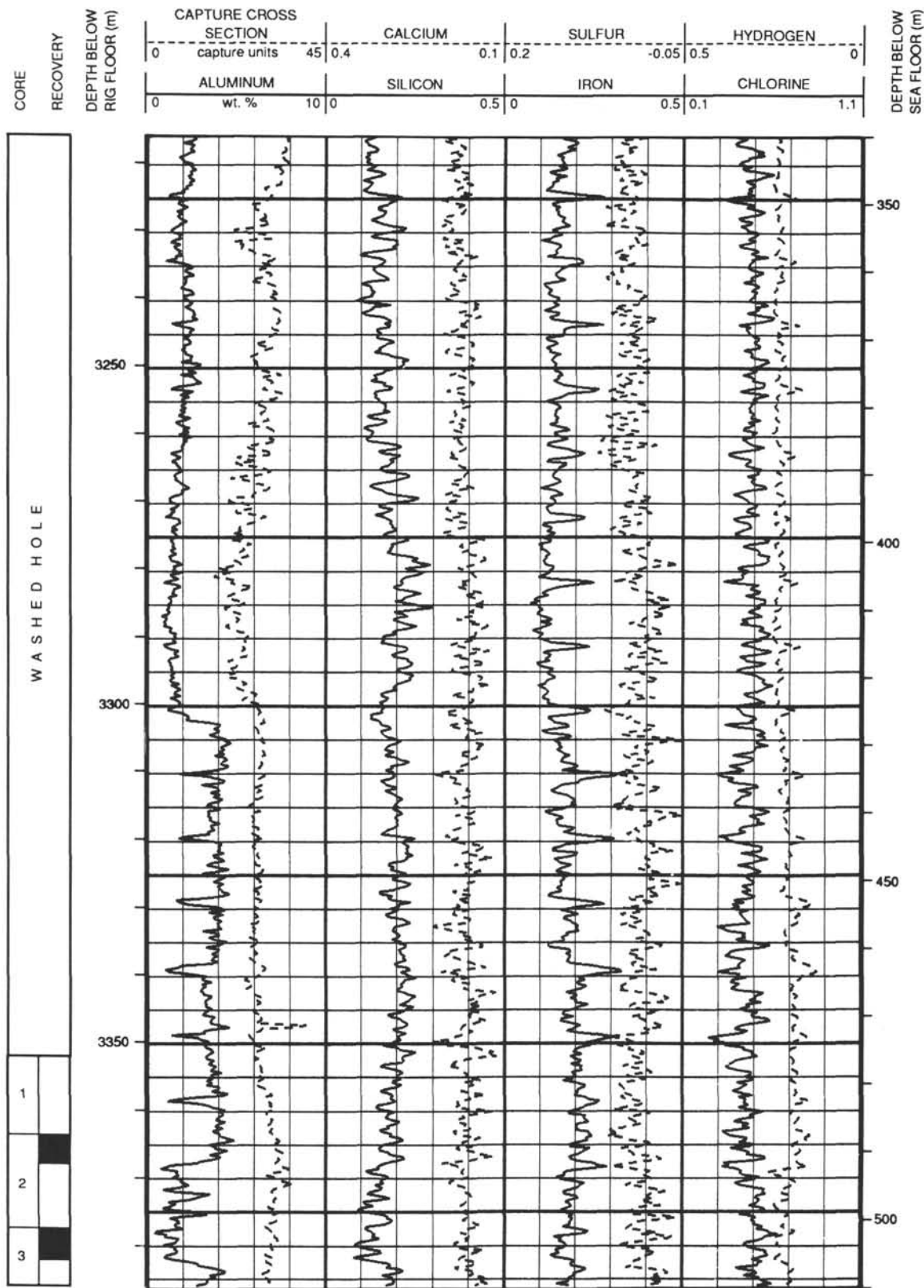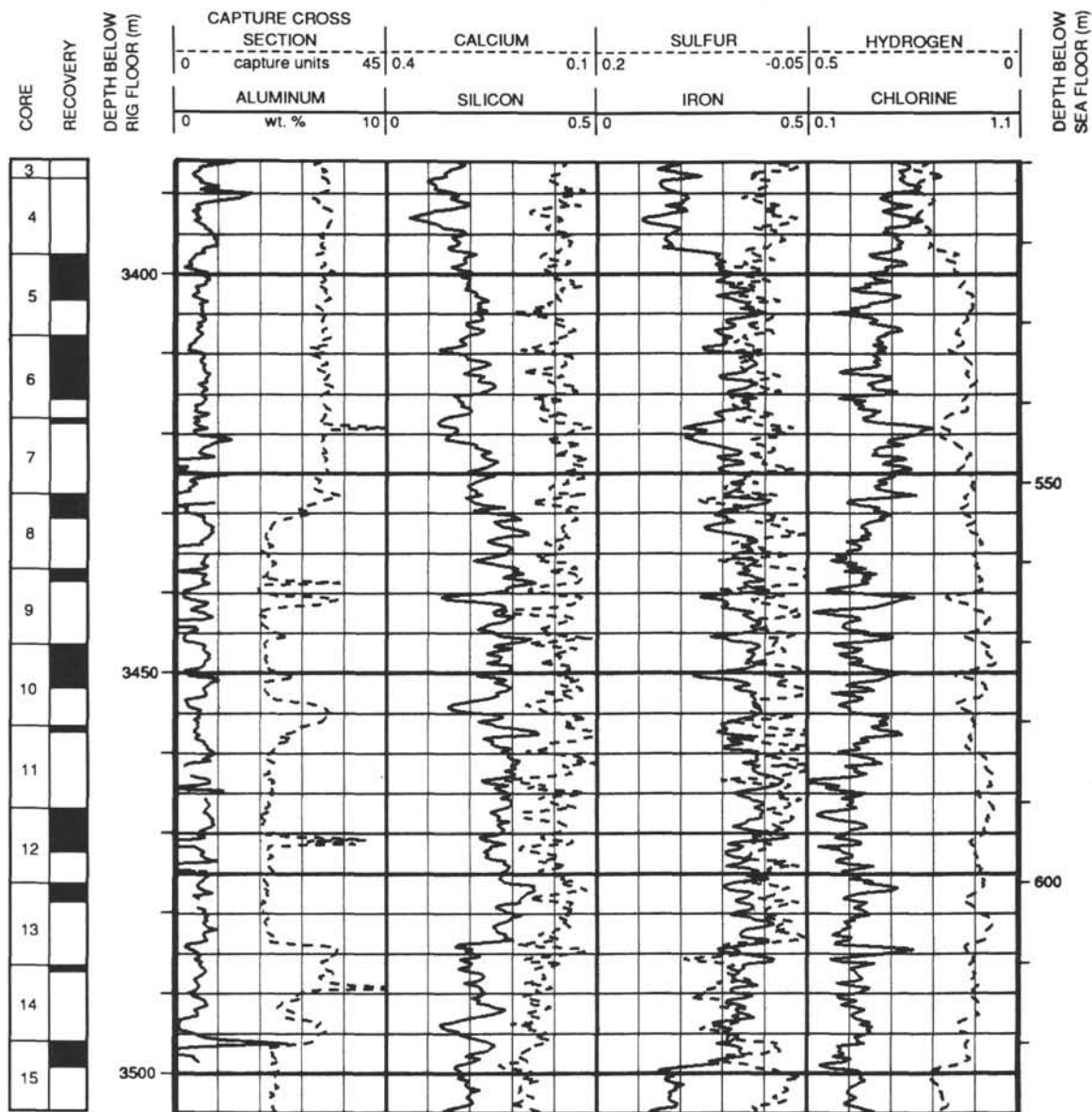
Summary Log for Site 797

Summary Log for Site 797 (continued)
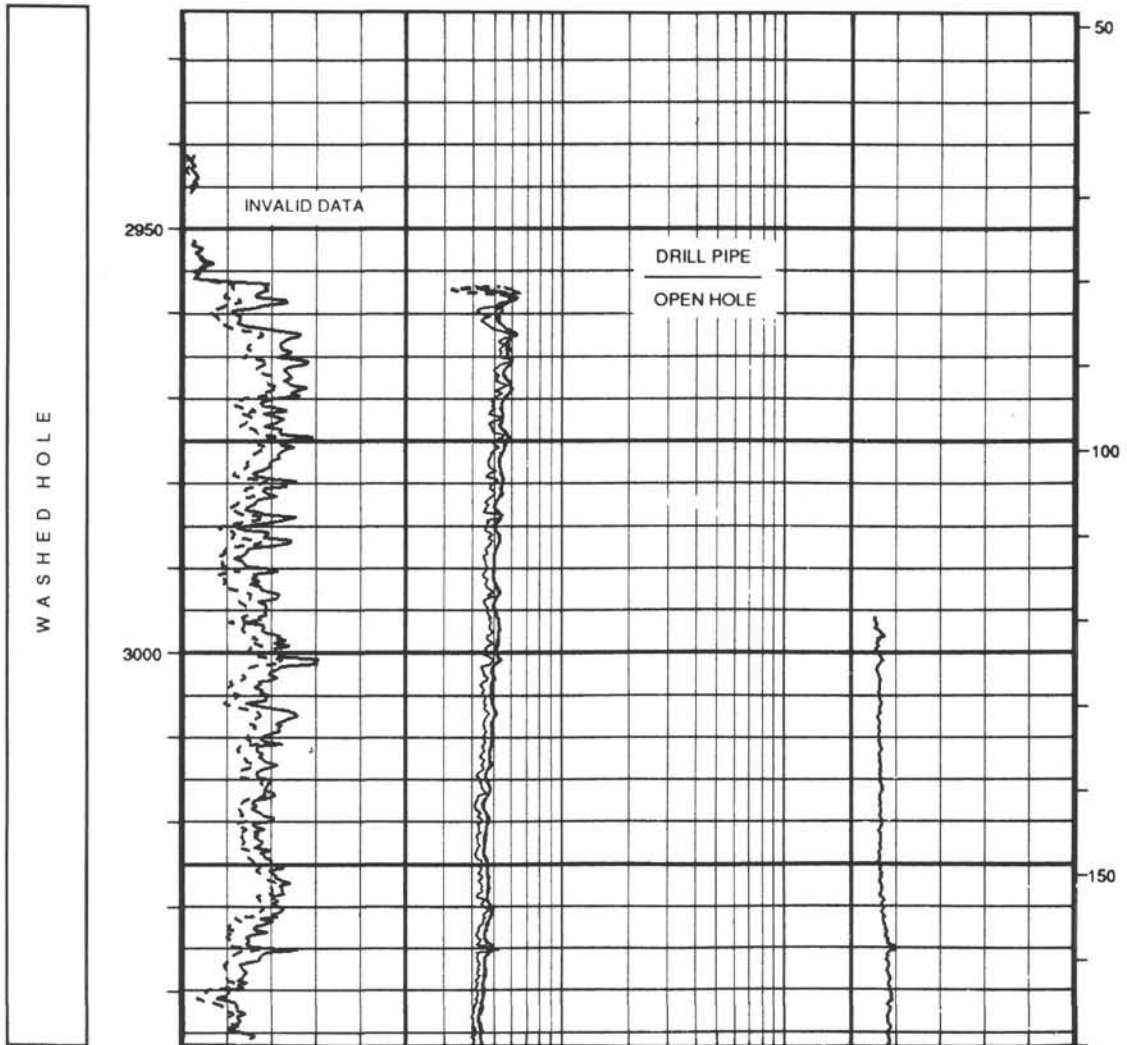
Summary Log for Site 797 (continued)
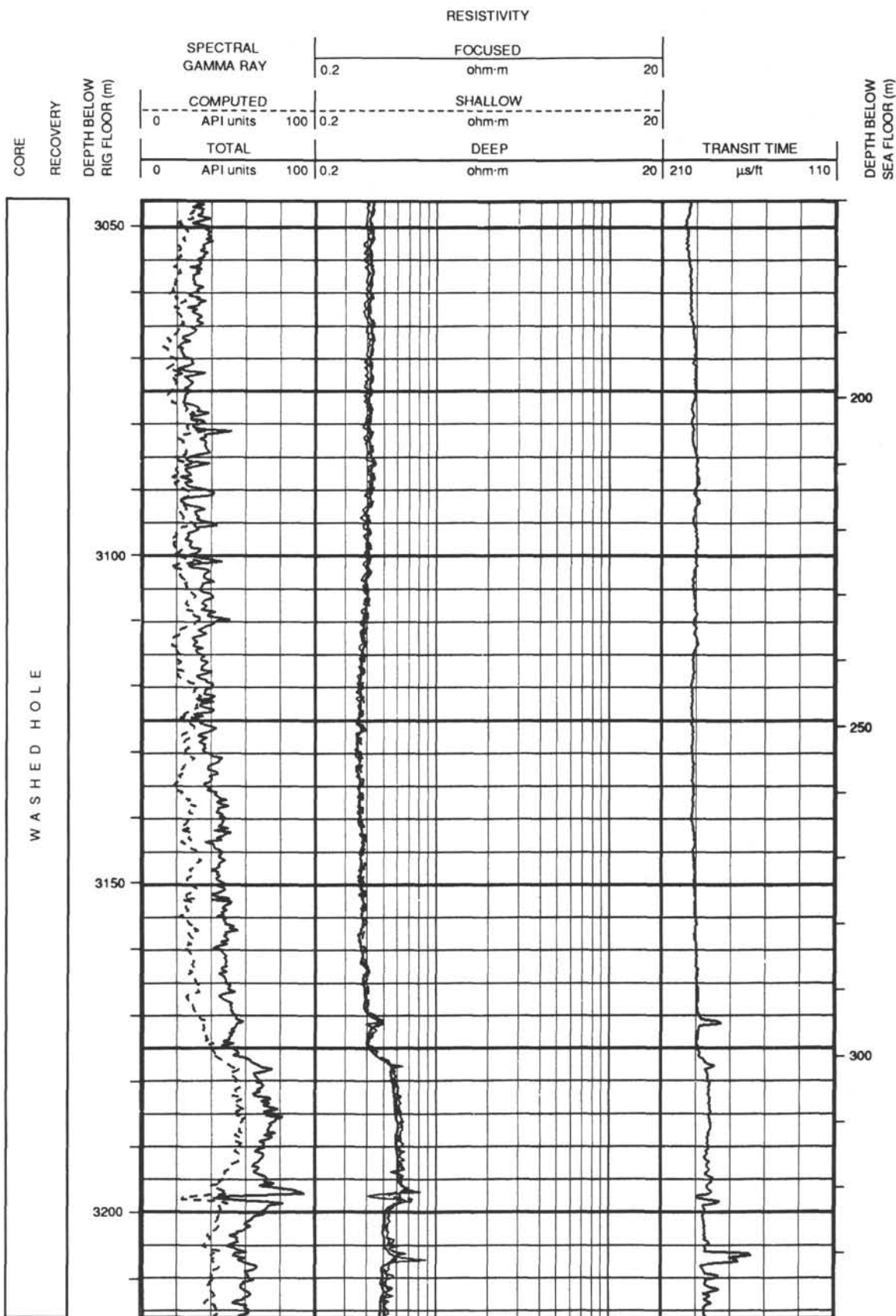
Summary Log for Site 797 (continued)

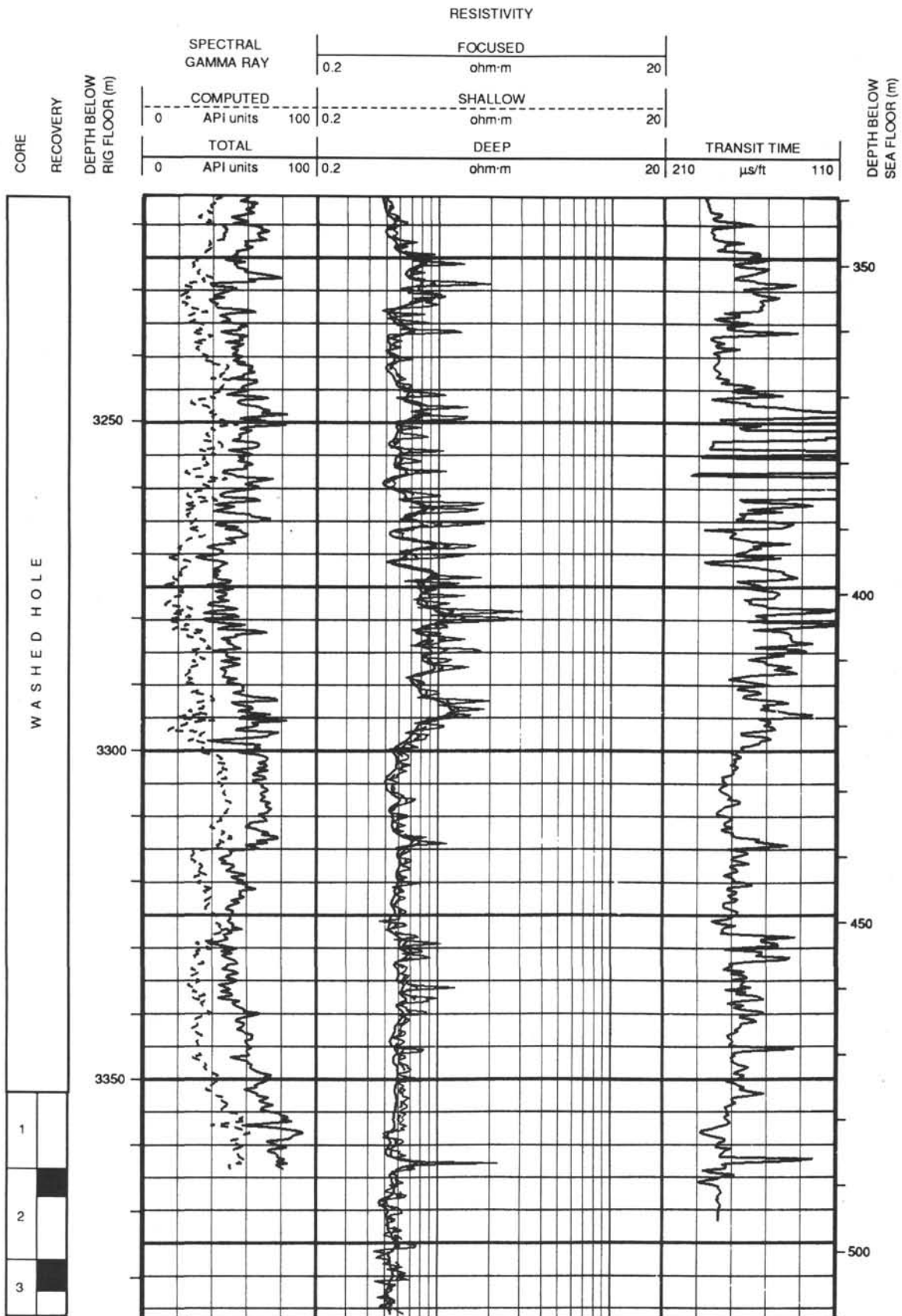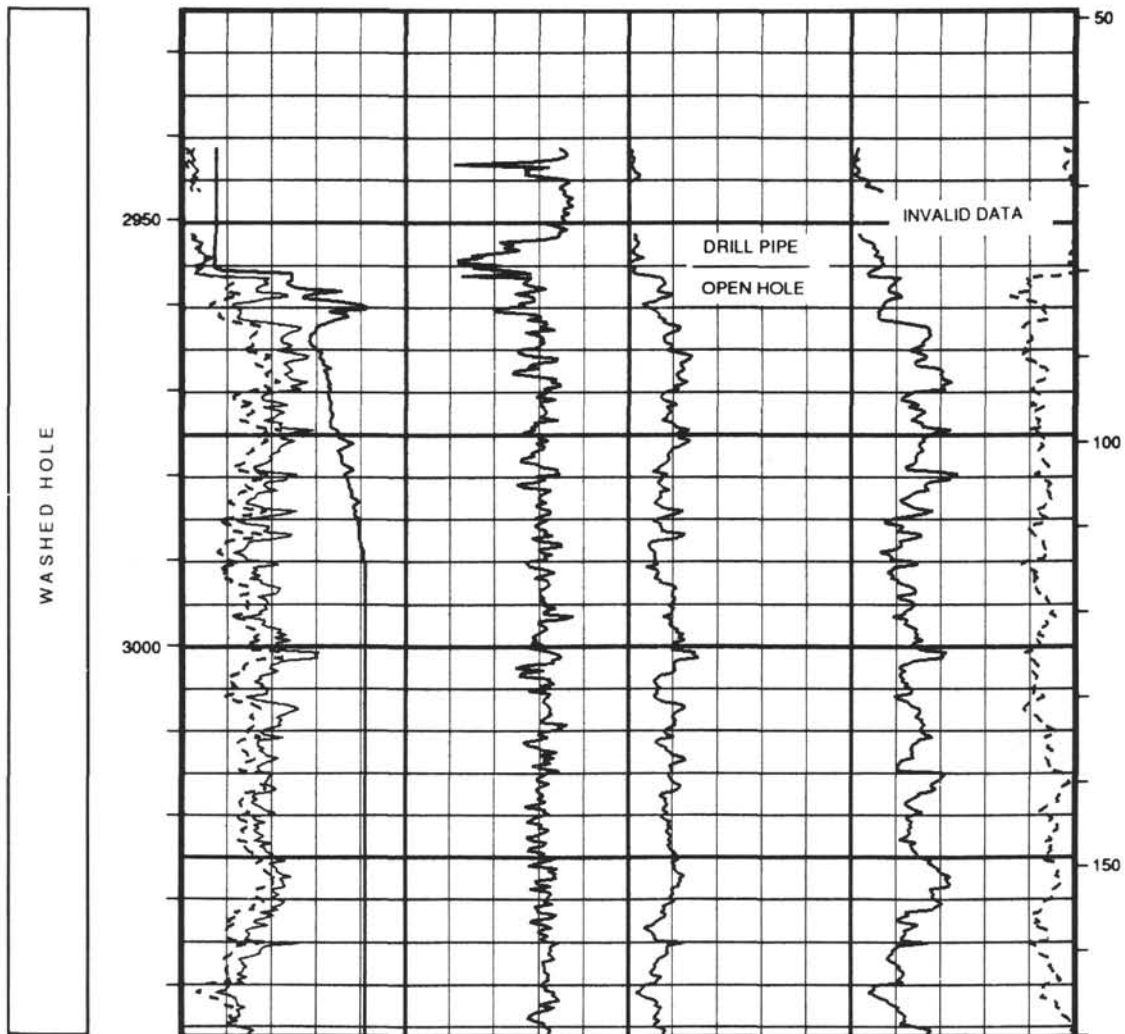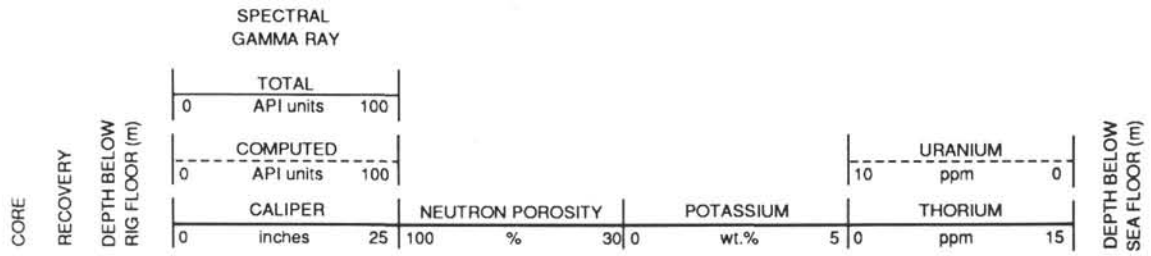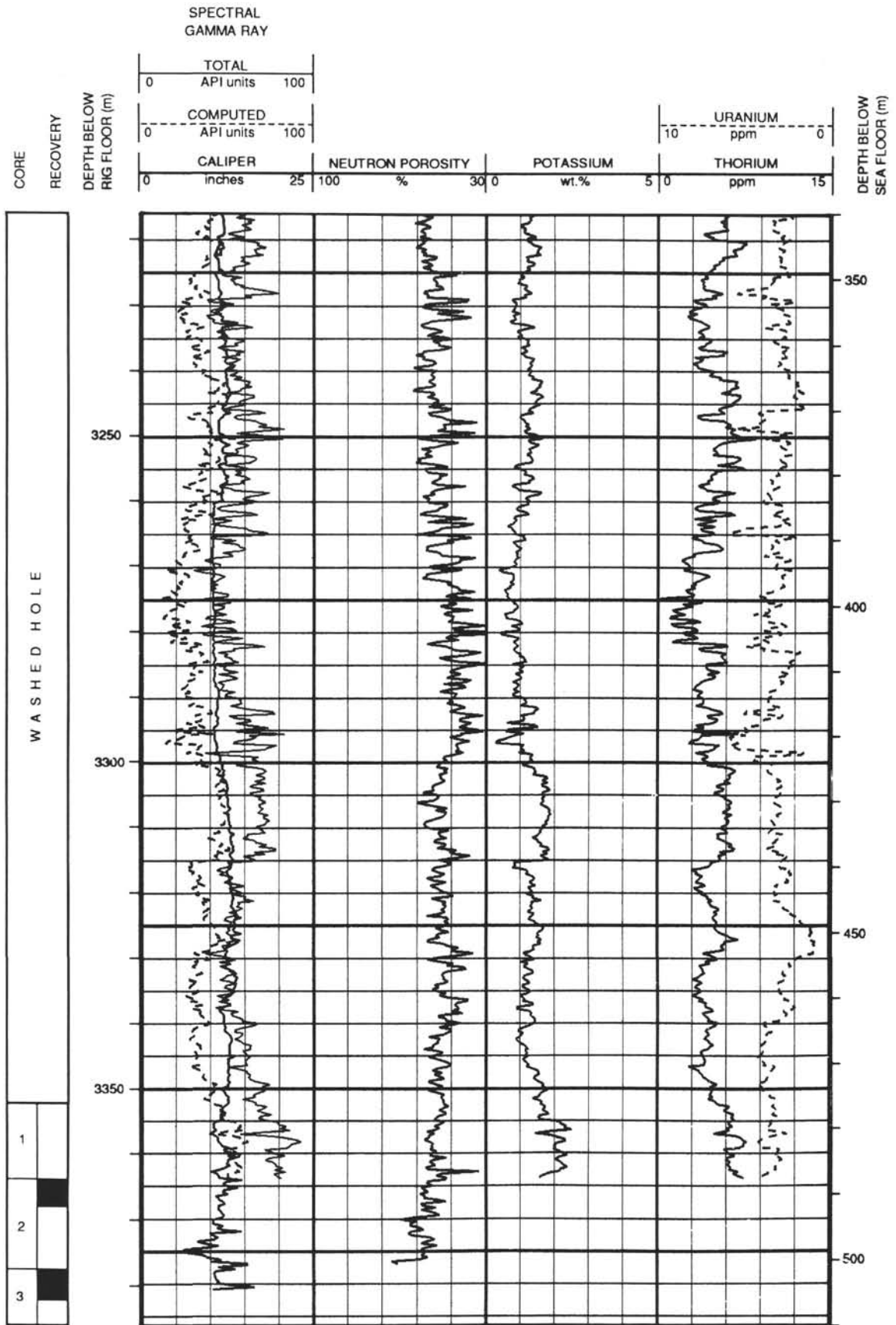## Summary Log for Site 797 (continued)

Summary Log for Site 797 (continued)

Summary Log for Site 797 (continued)

Summary Log for Site 797 (continued)

Summary Log for Site 797 (continued)

Summary Log for Site 797 (continued)